UNIVERSIDAD CARLOS III DE MADRID

TESIS DOCTORAL

Applications of Ring Resonators and Fiber Delay Lines for Sensors and WDM Networks

Autor:
Julio Montalvo García

Directora:
Carmen Vázquez García

DEPARTAMENTO DE TECNOLOGÍA ELECTRÓNICA

Leganés, Febrero de 2008

TESIS DOCTORAL

APPLICATIONS OF RING RESONATORS AND FIBER DELAY LINES FOR SENSORS AND WDM NETWORKS

Autor: Julio Montalvo García

Director/es: Carmen Vázquez García

Firma del Tribunal Calificador:

Firma

Presidente: Manuel López-Amo Sainz

Vocal: Pedro Corredera Guillén

Vocal: Bruno Fracasso

Vocal: José Manuel Baptista

Secretario: José Manuel Sánchez Pena

Calificación:

Leganés, de de

Agradecimientos

Quiero expresar mi agradecimiento a todas las personas que directa e indirectamente me han ayudado a finalizar este trabajo.

A mi madre; por su cariño, su sacrificio y su apoyo incondicional.

A todos mis amigos, por infundirme alegría y despejar mi mente en momentos de obcecación. A Emilio, Vicente y Manuel, por continuar ahí, por compartir sus puntos de vista y su talento conmigo.

A mis compañeros de piso, David y Gorka; por su paciencia, por aguantar mis cabreos y anotar mis frases apoteósicas.

A mis compañeros y mi maestro de aikido, por traer este deporte a la universidad.

A todos aquellos compañeros del Departamento de Tecnología Electrónica que, con su profesionalidad y respeto, me han servido de ejemplo y ayuda para superar las dificultades y conseguir mis objetivos. En especial a todos mis compañeros del Grupo de Displays y Aplicaciones Fotónicas, a todos los proyectandos, doctorandos, y doctores: por compartir su tiempo conmigo y hacerme sonreir siempre con su excelente sentido del humor. En el día a día, con ellos he podido entender mejor el sentido de todo el esfuerzo realizado durante estos años.

A todos los miembros de la secretaría del Departamente de Tecnología Electrónica, por sus gestiones y su atención.

A Carmen y Pepe; por haberme brindado múltiples oportunidades para aprender, y por sus aportaciones económicas en momentos difíciles.

Especial agradecimiento a Carmen, directora de este trabajo y núcleo impulsor del mismo; por haberme enseñado de primera mano la importancia de la precisión y la responsabilidad científica, por su confianza, su tolerancia y su fuerza.

También agradezco a los doctores Manuel López-Amo, Alayn Loayssa e Ignacio Matías su amable trato en Pamplona y sus valiosas sugerencias durante mi estancia en septiembre de 2006 en la Universidad Pública de Navarra.

Igualmente extiendo mis agracedimientos a los doctores José Manuel Baptista, José Luis Santos y Orlando Frazão por su supervisión y sus aportaciones esenciales a mi trabajo en la Unidad de Optoelectrónica y Sistemas Electrónicos del INESC[1], durante mi estancia en junio de 2007 en Oporto.

Asimismo, quiero agradecer al Dr. Kevin Heggarty su ayuda con el inglés científico y su excelente recibimiento en Brest durante la escuela de verano de ePhoton/ONe+ en Julio de 2007, y al Dr. Bruno Fracasso por sus clases de VPI y sus interesantes recomendaciones.

Finalmente, deseo expresar mi gratitud a todas las entidades financiadoras que han hecho posible en último término este trabajo: la Comunidad Autónoma de Madrid, el Ministerio de Educación y Ciencia, la Unión Europea y la Universidad Carlos III de Madrid. En concreto, debo mencionar a:

- Los proyectos de la Comisión Interministerial de Ciencia y Tecnología (CICYT): TIC2003-03783 (DISFOTON) y TEC2006-13273-C03-03-MIC (FOTOCOMIN).
- El programa de I+D+i de la Comunidad Autónoma de Madrid: FACTOTEM-CM (S-0505/ESP/000417).
- La Acción Integrada Hispano-Portuguesa del Plan Nacional de I+D+i 2004-2007: Self-referenced fibre optic intensity configurations for single and multi-sensors (HP2007-0093).
- El proyecto cofinanciado por la Universidad Carlos III de Madrid y la Comunidad Autónoma de Madrid: Fotónica en visualización, comunicaciones y sensores (CCG06-UC3M/TIC-0619).

---

[1] Instituto de Engenharia de Sistemas e Computadores do Porto.

- Las ayudas a la movilidad de investigadores en formación que me concedió la Universidad Carlos III de Madrid en 2006 y 2007.

- La Red Temática Europea SAMPA (HPRN-CT-2002-00202) del 5^o Programa Marco de la Unión Europea.

- La Acción Europea FIDES (COST Action 299) del 6^o Programa Marco de la Unión Europea.

- Y, por último, las Redes de Excelencia Europea ePhoton/ONe+ (FP6-IST-027497) y BONE (FP7-ICT-216863), del 6^o y 7^o Programa Marco de la Unión Europea, respectivamente.

Este trabajo es el resultado de mucho esfuerzo y una extensa colaboración entre múltiples personas, sin todas ellas no hubiera sido posible. ¡Muchas gracias a todos!.

Contents

3 Ring Resonator based Self-Referencing Techniques for Optical Intensity Sensors 65

List of Figures

Chapter 1

Introduction

1.1 About This Document

This document has been written in LaTeX and has been typeset using TeXShop, which is a Mac OS X program included in the free MacTex distribution and provided under the GNU General Public License (GPL).

The reference database of this research work has been managed using the freely distributable program JabRef, a bibliography reference manager using the BibTeX file format, the standard LaTeX bibliography reference format. JabRef is also provided under the GNU GPL.

Please visit http://www.gnu.org/licenses/ for more information about the licences.

1.2 Motivation and Objectives of This Work

The field of photonic technologies has been fostering intensive international research during the last years, focusing on the deployment of cost-effective optical technologies as the foundation for the future broadband services, as well as on the development and standardisation of optical fiber applications, such as remote optical sensing, biosensors, civil engineering, military applications and satellite communications.

In this general environment, this work specifically focuses on the development of new multiplexing and measurement techniques for optical sensors, as well as on the design, analysis and simulation of novel devices for future optical communication networks.

The work comprised in this document has been developed in the framework of the activities carried out in the Displays and Photonics Applications Group (GDAF) at University Carlos III of Madrid [1], which has been devoted for several years to the design and development of optical devices and sensors for their applications in Wavelength-Division-Multiplexed (WDM) networks.

The first objective of this work has been the development of new measurement techniques for optical sensors.

Intrinsically safe multimode (MM) and single-mode (SM) fiber sensors can be made for measuring a wide variety of physical magnitudes, such as strain, corrosion, humidity or temperature, among others. Recently, Photonic Crystal Fibers (PFC) are also offering new possibilities to fiber-based sensor devices.

On the one hand, one extensively investigated transducing mechanisms in optical sensing applications is the intensity modulation. Following simple configurations, intensity sensors modulate the optical power loss as the physical magnitude changes, thus providing the measurement as an optical intensity modulation signal. Single-mode fiber optic technology, with very low propagation loss (typically 0.2 dB/km), enables medium-reach networks with link lengths of up to 50 km without optical amplification, thus allowing an efficient remote interrogation of optical sensors.

Nevertheless, intensity sensors in remote configurations need a self-referencing method to minimize the influences of long-term aging of source and receptor characteristics, as well as undesirable random short-term fluctuations of optical power loss in the fiber link connecting the central office (CO), where the measurements are taken, to the remote sensing points, where the optical sensors are located.

Different self-referencing approaches, such as time normalization, fiber bypassing and frequency/wavelength normalization have been reported in the last two decades, providing mechanisms whereby the intensity variation of the light at the sensing head may be distinguished and measured independently of all the undesirable perturbations.

In the case of the frequency-based self-referencing methods, radio frequency (RF) modulated Fabry-Perot (FP), Mach-Zehnder, Michelson and Ring Resonator (RR) incoherent configurations in MM fiber technology have been reported.

In this work, we have studied and experimentally demonstrated new optical configurations based on RF modulated SM fiber ring resonators (RR), fiber delay lines (FDLs) and fiber Bragg gratings (FBGs), for addressing and self-referencing fiber-optic intensity sensors (FOS), both in transmission and reflection modes. The new methods achieve a significant flexibility and sensitivity enhancement with regards to previous measurement techniques, as well as compact sensing heads at the remote points and easy reconfiguration.

A second objective of this work has been to promote, study and verify new multiplexing strategies to implement and scale multi-sensor fiber optic networks using low-cost off-the-shelf devices, enhancing the power budget and keeping the self-reference of the measurements.

In order to achieve original contributions in this field of interest, we have focused in the low-cost Coarse WDM technology and the ITU-T G.694.2 recommendation, where a grid of wavelengths[1] with a 20 nm channel spacing for target distances of up to 50 km is specified. CWDM technologies have lately been promoted in the field of telecommunication as standards for metro applications with shorter distances, lower network capacity and cost than Dense WDM: they require simpler, wider tolerance laser manufacturing

---

[1] There are 18 wavelengths currently specified with nominal wavelengths ranging from 1270 nm to 1610 nm inclusive.

practices, less accurate laser temperature control and reduced design complexity and cost of optical filters. Moreover, in most of the situations, CWDM systems do not need optical amplification. These relaxed requirements make the CWDM technology an interesting approach for building low-cost self-referenced sensor networks, providing efficient routing of the optical power and compact topologies for remote addressing and self-referencing optical intensity sensors.

On the other hand, access networks deploying the traditional media by Digital Subscriber Line (DSL) or cable modem techniques, are reaching their limits, while the user bandwidth demands keep increasing. This growing demand for capacity in the access network drives optical fiber closer to the end user, being the architecture based on a Passive Optical Network (PON) a low-cost, scalable and efficient approach. Actually, Wavelength-Division-Multiplexed PONs are very recently being adopted by some operators for provisioning telephone, high-definition television and high-speed internet access (triple-play service).

In this work, we have studied and experimentally demonstrated new CWDM optical sensor networks, following the access PON architecture and simultaneously developing some of the proposed self-referencing techniques in reflection mode. With the CWDM PON architecture, the routing of optical power is optimized and the power budget of the sensor network is enhanced, permitting longer sensor interrogation distances. Moreover, a Dense WDM upgrade of the network for interrogating a large amount of sensors (around 200) has also been discussed.

Finally, in this work we have also considered the core and metro networks, in order to contribute to the strategic international objective of optical broadband communications and services. In this environment, optical high-speed transmission and all-optical switching are fundamental aspects of optical networking. In the international research scenario, new modulation formats, non-standard fibers and transparent transmission techniques, among other issues, are promoting intensive research. On the other hand, as the complexity and capacity of the network grows, new devices providing flexibility and tunability for performance optimization are required. Operation of the devices in the optical domain, with no need for optical-to-electrical conversion, is also a very desirable situation.

Optical ring resonators in coherent regime of operation, usually fabricated in integrated optic technology, have been used by researchers with a large variety of applications in high-speed Dense WDM (DWDM) optical communication networks. Several devices have been reported using this structure to achieve different devices such as all-optical tunable filters, add-drop multiplexers, modulators, dispersion compensators, delay lines, demultiplexers and switches, as well as photonic bio-sensors.

In this field of interest, the GDAF has recently proposed the ring resonator with an internal Sagnac cavity (RR-SG) as a novel photonic stage for all-optical signal processing in ultra-dense WDM systems [2, 3].

On the other hand, in fiber transmission links of core and metro networks operating at high bit rates, the chromatic dispersion (CD) can be one of the main restrictions to the system performance. CD is an intra-channel degradation effect that takes place as a short light pulse propagates along an optical fiber. In SMF links with typical chromatic dispersion of 17 ps/nm·km (G.652 standard), bit rates in the order of Gb/s at the C-band (1530-1565 nm) are critical for fiber links with distances larger than 100 km. Moreover, by using optical amplifiers, the power budget of an existing transmission link can be maintained for much longer distances, but the impact of CD is higher, because it is proportional to the length of the fiber, and the quality of the communications can decrease drastically.

In this work, we have proposed the RR-SG configuration as an optical filter for in-line chromatic dispersion management in high-speed digital transmission systems with optical fiber. An analytical study of the RR-SG filter is developed and simulations using VPIphotonics^{TM} software are reported, employing compound filters with RR-SG filters as Dispersion Compensating Modules (DCM) in SMF transmission links at 5 Gb/s with chromatic dispersion (CD) and noise from amplifiers.

1.3 Contents of the Work

In chapter 2 of this document, an introduction to the discrete-time optical signal processing [4] theory is reported, and the descriptions in the Z-Transform domain of common optical stages such as the Mach-Zehnder, Michelson, the Sagnac loop and the Ring Resonator configurations are studied. The main optical architectures based on the RR for digital filter synthesis and some RR-based devices recently fabricated in integrated optic technology are also briefly reviewed.

The notation given in this chapter serves as analytical framework for more complex problems considered in the next chapters of the document.

A novel self-referencing configuration using radio-frequency (RF) modulated fiber-optic ring resonators (RR) in transmission operation is reported in Chapter 3 of this document [5], achieving remote, all-optical and colorless self-referencing of optical intensity sensors. Two different self-referencing methods are comparatively studied and verified in the chapter, and an example of sucrose concentration sensor is reported and considered for self-reference and sensitivity optimization.

In Chapter 4, different reflective configurations using fiber Bragg gratings are reported for self-referencing intensity sensors. Fiber Bragg gratings are a nice approach to build reflective self-referencing configurations in remote sensing points. Reflective configurations permit to avoid an additional return fiber, thus achieving more compact and efficient sensor interrogation topologies. As the light passes through the sensor configuration twice, once for each sense of propagation, the measurement sensitivity is also enhanced. Finally, an interesting possibility that arises from the use of FBGs is the wavelength-division multiplexing of different sensors, because FBGs actually perform as wavelength-dependent optical reflectors.

Taking advantage of the properties and potential of FBGs, a novel RR configuration in reflection mode is proposed and demonstrated, employing a fiber Bragg grating in the RR through port [6].

Chapter 4 also comprises the study of a reflective configuration using two FBGs with different central wavelengths, with a fiber-optic intensity sensor and a fiber delay line located between them [7]. In the chapter, the frequency response of this all-optical configuration is described using the theory of digital filters, and a new self-referencing parameter with double sensitivity is proposed and verified, employing two different modulation frequencies.

Finally, a novel electro-optical configuration is reported, replacing the fiber delay line with an electronic delay in the reception stage, thus avoiding long fiber delay coils in the remote sensing points and achieving a compact, flexible and re-configurable self-referencing technique [8].

In chapter 5 of this document, a Coarse WDM Pasive Optical Network (PON) topology is studied and demonstrated for self-referencing optical intensity sensors. The network topology is verified using the two all-optical self-referencing methods described in Chapter 4, that is, the RR configuration in reflection mode [9] and the configuration with a fiber delay line and double sensitivity.

Chapter 6 studies the RR with an internal Sagnac loop (RR-SG) filter for chromatic dispersion management in digital transmission links over optical fiber. The configuration is related to the framework of all-pass filters and a modified configuration for enhancing the dispersion management potential of the RR-SG configuration is proposed. The chapter also reports advanced simulations of compound filters using RR and RR-SG stages in cascade, as Dispersion Compensating Modules (DCM) in high-speed optical transmission links, using software from VPIphotonics^{TM}.

The main conclusions of this work and future research tasks are reported in Chapter 7.

A summary of the work is written in Spanish in Chapter 8.

The basics of the VPI simulation software and other details of the simulations reported in Chapter 6 are given in Appendix A.

A detailed description of the calibrated measurements on optical ring resonators using the Agilent 8703B Lightwave Component Analyzer and some reference data about this instrument are given in Appendix B.

Finally, the list of references used for this research work and related publications and patents of the author are attached.

1.4 Acknowledgements

The research work of this dissertation has been supported by the following Spanish projects: TIC2003-03783 (DISFOTON) and TEC2006-13273-C03-03-MIC (FOTOCOMIN) of the Spanish Interministerial Comission on Science and Technology (CICYT), FACTOTEM-CM:S-0505/ESP/000417 and FENIS-CCG06-UC3M/TIC-0619 of Comunidad Autónoma de Madrid.

Additional financial support was obtained from the European Thematic Network SAMPA[2]: Synclinic and Anticlinic Mesophases for Photonic Applications (HPRN-CT-2002-00202), COST Action 299 FIDES: Optical Fibres Dedicated to Society, Integrated Action Hispano-Portuguesa (HP2007-0093) and from the European Networks of Excellence: ePhoton/ONe+ (FP6-IST-027497)[3] and BONE: Building the Future Optical

---

[2] SAMPA was carried out during the Fifth Framework Programme (FP5) of the European Union.

[3] COST Action 299 and ePhoton/ONe+ are supported by the Sixth Framework Programme (FP6) of the European Union.

Network in Europe (FP7-ICT-216863)[4].

Some results contained in chapter 3 were obtained during a research stay in September 2006 at the Department of Electrical and Electronics Engineering at Public University of Navarra, in the Group of Optical Communications and Electronic Applications, leaded by Prof. Dr. Manuel López-Amo.

Part of the work comprised in chapters 4 and 5 was done as a collaboration between the GDAF and INESC Porto, within the framework of the COST-299 Action FIDES, and the scientific supervisors of this collaboration were Carmen Vázquez and José Manuel Baptista. I thank both of them for both personal and scientific reasons. Orlando Frazão and José Luis Santos are also acknowledged for their essential contributions and kind assistance during my research stay at the INESC Porto facilities, from 7^{th} June to 7^{th} July.

Mobility Actions of University Carlos III of Madrid in 2006 and 2007 are acknowledged for funding the research stays in Pamplona (Spain) and Porto (Portugal).

Finally, the GNU Project, the Free Software Foundation (FSF), the TeX Users Group (TUG), and the developers of TexShop and JabRef are also acknowledged for their free software.

---

[4] BONE is supported by the Seventh Framework Programme (FP7) of the European Union.

Chapter 2

Introduction to Discrete-Time Optical Signal Processing

This chapter deploys the mathematical notation that will be followed in the rest of the document. Following the Z-Transform formalism, it describes a theoretical framework with the most important concepts regarding linear systems and signal processing focusing on the theory of optical filter design and analysis [10]. The notation links directly to the one employed in the signal processing toolbox of the software *Matlab*®, thus allowing quick calculations and easy programming.

The described mathematical analysis is applied to some of the most important optical configurations, such as the Mach-Zehnder, Michelson, Sagnac and Ring Resonator [11, 12]. In the reference [4] a general theory of microwave optical discrete-time signal processing is presented in more detail.

Some of the most relevant compound photonic architectures for digital filter synthesis are also briefly reviewed in this chapter.

2.1 Notation and Definitions

A discrete-time signal $x[n]$ is a finite or infinite sequence of numbers, generally complex. It can be obtained from sampling a continuous-time signal at instants $t = n \cdot \tau$, being τ the sampling period for integer n.

The impulse response of a multi-stage delay line optical filter, where every optical transit time is a multiple of a characteristic time delay τ, can be described using a sequence. In the analysis of this kind of filters, the delay time τ is identified with an equivalent sampling period, as in the case of a digital filter. This allows to employ very powerful and well established mathematical theories, as the Discrete Fourier Transform (DFT) and its generalization, the Z-Transform, for the study of this kind of optical filters.

In the following, an introduction to both transforms is attached with the definitions and notation that will be used all along this document.

2.1.1 Discrete Fourier Transform of a Sequence

The DFT of a sequence has the expression:

$$X(\Omega) = \sum_{n=-\infty}^{n=+\infty} x[n] \cdot \left(e^{j \cdot \Omega}\right)^{-n}, \quad \Omega \in \mathbb{R} \tag{2.1}$$

being X periodical with period 2π. Optical filters with characteristic transit times have always a periodical frequency response.

In the framework of this work, Ω represents the *angular frequency* (rad):

$$\Omega = \frac{2\pi f}{FSR} \tag{2.2}$$

where f is the frequency (Hz) and the Free Spectral Range (FSR) is defined as follows:

$$FSR = \frac{1}{\tau} \tag{2.3}$$

The *normalized frequency* is defined in the following way:

$$\nu = f \cdot \tau \tag{2.4}$$

Fourier Series Representation of Discrete-Time Signals

For a given finite sequence $x[n]$ of N numbers, the N coefficients of the Fourier series representation of the infinite periodical signal constructed from repeating the finite sequence are calculated through the expression:

$$c(m) = \sum_{n=0}^{N-1} x[n] \cdot \left(e^{j \cdot \frac{2\pi}{N} \cdot m}\right)^{-n}, \quad m = 0, \ldots, N-1 \tag{2.5}$$

In the former equation it can be noted that these coefficients correspond to the values of the DFT of the original finite sequence, but evaluated in N points, this is:

$$c(m) = X\left(\Omega = \frac{2\pi}{N} \cdot m\right), \quad m = 0, \ldots, N-1 \tag{2.6}$$

Matlat® provides quick algorithms to calculate the coefficients $c(m)$ of the Fourier series representation, by employing the command $FFT(X)$, being X a sequence of N numbers. If the DFT of the finite signal is wanted with high precision, it is usual to add zeros at the end of the signal in order to increase the number N and, as a consequence, the number of the calculated points of the DFT.

2.1.2 Z-Transform (ZT) of a Sequence

For a discrete-time linear time-invariant system with impulse response $h[n]$, the system response $y[n]$ to a complex exponential input z^n is:

$$y[n] = H(z) \cdot z^n \tag{2.7}$$

where:

$$H(z) = \sum_{n=-\infty}^{+\infty} h[n] \cdot z^{-n} \tag{2.8}$$

Equation (2.8), namely analysis equation, defines the Z-Transform of the system impulse response. This series does not necessarily converges in all the points of the complex plane, but only in the Region of Convergence (ROC).

The DFT is a particularization of the ZT, evaluated in the points of the circunference whose radius equals one. This can be seen comparing the expressions (2.1) and (2.8).

The environment of applications of this transform comprises the design and analysis of optical filters with characteristic transit times. This is caused, among other reasons, because of the fact that a delay time has a very simple representation in the ZT domain, because of the following property:

$$\partial[n-m] \leftrightarrow z^{-m} \tag{2.9}$$

This allows to obtain very easily the impulse response of delay line optical filters in the discrete-time domain and then, by using (2.9), achieving the system representation in the ZT domain in a very simple way. A detailed example of this procedure can be found in [12] for the optical ring resonator configuration.

The Z-Transform allows:

- the representation of digital systems in terms of blocks of linear and time-invariant systems, described with rational complex functions

- the analysis and characterization of the frequency response of digital filters in a comfortable way
- the study of the stability and frequency response of feedback systems using simple techniques

The techniques related to the Z-Transform theory are mainly the zero-pole diagrams, the root-locus analysis and the Nyquist stability criterion. These techniques can be directly employed for the case of optical delay line filters, as it will be shown in the following section and chapters.

2.2 Digital filters: Modelling Optical Configurations as Linear Systems

A linear optical filter with time delays multiples of a characteristic transit time τ can be modelled as a digital filter through the following difference equation:

$$y(n) = \sum_{k=0}^{M} b_k \cdot x(n-k) - \sum_{p=1}^{N} a_p \cdot y(n-p) \tag{2.10}$$

In Eq. (2.10) x represents the input sequence to the filter and y the output sequence. For feedback optical configurations N may tend to infinite.

For this kind of optical configurations, the transit time τ is physically related to the characteristic delay length L as follows:

$$L = \frac{c}{n_g \cdot \tau} \tag{2.11}$$

where c is the speed of light in vacuum and n_g is the effective group refractive index of the optical paths of the filter configuration. Any optical path of the optical configuration have a length L or an integer multiple.

The impulse response of the digital filter in the Z-Transform domain is:

$$H(z) = \frac{\sum_{k=0}^{M} b_k \cdot z^{-k}}{1 + \sum_{p=0}^{N} a_p \cdot z^{-p}} = \frac{B(z)}{A(z)} \tag{2.12}$$

Note that in Eq. (2.12), B and A are two polynomials with order M and N, respectively.

Matlab® provides the function $filter(B, A, X)$, which is useful to deploy the filtering algorithm described in the difference equation, taking as input values the sequence X, and using the characteristic polynomials B and A. Additionally, a number n of values of the frequency response of the filter can be calculated by using the available function $freqz(B, A, n)$.

The model using characteristic polinomials in the Z-Transform domain links the optical filters theory with the algebra of complex numbers, which is deeply developed from a mathematical point of view.

The roots (z_k) of the polinomial A are the *zeros* of the system transfer function; on the other hand, the roots (p_p) of the polinomial B are the *poles.* These roots are, in general, complex numbers.

An alternative to the representation in (2.12) where the poles and the zeros appear explicitly is:

$$H(z) = \Gamma \cdot \frac{\prod_{k=1}^{M}(1 - z_k \cdot z^{-1})}{\prod_{p=1}^{N}(1 - p_p \cdot z^{-1})} \tag{2.13}$$

The Z-Transform theory determines that for a stable filter the modules of the poles must be less than one ($|p_p| < 1$).

Matlab® allows to visualize the zeros and poles of any filter in the complex plane through the command $zplane(B, A)$, where A, B are given as row vectors.

When the module of a filter is evaluated in the unit circle of the complex plane, using the change of variable:

$$z = e^{j\cdot\Omega} \tag{2.14}$$

and Euler's identity:

$$e^{j\cdot\Omega} = \cos\Omega + j \cdot \sin\Omega \tag{2.15}$$

the system frequency response is obtained.

This model provides the physical interpretation of the optical configuration behavior by using:

$$\Omega = \frac{2\pi}{\lambda} \cdot n_g \cdot L = 2\pi \cdot \frac{n_g \cdot L}{c} \cdot f \tag{2.16}$$

In Eq. 2.16 λ, f are the operating optical wavelength and frequency, respectively. The latter equation reveals that Ω represents the optical phase shift of the optical wave at frequency f after propagation through the characteristic delay path.

Identifying 2.16 and 2.2, the physical meaning of the Free Spectral Range is also revealed:

$$FSR = \frac{c}{n_g \cdot L} \tag{2.17}$$

The system output magnitude tends to zero or to infinite in the frequencies corresponding to the roots whose module equals one, depending on wether they are zeros or poles, respectively. The zeros with module greater than one are called maximum-phase zeros; the zeros with module less than one are called minimum-phase zeros.

Digital filters with Finite Impulse Response (FIR) only have zeros in their transfer function, while Infinite Impulse Response (IIR) filters must have at least one pole in their transfer function.

By using the Z-Transform formalism, the frequency response of linear optical filters with a characteristic transit time can be analyzed in a very comfortable and efficient way. The mathematical framework can be useful not only for analysis, but also for the development of optical filter synthesis algorithms. Additionally, the theory can be easily interpreted from a physical point of view.

The following subsections develop the study of this theory in further detail.

2.2.1 Magnitude Response

The distance of the poles and zeros to the unitary circunference in the complex plane is the only aspect determining the magnitude response of a transfer function.

It is common to use the expression of the filter magnitude squared, which is:

$$|H(\Omega)|^2 = |\Gamma|^2 \cdot \frac{\prod_{k=1}^{M}\left(1 - 2|z_k| \cdot \cos(\Omega - \phi_{z_k}) + |z_k|^2\right)}{\prod_{p=1}^{N}\left(1 - 2|p_p| \cdot \cos(\Omega - \phi_{p_p}) + |p_p|^2\right)} \tag{2.18}$$

2.2.2 Phase Response: Group Delay and Quadratic Dispersion

The group delay, normalized with respect to the characteristic transit time τ, of a digital filter described with the Z-Transform, has the following expression:

$$\tau_n = -\frac{d}{d\Omega}\left[\arctan\left(\frac{\Im H(z)}{\Re H(z)}\right)\right] \tag{2.19}$$

The absolute group delay is:

$$\tau_g = \tau \cdot \tau_n \tag{2.20}$$

For a filter with M zeros and N poles, the general expression of the normalized group delay is:

$$\tau_n = \sum_{i=1}^{N} \frac{|p_i| \cdot (cos(\Omega - \phi_{p_i}) - |p_i|)}{1 - 2|p_i| \cdot \cos(\Omega - \phi_{p_i}) + |p_i|^2} - \sum_{i=1}^{M} \frac{|z_i| \cdot (cos(\Omega - \phi_{z_i}) - |z_i|)}{1 - 2|z_i| \cdot \cos(\Omega - \phi_{z_i}) + |z_i|^2} \tag{2.21}$$

Two zeros with inverse modules and the same phase provide a group delay which equals 1, thus achieving a filter with a linear phase response with frequency.

The normalized quadratic dispersion of a filter is defined as follows:

$$D_n = \frac{d\tau_n}{d\nu} \tag{2.22}$$

The absolute quadratic dispersion ($ps/nm \cdot km$) is:

$$D = -c \cdot \left(\frac{\tau}{\lambda}\right)^2 \cdot D_n \tag{2.23}$$

where c is the speed of light and λ represents the operating wavelength of the optical filter.

2.2.3 Regime of Operation of Optical Filters

When it is verified a deterministic relation between the optical phase of the different ports of an optical network, where an optical carrier has been launched into, the optical fields interfere in each port and the regime of operation is called *coherent*. This coherent regime of interference can be only achieved by employing optical sources with coherence time much greater than any transit time between the optical ports of the configuration.

On the other hand, when the coherence time of the optical source launched into the optical filter is much less than the transit times between the ports, the optical phase at each one is completely random. In this case, the optical power reaching the photodetector at an output port is obtained as the sum of the optical powers that contribute to the filter implementation. In this case, the regime of operation is called *incoherent*.

An approximation to the coherence length in vacuum for light with a Gaussian spectral profile is [13]:

$$L_{coh} \approx \frac{\lambda_0^2}{\Delta\lambda} \tag{2.24}$$

where $\lambda_0, \Delta\lambda$ are the central wavelength and the 3 dB bandwidth of the optical source. This equation is a good approximation to the spectral density distribution of the light from Light Emitting Diodes (LED) and Super-luminiscent LEDs (SLEDs).

In the following sections, the Z-Transform representations of some of the most important optical configurations are obtained. Single-mode propagation of the optical field is considered, and schematics using guided paths (either waveguides or optical fibers) are provided as photonic implementation of the configurations.

Optical couplers, see Fig. 2.1, are a common device for the configurations under study, being the matrix description of this element [11]:

$$\begin{pmatrix} Y_1 \\ Y_2 \end{pmatrix} = \sqrt{\gamma} \cdot \begin{pmatrix} \sqrt{1-\kappa} & j \cdot \sqrt{\kappa} \\ j \cdot \sqrt{\kappa} & \sqrt{1-\kappa} \end{pmatrix} \cdot \begin{pmatrix} X_1 \\ X_2 \end{pmatrix} \tag{2.25}$$

where x and y represent electrical fields, γ are the coupler power excess losses[1] and κ is the cross-coupling power coefficient.

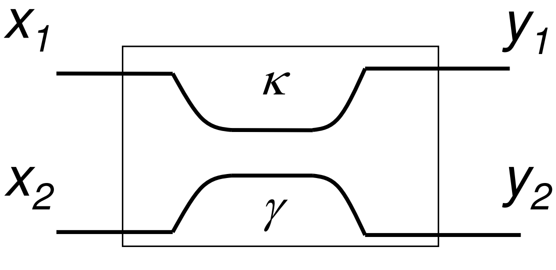

Figure 2.1: Schematic of an optical coupler.

For coherent filters the transfer functions represent the response in the optical field domain, while in the case of incoherent filters the transfer functions represent the response in the optical power domain.

---

[1] With this definition, for an ideal lossless coupler γ equals 1. The notation of this parameter in [11] is $1-\gamma$.

2.2.4 Insertion Losses of an Optical Filter

For coherent regime of interference, the transfer function of an optical filter has a spectral periodicity much greater than the spectral linewidth of the optical source. In this case, the optical power losses correspond to the squared magnitude response of the filter at the operating optical frequency.

On the other hand, for incoherent regime of operation, to obtain the total power attenuation of the light is not trivial. This is caused because the spectral periodicity, this is the FSR, is much smaller than the spectral width of the optical source. In this situation, the power density of the optical source is scaled by a different value at each optical frequency.

For this case it is very useful to model the input to an optical incoherent filter as a random complex signal. These signals are usually described by a reduced number of statistical parameters rather than using their samples, which are unpredictable in each realization of the experiment. Nevertheless, it is possible to know the effect of an optical filter over the random signal $x[n]$, called stochastic process.

For an stationary stochastic process $x[n]$, its autocorrelation is defined as follows [14]:

$$\phi_{xx}[m] = \varepsilon\left(x[n] \cdot x[n+m]\right) \tag{2.26}$$

where the operator $\varepsilon(\cdot)$ represents the average value of the signal at one instant.

On the other hand, for a filter with a known impulse response $h[n]$, its deterministic autocorrelation is defined as:

$$c_{hh}[m] = \sum_{k=-\infty}^{+\infty} h[k] \cdot h[k+m] \tag{2.27}$$

The DFT of this autocorrelation, namely $C_{hh}\left(e^{j\cdot\Omega}\right)$, is exactly the module squared of the DFT of $h[n]$:

$$C_{hh}\left(e^{j\cdot\Omega}\right) = \left|H\left(e^{j\cdot\Omega}\right)\right|^2 \tag{2.28}$$

The DFT of $\phi_{xx}[m]$, expressed as $\Phi_{xx}\left(e^{j\cdot\Omega}\right)$, represents the power spectral density of the input sequence $x[n]$. It can be shown that, when the sequence is a stationary stochastic process, the spectral density of the filter output, $\Phi_{yy}\left(e^{j\cdot\Omega}\right)$, follows the expression:

$$\Phi_{yy}\left(e^{j\cdot\Omega}\right) = \left|H\left(e^{j\cdot\Omega}\right)\right|^2 \cdot \Phi_{xx}\left(e^{j\cdot\Omega}\right) \tag{2.29}$$

On the other hand, the average of the total output power is obtained in the following way:

$$\varepsilon\left(y^2[n]\right) = \phi_{yy}[0] = \frac{1}{2\cdot\pi}\int_{-\pi}^{+\pi}\Phi_{yy}\left(e^{j\cdot\Omega}\right)d\Omega \tag{2.30}$$

For a stable digital filter $h[n]$, represented with the Z-Transform of its impulse response, $H(z)$, using the Weiner-Klintchine theorem (or Parseval's identity) it is obtained:

$$\sum_{i=-\infty}^{+\infty}|h(i)|^2 = \frac{1}{2\pi}\int_{-\pi}^{+\pi}\left|H\left(z=e^{j\cdot\Omega}\right)\right|^2\cdot d\Omega \tag{2.31}$$

Considering an input spectral density with a flat and unitary shape, this is, $\Phi_{xx}=1$, the total output power represents the power insertion losses of the optical filter $h[n]$, being (2.31) its expression.

For a finite impulse response with N values, the insertion losses can be calculated using the DFT:

$$\sum_{i=0}^{N-1}|h[i]|^2 = \frac{1}{N}\sum_{m=0}^{N-1}\left|H\left(\Omega=\frac{2\pi}{N}\cdot m\right)\right|^2 \tag{2.32}$$

For an infinite impulse response, an approximation to the insertion losses can be calculated employing eq. (2.32), using a large number of samples of the DFT.

2.3 The Michelson Interferometer (MI)

In Fig. 2.2 it is shown the photonic implementation of a Michelson interferometer using and optical coupler and Bragg gratings (BG), being $r_1(\lambda)$ and $r_2(\lambda)$ the reflectivities of the gratings as a function of the wavelength.

The guided optical paths are represented using lines as either waveguides or optical fibers.

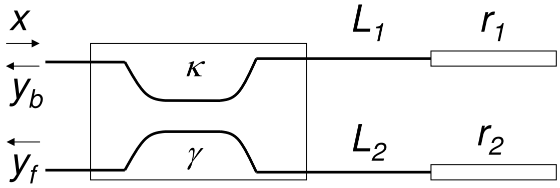

Figure 2.2: Optical Michelson Interferometer (MI) schematic using guided optics.

In the following, the transit times within the two BG branches are considered to be identical, this is $L = L_1 = L_2$. On the other hand, optical interference is taken as a premise, so a coherent behavior of the configuration is considered.

The transfer functions from the input port x to the output ports using the Z-Transform are the following:

$$H_b(z) = \frac{Y_b(z)}{X(z)} = \gamma \cdot [(1-\kappa) \cdot r_1(\lambda) - \kappa \cdot r_2(\lambda)] \cdot z^{-1} \tag{2.33}$$

$$H_f(z) = \frac{Y_f(z)}{X(z)} = -j \cdot \gamma \cdot \sqrt{\kappa \cdot (1-\kappa)} \cdot [r_1(\lambda) + r_2(\lambda)] \cdot z^{-1} \tag{2.34}$$

H_f represents the transmissive transfer function, while H_b represents the reflective transfer function. Both functions represent the electrical field of the optical wave.

As it has been stated previously, by using the change of variable $z = e^{j\cdot\Omega}$ and Euler's identity $e^{j\cdot\Omega} = \cos\Omega + j \cdot \sin\Omega$, being $\Omega = 2\pi \cdot \frac{n_g \cdot L}{c} \cdot f$, the response of the system with regards to frequency f can be obtained[2].

The most useful implementation takes place in the case of identical Bragg gratings, achieving a compensated interferometer. It is interesting to highlight the fact that the reflective output is zero for $\kappa = 0.5$. In any case, the frequency response is constant all along the bandwidth of the Bragg gratings.

2.4 The Sagnac Interferometer (SGI)

In Fig. 2.3 it is shown a Sagnac interferometer schematic constructed in guided optics.

As in the case of the Michelson interferometer, a coherent interference is considered. The parameter H represents the power balance within the feedback loop, identical in both senses of light propagation. If optical attenuation takes place in the loop, then $H < 1$; on the opposite, if optical amplification is verified, $H > 1$.

Considering $X_2 = 0$ and using the Z-Transform, the transfer functions from port x_1 to the output ports y_1, y_2 are the following:

$$H_1(z) = \frac{Y_1(z)}{X_1(z)} = j \cdot 2 \cdot \gamma \cdot \sqrt{\kappa \cdot (1-\kappa)} \cdot \sqrt{H} \cdot z^{-1} \tag{2.35}$$

$$H_2(z) = \frac{Y_2(z)}{X_1(z)} = \gamma \cdot (1 - 2 \cdot \kappa) \cdot \sqrt{H} \cdot z^{-1} \tag{2.36}$$

The magnitude response of this coherent configuration is constant, as in the case of the coherent Michelson interferometer. Both configurations are usually employed as part of compound optical configurations in coherent operation to achieve more flexibility and higher order filters.

---

[2] The parameters c, n_g are the speed of light in vacuum and the effective group refractive index in the optical delay length L, respectively.

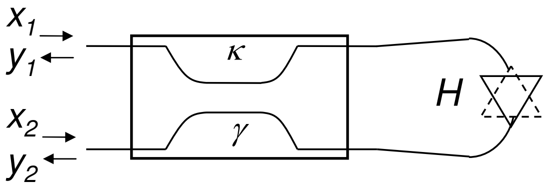

Figure 2.3: Optical Sagnac Interferometer (SGI) schematic using guided optics.

2.5 The Mach-Zehnder Interferometer (MZI)

Fig. 2.4 shows the schematic of an optical Mach-Zehnder interferometer using guided optics, being γ_1, γ_2 and κ_1, κ_2 the couplers excess losses and power cross-coupling coefficients, respectively.

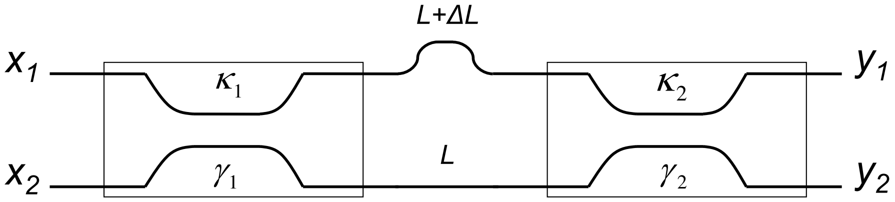

Figure 2.4: Optical Mach-Zehnder Interferometer (MZI) schematic using guided optics.

The electrical input and output fields are related as follows:

$$\begin{pmatrix} Y_1 \\ Y_2 \end{pmatrix} = \Phi_{MZI} \cdot \begin{pmatrix} X_1 \\ X_2 \end{pmatrix} \tag{2.37}$$

For ΔL much smaller than the coherence length of the optical source launched into the configuration, a coherent interferometer is achieved.

The complete analytical expression of the matrix Φ_{MZI} is [10]:

$$\Phi_{MZI} = \sqrt{\gamma_1 \cdot \gamma_2} \cdot \begin{pmatrix} H_{11}(z) & H_{12}(z) \\ H_{21}(z) & H_{22}(z) \end{pmatrix} \tag{2.38}$$

where[3]:

$$H_{11} = -\sqrt{1-\kappa_1} \cdot \sqrt{1-\kappa_2} + \sqrt{\kappa_1 \cdot \kappa_2} \cdot z^{-1} \tag{2.39}$$

$$H_{12} = j \cdot \left(\sqrt{(1-\kappa_1) \cdot \kappa_2} + \sqrt{\kappa_1 \cdot (1-\kappa_2)} \cdot z^{-1} \right) \tag{2.40}$$

$$H_{21} = j \cdot \left(\sqrt{\kappa_1 \cdot (1-\kappa_2)} + \sqrt{(1-\kappa_1) \cdot \kappa_2} \cdot z^{-1} \right) \tag{2.41}$$

$$H_{22} = \sqrt{\kappa_1} \cdot \sqrt{\kappa_2} - \sqrt{(1-\kappa_1) \cdot (1-\kappa_2)} \cdot z^{-1} \tag{2.42}$$

All these transfer functions have the form of FIR filters with one zero. In the book [10] these are named single-stage moving average (MA) filters.

For this configuration, the characteristic transit time and the free spectral range are calculated in the following way:

$$\tau = \frac{c}{n_g \cdot \Delta L} \tag{2.43}$$

$$FSR = \frac{1}{\tau} \tag{2.44}$$

While in the former Michelson and Sagnac coherent interferometers neither zeros nor poles take place in the frequency response, in the case of the Mach-Zehnder both output responses show one zero.

For any optical configuration represented in the Z-Transform domain, it is important to calculate the frequencies in which the minimum transmission may take place. This calculation is reported in the next subsection for the coherent Mach-Zehnder interferometer.

---

[3] The off-diagonal transfer functions H_{12}, H_{21} are the opposite to the ones in [10], because in this reference a minus sign is added to the cross-coupling coefficients of the coupler model described in Eq. 2.25.

2.5.1 Location of the Zeros of the MZI

The zero transmission in H_{11} and H_{22} occurs in the normalized frequencies:

$$\nu = n, \quad n = 0, 1, \ldots, \infty \tag{2.45}$$

while for H_{12} and H_{21} they take place in:

$$\nu = n + \frac{1}{2}, \quad n = 0, 1, \ldots, \infty \tag{2.46}$$

Provided the value of ΔL, the FSR is calculated through Eqs. 2.43 and 2.44, the absolute frequencies are found considering Eq. 2.4:

$$f = FSR \cdot \nu \tag{2.47}$$

2.6 The Optical Ring Resonator (RR)

Fig. 2.5 shows the schematic of an optical ring resonator built in guided optics, where H represents the power balance within the feedback loop[4].

The characteristic transit time τ of this configuration is found in the feedback loop as the light propagation time through the length L and is calculated with the next equation:

$$\tau = \frac{n_g \cdot L}{c} \tag{2.48}$$

where n_g is the effective group refractive index of the feedback path, being either a waveguide or an optical fiber.

The absolute frequency periodicity of the RR is the free spectral range, calculated

---

[4] In [11] the notation is slightly different, H representing the field balance within the loop, not the power balance.

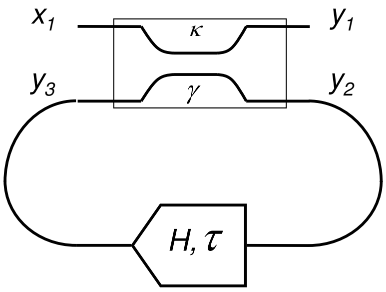

Figure 2.5: Optical Ring Resonator (RR) schematic using guided optics.

in the following way:

$$FSR = \frac{1}{\tau} \tag{2.49}$$

Depending on whether the coherence length of the employed optical source is higher or smaller than the delay length L, the regime of operation of the configuration will be coherent or incoherent. The transfer function of the ring resonator for both situations will be obtained in the next subsections using the Z-Transform formalism.

2.6.1 Analysis of the RR Coherent Interferometer

The transfer functions from input port x_1 to the output ports y_1, y_2, y_3 are obtained as the Z-Transform of the impulse responses of the configuration at each output.

The transfer function from x_1 to y_1 is the following:

$$H_1(z) = \frac{Y_1(z)}{X_1(z)} = \Gamma_1 \cdot \frac{1 - z_1 \cdot z^{-1}}{1 - p_1 \cdot z^{-1}} \tag{2.50}$$

where:

$$\Gamma_1 = \sqrt{\gamma \cdot (1-\kappa)} \tag{2.51}$$

$$z_1 = \sqrt{\frac{\gamma \cdot H}{1 - \kappa}} \tag{2.52}$$

$$p_1 = \sqrt{\gamma \cdot H \cdot (1 - \kappa)} \tag{2.53}$$

The transfer function from x_1 to y_2 is:

$$H_2(z) = \frac{Y_2(z)}{X_1(z)} = \Gamma_2 \cdot \frac{1}{1 - p_1 \cdot z^{-1}} \tag{2.54}$$

being:

$$\Gamma_2 = j \cdot \sqrt{\gamma \cdot \kappa} \tag{2.55}$$

Finally, the transfer function from x_1 to y_3 is:

$$H_3(z) = \frac{Y_3(z)}{X_1(z)} = \sqrt{H} \cdot \Gamma_2 \cdot \frac{z^{-1}}{1 - p_1 \cdot z^{-1}} \tag{2.56}$$

The three former transfer function represent electrical fields of the optical signal. The power magnitude response can be obtained considering Eq. 2.18. This power magnitude will be squared again when measuring the optical output with a square-law photodetector.

Location of the Zeros and Poles of the Coherent RR

Output y_1 is the only one with zeros in the corresponding transfer function, $H_1(z)$. The zero transmission at this output is achieved when z_1 lies on the unit circle and, more precisely:

$$z_1 = 1 \tag{2.57}$$

This condition implies a relation between κ and H which can be calculated using (2.52).

The zeros occur on the normalized frequencies:

$$\nu = n, \quad n = 0, 1, \ldots, \infty \tag{2.58}$$

as in the MZI.

Poles take place at the three considered outputs in the same normalized frequencies of Eq. 2.58. An infinite magnitude response is predicted when p_1 lies on the unit circle and, more exactly:

$$p_1 = 1 \tag{2.59}$$

Once again, this condition implies a relation between κ and H which can be calculated using (2.52). Nevertheless, $|p_1|$ must be less than 1 to assure filter stability.

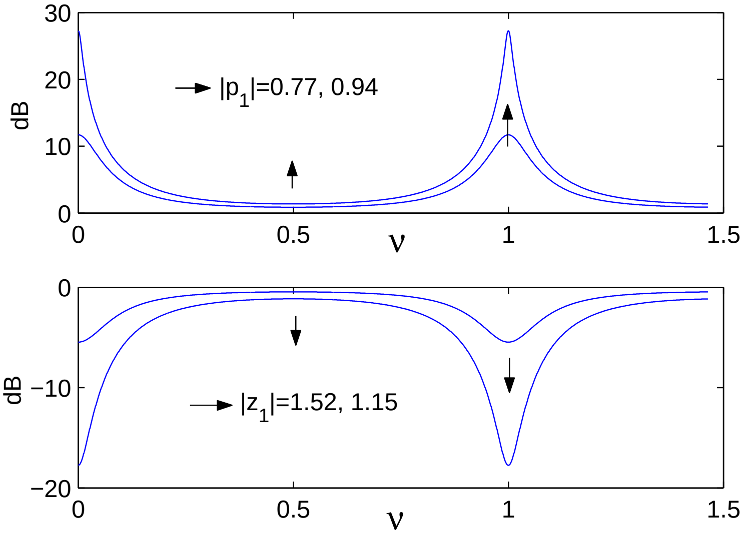

Figure 2.6: Optical power magnitude response of the coherent RR at output y_1 versus normalized frequency ν. $\gamma = 1, \kappa = 0.7$.

In Fig. 2.6 it is shown the optical power magnitude response of the coherent RR versus normalized frequency at output y_1 for different modules of the pole and zero as they tend to 1.

Ring Resonator Full Width Half Maximum ($FWHM$) and Finesse ($\digamma$)

In [15] the bandwidth in rad/seg within half the maximum magnitude response at the pole frequency, $FWHM$, is reported near the pole condition at output y_2 of the RR. The value of $FWHM$, neglecting the coupler excess losses, follows the expression [15]:

$$FWHM_{y_2} \simeq \frac{2 \cdot \kappa^2 \cdot c}{n_{ef} \cdot L} \tag{2.60}$$

In [16] the same parameter $FWHM$ is calculated at output y_1, within the points verifying the conditions:

$$|y_1(\Omega)|^2 = \frac{1 + |y_1|^2_{min}}{2} \tag{2.61}$$

In this situation, the parameter takes the value:

$$FWHM_{y_1} = \frac{1}{\pi \cdot \tau} \cdot \frac{1 - \sqrt{\gamma \cdot \ H \cdot (1-\kappa)}}{\left(\sqrt{\gamma \cdot \ H \cdot (1-\kappa)}\right)^{1/2}} \tag{2.62}$$

Eq. (2.60) is very interesting to calculate the linewidth of the emission modes of RR based lasers. On the other hand, eq. (2.62) can be used to estimate the waveguide power losses through indirect measurements using the RR configuration.

In both cases, the finesse $\digamma$ is defined as the ratio between the free spectral range and the full width half maximum:

$$\digamma = \frac{FSR}{FWHM} \tag{2.63}$$

Finally, the quality factor Q is defined as the ratio between the operating resonance frequency and $FWHM$.

Photonic Devices Based on the RR Coherent Configuration

Photonic devices in coherent regime of operation are usually the most suitable choice for high-speed optical signal processing in modern optical communication networks, because they have much smaller transit times than incoherent configurations and so their operation bandwidth is much higher.

Among the optical configurations serving as blocks for the synthesis of coherent photonic filters, the ring and disk resonators have received considerable attention.

From an experimental point of view, achieving a coherent optical signal processor in optical fiber technology comes up with serious difficulties. This is caused because the transfer function depends on the optical phase relation between the ports, and very slight variations of the fiber paths because of vibration or thermal expansion can alter drastically the filter frequency response. As a consequence, it is mandatory for any experimental set up of this kind that very stable platforms are employed. Even electronic feedback control systems may be necessary for a set up stabilization.

Despite these difficulties, fiber optic ring resonators in coherent regime of operation were verified experimentally with optical gain ($H > 1$) in 1991 [17] and an spectrum analyzer with resolution better than 100 KHz [18] was achieved using the configuration. On the other hand, passive fiber optic ring resonators ($H < 1$) in coherent regime were characterized in magnitude and phase in 1995 by employing a network analyzer [19] and using other techniques in 1996 [20]. More recently, the fiber optic ring resonator has been verified with a high finesse (F=56) [21] and compound structures using Sagnac loops within the RR feedback path have also been successfully demonstrated in passive configurations [22, 23].

In order to avoid the practical difficulties of achieving fiber ring resonators in coherent regime, the configuration is usually fabricated in integrated-optic technology with radius in the order of the micron. Currently, the microring and microdisk resonators are serving as basic elements for many integrated devices with applications in Dense WDM networks, such as high-order filters [24, 25], switches [26, 27], modulators [28, 29], add-drop filters [30, 31] and demultiplexers [32], among other devices.

Micro-ring resonators fabricated in planar technology offer significant advantages over discrete thin-film-filters (TFF), because arbitrarily high-order filters can be fabricated in a single dielectric layer, as opposed to the TFF, requiring hundreds of layers in some cases.

Integrated ring resonators have been demonstrated since the middle eighties in different technologies, such as GaAs/AlGaAs [33, 24, 34], Ge-doped SiO_2-Si [35], Si-SiO_2 [36, 30], SiON-SiO_2 [27, 37, 38], silicon-on-insulator (SOI) [39], InGaAsP/InP [40, 41, 42] and polymeric materials [43, 44]. The study of mode field profiles, bending and transition losses in curved optical channel waveguides is a very important issue, because these aspects are critical in the performance of ring-based photonic structures [45].

Different approaches for fixing the operation point of integrated ring resonators and for providing frequency tunability have been reported in the last decade. The quality factor and the critical coupling of the ring resonator can be controlled using the thermo-optic effect in waveguides [46], controlling the coupling factor between the waveguide and the resonator electro-optically [47, 40], by carrier injection [29] or through integration of a semiconductor optical amplifier in the ring [41]. On the other hand, frequency tunability can be achieved by using the thermo-optic effect [25, 27], by incorporating liquid crystals as cladding layers in SOI microring resonators [39], by illuminating the microdisk with infrared light [42] or by using an internal Sagnac loop in the ring [22, 23, 2].

2.6.2 Analysis of the RR Incoherent Configuration

Assuming an incoherent regime of operation, the transfer functions of the RR configuration, see Fig. 2.5, from input port x_1 to output ports y_1, y_2, y_3 are obtained as the

Z-transform of the corresponding impulse responses.

The transfer function from input x_1 to output y_1 $\left(H_1(z) = \frac{Y_1(z)}{X_1(z)}\right)$, follows the expression (2.50), being the parameters:

$$\Gamma_1 = \gamma \cdot (1 - \kappa) \tag{2.64}$$

$$z_1 = \gamma \cdot H \cdot \frac{1 - 2 \cdot \kappa}{1 - \kappa} \tag{2.65}$$

$$p_1 = \gamma \cdot H \cdot (1 - \kappa) \tag{2.66}$$

The transfer function from input x_1 to output y_2 $\left(H_2(z) = \frac{Y_2(z)}{X_1(z)}\right)$ follows the expression of 2.54 with:

$$\Gamma_2 = \gamma \cdot \kappa \tag{2.67}$$

Finally, the transfer function from input x_1 to y_3 is:

$$H_3(z) = \frac{Y_3(z)}{X_1(z)} = H \cdot z^{-1} \cdot H_2(z) \tag{2.68}$$

The three former transfer functions represent the optical power response of the incoherent RR. These functions will be squared when measured with an standard photodetector following a square-law detection, thus the measurements would correspond exactly with the result given by Eq. 2.18 using the equations given in this subsection.

From an experimental point of view, the incoherent RR is much more stable and repeatable than the coherent RR interferometer. The reason is that the optical phase relation between optical waves is completely random, so no optical interference takes place. The response at each port consists of the power addition of all the lightwaves propagating through the configuration.

Location of the Zeros and Poles of the Incoherent RR

The zeros of the incoherent RR configuration take place only at output y_1 in the normalized frequencies:

$$\nu = \frac{2 \cdot n - 1}{2}, \quad n = 1, 2, \ldots, \infty \tag{2.69}$$

In order to achieve a zero transmission at these frequencies it is mandatory that $\kappa > 0.5$, otherwise the filter would be unstable. It can also be demonstrated that the zero transmission can be obtained without optical gain ($H < 1$) only for $\kappa > 2/3$. This is an important information for the applications of RR-based self-referencing techniques in passive wavelength multiplexed sensor networks, as it will be studied more deeply in the next chapter.

For outputs y_2, y_3 the poles of the incoherent RR configuration take place at the normalized frequencies:

$$\nu = n, \quad n = 1, 2, \ldots, \infty \tag{2.70}$$

The optical power magnitude response of the incoherent RR at output y_1 is shown in Fig. 2.7 versus normalized frequency ν for different modules of $|z_1|, |p_1|$.

2.6.3 Insertion Losses of the Incoherent RR

As it will be deeply studied in the next chapter of this document, the output y_1 of the incoherent RR can be very useful for self-referencing remote fiber-optic intensity sensors. In the case of multiplexed optical sensor networks, the optical power budget must be considered very carefully to achieve the desired signal to noise ratio in the measurements. The insertion losses of any optical configuration used in the remote sensing point play an important role to calculate the network power budget, thus allowing to design the

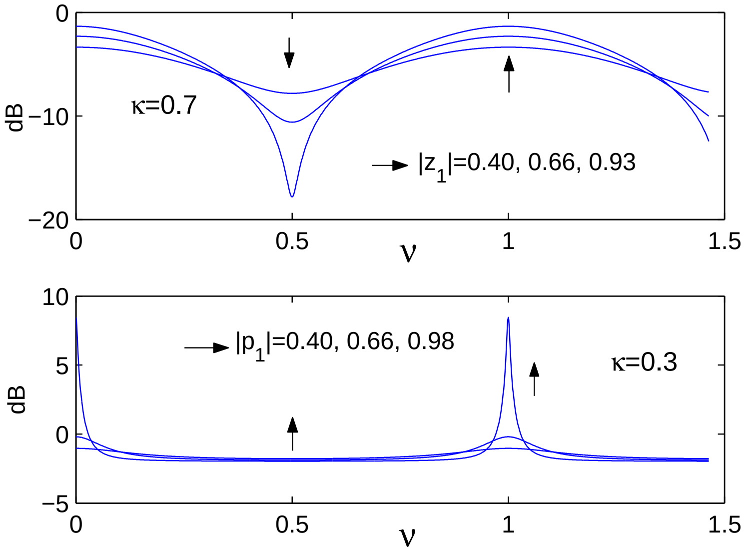

Figure 2.7: Optical power magnitude response of the incoherent RR at output y_1 versus normalized frequency ν. $\gamma = 1$.

complete network regarding maximum distance and number of multiplexed sensors.

In Fig. 2.8 the RR power insertion losses from x_1 to output y_1 are shown versus the cross-coupling coefficient κ at the resonance condition ($|z_1| = 1$) and for two more cases around it; firstly, for H being 1.5 dB above the resonance condition ($|z_1| = 1.41$) and, secondly, for H being 1.5 dB below resonance ($|z_1| = 0.71$). The effect of the coupler excess loss γ is also considered in the figure.

The graph has been obtained providing Eqs. 2.32 and 2.50 to the software $Matlab$® using the parameters corresponding to the incoherent RR configuration.

The figure shows how the optical power losses from input to output increase with the cross-coupling factor, losing more than 10 dB for cross-coupling factors around 0.95.

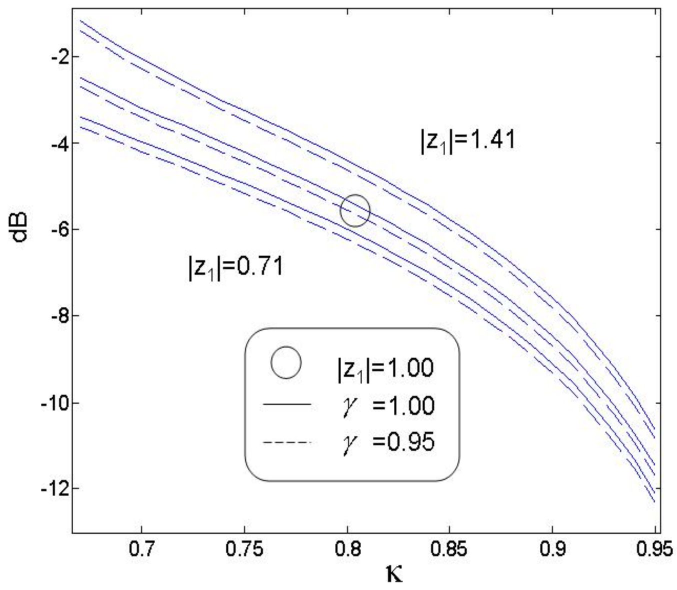

Figure 2.8: Optical insertion losses of the incoherent passive RR at output y_1 versus cross-coupling factor κ near resonance ($|z_1| = 1$).

2.7 Compound Photonic Filters

In order to enhance the performance and provide more flexibility to a photonic configuration, it is usual to interconnect different stages to form a compound filter of a higher order than the isolated stages. Several compound architectures for IIR and FIR photonic filter synthesis have been reported in the last two decades. In this section, some of the most relevant are briefly reviewed.

2.7.1 FIR Photonic Filters Architectures

A tapped delay line structure form (transversal filter), consisting of an optical waveguide with taps distributing at constant intervals along its length, was reported by Sasayama et al. in 1991 [48]. The general architecture is shown in Fig. 2.9.

The structure provides coherent combination of tapped signals, using phase-shifters, tunable power splitters and a combiner. Optical transversal filters are Finite Impulse

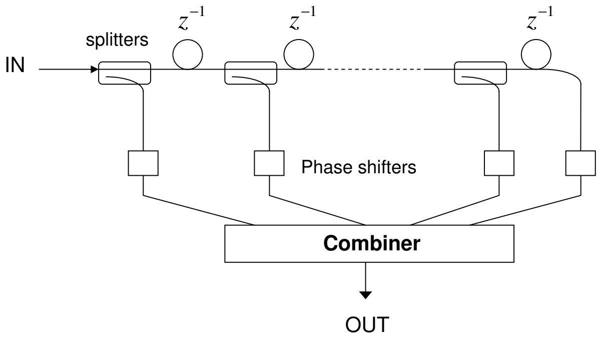

Figure 2.9: General photonic architecture for synthesis of transversal filters.

Response filters which, using coherent interference, can express arbitrary tap-weighting coefficients. Photonic filters with 4 and 8 taps, capable of processing broadband signals over 4 THz and performing an out-of-band rejection ratio above 20 dB were actually fabricated using silica-based single-mode waveguides, monolithically integrated on a silicon substrate [48].

The synthesis of FIR filters using coherent Mach-Zehnder interferometers (MZI) coupled along a straight waveguide in a lattice structure, using directional couplers, optical delay lines and phase shifters, was reported by K. Jinguji and M. Kawachi in 1995 [49]. The circuit configuration of the proposal is shown in Fig. 2.10(a). By using the proposed synthesis technique, the designs for a linear phase Chebyshev filter, a multi-channel selector and a group-delay dispersion equalizer were obtained.

More recently, design algorithms employing Mach-Zehnder lattice configurations have been reported to realize FIR half-band filters, achieving the desired power transmittance spectra with a reduced number of photonic components [50].

2.7.2 IIR Photonic Filters Architectures Using MZI and RR

A photonic filter synthesis technique employing fiber couplers, delay lines and phase shifters to form independent multi-stage all-pole and all-zero configurations was reported

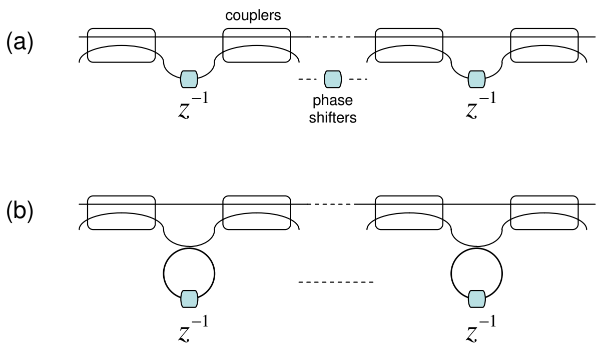

Figure 2.10: MZI lattice (a) and MZI lattice with ring resonators (b).

in 1994 by Ngo et al. [51] for applications in long-haul coherent lightwave transmission systems. It is assumed that the coherence length of the optical source is much longer than the basic length of the fiber delay lines, in order to allow coherent interference of the delayed signals in the system. The schematics of the proposed blocks for the general synthesis architecture are shown in Fig. 2.11.

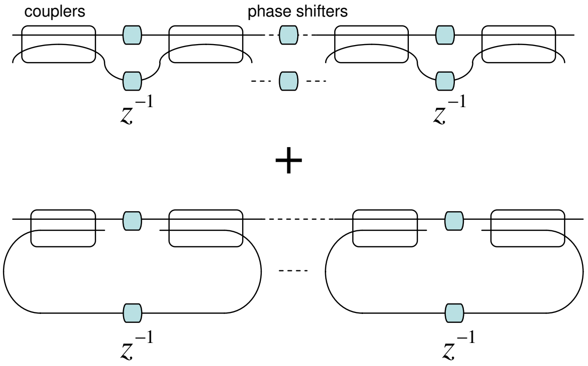

Figure 2.11: MZI lattice with phase shifters for synthesis of zeros (up) and double-coupler with feedback loop cascade for synthesis of poles (down).

By employing the proposed all-zero and all-pole independent configurations in tandem, the synthesis of Butterworth-type lowpass, highpass and bandpass filters is reported. Possible applications of the designed optical filters as pulse equalizers and receiver shaping filters are also discussed in [51]. As in fiber-optic coherent systems the optical phase is very sensitive to environmental fluctuations, such as pressure and temperature changes or mechanical vibrations, it is suggested that the systems are carefully shielded and isolated from any possible source of perturbations [52].

A modification of the FIR lattice-form optical delay-line-circuit structure (Fig. 2.10(a)) was reported by K. Jinguji in 1996 [53], including a ring waveguide in an arm of each Mach-Zhender interferometer (MZI), see Fig. 2.10(b).

By using the recirculating loop in the MZI, it is possible to realize the same filter characteristics as infinite impulse response (IIR) digital filters. In Jinguji's article, a filter synthesis algorithm is described based on scattering matrix factorization and expressing the transfer function of the ring waveguides with rational functions in the Z-Transform domain.

Synthesis examples of IIR optical frequency filters are also reported in the mentioned article, including a fifth-order elliptic filter, a sixth-order Butterworth filter, an eighth-order group delay dispersion equalizer and a ninth-order multi-channel selector. Errors in the circuit parameters, influence of waveguide loss and frequency shifts of the filter spectrum are also important issues considered in the work.

In 1999, Lenz and Madsen reported a general recursive all-pass filter design approach for dispersion control in WDM systems [54], following a matrix formalism and employing a Z-Transform description of the configurations. All-pass filters are linear systems with a constant amplitude response over all the frequencies. The ring resonator without internal losses is presented as a single-stage all-pass filter. In 2000, Madsen proposed a general IIR optical filter design approach based on all-pass filters [55], being the cascade of RR an important block in the proposed architecture, see Fig. 2.12.

Fabrication examples following compound structures with MZI and RR are the silica-on-silicon 5 GHz-spaced demultiplexer reported in [56], the 15 nm-FSR notch filters

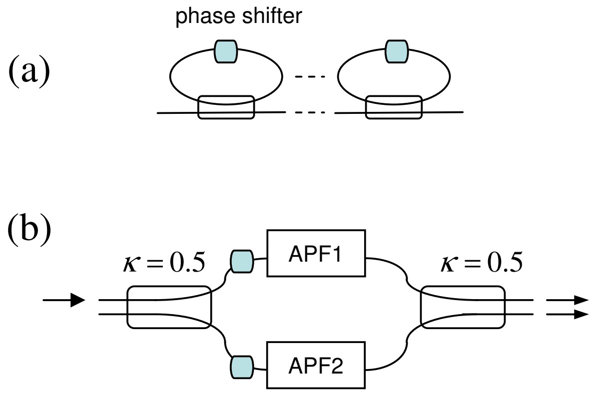

Figure 2.12: Cascade of single-stage RR-based all-pass filters (APF) (a) and general bandpass filter architecture using all-pass filter decomposition (b).

using GaAs-AlGaAs technology reported in [24], the passband flattened interleaver with 50 GHz-FSR fabricated in SiON waveguide technology reported in [37], and the active InP-InGaAsP modulator using multimode interference couplers and a resonator reported in [40].

The filter reported in [37] can be used for optical sideband filtering of satellite signals in an optical beam-forming system for phased-array antennas. This example of application has been recently studied in Jorge Peña's Master Thesis, carried out in the framework of an Erasmus mobility program between University Carlos III of Madrid (UC3M) and University of Twente (The Netherlands)[5].

2.7.3 IIR Photonic Filter Synthesis Techniques Using RR

Orta et al. reported in 1995 a method for the synthesis of optical filters using direct-coupled ring resonators employing directional couplers and delay lines [57]. The photonic architecture employed in the synthesis method can be seen in Fig. 2.13(a).

The photonic structure is studied exploiting the well-known methods developed for

---

[5] Julio Montalvo performed as co-advisor of this Masther Thesis at UC3M.

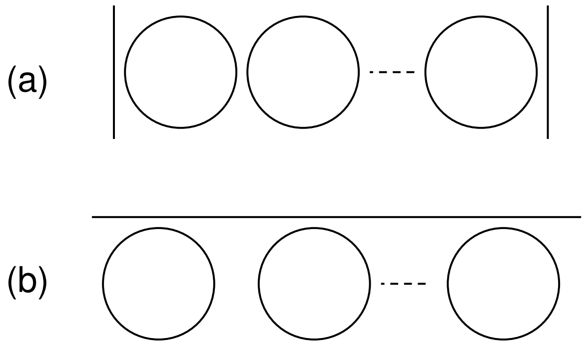

Figure 2.13: Schematic of lattice (a) and cascade (b) structures using ring resonators for photonic synthesis of digital IIR filters.

the design of FIR filters. With the proposed synthesis approach, the filter design is reduced to the determination of the suitable polynomial by positioning its zeros. A design example of a Chebyshev-type bandpass filter of sixth order was also presented [57]. Nevertheless, waveguide and coupling losses are not taken into account in the described synthesis procedure.

In 1996, Madsen and Zhao studied the same configuration as a concatenation of single-pole stages [58], extending the Z-transform analysis to include loss of waveguides and fabrication errors, and giving guidelines for the planar waveguide realization of the designed filters. Measurements on fabricated devices using Ge-doped SiO_2 waveguides on silicon substrate were also reported.

In 1998, Madsen and Lenz studied different photonic structures as all-pass filters for phase-response design [59]. Among them, ring lattices and cascades (see Fig. 2.13) are discussed for compensation of fiber dispersion. A fabrication example of a dispersion compensator using the configuration in Fig. 2.13(b) was reported using Ge-doped SiO_2 waveguides in a silicon substrate [35], demonstrating effectiveness in a 320-km, seven channel non-linear system simulation for signals at 2.5 Gb/s.

A generalization of the structure of Fig. 2.13(a) for the synthesis of optical bandpass filters for WDM systems, employing different loop lengths at each resonator stage, was reported by Melloni et al. in 2002 [60]. The technique is explained in detail for Butterworth and Chebyshev frequency responses, and applications such as channel add-drop, demultiplexing, multichannel filtering and interleavers are discussed in the paper. Fabricated devices using the architecture of Fig. 2.13(a) have been reported in [38, 25].

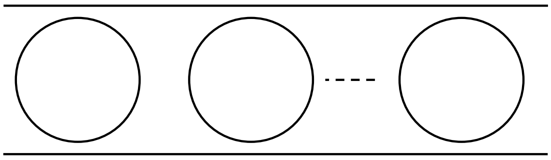

Figure 2.14: Parallel-coupled ring resonator configuration for IIR filter synthesis.

The cascade of ring-resonators using two waveguides, forming a linear array of resonators (see Fig. 2.14), has also been reported for filter synthesis in [61, 62, 63].

A synthesis method for the implementation of optical filters has been recently reported using the Sagnac interferometer in a ring resonator (SIRR) as all-pole second order filter in a multi-stage cascade structure [3], see Fig. 2.15. More details on the multi-stage synthesis architectures using the Sagnac interferometer in ring resonators can be found in [11].

2.8 Summary and Conclusions

In this chapter, the theory of the Z-Transform has been linked to the optical signal processing framework. The Z-Transform formalism has been used to analyze classical optical configurations such as the Michelson, Mach-Zehnder, Sagnac and the ring resonator. These configurations have been modelled as discrete-time optical signal processors and their transfer functions have been presented as rational system functions in the Z-Transform domain. A mathematical notation has been presented as the theoretical

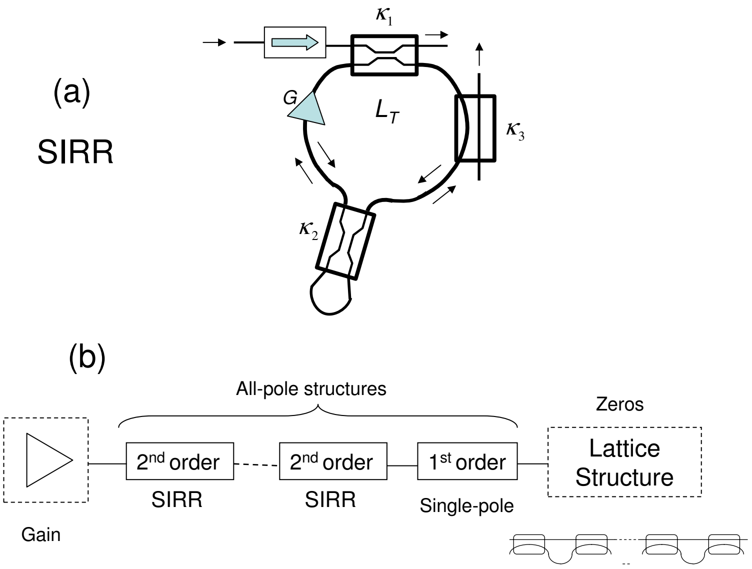

Figure 2.15: Schematic of the RR with a Sagnac interferometer (a) and block diagram of the multistage synthesis structure (b).

basis for the rest of the thesis.

Focusing on the ring resonator configuration, the magnitude frequency response has been studied and a novel compact formula for calculating the insertion losses have been reported for the incoherent RR, regarding power budget considerations for multiplexed sensor networks using RR in the remote sensing points, which will be described in Chapter 5 of this document.

Finally, some of the main compound photonic architectures for digital filter synthesis have been briefly reviewed in the chapter.

Chapter 3

Ring Resonator based Self-Referencing Techniques for Optical Intensity Sensors

3.1 Introduction

Over the past years, intensive research and development efforts have produced a large body of fiber-optic sensor technology, based on multi-mode (MM) and single-mode (SM) fibers.

Fiber-optic sensors being electrically passive can remotely operate in the presence of strong electromagnetic interference, hostile environment and explosiveness. The applications of fiber optic smart structures [64] are widely known for the measurement of temperature, pressure, force, displacement, acceleration, corrosion, humidity and gas concentration among other measurands.

In recent optical sensing applications, one extensively investigated transducing mechanisms is the intensity modulation. In general, intensity sensors usually use a simple but effective measuring process for detection and they need a self-referencing method to minimize the influences, on the accuracy of measurements, of long-term aging of optical source characteristics as well as short-term fluctuations of optical power loss in the leads to and from the transducer [65]. These are inevitable in practical engineering applications, specially those that involve remote operation.

A general schematic for supporting remote optical intensity sensors is shown in Fig. 3.1. In this system, the transmission and reception stages are located in a single point, namely Central Office (CO), where the light is launched into a lead fiber towards the remote sensing point, where it passes through the optical sensor and returns to the CO through a return fiber.

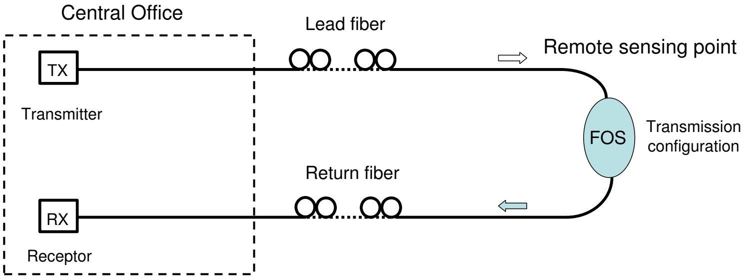

Figure 3.1: General schematic of a fiber link for remotely addressing fiber-optic intensity sensors (FOS) with a transmission configuration in the sensing point.

Different self-referencing approaches have been reported in the last two decades, providing mechanisms whereby the intensity variation of the light at the sensing head may be distinguished and measured independently of all the undesired perturbations.

In the following subsections, some interesting examples of intensity sensors and self-referencing approaches recently published are briefly described.

3.1.1 Fiber Optic Sensors

In MM fiber, an optical sensor for monitoring the corrosion of aluminum alloys is reported in [66], with applications in modern military aircraft maintenance. Another example of MM fiber-optic sensor is the optical hydrophone reported in [67] for high frequency measurements of ultrasound fields up to 100 MHz.

In SM fiber, a pressure sensor is reported in [68], based on the intrinsic properties of a communication grade SM optical fiber (Corning SMF28). The principle of this latter sensor is the transduction of pressure to optical path change in the SM fiber. Another examples of SM fiber-optic sensors are the temperature sensor reported in [69] and the humidity sensor based on tapered SM optical fibers, whose design and fabrication process are described in [70].

On the other hand, the new technology of Photonic Crystal Fibers (PFC) has become in recent years a subject of extensive research, showing great potential on optical sensing applications [71, 72]. They can be designed to discriminate the sensitivity to temperature from other sensitivities, simplifying the detection systems needed to reduce unwanted cross-sensitivities. PCFs with absolute single-mode and single-polarization operations in the third window of transmission have also been manufactured and characterized [73, 74].

3.1.2 Self-Referencing Techniques for Optical Intensity Sensors

Most of the widely published self-referencing techniques for intensity-modulated optical sensors correspond to one of the following schemes: time-division normalization, fiber bypassing and wavelength/frequency referencing.

A time division self-referencing mechanism was reported in [75], using as measurement parameter the ratio between the intensity of two optical pulses with a relative delay time. The technique consisted of incorporating an intensity transducer in the feedback loop of a MM fiber ring resonator, thus modulating and delaying in time the intensity with regards to the reference intensity pulse.

A wavelength normalization strategy was described in [76]. A Broadband Light Source (BLS) was divided in two wavelengths at the sensing point, one reaching the sensor and one used as a reference. These two wavelengths were then recombined and separated again at the receptor, where the signals were processed to eliminate light level changes in the fiber link caused by cable bends or connector losses, that may result in proportional signal modulation in both channels. The compensation of the light source intensity fluctuations can be performed using a reference light intensity signal provided by the transmitter.

A fiber bypassing strategy for self-referencing optical intensity sensors was reported in [77]. In this work, the optical power is split by and 1x2 optical coupler and launched into the two fiber leads connected to the remote sensing point. The two counterpropagating signals reach the sensing point, and the reference optical signal bypasses the sensor through an optical circulator. The main drawback of this configuration is the large number of components to build the complete remote link and the high insertion losses due to the use of 2x1 optical couplers. Nevertheless, the technique takes advantage of a compact configuration in the sensing point and a simple transmission and demodulation stages, because no frequency-modulation is needed.

Frequency-based self-referencing methods have been reported using radio frequency (RF) modulated Fabry-Perot (FP) [78], Mach-Zehnder, Michelson [79] and Ring Resonator (RR) [80] incoherent configurations in MM fiber technology. In these works, the basic idea is to encode the sensor intensity modulation in the radio-frequency magnitude response of an incoherent optical configuration, and to deploy a normalization of the measurement parameter at the reception stage to achieve self-reference.

More recently, self-referencing has been achieved in a wavelength multiplexing configurations using SM fibers instead of MM fiber. In [81], a reflective ladder topology using Fiber Bragg Gratings (FBG) and a Michelson configuration at the remote sensing point is reported for wavelength multiplexing and self-referencing optical intensity sensors.

In this chapter, we propose to use the incoherent RR for remotely addressing and self-referencing fiber-optic intensity sensors (FOS) with enhanced sensitivity [5, 82, 83, 84]. As the RR is an infinite impulse response configuration, the magnitude response at resonance is sharper than in other optical configurations.

In the following sections, two self-referencing methods of a novel frequency-based approach using a RF-modulated optical RR configuration are described in detail and comparatively analyzed. Effect of optical amplification on the self-referencing measurements is also discussed for the first time within this configuration. Both methods rely on the ratio between the amplitudes of the RF signals corresponding to the interference in an incoherent RR.

The first normalization method is named the *frequency normalization method*; two frequency channels are used, the sensor channel at frequency f and the reference channel at a reference frequency f_r, see Fig. 3.2. The second method is named *two-ports normalization method*, in which the optical power is modulated by a single RF electrical signal at frequency f, being output Y_1 used as the sensor channel and output Y_2' used as the reference channel, using a directional coupler inside the RR loop, see Fig. 3.7.

The following sections consider the Z-Transform analysis of the incoherent RR in subsection 2.6.2 and use the identity:

$$e^{j\cdot\Omega} = \cos\Omega + j \cdot \sin\Omega \tag{3.1}$$

in order to find the frequency response of the proposed configurations, after the change of variable $z = e^{j\cdot\Omega}$.

The expression of the angular frequency is $\Omega = 2\cdot\pi\cdot n_g\cdot L\cdot f/c$, being n_g the effective group refractive index of the RR feedback loop with length L, c the speed of light in vacuum and f the operating frequency.

3.2 Frequency Normalization Self-Referencing Technique

The proposed sensing scheme for self-referencing intensity based fiber-optic sensors (FOS) is shown in Fig. 3.2 for the frequency normalization method. It is a RR consisting of a variable optical coupler with a FOS located within the feedback loop, with optionals optical attenuator (A) and amplifier (G). These two latter components may be required to achieve a proper RR operating point; nevertheless, low-cost operation designs should avoid the need for amplification.

Let $F(m)$ be the intensity modulation function of the FOS with regards to the relevant physical magnitude under measurement (m), namely *measurand* from now on.

In this first normalization method, a light source (LS), either a Laser Diode (LD) or a Light Emitting Diode (LED), depending on power budget, is intensity-modulated by two signals at frequencies f and f_r at the same time. In order to assure incoherent regime, the loop length L must be much greater than the coherence length of the light source.

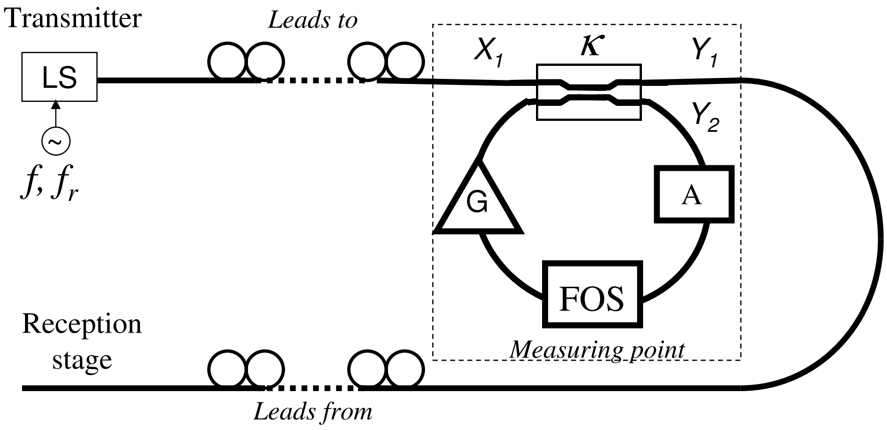

Figure 3.2: Proposed schematic of the sensor configuration: frequency normalization method.

The optical power travels through the input optical fiber leads, allowing long remote operation distances if needed, because SM fibre leads are used; then the optical power enters through input x_1 into the ring resonator, where the measurand modulates the RR loss at the measuring point, and the RR output power transfer function at output y_1 can be designed to be very sensitive to these variations.

A RR under incoherent regime acts as a notch, an all-pass or a selective filter depending on the net power balance H in the loop, which can be obtained as follows:

$$H = \exp(-\alpha \cdot L) \cdot A \cdot G \cdot \gamma \cdot F(m) \tag{3.2}$$

where: G, A are the power gain and attenuation within the loop, respectively; α is the fiber attenuation propagation constant, m is the measurand, $F(m)$ is the FOS power modulation curve, γ, κ are the excess loss and cross-coupling constant of the coupler and, finally, L is the length of the feedback loop. Provided that undesirable power fluctuations may occur due to optical source power fluctuations or loss variations in the optical paths to the remote sensing point, the optical signal at the reception stage is proportional to the output Y_1 of the RR configuration, whose corresponding transfer function can be particularized as follows:

$$\frac{Y_1(\Omega)}{X_1(\Omega)} = \gamma \cdot (1-\kappa) \left(\cdot \frac{1 + z_1^2 + 2 \cdot |z_1| \cdot \cos\Omega}{1 + p_1^2 - 2 \cdot p_1 \cdot \cos\Omega} \right)^{\frac{1}{2}} \tag{3.3}$$

In the latter equation, a passive notch filter response is a premise ($H < 1, \kappa > 2/3$), see section 2.6.2. In order to compensate the power fluctuations outside the RR loop affecting this frequency response, we propose to provide the frequency normalization mechanism by means of the self-referencing parameter R_{M1}, defined as follows:

$$R_{M1}(\Omega) = \left| \frac{y_1(\Omega)}{y_1(\Omega = \Omega_r)} \right| \tag{3.4}$$

where $\Omega_r = 2 \cdot \pi \cdot k$ for integer k.

At the reception stage, the optical power at the angular frequency Ω_r is used as the reference channel. It is assumed the same modulation response at Ω and Ω_r in the transmitter and a flat passband in the receiver at both frequencies. As both numerator and denominator of the latter equation are affected by the same random power fluctuations, the self-reference of this measuring parameter is assured. In order to achieve high sensitivity to the variations of the measurand m, the sensor channel frequency must be around a zero transmission frequency, $\Omega_0 = \pi \cdot (2 \cdot n - 1)$ for integer n, and near the resonance condition:

$$H_0 = \frac{1-\kappa}{\gamma \cdot (2 \cdot \kappa - 1)} \tag{3.5}$$

for $\kappa > 0.5$.

In order to deploy the measurement of this parameter at the reception stage, it is necessary to interpret physically Eq. 3.4 and to determine the values of the sensor frequency f and the reference frequency f_r.

The reference frequency is obtained considering $\Omega = 2 \cdot \pi \cdot n$, and it can take any of these values:

$$f_r = FSR \cdot n, \quad n = 0, 1, \ldots, \infty \tag{3.6}$$

This frequency is chosen as a reference because it is the least sensitive to the variations of H.

On the other hand, the sensor frequency f must be around a zero transmission frequency:

$$f_0 = FSR \cdot \frac{2n-1}{2}, \quad n = 1, 2, \ldots, \infty \tag{3.7}$$

The closer the sensor frequency f is to f_0, the more sensitive R_{M1} is with respect to the ring losses power modulation caused by m.

In Figs. 3.3 and 3.4 it is shown the self-referenced parameter R_{M1} in natural units (n.u.) versus the sensor angular frequency Ω and ring losses H, respectively.

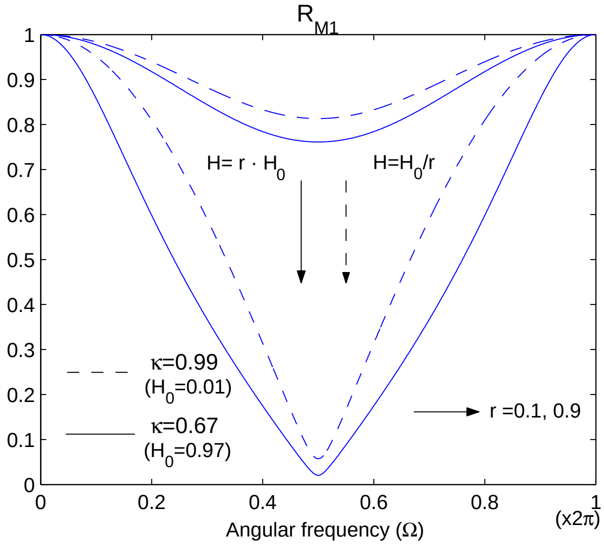

Figure 3.3: Frequency normalization self-referencing parameter versus angular frequency (Ω) for different values of κ and H. $\gamma = 1$. H_0 is given by Eq. 3.5.

Fig. 3.3 shows R_{M1} for different values of κ, from the minimum value to achieve a notch filter with the incoherent RR configuration ($\kappa = 2/3$, continuous lines), to higher values around 1 (dashed lines), so it shows the two extremes of possible cross-coupling values of the configuration. For angular sensor frequencies tending to $\Omega_0 = \pi$ the variations of R_{M1} show the maximum dynamic margin. The two curves for each value of κ in Fig. 3.3 correspond to values of H ranging around 10 dB tending to the resonance condition H_0, in a comparable way through the auxiliar variable r.

On the other hand, the shape of R_{M1} versus the ring losses H is shown in Fig. 3.4, for different values of the coupling coefficient κ. As κ tends to 1, the self-referencing parameter is more sensitive to the ring loss. The value of the angular frequency is chosen very close to π, which is a resonance frequency and corresponds to a sensitive performance of the self-referencing parameter.

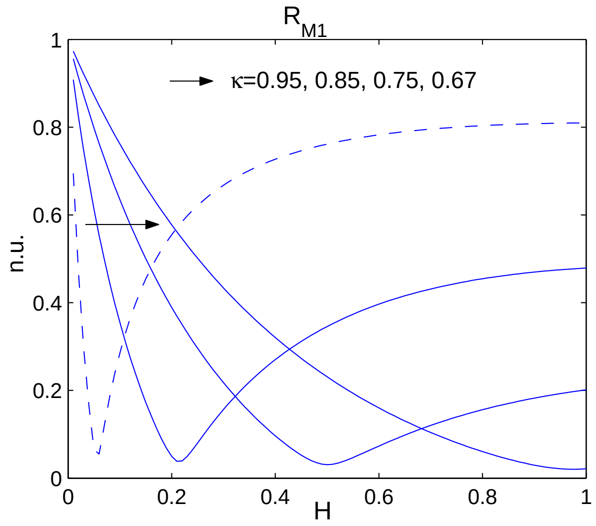

Figure 3.4: Frequency normalization self-referencing parameter versus ring losses (H) for different values of κ. $\Omega = 0.98 \cdot \pi, \gamma = 1$.

3.2.1 Effect of Amplification in the RR Feedback Loop

Up to now, we have just explored the configuration performance when the reference power at channel frequency f_r remains approximately constant. However, by employing optional amplification to obtain optical net gain in the RR configuration, it is possible to achieve the pole condition:

$$H_p = \frac{1}{\gamma \cdot (1 - \kappa)} \tag{3.8}$$

For H close to this value, the optical power at the reference frequency f_r can theoretically increase as much as wanted, but the undesirable condition of instability might be obtained if $|p_1| > 1$.

Extremely high dynamic ranges of R_{M1} could theoretically be obtained if condition 3.8 was achieved at the same time than a condition of minimum (3.5), being the power ratio between reference and sensor frequencies theoretically infinite. Nevertheless, that is only possible for the simultaneous conditions:

$$\kappa = 2 - \sqrt{2}, H = \frac{1}{\gamma \cdot (2 - \sqrt{2})} \tag{3.9}$$

To keep the RR design stable it is mandatory:

$$|p_1| = \gamma \cdot H \cdot (1 - \kappa) < 1 \tag{3.10}$$

In Fig. 3.5, R_{M1} is drawn versus H in *decibels* (dB) for different values of the coupling factor κ, being this coefficients below 2/3 for some of the curves. The logarithmical scale shows how, for a given value of Ω, the dynamic margin of R_{M1} increases more than 10 dB when the premise of $H < 1$ is not considered. The value of Ω is chosen close to π for a sensitive design, and the dynamic margin of the self-referencing parameter also increases as Ω tends to π, but so does its non-linearity with regards to H.

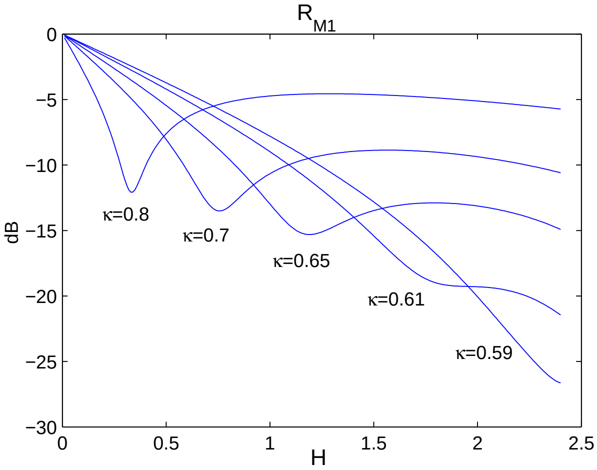

Figure 3.5: Frequency normalization self-referencing parameter versus power balance (H) for different values of κ. $\Omega = 0.95 \cdot \pi, \gamma = 1$.

The use of amplification ($H > 1$) in the incoherent RR with coupling factor values below 2/3 is also good for the linearity of the self-referencing parameter R_{M1}, as it will be shown in the next subsection.

3.2.2 Normalized Sensitivity of the Frequency-Based Self-Referencing Parameter R_{M1}

Let S_m be the sensitivity of the intensity sensor with regards to the variations of the measurand, m.

$$S_m = \frac{\partial F(m)}{\partial m} \tag{3.11}$$

In this subsection, the effect of using the ring configuration for self-referencing the intensity sensor is studied with regards to sensitivity and linearity. As it has been reported in previous sections, R_{M1} changes very quickly with regards to H near the resonance condition $H = H_0$. Nevertheless, as the self-referencing parameter tends to zero near this condition, the derivative $\frac{\partial R_{M1}}{\partial m}$ does not account for the rapid variations of R_{M1} that take place in a logarithmical scale. In order to highlight the performance of the self-referencing parameter in a logarithmical scale, which can be a common case of an experimental set-up, we define the normalized sensitivity S_{N1} as follows:

$$S_{N1} = \frac{1}{R_{M1}} \cdot \frac{\partial R_{M1}}{\partial m} \tag{3.12}$$

It can be seen that:

$$S_{N1} = \frac{1}{R_{M1}} \cdot \frac{\partial R_{M1}}{\partial H} \cdot \frac{\partial H}{\partial m} \tag{3.13}$$

$$\frac{\partial H}{\partial m} = H^* \cdot S_m \tag{3.14}$$

where $H^* = \gamma \cdot \exp(-\alpha \cdot L) \cdot A \cdot G$.

We define the sensitivity enhancement factor with regards to S_m, namely E_1, as follows:

$$E_1 = \frac{S_{N1}}{S_m} \tag{3.15}$$

The higher the value of this sensitivity enhancement factor, the more sensitive is the self-referencing parameter to the intensity modulation induced by the measurand, m. Considering carefully the expression of E_1, we find that:

$$E_1 = \frac{H^*}{R_{M1}} \cdot \frac{\partial R_{M1}}{\partial H} = H^* \cdot \frac{\ln 10}{10} \cdot \frac{\partial \left(10 \cdot \log R_{M1}\right)}{\partial H} \tag{3.16}$$

When neither attenuation nor optical gain is added to the intensity sensor modulation, $H^* = 1$ except for the fiber losses, which are negligible. Finally the expression of E_1 yields:

$$E_1 = 0.23 \cdot \frac{\partial R_{M1}(dB)}{\partial H} \tag{3.17}$$

where R_{M1}(dB)=$10 \cdot \log R_{M1}$.

Eq. 3.17 shows that E_1 represents the variations of R_{M1} in *decibels* with regards to the RR power balance H, and simultaneosly accounts for a sensitivity enhancement with regards to the sensitivity of the intensity sensor to the measurand variations, see Eq. 3.15. In Fig. 3.6 this enhancement coefficient is shown for different coupling values tending to the singular value $\kappa_p = 2 - \sqrt{2}$, where the pole and zero condition can be achieved simultaneously, at the expense of needing optical gain in the RR loop.

As it can be seen in the figure, higher enhancement factors are achieved near the resonance condition for each value of κ, but the abrupt changes show the high non-linearity of the self-referencing measurements. As the coupling factor tends to the singular value κ_p, the effect of the pole at the reference angular frequency Ω_r takes place. Actually, the best linearity of R_{M1} is expected to happen around values of κ close to κ_p, because the enhancement factor E_1 is quite constant in most of the range covered by H, see

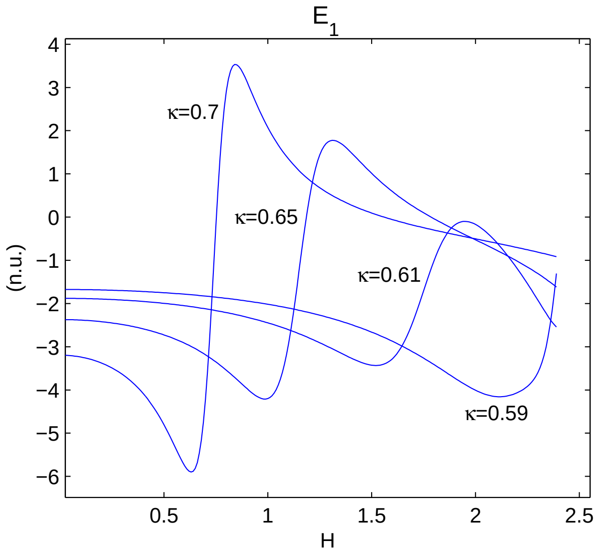

Figure 3.6: Sensitivity enhancement parameter E_1 versus power balance (H) for different values of κ. $\Omega = 0.95 \cdot \pi, \Omega_r = 0.02 \cdot \pi, \gamma = 1$.

Fig. 3.6. This design is optimal because it leads to low optical insertion loss of the RR from input port x_1 to output port y_1 and a good sensitivity of R_{M1} is achieved, even for $H < 1$. Actually, for $\kappa = 0.59$, the expected dynamic range of R_{M1} is more than 7 dB when H ranges between 0 and 1, see Fig. 3.5.

3.3 Two-Ports Normalization Self-Referencing Technique

The two-ports normalization approach, see Fig. 3.7, uses a single modulation frequency f, a remote RR configuration in the sensing point with a coupler inside the feedback loop for measuring Y_2 and two fiber down-leads under identical external conditions. In this method, the self-referencing measurement parameter, namely R_{M2} is defined as follows:

$$R_{M2}(\Omega) = \left| \frac{Y_2'(\Omega)}{Y_1(\Omega)} \right| \tag{3.18}$$

Provided that the two fiber leads from the sensor point are affected by the same power fluctuations, the self-reference of this measuring parameter is assured. As in the case of the frequency-based self-referencing technique described in the previous section, the most sensitive design with respect to the sensor power modulation is achieved near the frequency of the zeros, $\Omega = \pi \cdot (2 \cdot n - 1)$ for integer n, and near the resonance condition:

$$H_{02} = \frac{1-\kappa}{\gamma' \cdot (1-\kappa') \cdot \gamma \cdot (2 \cdot \kappa - 1)} \tag{3.19}$$

for $\kappa > 0.5$, being γ', κ' the power excess loss and cross-coupling factor, respectively, of the additional optical coupler in the feedback loop.

After some operations, Eq. 3.18 yields:

$$R_{M2}(\Omega) = \frac{\kappa \cdot \gamma' \cdot \kappa'}{\sqrt{(1-\kappa)^2 + r^2 - 2 \cdot (1-\kappa) \cdot r \cdot \cos\Omega}} \tag{3.20}$$

where $r = \gamma \cdot \gamma' \cdot H \cdot (1-\kappa') \cdot (1 - 2 \cdot \kappa)$.

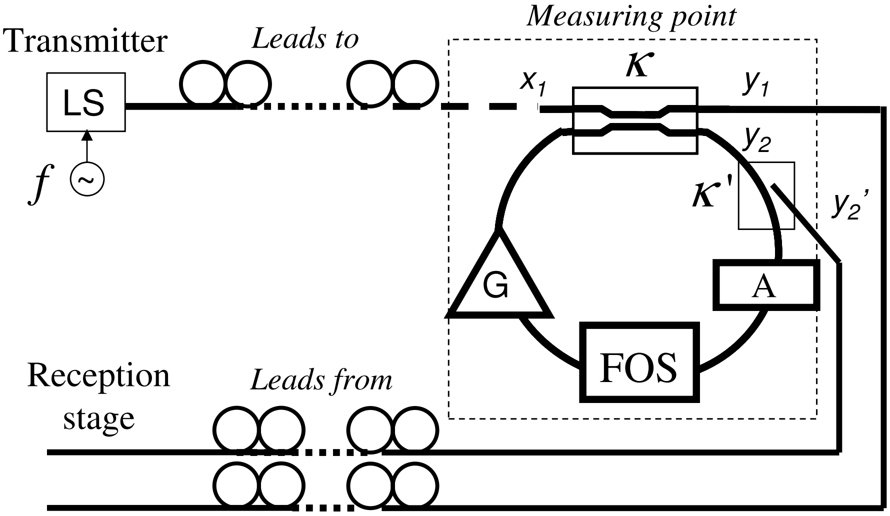

Figure 3.7: Proposed schematic of the sensor configuration: two-ports normalization method.

In order not to include additional power loss in the ring, it is recommended to use small values of κ'.

In Fig. 3.8, the theoretical shape of R_{M2} versus power modulation H is shown for different values of κ'. A medium value of κ between 2/3 and 1 is chosen for a sensitive design without need for optical amplification, and the value of the angular frequency is close to π for the same reason. The peak values of R_{M2} increase as κ' does, so in this figure the values of the self-referencing parameter have been scaled by κ' in order to have comparable curves. It can be seen that as κ' increases the critical value H_{02} is also greater, so in a first approach it would be recommended not to use design values of this parameter greater than 0.1.

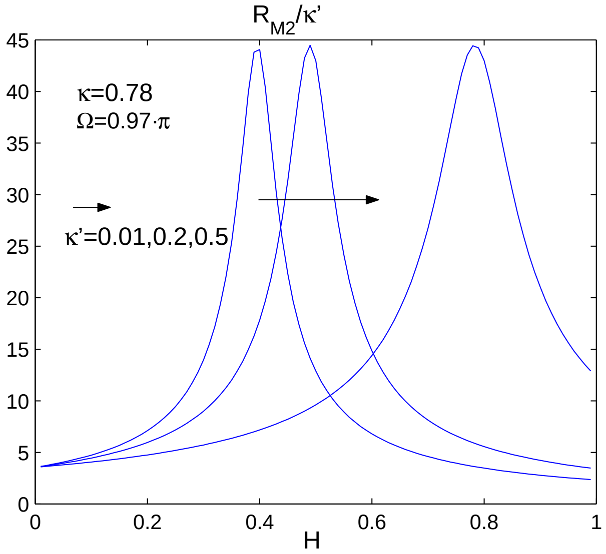

Figure 3.8: Two-ports self-referencing parameter versus H for different values of κ'. $\Omega = 0.97 \cdot \pi, \gamma = \gamma' = 1$.

3.3.1 Normalized Sensitivity of the Two-Ports Self-Referencing Parameter R_{M2}

The normalized sensitivity of R_{M2} is:

$$S_{N2} = \frac{1}{R_{M2}} \cdot \frac{\partial R_{M2}}{\partial m} \tag{3.21}$$

The sensitivity enhancement factor is defined identically that for R_{M1}:

$$E_2 = \frac{S_{N2}}{S_m} \tag{3.22}$$

The two enhancement parameters E_1, E_2 are drawn in Fig. 3.9. The enhancement factor E_1 has opposite sign that E_2, so in the latter figure its absolute value $|E_2|$ is drawn in order to have comparable curves. Both enhancement parameters show a very similar performance.

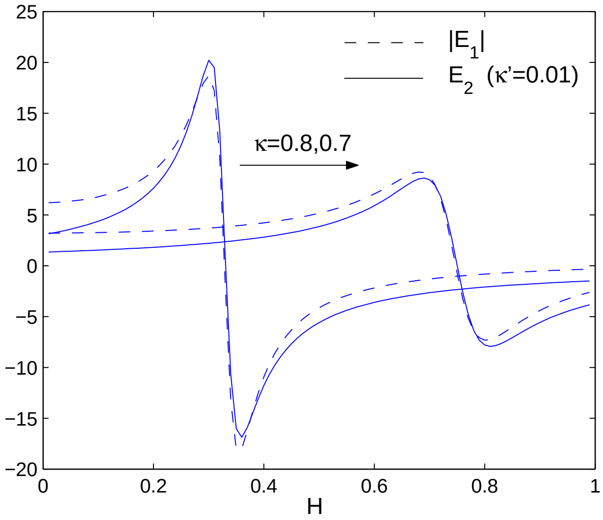

Figure 3.9: Sensitivity enhancement parameter of the two self-referencing methods versus H for different values of κ. $\Omega = 0.98 \cdot \pi, \gamma = \gamma' = 1$.

3.4 Phase-Induced Intensity Noise in the Passive Incoherent RR

The noise at output Y_1 of the incoherent RR is shaped by the contributions of different terms, and the dynamic margin of the output electrical signal in this configuration is limited from below by this noise. The noise induced by the optical source is in most of the cases the dominant contribution to the total noise, but other contributions are the detection shot noise, the dark current of the photo-detector and the thermal noise. The optical source induces noise at the output of the RR not only because of its inherent intensity noise, which is filtered by the frequency response of the RR, but also because of its phase fluctuations.

After proposing the passive incoherent RR acting as a notch filter for self-referencing intensity sensors, it is clear that the study of the interplay between noise filtration and noise generation in this configuration is very interesting, because it is directly related to the signal to noise ratio of the self-referencing measurements.

In certain cases, the phase-induced noise can be much higher than the intensity noise induced by the optical source, as it was experimentally demonstrated in [85]. In this work, the phase-induced noise in a recirculating delay line built in single-mode fiber with a length of 27 cm, excited with a multimode continuous wave semiconductor laser diode, was 20 dB stronger than the characteristic intensity noise of the optical source. Additionally, it was demonstrated that the phase-induced noise spectrum does not show the same shape versus frequency that the magnitude response of the configuration.

The noise spectra of the phase-induced intensity noise in optical systems driven by low-coherence sources was first analytically studied in [86]. For an optical multi-path system with a characteristic transit time τ, under the assumption of polarization maintaining and when the spectral dispersion can be neglected, the output field $y(t)$ can be expressed as a superposition of delayed versions of the input field $x(t)$ as follows [86]:

$$y(t) = \sum_{n=0}^{+\infty} F_n \cdot x(t - n \cdot \tau) \tag{3.23}$$

where F_n are complex weighting coefficients which depend on the system parameters.

From now onwards, the intensity noise of the optical source is neglected and it is assumed an unit amplitude input field of the form:

$$x(t) = exp\left[j \cdot (\omega_0 \cdot t + \phi(t))\right] \tag{3.24}$$

where $\phi(t)$ is a Wiener-Levy random process. A thermal-like low coherence optical source with either Lorentzian or Gaussian shapes is considered, which is a realistic situation for most of the cases.

Under incoherent regime, the power intensity $i(t)$ obtained at an output photodetector is [86]:

$$i(t) = \sum_{n=0}^{+\infty} \sum_{m=0}^{+\infty} F_n \cdot F_m^* \cdot exp\left[(m-n)\omega_0 \cdot \tau + \phi(t - n \cdot \tau) - \phi(t - m \cdot \tau)\right] \tag{3.25}$$

and the evaluation of the ensemble average of $i(t)$ is:

$$\langle i \rangle = \sum_{n=0}^{+\infty} |F_n|^2 \tag{3.26}$$

According to the Wiener-Khinchine theorem [87], the power spectrum of the output intensity $i(t)$ is the Fourier Transform of its autocovariance function, given by:

$$c_i(t_1, t_2) = \langle i(t_1) \cdot i(t_2) \rangle - < i >^2 \tag{3.27}$$

Finally, the power spectrum of the source-induced noise is obtained by Fourier trans-forming Eq. 3.27.

For the case of the incoherent RR, the maximum contribution of the phase-induced intensity noise, which might be much stronger than the characteristic intensity noise of the optical source, is experimentally verified at frequencies around the multiples of $FSR/2$, while notches take place in integer multiples of FSR [85, 86].

Unfortunately, in the case of the incoherent RR and the two self-referencing methods described in the former sections, the sensor frequencies for sensitive designs are located around the multiples of $FSR/2$, so in optical systems where the phase-induced noise of the optical source is dominant, this can be the main restriction for a practical implementation of the RR-based self-referencing configuration.

If we try to apply previous studies to the proposed self-referencing techniques, it can be seen that, depending on the type of optical source, either the characteristic intensity noise of the optical source or the phase-induced intensity noise can be dominant in the output of the RR. For example, for a Fabry-Perot laser with a linewidth of 5 nm, launched into a RR with a feedback loop of 19 m, the intensity noise is dominant and the output noise spectra follows the magnitude response of the RR [88]. On the opposite, when a Distributed-FeedBack (DFB) laser with a linewidth of 0.1 nm is employed in a RR with a feedback loop of 2193 m, the phase-induced noise is dominant and its spectra follows the shape versus frequency predicted in [86].

The phase-induced noise in the amplified fiber optic RR configuration has also been studied in [89, 90].

3.5 Experimental Validation of the Self-Referencing Techniques

In order to verify the feasibility of the proposed configurations, an experimental set-up using a DFB laser diode (LD) emitting an optical power of around 0 dBm at $1.5\mu m$

with a linewidth of 5 MHz was developed. We internally modulated the LD with a RF signal coming from the tracking generator of a RF spectrum analyzer (Tektronix 2714). The optical detection was carried out by an optical-to-electrical (OE) converter (Thorlabs D400FC). The sensing schemes to be characterized were developed with a polarization maintaining 2X2 variable ratio fibre coupler from Fiberpro, an optional Erbium-Doped Waveguide Amplifier (EDWA) from TeemPhotonics and a single-mode fiber loop with an approximate length of 1056 m. This long fiber delay line is required to assure incoherent regime of operation with the DFB laser, but it could be much shorter if a cheaper optical source with lower coherence length was employed.

A SM fiber variable optical attenuator (VOA), operating as a generic intensity fiber-optic sensor (FOS), has been used to calibrate the configuration in both self-referencing methods. Mostly FC/APC connectors were used in the set-ups. Both calibration curves are shown in Fig. 3.10 and Fig. 3.11 for the frequency-based and the two-ports self-referencing approaches, respectively [5].

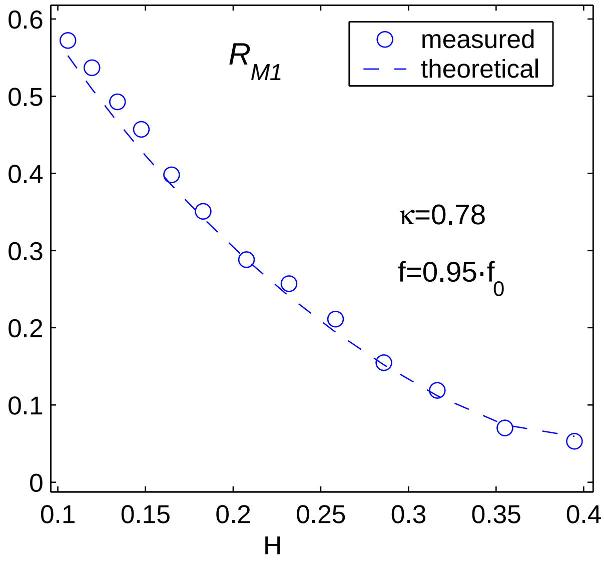

Figure 3.10: Calibration curves showing measurements of R_{M1} for $f = 1.302$ MHz and $f_r = 1.207$ MHz, using the frequency normalization method (see Fig. 3.2).

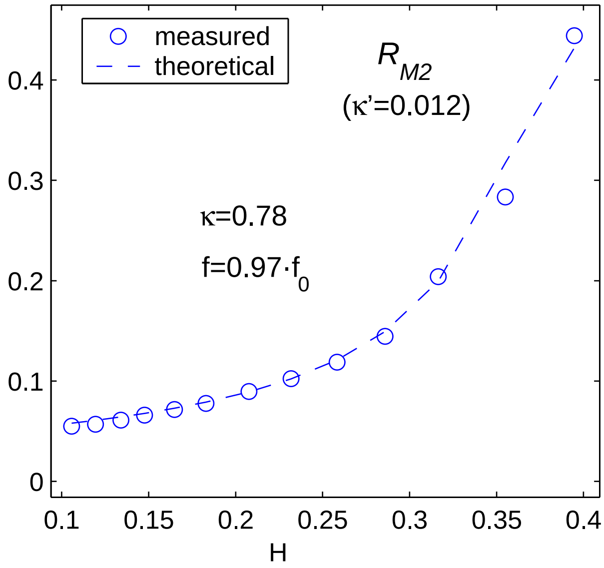

Figure 3.11: Calibration curves showing measurements of R_{M2} for $f = 1.302$ MHz, using the two-ports normalization method (see Fig. 3.7).

A second experiment has also been carried out using the same experimental set-up, but replacing the VOA with a fiber-optic sensor based on bending losses in SM optical fibers. This self-made fiber-optic sensor consists of a knot made of standard SM optical fibre cable with elliptic shape having a curvature radius r of 2.25 cm.The behaviour of the self-referencing techniques was also verified properly, by emplacing metallic loads over the prototype, see Fig. 3.12.

In Fig. 3.13, two photographs showing the performance of the scale model are shown. The photograph in the left corresponds to the FOS with neither the support nor any weights. Next measurements were taken in steps of 50 gr, being the first burden (100 gr.) the physical support for the loads. The photograph in the right corresponds to the FOS when a weight of 500 gr. is lying on the support of the sensor prototype. Temperature has been changed from 21^{o}C to 34^{o}C and no amplitude fluctuations were observed.

Finally, the effect of including a multimode (MM) G.651 fiber patchcord with a length of 1 meter as a fiber-optic strain sensor in the single mode fiber loop was studied [83].

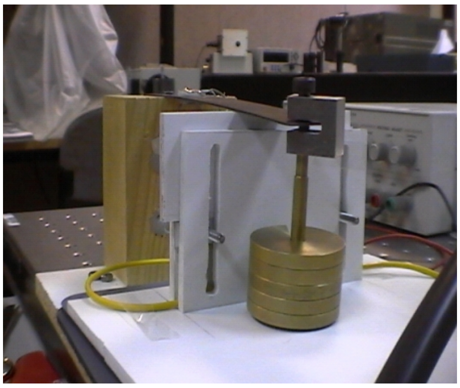

Figure 3.12: Photograph of the scale model and the weights.

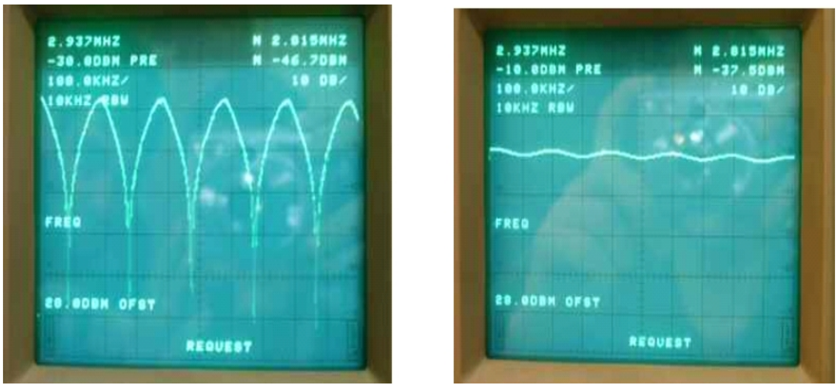

Figure 3.13: Screen of the spectrum analyzer showing measurements at output Y_1 of the RR using the scale model with no load (left) and with a total weight of 500 grams (right).

The MM strain sensor has been built by peeling 20 cm of the jacket of the patchcord and twisting it in 10 spirals around an elastic cylinder of 0.4 cm diameter. A MM fiber-optic intensity sensor with 5 dB extinction ratio[1] and nominal insertion losses of 4 dB was achieved. These values are under the margin of operation of the RR configuration.

3.6 Comparative Discussion on the RR-Based Self-Referencing Techniques

The frequency-based self-referencing method is more suitable for remote operation of sensors than the two-ports method, as there is only one down-lead fiber from/to the sensor point. On the other hand, when simpler modulators and reception stages are preferred, the two-ports self-referencing method is the best option, as it avoids the need for two modulating frequencies. This method is less cost-effective in case of remote operation, as two down-lead fibers are needed. Self-reference is only assured if both down-leads are attached one to each other so that the environmental variations are exactly the same for both fibers. Additionally, a second optical coupler is needed to measure the power in the recirculating fiber loop, Y_2. The cross-coupling coefficient of this coupler, κ', should be very small, around 1%, so that the loop power balance, H, is not affected and the resonance condition is not altered. As a consequence of this, the measured power Y_2' is usually much smaller than Y_1, resulting a measuring parameter R_{M2} with opposite variations with regards to the variations of R_{M1}.

As regards sensitivity, both methods are almost equivalent, see Fig. 3.9, so designers should choose one of the methods depending on other parameters rather than sensitivity, and above all special attention should be paid to the situations where the measuring point is far from the optical source, being the frequency-based normalization method

---

[1] The extinction ratio is defined as the ratio between the maximum and minimum loss induced by the optical intensity sensor.

the most appropriate in these cases.

Finally, the frequency normalization method is more convenient with regards to the noise level of the measurements, due to the fact that the reference port in the two-ports normalization method suffers a large attenuation because of the use of the additional coupler inside the RR loop, see Fig. 3.7.

3.7 Design Optimization Example: High Sucrose Concentration Optical Sensor

In this section, we study an intensity sensor fabricated in standard step-index single-mode fiber technology. This sensor was designed and fabricated at the Public University of Navarra, in the Department of Electrical and Electronic Engineering. The facilities and equipment employed for the calibration of this sensor were provided at the same department. This work was carried out in collaboration with Dr. Manuel López Amo, Dr. Ignacio R. Matías and Dr. Jesús M. Corres.

The issues that will be considered in this section are the tolerance of the measurement parameter to external power fluctuations of the optical source, the insertion loss of the ring resonator, the dynamic margin of the measurement parameter and the sensitivity of the self-referencing technique. These aspects will be discussed carefully all along this section for the specific case of an optical sucrose sensor.

3.7.1 Sensor Description and Calibration

The sensor under analysis is an evanescent-field sensor which consists of a tapered standard single-mode optical fiber whose thinner part is coated with a polymeric nano-film sensitive to humidity [70], see Fig. 3.14. The tapered fiber operates as an optical transducer sensitive to the changes of the surrounding refractive index. These changes can be induced by immersing the taper into a liquid solution of sugar mixed with water in high concentration, namely m (gr/100ml). An external cavity laser diode tuned at 1550 nm emitting 0 dBm[2] was employed as optical source for the calibration of the sensor, immersing the tapered fiber into different liquids with increasing sucrose concentrations. The power transmission response of the sensor immersed in pure water as a function of sucrose concentration in water (m) is reported in Fig. 3.15, showing a sensitivity of $1.75 dB/gr \cdot ml$.

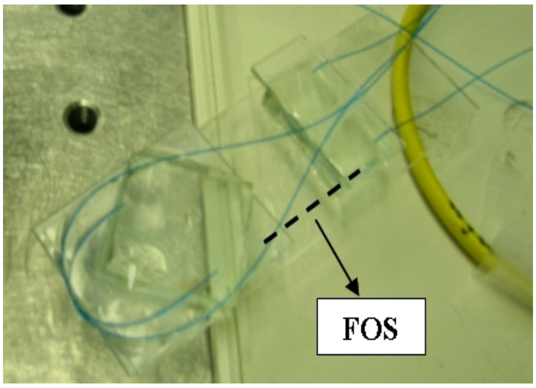

Figure 3.14: Photograph of the tapered fiber as an optical transducer sensitive to sucrose concentration in pure water.

3.7.2 Description of the Self-Referencing Technique

The measurement technique is based on the frequency-based self-referencing approach described previously in this chapter, using the ring resonator configuration for remote measurements, see Fig. 3.16.

The configuration consists of a lightwave source (LS) modulated in intensity by two electrical signals at frequencies f (sensor) and f_r (reference). The modulated optical signal travels through a single-mode fiber lead to the input x of the self-referencing configuration located in a remote sensing point. The self-referencing configuration consists of a ring resonator with an optical coupler with cross-coupling factor and excess loss

---

[2] Model Santec TSL-210. The typical linewidth of this laser is greater than 20 MHz with the coherence control activated and lower than 500 kHz without coherence control.

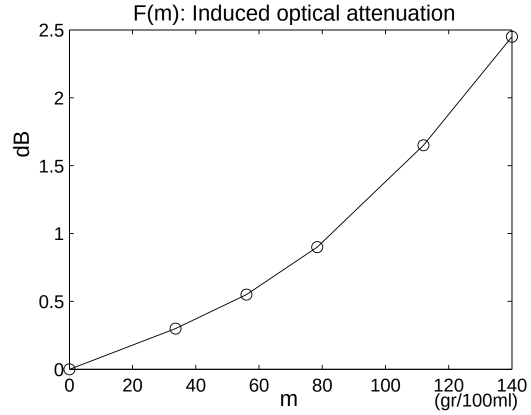

Figure 3.15: Measurements of the optical attenuation (dB) induced by the sensor as a function of sugar concentration.

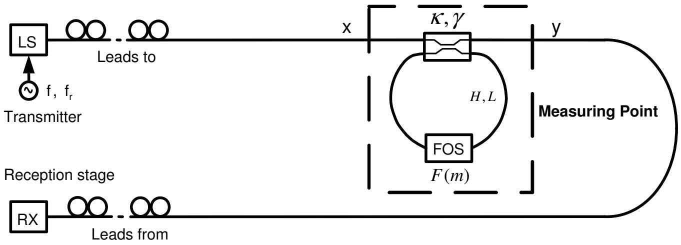

Figure 3.16: Self-referencing configuration based on the ring resonator for remote measurements on an intensity fiber-optic sensor (FOS).

κ, γ, respectively, and a feedback fiber loop with a length L. An intensity fiber optic sensor (FOS) is emplaced within the feedback loop of the ring resonator, where a power attenuation $F(m)$ takes place, induced by the measurand m.

As it was described previously in this work, the modulation of the ring loss by the intensity sensor ($H = \gamma \cdot exp(-\alpha \cdot L) \cdot F(m)$) results in the change of the magnitude response of the output signal y, depending on the measurand m, which in this case is the sucrose concentration.

Finally, the optical output y travels to the reception stage through the lead fiber from the remote sensing point. The spectral periodicity, or Free Spectral Range (FSR), of the output signal y is:

$$FSR = \frac{c}{n_g \cdot L} \tag{3.28}$$

where c is the speed of light in vacuum and n_g the effective group index of the single mode fiber (typically $n_g = 1.45$).

In the reception stage (RX), the ratio between the optical power at frequencies f_r and f is obtained in order to achieve the self-referencing measurement parameter, R_m. The change of the magnitude response in y can be very drastic if the design parameters are appropriate, so the sucrose sensor sensitivity can be increased by using the frequency-based self-referencing technique.

The employed measurement parameter is:

$$R_m = R_{M1}(\Omega = \pi \cdot (2 \cdot k - 1)) \tag{3.29}$$

for integer k.

For this specific case, R_m yields:

$$R_m = \left| \frac{(1+z_1)\cdot(1-p_1)}{(1-z_1)\cdot(1+p_1)} \right| \tag{3.30}$$

where $z_1 = \gamma \cdot H \cdot \frac{1-2\cdot\kappa}{1-\kappa}$ and $p_1 = \gamma \cdot H \cdot (1-\kappa)$.

As it was previously described in this work, the resonance condition takes place at $H = H_0 = \frac{1-\kappa}{\gamma\cdot(1-2\cdot\kappa)}$.

The possible values of the reference frequency f_r are given by:

$$f_r = FSR \cdot k \tag{3.31}$$

for integer k.

On the other hand, the possible values of the sensor frequency f are given by:

$$f = FSR \cdot (k - \frac{1}{2}) \tag{3.32}$$

for integer k.

Provided that no optical amplification takes place within the feedback loop of the RR, the power density at the reference frequency shows minimal response to the loss modulation H induced by the fiber-optic sensor. As the external variations influencing the optical power outside the RR feedback loop affect identically at f and f_r, the ratio of the power density at those two frequencies is not altered by other aspects than the sucrose concentration m, thus achieving the self-reference property of the measurement parameter R_m.

3.7.3 Ring Resonator Design Optimization

The self-referencing parameter behavior is defined by two parameters of the ring resonator, the internal loss H and the coupling factor κ, considering the excess loss negligible ($\gamma = 1$). On the following, the optimal values of these parameters for the specific sensor under study are investigated.

The original dynamic margin of the sucrose sensor must be kept in the self-referencing configuration and the sensitivity should be enhanced. As the sucrose sensor has a dynamic margin of 2.45 dB, see Fig. 3.15, the self-referencing parameter R_m must have at least the same range of variations. This will be accomplished provided that the design is close to the resonance condition.

The insertion losses of the tapered fiber are 3.2 dB, this is 0.47 in natural units, so the minimum ring loss $H_{min} = 0.47$ in the feedback loop, provided that neither optical attenuation nor amplification is used, which is the most cost-effective option. The best value of H should be kept around this value in order to achieve a low value of the average optical power loss from point x to point y, see Fig. 3.16. The maximum attenuation induced by the sensor is 5.6 dB, this is $H_{max} = 0.27$ in natural units.

The configuration still allows the freedom to choose the coupling factor of the configuration, but the RR power losses in the through port increase as κ takes values close to 1, so this value should be, in principle, as low as possible. A limitation to this rule arises from the fact that, in order to achieve a minimum of the transfer function at port y without optical amplification in the RR, it is mandatory that $\kappa > 2/3$.

In Fig. 3.17, the theoretical values of R_m are drawn versus the coupling factor for the minimum (H_{min}) and maximum (H_{max}) values of the calibration curve of the sucrose sensor.

Fig. 3.18 shows the total dynamic margin of R_m versus the direct coupling factor of the RR configuration, considering $H = H_{min}$ the initial point of operation. The dynamic margin is calculated as the ratio between the value of R_m with $H = H_{max}$ and its value with $H = H_{min}$. The figure shows that the measurement parameter achieves higher dynamic margins than that of the sensor (2.45 dB) in two regions and, as a consequence, a sensitivity enhancement would be obtained. Between the two regions,

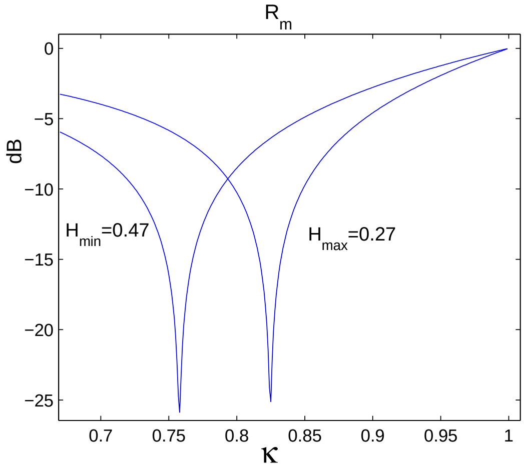

Figure 3.17: Theoretical self-referencing parameter versus cross-coupling factor for the minimum and maximum attenuation values induced by the sucrose sensor.

region 1 corresponds to lower values of the cross-coupling factor. It is recommended that the operating point for the self-referencing measurements is set in this region 1, because the RR insertion losses are lower. These losses are a key issue for the power balance optimization in multiplexed optical networks, so they must be kept to the lowest as far as possible.

On the other hand, in order to obtain high sensitivity performance, the operating point should be close to a resonance condition, which in the case of region 1 is around $\kappa = 0.75$.

3.7.4 Measurements on the Self-Referencing Configuration

The optimal design obtained in the former section is implemented and characterized using the Agilent 8703B Lightwave Network Analyzer, employing its internal distributed-feedback (DFB) laser diode in the 1550 nm region as optical source. The RF modulated lightwave launched into the RR configuration is -5.95 dBm. In order to test comfortably the performance of the self-referencing technique, a precision variable optical attenuator

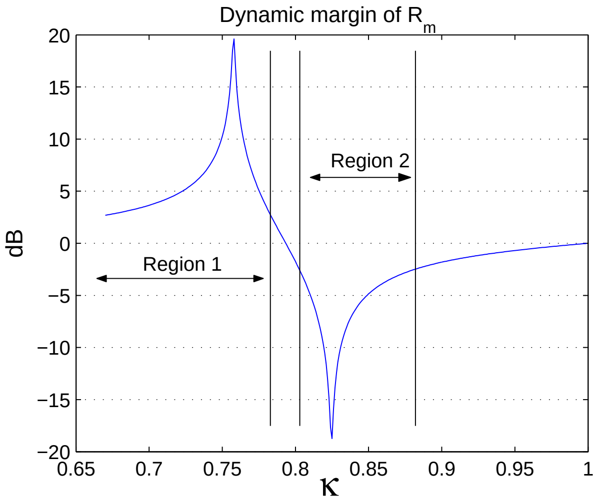

Figure 3.18: Dynamic margin of the self-referencing parameter versus coupling factor value for the sucrose concentration optical sensor.

(Agilent 81571A) is used to emulate the sucrose sensor. To ensure RR incoherent regime, a 100 meters single-mode fiber span connected to the transducer emulator is used as feedback path of a variable coupler from Fiberpro, Inc. This fiber length could be much shorter if other kind of light source such as a Fabry-Perot (FP) laser diode or a superluminiscent light-emitting diode (SLED) was used.

The self-referencing parameter R_m is obtained as the ratio between the power at the sensor and reference frequencies, provided by the network analyzer, see Fig. 3.19. The transducer attenuation has been emulated over its entire dynamic margin (2.45 dB), thus assessing the performance of the self-referencing configuration for the specific case of the sucrose concentration optical sensor.

The start point of the RR internal losses is $H = -4.3dB$, which accounts for the insertion loss of the sucrose sensor (3.2 dB) and 1.1 dB additional losses caused by connectors losses. From the measurements shown in Fig. 3.19, it is obtained a dynamic margin of 5.5 dB for the self-referencing parameter R_m, thus the dynamic margin of the measurements has increased more than 3 dB. By using the self-referencing technique,

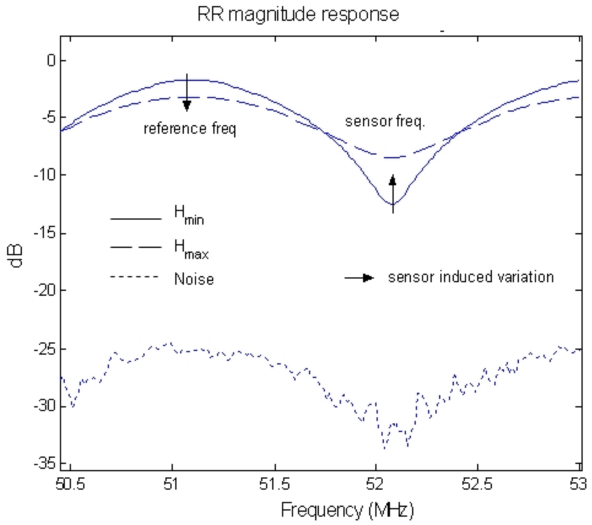

Figure 3.19: Measured variations of the RR magnitude response at output port y induced by the FOS emulator over its entire dynamic margin of 2.45 dB. $\kappa = 0.78$.

the sensitivity of the sucrose sensor is increased from 1.75 $dB/gr \cdot ml$ to 3.92 $dB/gr \cdot ml$.

The total optical loss from input port x to output port y has been measured and it is around 4 dB, very close to the intrinsic 3.2 dB of the FOS, so the power penalty due to the use of the self-referencing technique is not critical.

In order to test the insensitivity of the measurements to external power fluctuations such as source power or fiber cables attenuation changes, we use a manual variable optical attenuator (VOA) to attenuate the light source from 0 to 7 dB, see Fig. 3.20. Three measurements of R_m were taken for each value of the attenuation, and the mean values of the self-referencing parameter are drawn in the figure. A maximum relative change of 1% in R_m takes place.

3.8 Summary and Conclusions

In this chapter, two novel measurement mechanisms based on an incoherent ring resonator configuration have been proposed for self-referencing single-mode (SM) and multi-

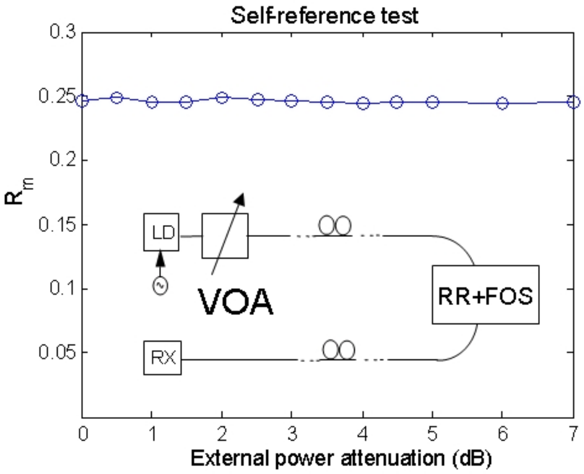

Figure 3.20: Measured sensitivity of the self-referencing parameter R_m to external power attenuation of the RF modulated optical source. $\kappa = 0.78$.

mode (MM) fiber-optic intensity sensors in remote sensing points. A first method is called frequency-based self-referencing method, and the second one is called two-ports self-referencing method. Both methods rely on the ratio between two signals in order to assure the property of self-reference. The two methods have been described and analyzed in detail, defining the two corresponding self-referencing parameters and studying their performance with regards to the design parameters. Sensitivity, linearity and dynamic margin are also theoretically considered. A comparative discussion between the two self-referencing measurement parameters has also been reported, and the effects of amplification within the RR loop in the frequency-based self-referencing approach has been considered and mathematically analyzed.

Both self-referencing techniques have been validated experimentally using a SM variable optical attenuators operating as a generic sensor. Moreover, two self-made prototypes of fiber-optic strain sensors made of SM and MM fiber have been included in the self-referencing configurations, showing the feasibility of the proposed techniques. The RR configuration has also been optimized for an specific case of an optical sucrose concentration sensor, made of a tapered single-mode fiber, providing a sensitivity enhancement by using the frequency-based self-referencing approach.

By employing the proposed configurations, the measurements are self-referenced and the sensitivity of the intensity sensor can be improved, being its point of operation controlled through a variable ratio coupling coefficient and optionals optical amplification or attenuation of the power balance in the feedback loop.

The self-referencing technique optimization can be easily derived from our study for any specific intensity sensor, provided that the insertion loss and dynamic margin are known. Measurements resolution is limited by the optical source induced noise, stability of κ and gain stabilization in the case of amplified configurations. Better measurements are expected using lower coherence optical sources. Digital signal processing can also be applied at the reception stage to reduce noise, as reported in [91]. The experiments show that the sensor is not affected by environmental temperature perturbations.

Chapter 4

Reflective Self-Referencing Techniques for Optical Intensity Sensors Using Fiber Bragg Gratings

4.1 Introduction

Fiber Bragg Gratings (FBG) are passive components based on the properties of diffraction in periodical structures and the guiding properties in optical waveguides. They reflect the optical power within a specific waveband, with a characteristic central wavelength, namely λ_B, and let the rest of the spectrum propagate in the transmission direction. The most characteristic parameter of a FBG is the ratio between the reflected and the incident optical powers within the reflecting bandwidth, which is named reflectivity.

FBGs are very useful components for multiple applications, such as multiplexers and demultiplexers in Dense WDM systems [92], optical tunable dispersion compensators [93] for long haul communication networks, tunable lasers [94] and optical FM demodulators [95].

On the other hand, interrogation techniques based on FBGs are effective approaches for addressing optical intensity sensors, because they provide reflective configurations that permit the use of fiber leads in both propagating directions of the light. In these configurations, the transmission and reception stages can be located in a single point, namely central office (CO). From this central office the light is leaded to the remote sensing point through a fiber link, and the reflected light, which comprises the information of the sensor-induced intensity modulation, returns to the central office through the same fiber link as a counter-propagating optical signal, see Fig. 4.1.

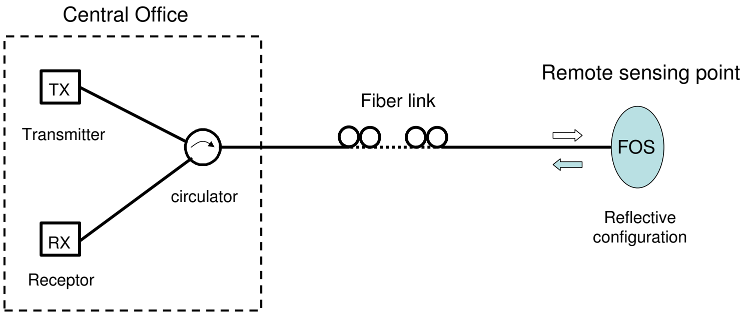

Figure 4.1: General schematic of a bidirectional fiber link for remotely addressing fiber-optic intensity sensors (FOS) with a reflective configuration in the sensing point.

Recently, an ultra-long-distance method for long-distance FBG-based sensor systems has been reported [96]. In this work, seven FBGs with a bandwidth of 0.3 nm were connected in series at 20 km intervals for remote strain measuring. Using a 10 dBm power-controlled wavelength-swept light source from 1520 nm to 1580 nm every 0.22 ms, the monitoring of FBG reflection wavelengths was achieved with no optical amplification at a maximum distance of 120 km. With this interrogation technique, the signal-to-noise ratio of the measurements does not depend on the transmission distance, being the estimated maximum fiber length around 240 km, limited by the shot noise level (-82 dBm). Authors consider this technique possibly useful in tsunami early warning systems.

Not only the use of FBG in sensor networks provide an effective and compact strategy for exploiting long-distance fiber links bidirectionally; actually, the sensitivity of the transducer can be enhanced because it is possible to make the optical signal travel through the intensity sensor twice, once for each propagating direction.

FBGs are also a well-known, low-cost and excellent technology to achieve wavelength-division-multiplexing of optical sensors, because they can be used as spectral filtering devices of broadband light sources.

Finally, FBGs can be used in self-referencing optical configurations for remotely addressed fiber-optic intensity sensors.

A reflective sensor configuration in multi-mode fiber technology was reported in 1986 using a Fabry-Perot (FP) configuration for self-referencing radio-frequency modulated optical intensity sensors [78]. In this work, an optical cavity with 3.5 meters of MM fiber was realized with a fiber connector and a proximity sensor based on the power back-coupling on the fiber end, where the light is re-injected using a moving mirror. In 2001, the FP configuration was also employed for self-referencing intensity sensors [97], employing simultaneous coherent and incoherent regimes of operation in order to combine the advantages of fiber interferometry and intensity-based devices into a single sensor system.

A self-referencing approach in SM fiber technology using two FBG with different central wavelengths and a fiber delay coil was demonstrated in 2002 to provide a reflective self-referencing configuration for RF-modulated optical intensity sensors [7]. The additional concept of wavelength separation was included in this work, thus allowing wavelength-division-multiplexing of different sensors. The spectral filtering of the FBG was used to achieve a wavelength-based bypass self-referencing strategy. A spatial bypassing strategy for self-referencing was also developed using a circulator and two counter-propagating signals at the same wavelength in [77].

RF-modulated Michelson [79] and multiple beam Sagnac [98] configurations in MM fiber technology have also been reported for self-referencing intensity sensors. In the Michelson configuration, the reflective elements were mirrors fabricated by silver deposition on the fiber ends; in the case of the Sagnac topology, the configuration itself is a reflective approach. More recently, reflective sensor configurations in single-mode fiber technology have been demonstrated employing Michelson configuration with optical feedback [81] and fiber ring resonators [6, 99]. In both works FBGs are used to provide reflective operation, and the self-referenced measurements are achieved by a frequency-based demodulation technique of the reflected signal in the central office, relying either on the phase or the magnitude response of the configuration versus modulation frequency.

In this chapter, reflective self-referencing mechanisms using fiber ring resonators (RR) and delay lines are studied in detail. Firstly, a RR based configuration in reflection mode using a FBG is studied and experimentally verified [6, 99]. Secondly, the configuration consisting of a fiber optic sensor (FOS) and a fiber delay line located between two FBGs [7] is employed to achieve a novel self-referencing parameter with enhanced sensitivity. Finally, a novel electro-optical configuration [8] is presented in the last section of this chapter, replacing the fiber delay coil by a reconfigurable electronic delay at the reception stage, thus achieving a compact remote sensor head and a flexible demodulation scheme in the electronic domain. In the following sections, all these aspects are developed in detail.

4.2 Ring Resonator Self-Referencing Configuration in Reflection Mode Using FBGs

The first self-referencing measurement technique described in this chapter is based on the RR transmission configuration reported in [5] with an intensity fiber optic sensor (FOS) in the feedback loop. This configuration was proposed and analyzed for remote addressing of optical intensity sensors in chapter 3 of this document. An improved self-referencing configuration in reflection mode is achieved by adding a fiber Bragg grating at the output fiber of the RR [6, 99], see Fig. 4.2.

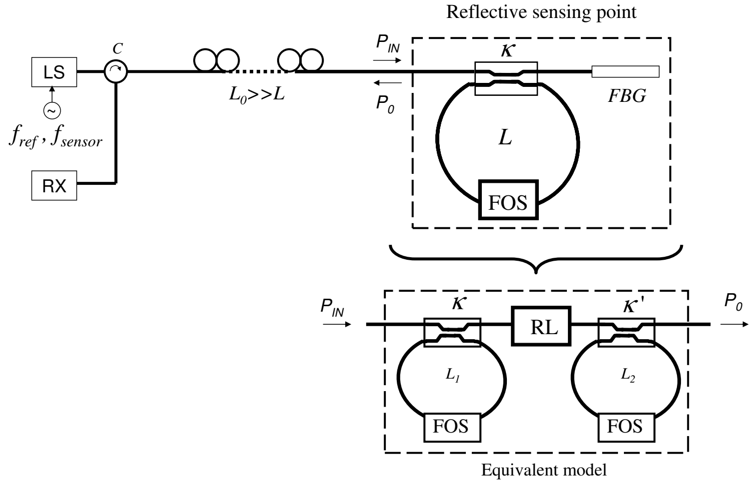

Figure 4.2: RR self-referencing technique schematic for remote addressing of fiber optic intensity sensors (FOS) in reflective configuration. LS: Light Source; C: Circulator; RX: Reception Stage; FOS: Fiber Optic Sensor. FBG: Fiber Bragg Grating. RL: Reflection Losses of the FBG. L: Length of the RR feedback loop.

4.2.1 Description and Analysis of the Configuration

A RF-modulated light at frequencies f_{ref}, f_{sensor} is launched to the remote sensing point through an optical circulator (C), reaching the self-referencing configuration through a single-mode fiber link with length L_0, much longer than the RR feedback loop, L. κ, κ'

are the cross-coupling coefficients of the optical coupler in the forward and backward propagating directions of light, respectively, being almost identical for symmetrical couplers ($\kappa \simeq \kappa'$). The circulator is also used to extract the reflected signal coming back to the central office in the same fiber lead, thus simplifying the schematic. This configuration has the doubled sensitivity in comparison with the RR transmission configuration [5], because the light passes twice through the configuration, once for each propagating direction. By means of using a FBG in the direct output port of the RR, the configuration opens up wavelength-division-multiplexing capabilities. The technique can be used in microfiber loop resonators [100], where the microfiber loop is the sensing element itself.

Provided that neither optical amplification nor attenuation is induced in the RR feedback loop, except for the sensor-induced power modulation $F(m)$, being m the external magnitude of interest, the total power balance within the RR feedback path is:

$$H = \exp(-\alpha \cdot L) \cdot \gamma \cdot F(m) \tag{4.1}$$

Where γ is the excess loss of the optical coupler and α is the fiber attenuation constant in nepers per unity of length. The characteristic transit time of the RR is $\tau = \frac{c}{n_g \cdot L}$, where c, n_g are the velocity of light in vacuum and the effective group index in the optical fiber, respectively.

The configuration can be analyzed in either coherent or incoherent regime of operation: in the following, we assume that the optical source coherence length is much shorter than the loop length L, so incoherent optical regime takes place. The symmetric decomposition shown in Fig. 4.2 in two fiber RR in series, assuming bidirectional intensity sensor response, can be used as model for the reflective structure. This configuration optimizes the second-order filter response in terms of symmetry, because the two rings are physically the same, and the same point of operation for the two equivalent resonators ca be achieved with one sole adjusting process as regards coupling factor ($\kappa = \kappa'$) and loop length ($L_1 = L_2 = L$). Because of that, the configuration is insensitive to coupling factor and loop length fabrication tolerances for symmetric bidirectional optical couplers and intensity sensors. The magnitude response of the reflective configuration $|H_p|$ with regards to angular frequency Ω equals the response of the transmission configuration of Eq. 3.3 squared, this is:

$$|H_p(\Omega)| \equiv \Gamma' \cdot \frac{1 + z_1^2 + 2 \cdot |z_1| \cdot \cos\Omega}{1 + p_1^2 - 2 \cdot p_1 \cdot \cos\Omega} \tag{4.2}$$

where $\Gamma' = \gamma^2 \cdot (1-\kappa)^2 \cdot RL$, $z_1 = \gamma \cdot H \cdot \frac{1-2\cdot\kappa}{1-\kappa}$ and $p_1 = \gamma \cdot H \cdot (1-\kappa)$, being $\kappa > 2/3$ and $H < 1$.

Assuming that input optical power is constant versus angular frequency, $\Omega = 2\cdot\pi\cdot f\cdot\tau$, the self-referencing parameter R_M is given by:

$$R_M = \left| \frac{H_p(\Omega_s)}{H_p(\Omega_r)} \right| \tag{4.3}$$

where $\Omega_s = 2 \cdot \pi \cdot f_{sensor} \cdot \tau$ and $\Omega_r = 2 \cdot \pi \cdot f_{ref} \cdot \tau$. Both $|H_p|$ and R_M are periodical with regards to frequency with period, or free spectral range (FSR), being $FSR = \frac{1}{\tau}$.

A ratio-metric measurement is achieved by modulating the optical source at two different frequencies f_{ref}, f_{sensor} and using the RR in a reflection configuration at each measuring point.

The optimal values of the modulation frequencies were discussed in chapter 3 of this document, being f_{sensor} around a zero transmission frequency $f_0 = \frac{2\cdot k-1}{2} \cdot FSR$ and $f_{ref} = FSR \cdot k$, for integer k.

The power loss of the average optical power reaching at the sensing point equals the RR insertion loss of the RR plus the reflection loss (RL) of the FBG. The insertion loss of the RR can be calculated using Parseval's identity[1] [6]:

$$\sum_{i=0}^{N-1} |h[i]|^2 = \frac{1}{N} \sum_{m=0}^{N-1} \left| H\left(\Omega = \frac{2\pi}{N} \cdot m \right) \right|^2 \tag{4.4}$$

4.2.2 Experimental Validation of the Reflective Self-Referencing Configuration Using RR and FBGs

The reflective self-referencing configuration shown in Fig. 4.2 has been implemented using standard single-mode fiber with angled physical contact fiber connectors (FC/APC) and a fiber Bragg grating from O/E Land INC. Index matching get was deposited at the FBG transmission port to avoid undesired reflections. The intensity sensor is emulated using a bidirectional variable optical attenuator (VOA). The RR loop length is 100 meters, without considering coupler and VOA pigtails, thus ensuring incoherent operation. A fixed optical coupler was used to achieve better stability in the coupling coefficient than with variable ratio couplers. A laser diode at 1552.2 nm is used as optical carrier, and the Agilent 8703B Lightwave Component Analyzer (LCA) is used for characterizing the self-referencing configuration with regards to modulation frequency from a minimum value of 50 MHz up to 20 GHz. A frequency window of 4.5 MHz with 201 points and 100 Hz intermediate frequency filter is set in the measurements. Two sets of measurements have been taken, first to validate the theoretical model and secondly to verify the isolation of the measurements from the effects of fiber lead attenuation and power fluctuations of the optical source. The value of κ must be selected for avoiding the need for optical amplification and having acceptable insertion losses.

A RR configuration with $\kappa = 0.79, H = 0.7, \gamma = 0.95$ has been characterized versus modulation frequency using the LCA, see Fig. 4.3. Both the analytical equations and the *freqz* function of the MATLAB Signal Processing Toolbox can be used to find the theoretical RR transfer functions. In the RR reflective configuration, smalls devia-

---

[1] Please see Chapter 2 of this document, Eq. 2.32 in page 42.

tions may arise from coupler and VOA asymmetries between the backward and forward propagation. The shape of the transmission RR fits very well the theory, actually just a 0.1 dB variation is noticed in the value of the minima. The double sensitivity of the reflective configuration is also verified in the screen of the LCA. The RR insertion losses have been measured for two different pairs of κ, H near the resonance condition $H_0 = \frac{1-\kappa}{\gamma \cdot (2 \cdot \kappa - 1)}$ ($\kappa > 0.5$). For $\kappa = 0.93$ and $\kappa = 0.81$ the measured RR insertion losses are 11 dB and 7.7 dB, respectively.

In order to validate the self-referencing technique, we have also emulated the main fiber lead power fluctuations by employing an additional VOA in the central office located just after the optical circulator, see Fig. 4.2.

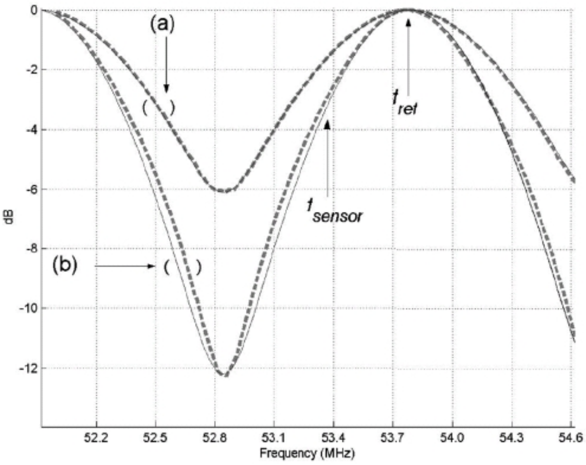

Figure 4.3: Normalized RR magnitude response with $\kappa = 0.79, H = 0.7$ for the transmission (a) and reflective (b) configurations. Measurements are drawn in dashed lines, theoretical curves are in continuous lines.

Power attenuation has been induced adjusting the VOA from 0 dB to 8 dB. A set of R_M measurements has been taken versus the power attenuation, using f_{ref}=53.86 MHz and f_{sensor}=53.35 MHz, keeping $\kappa = 0.79$. The mean, maxima and minima measured values of R_M are graphically represented in Fig. 4.4, showing relative errors below 0.6%.

Regarding the experimental setup, the importance of keeping FC/APC connectors

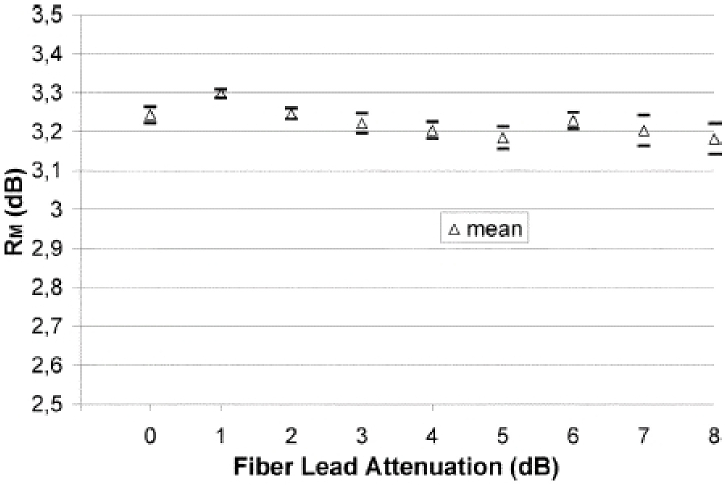

Figure 4.4: R_M measurements versus fiber lead induced attenuation for a RR self-referencing technique in reflective configuration with $\kappa = 0.79, \gamma = 0.05, H = 0.7$, $f_{ref} =$ 53.86 MHz, $f_{sensor} = 53.35$ MHz.

properly aligned to avoid undesired reflections is remarkable: final prototypes will avoid any connector by using splices. As the value of the sensor frequency tends to a zero transmission frequency, the relative errors increase. Polarization maintaining fiber and couplers can be used to delimit the influence of loop fiber birefringence on the measurements.

4.3 Reflective Self-Referencing Techniques Using Delay Lines and FBGs

A basic configuration without frequency modulation using two FBGs with different central wavelengths and an intensity sensor located between them is shown in Fig. 4.5.

Two continuous optical waves at a reference wavelength (λ_R) and a sensor wavelength (λ_S) reach the remote sensing point with total average powers P_{Ri}, P_{Si}, respectively.

In this basic configuration and in the following of this chapter, it is assumed that

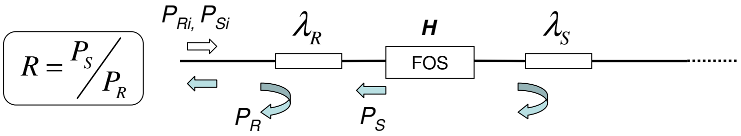

Figure 4.5: FBG based reflective configuration in the remote sensing point using continuous waves for self-referencing fiber-optic intensity sensors (FOS).

both reflected spectra at the two FBGs do not overlap in wavelength, so that the optical crosstalk can be ignored. The optical power reflected at the reference wavelength P_R is used as a reference channel, while the measurand induced attenuation H causes a power variation at the sensor wavelength, which can be read in signal P_S. The ratio $R = \frac{P_S}{P_R}$ can be used as self-referenced measurement parameter, because all the power fluctuations taking place out of the sensing point are identical at both the reference and sensor wavelengths, specially if both wavelengths are close one to each other.

Provided that the reflectivities of the reference and sensor FBGs are R_R, R_S, respectively, the self-referencing measurement parameter yields:

$$R = \frac{P_{Si} \cdot R_S}{P_{Ri} \cdot R_R} \cdot T^2 \cdot H^2 \tag{4.5}$$

where T is the transmission coefficient, taking into account the loss induced at λ_S due to the insertion loss in the reference FBG.

It can be seen that the self-referencing parameter is sensitive to the sensor-induced intensity modulation H squared, because the sensor lightwave passes through the transducer twice, once for each propagating direction.

The main issues to consider regarding this configuration are the restrictions on the reflectivities of the FBGs and the measurand-induced intensity modulation range, for a required signal to noise ratio (SNR) in the self-referencing measurement parameter.

A second configuration using RF-intensity modulation of the optical signals and a fiber delay coil of length L emplaced between the two FBGs is shown in Fig. 4.6 [7]. It consists of an amplitude-to-phase conversion technique, also suitable for wavelength-division-multiplexing and self-referencing optical intensity sensors.

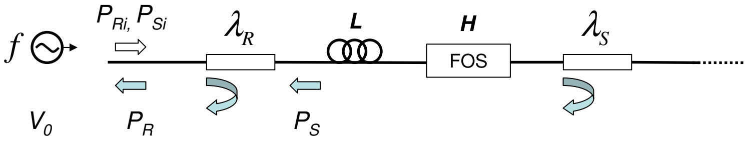

Figure 4.6: Reflective configuration in the remote sensing point using two FBGs and a fiber delay line for self-referencing fiber-optic intensity sensors (FOS).

In the next subsections of this chapter, a novel approach for describing this latter configuration by using a digital filter model is presented and employed to analyze the frequency response using the Z-Transform formalism. A novel self-referenced measurement parameter enhancing the sensitivity of the previous works is also proposed and experimentally demonstrated.

4.3.1 Fiber Bragg Grating (FBG) Based Self-Referencing Measurement Technique with Enhanced Sensitivity

In the optical configuration shown in Fig. 4.6, two optical signals with average optical powers P_{Ri}, P_{Si} around the reference (λ_R) and sensor (λ_S) wavelengths, respectively, are intensity-modulated at frequency f in the central office and launched into the optical fiber to the remote sensing point. The power envelope of both optical signals can be described in the time domain using:

$$p_{ri} = P_{Ri}(\lambda_R) \cdot (1 + m_r \cdot \cos(2\pi \cdot f \cdot t)) \tag{4.6}$$

$$p_{si} = P_{Si}(\lambda_S) \cdot (1 + m_s \cdot \cos(2\pi \cdot f \cdot t)) \tag{4.7}$$

where m_r, m_s are the modulation indexes of the reference and sensor channels, respectively. These indexes can be almost identical if the wavelengths of the two optical signals are very close and the average powers are similar.

Let P_R, P_S be two complex numbers representing the reflected optical power of the RF optical waves at the reference and sensor wavelengths, respectively. The reflected optical wave at the sensor wavelength λ_S is phase-shifted Ω radians with regards to the signal at the reference wavelength as a consequence of the group delay of the light in the fiber delay coil with length L. A power attenuation is also induced at this wavelength due to the intensity sensor response. The expressions of both complex phasors are:

$$P_R = m_r \cdot R_R \cdot P_{Ri} \tag{4.8}$$

$$P_S = m_s \cdot R_S \cdot P_{Si} \cdot e^{-j \cdot \Omega} \cdot T^2 \cdot H^2 \tag{4.9}$$

being R_R, R_S the reflectances of the reference and sensor FBGs at wavelengths λ_R, λ_S, respectively.

Once that both signals at the two wavelengths reach the central office, they add on an intensity basis in a linear photo-detector, with responsivities d_r, d_s at the reference and sensor wavelengths, respectively. These two parameters can be almost identical if the wavelength of the two optical signals are very close. The electric current signal obtained after the optical-to-electrical conversion in the photo-detector can be described with the phasor:

$$I_0 = d_s \cdot P_S + d_r \cdot P_R \tag{4.10}$$

After the current-to-voltage conversion of I_0 in the reception electronics, a proportional signal V_0 is finally obtained:

$$V_0 = k_0 \cdot I_0 \tag{4.11}$$

where k_0 is the global transimpedance constant related to the electronic receptor.

The sensor-induced power modulation H induces phase variations in this electrical signal. This phase response can be used as a self-referencing measurement parameter, ϕ. In the next sub-section, a digital filter model of this configuration is presented and employed to analyze the frequency response using the Z-Transform.

4.3.2 Digital Filter Model

The filter schematic of the fiber-optic configuration in Fig. 4.6 can be found in Fig. 4.7, where dashed lines correspond to the electrical domain and continuous lines correspond to the optical domain.

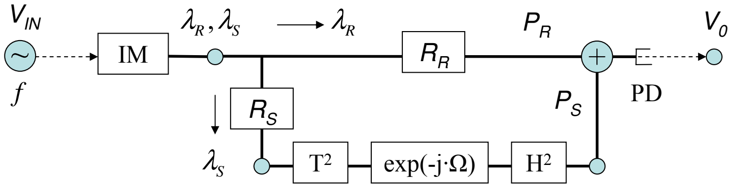

Figure 4.7: Schematic of the optical configuration as a finite impulse response (FIR) digital filter. IM: Optical intensity modulator; R_R, R_S: reference and sensor FBG reflectances, respectively; PD: Photo-detector; H: sensor power modulation; Ω: Phase shift induced by the fiber coil of length L in the RF signal modulating the optical carrier.

Either two optical signals or a broadband spectrum with optical power density around the two reference and sensor wavelengths are launched into an optical intensity modulator (IM). An electrical voltage signal at frequency f and amplitude V_{IN} drives the linear IM. The electro-optical modulation efficiency parameters k_r, ks at the reference and sensor wavelengths are related to m_r, m_s, respectively, through:

$$k_r \cdot V_{IN} = m_r \cdot P_{Ri} \tag{4.12}$$

$$k_s \cdot V_{IN} = m_s \cdot P_{Si} \tag{4.13}$$

In the remote sensing point, the modulated optical signal is sliced in wavelength and reflected by two FBGs at the remote sensing point. The signal at the reference wavelength follows the through-path of filter schematic, while the signal at the sensor wavelength travels through the delay fiber and is attenuated by the intensity sensor and phase-shifted Ω radians, due to the propagation time in the delay fiber of length L. The value of the phase shift is the following:

$$\Omega = \frac{2\pi}{c} \cdot n_g \cdot f \cdot 2 \cdot L \tag{4.14}$$

being c the speed of light and n_g the effective group refractive index of the optical fiber.

This is the relative phase delay of the RF signal at the sensor wavelength with regards to the signal at the reference wavelength. The Free Spectral Range of the configuration is:

$$FSR = \frac{c}{n_g \cdot 2 \cdot L} \tag{4.15}$$

Identifying a generic electrical phase-shift (Ω) with the characteristic transit time of an equivalent digital filter, $z^{-1} = \exp(-j \cdot \Omega)$, the transfer function from Eq. 4.11 can be expressed in the Z-Transform domain as follows:

$$\frac{V_0}{V_{IN}} = \alpha \cdot \left(1 + \beta \cdot z^{-1}\right) \tag{4.16}$$

where:

$$\alpha = k_0 \cdot k_r \cdot R_R \cdot d_r \tag{4.17}$$

$$\beta = \frac{k_s \cdot R_S \cdot d_s \cdot P_{Si}}{k_r \cdot R_R \cdot d_r \cdot P_{Ri}} \cdot T^2 \cdot H^2 \tag{4.18}$$

As it can be seen in the latter expression, a power ratio between constant parameters[2] and the two involved optical signals takes place in the parameter β. Any power fluctuation external to the sensing point is compensated due to this ratio, thus assuring the self-reference of any measurement parameter based on β. The sensor power modulation H, which depends on the measurand, is encoded in the transfer function of the self-referencing configuration by means of the parameter β. The electrical phase response of the detected RF signal, namely ϕ, has the following expression:

$$\phi(\Omega) = \arctan\left(-\frac{\beta \cdot \sin\Omega}{1 + \beta \cdot \cos\Omega}\right) \tag{4.19}$$

being Ω the angular frequency corresponding to the absolute modulation frequency f.

The frequency response of the configuration, both in magnitude and phase, is periodical with regards to angular frequency with a period 2π. For a modulation RF signal at absolute frequency f, the corresponding normalized frequency is:

$$\nu = \frac{f}{FSR} \tag{4.20}$$

Eq. 4.19 shows that, for a fixed angular frequency, ϕ depends only on the parameter β, so ϕ is insensitive to power fluctuations except for the sensor-induced power modulation H in the sensing point, thus performing as a self-referencing measurement parameter.

Examining Eq. 4.16, it can be seen that β is a zero of the transfer function. So a

---

[2] Provided that the ratios between modulation coefficients k_s/k_r, detection coefficients d_s/d_r and FBG reflectivities R_S/R_R, due to aging of devices or thermal fluctuations, are constant in a long-term scenario.

zero transmission occurs when the following two conditions are fulfilled:

$$\beta = 1 \tag{4.21}$$

$$\Omega = \pi \cdot (2 \cdot k - 1) \tag{4.22}$$

for integer k.

In Fig. 4.8 the normalized magnitude response versus angular frequency of the configuration is shown within one Free Spectral Range. A zero transmission takes place at $\Omega = \pi$ for $\beta = 1$. The angular frequency of the zero transmission is the same that for the incoherent ring resonator configuration.

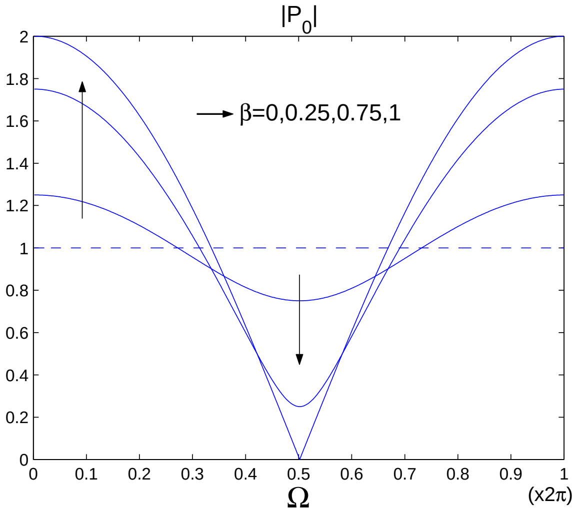

Figure 4.8: Magnitude response of the configuration versus angular frequency for different values of $\beta \in [0, 1]$. $\alpha = 1$.

The phase response of the transfer function described in Eq. 4.16 is represented graphically versus angular frequency in Figs. 4.9 and 4.10 for different values of β. From now on, this parameter, β, will be considered the power modulation parameter of the self-referencing configuration; nevertheless, the relation of β to the transducer intensity modulation H is shown in Eq. 4.18.

It is very interesting to remark that ϕ (see Eq. 4.19) is anti-symmetrical with respect to the angular frequency $\Omega = \pi$, this is:

$$\phi(\Omega) = -\phi(2\pi - \Omega) = -\phi(-\Omega) \tag{4.23}$$

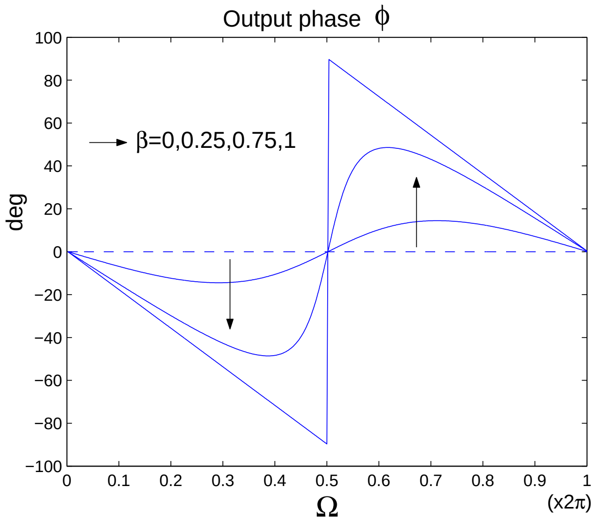

Figure 4.9: Phase response of the configuration, from Eq. 4.16, versus angular frequency for different values of $\beta \in [0, 1]$.

If $\beta < 1$, the phase response increases from 0 to positive values as β takes greater values, being $\Omega > \pi$, and the maximum values around 90 degrees occur at angular frequencies tending to $\Omega = \pi^+$. For angular frequencies lower than π, the phase response decreases from 0 to negative values as β tends to one, and the peak values around -90 degrees take place, once again, around angular frequencies tending to π^-, being $\Omega = \pi$ the frequency of the zero. This explanation is illustrated graphically in Fig. 4.9.

On the other hand, when $\beta > 1$, the phase response performance is similar and reaches peak values around ±180 degrees at angular frequencies close to π, see Fig. 4.10.

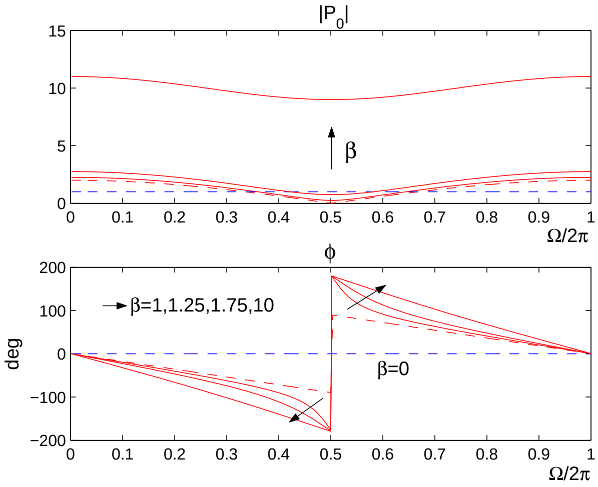

Figure 4.10: Transfer function of the configuration versus angular frequency for different values of $\beta > 1$. $\alpha = 1$.

There are different options in order to get values of β greater than 1. In the transmission stage, an unbalanced optical power ratio $\frac{P_{Si}}{P_{Ri}} > 1$ can be imposed. In some cases, the ratios k_s/k_r or d_s/d_r between the modulation and detection coefficients, respectively, can be greater than one. On the other hand, the FBGs can be fabricated so that $R_S/R_R > 1$. Finally, optical amplification between the two fiber Bragg gratings can be included.

4.3.3 Novel Self-Referencing Parameter with Enhanced Sensitivity

A novel measurement parameter φ is defined as follows:

$$\varphi(\Omega) = \phi(-\Omega) - \phi(\Omega) \tag{4.24}$$

for $\Omega \in [0, \pi)$.

Due to the anti-symmetry of ϕ, it yields:

$$\varphi(\Omega) = -2 \cdot \phi(\Omega) \tag{4.25}$$

As a consequence of this, the novel self-referencing parameter φ performs in a similar way to ϕ, but a significant enhancement is achieved, as the sensitivity is increased two times and the linearity and the self-reference are preserved.

Nevertheless, in order to get this novel self-referencing parameter to be measured, two different modulation frequencies f_1, f_2 are needed. These two frequencies can be obtained using:

$$f_1 = \frac{\Omega}{2\pi} \cdot FSR \tag{4.26}$$

$$f_2 = \left(1 - \frac{\Omega}{2\pi}\right) \cdot FSR \tag{4.27}$$

for $\Omega \in [0, \pi)$ in both cases.

Additionally, a post-processing of the two phase responses at these frequencies must be done to obtain the novel self-referencing parameter with enhanced sensitivity.

4.3.4 Sensitivity and Linearity of the Novel Self-Referencing Parameter φ With Respect to Power Modulation β

The shape of the self-referencing parameter versus β is shown in Figs. 4.11 and 4.12. It can be seen that for low values of Ω the most sensitive region is around $\beta = 0$, see Fig. 4.11; on the other hand, for values of Ω tending to π, a point of inflexion takes place at $\beta = 1$, where the fastest variations of φ are reached, see Fig. 4.12.

In order to have a more precise information, the analytical expression of the sensitivity of φ to the power modulation β is considered in Eq. 4.28, in units of radians.

$$S_\varphi = \frac{\partial \varphi}{\partial \beta} = \frac{2 \cdot \sin \Omega}{(1 + \beta \cdot \cos \Omega)^2 + \beta^2 \cdot \sin^2 \Omega} \tag{4.28}$$

Figs. 4.13 and 4.14 illustrate the behavior of S_φ with regards to β for different values

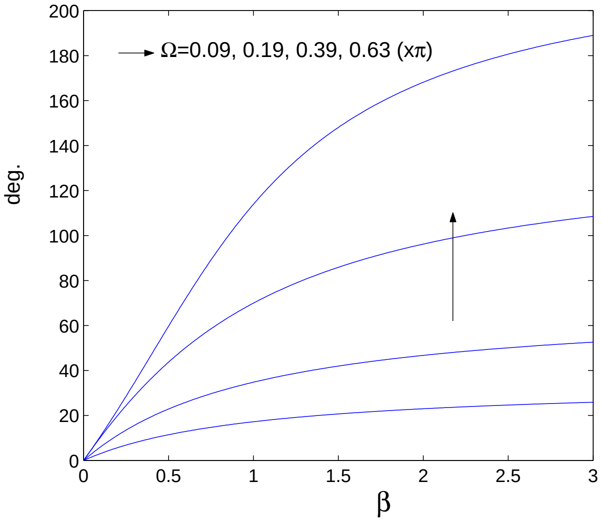

Figure 4.11: Novel self-referencing parameter φ versus power modulation β for different values of angular frequency Ω.

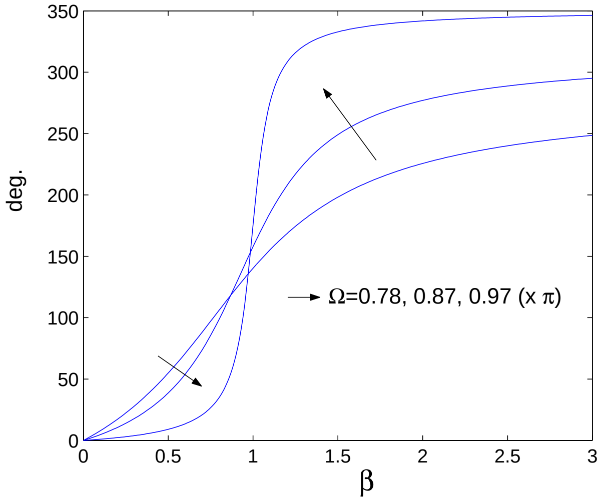

Figure 4.12: Novel self-referencing parameter φ versus power modulation β for different values of angular frequency Ω close to π.

of Ω. The most linear situation is around $\Omega = 0.6$. Values of β greater than 1.5 are not very useful because the sensitivities are very low.

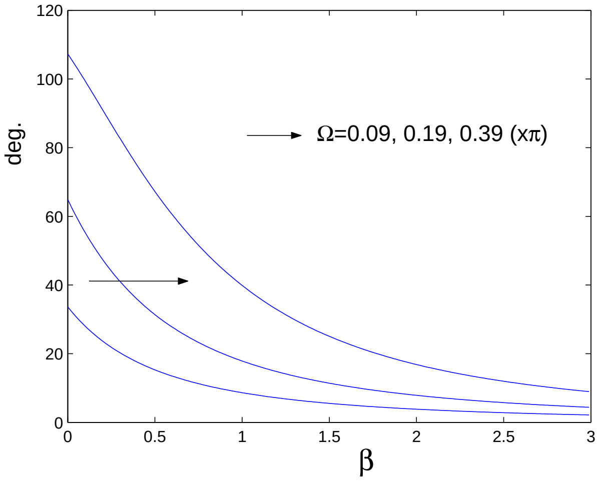

Figure 4.13: Sensitivity S_φ versus power modulation β for different values of angular frequency Ω.

4.3.5 Measurements and Experimental Validation

A schematic of the experimental set-up is shown in Fig. 4.15.

An electrical signal V_{IN} drives an Acousto-Optic Modulator (AOM) at frequency f_i ($i = 1, 2$), thus modulating the intensity of the light from a Super-Luminiscent Erbium Doped (SLED) Fiber Source from Photonetics, with spectral density within the C-band (1510-1560 nm). A TTL signal synchronized with V_{IN} is connected to the reference input (REF) of a lock-in amplifier from Stanford Research Systems, where it is used as phase reference.

The modulated broadband light passes through a broadband circulator (C) and reaches the remote self-referencing configuration, where a fiber-optic sensor (FOS) and a fiber delay coil with a length L of 450 meters are emplaced between two FBGs. For this fiber delay length, the frequency corresponding to $\Omega = \pi$ is around 115 kHz.

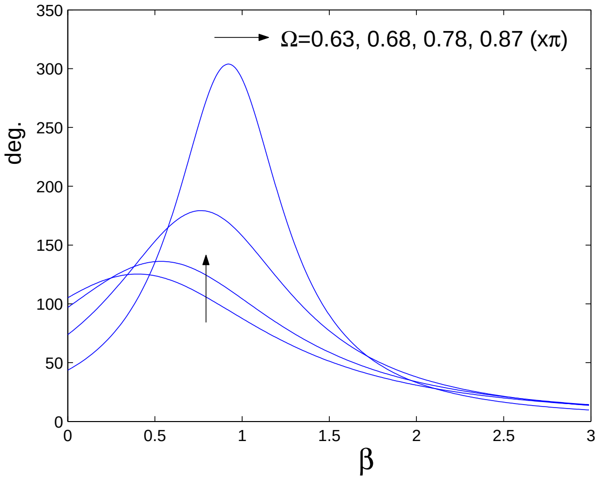

Figure 4.14: Sensitivity S_φ versus power modulation β for different values of angular frequency Ω close to π.

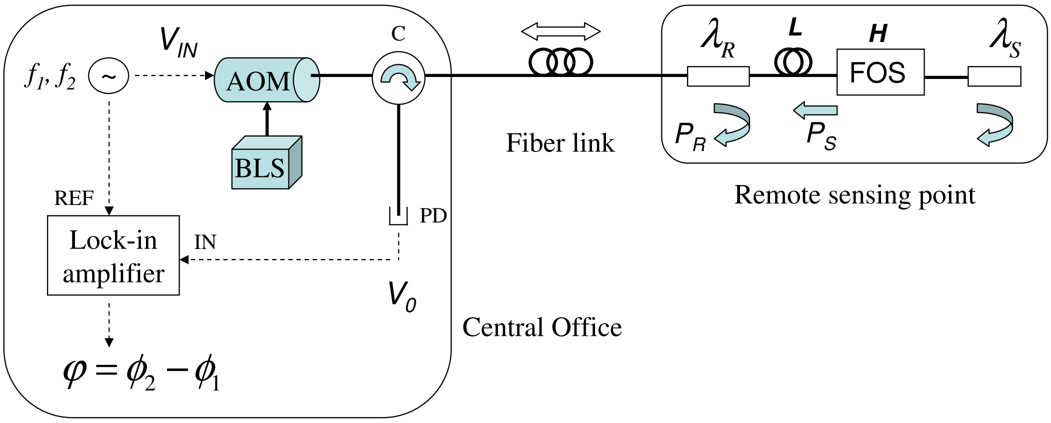

Figure 4.15: Schematic of the experimental set-up for the calibration of the self-referenced parameter φ versus β. BLS: Broadband Light Source, AOM: Acousto-Optic Modulator, C: Broadband Circulator, L: Length of the delay fiber, PD: PhotoDetector.

The spectral reflectivities of the two FBGs measured using an optical spectrum analyzer are shown in Fig. 4.16.

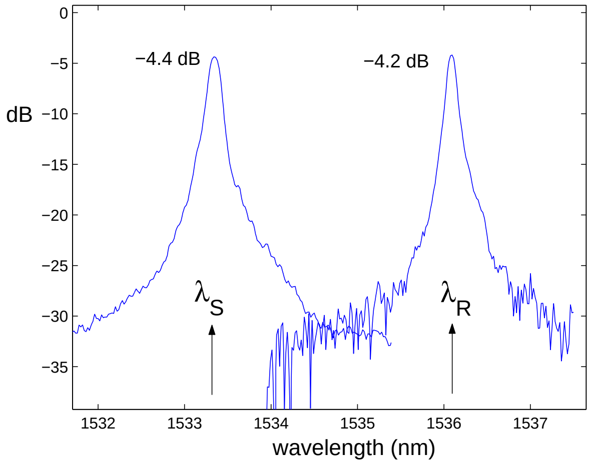

Figure 4.16: Normalized spectra reflected from the two FBGs with central wavelengths λ_S = 1533.3 nm and λ_R = 1536.1 nm. 3 dB bandwidths around 0.25 nm. Circulator insertion losses around 0.65 dB are included in the graph.

The FOS consists of a tapered single-mode fiber operating as a micro-displacement intensity sensor using a micro-positioning stage on an optical table, see Fig. 4.17. By tuning a Distributed-Bragg-Reflector (DBR) laser diode to the sensor wavelength and measuring the power attenuation at each position of the micro-positioner, the intensity calibration curve of the FOS response H has been measured and represented in arbitrary units (a.u.), see Fig. 4.18. In order to test the hysteresis of the sensor, two sets of measurements, marked as *forward* and *backward*, were taken for increasing and decreasing values of the displacement, respectively.

An InGaAs detector from DC-10MHz with switchable gain (Thorlabs PDA-400) has been employed as optoelectronic receiver, where the electrical signal V_0 is measured and delivered to the input of the lock-in amplifier, where the phase with regards to the reference TTL signal is obtained, depending on the value of the modulation frequency and the FOS-induced intensity modulation (H). The value of the modulation frequency

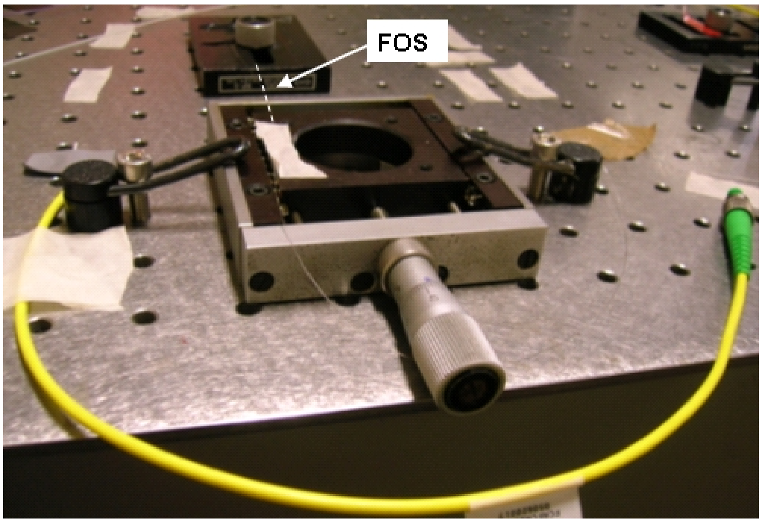

Figure 4.17: Photograph of the tapered single-mode fiber operating as an intensity fiber-optic micro-displacement sensor.

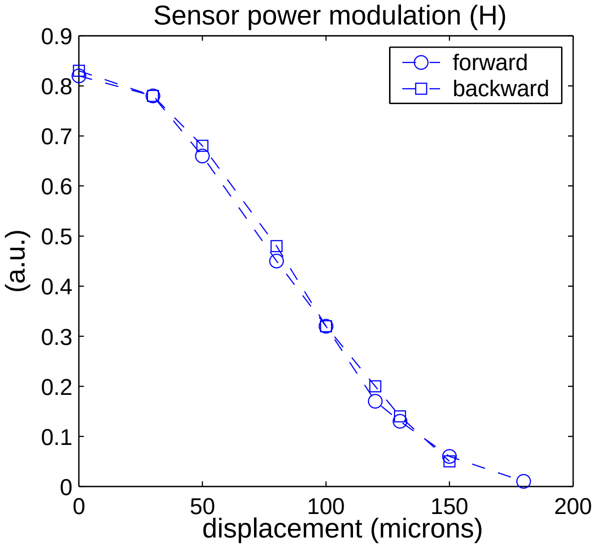

Figure 4.18: Calibration curve and hysteresis of the tapered single-mode fiber used as micro-displacement sensor.

f is alternatively changed between $f_1 = 80$ kHz and $f_2 = 140$ kHz, and the corresponding phase responses ϕ_1, ϕ_2 are recorded and subtracted to calculate the novel self-referenced parameter with enhanced sensitivity, $\varphi = \phi_2 - \phi_1$.

In order to calibrate the response of φ versus the parameter β, the ratio between the two reflected signals from the FBG, without modulation, was first measured, thus obtaining the value $\beta' = \frac{R_S \cdot P_{Si}}{R_R \cdot P_{Ri}} \cdot T^2 \cdot H^2$ as a fist approximation to β, see Eq. 4.18. After turning modulation on again, the corresponding values of ϕ_1, ϕ_2, φ are measured and represented versus the estimation of β, see Figs. 4.19 and 4.20, showing good agreement between theory and measurements[3]. The relation between β and H depends on the emission spectrum of the BLS. It has been verified that this value strongly depends on the total power emitted by the SLED-fiber optical source.

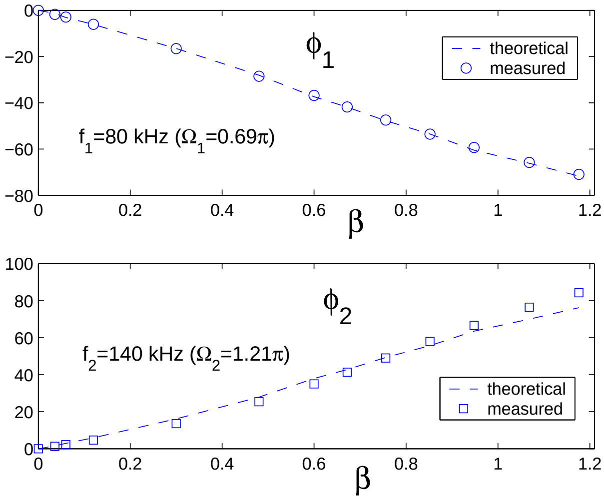

Figure 4.19: Self-referenced measurements (points) of ϕ_1 and ϕ_2 versus β and theoretical fit (lines).

The measurement parameter φ is insensitive to power fluctuations of the modulated optical source if they do not occur in the sensing point.

---

[3] The best agreement between the measurements and Eq. 4.24, using Eq. 4.19, takes place assuming $\frac{k_s \cdot d_s}{k_r \cdot d_r}$=1.2 in Eq. 4.18.

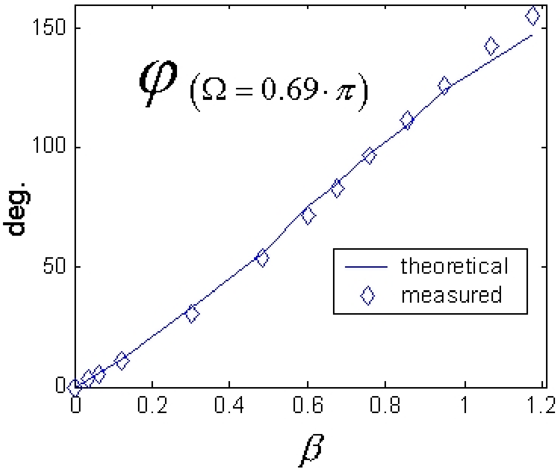

Figure 4.20: Novel self-referenced measurements (diamonds) of φ versus β and theoretical fit (lines).

4.4 Electronically Reconfigurable Delays at the Reception Stage: FBG-Based Self-Referencing Configuration Without Fiber Coil

All-optical incoherent signal processors based on fiber-optic technology [101, 102, 103] were reported in the early eighties aiming to overcome the bandwidth constraints of microwave and RF signal filters. In these photonic devices, the time delays in the optical paths are much higher than the coherence time of the employed optical sources and the coefficients of the filters are always positive.

On the other hand, when the time delays in the optical paths are comparable to the coherence time of the optical sources, the optical phase relations between the different ports are deterministic, and coherent filters are achieved. In order to achieve coherent optical interference, these filters are usually fabricated in integrated optics technology. Several photonic synthesis techniques based on transversal filters [48], delay line lattices [49] and ring resonators [57, 63, 3] have been reported in the last decade, providing greater design flexibility and higher processing bandwidths. Coherent filters are used to achieve high speed components for communication systems such as switches, modulators and tunable filters for dense WDM networks with ultra-high data traffic [29].

In the case of sensor networks, the amount of information to be addressed is usually very low and quasi-static, being low-cost devices, efficient multiplexing topologies and self-referenced measurements relevant aspects. In this environment, incoherent fiber-optic configurations with wavelength multiplexing and reflective operation are the most desirable approaches.

In optical self-referencing configurations, the optical power modulation of the sensor at the sensing point is related to the coefficients of the filter structure, thus encoding the shape of the filter response either in magnitude or in phase and performing self-referenced measurements. Unfortunately, RF modulated all-optical self-referencing techniques require long fiber delay coils in the order of 10 km in order to allow operating frequencies around 1 kHz. For a fixed phase-shift value Ω, there is a strong tradeoff between the length L of the delay fiber and the modulation frequency f. This is caused because, in these all-optical approaches, the propagation time of light along the delay fiber is used to achieve a phase-shift Ω between the radio-frequency (RF) electrical beating signals in the photo-detector. This tradeoff represents the main drawback of all-optical approaches for self-referencing intensity sensors. For a fixed phase-shift value Ω, the relation between modulation frequency and the length of a fiber delay coil is shown in Table 4.1, corresponding to the FBG-based self-referencing configuration studied in this chapter.

In this section, a novel RF electro-optical finite impulse response (FIR) configuration for self-referencing fiber-optic intensity sensors is reported [8]. It is based on the configuration reported in [7], but the long fiber delay coil in each remote measuring point is replaced by a compact and reconfigurable electronic delay in the processing unit, see

Modulation frequency (f)	Length of delay fiber (L)
100 kHz	287 m
50 kHz	574 m
25 kHz	1.15 km
2 kHz	14.35 km

Table 4.1: Tradeoff between modulation frequency f and length of delay fiber for the all-optical FBG-based self-referencing configuration. $\Omega = 0.55 \cdot \pi$, $c = 299,792,458 m/s$, $n_g = 1.45$.

Fig. 4.21.

4.4.1 Novel Electro-Optical Configuration

The proposed fiber-optic configuration with a remote intensity sensor emplaced within two Fiber Bragg Gratings (FBG) and the electrical reception stage is shown in Fig. 4.21(a), where optical paths are represented in continuous lines and electrical paths are marked in dashed lines.

The configuration consists of a light source with optical power around two wavelengths, λ_R (reference) and λ_S (sensor), intensity-modulated at frequency f. The modulated light is launched into a fiber link through a broadband circulator towards the remote sensing point, and the reflected wavelengths from it are recovered in the same circulator. The remote sensor configuration is similar to the configuration described in the previous section, see Fig. 4.6; it consists of two FBGs with an intensity fiber-optic sensor (FOS) located between them, but in this case the fiber delay coil of length L is avoided.

In the reception stage, the two optical signals at wavelengths λ_R, λ_S are separated by an optical demultiplexer and delivered to two distinct photo-detectors, thus obtaining two electrical signals at the same frequency f. The modulation signal recovered from the sensor wavelength, λ_S, is phase-shifted a constant value Ω in the electrical domain and added to the modulation signal recovered from the reference wavelength, λ_R, thus

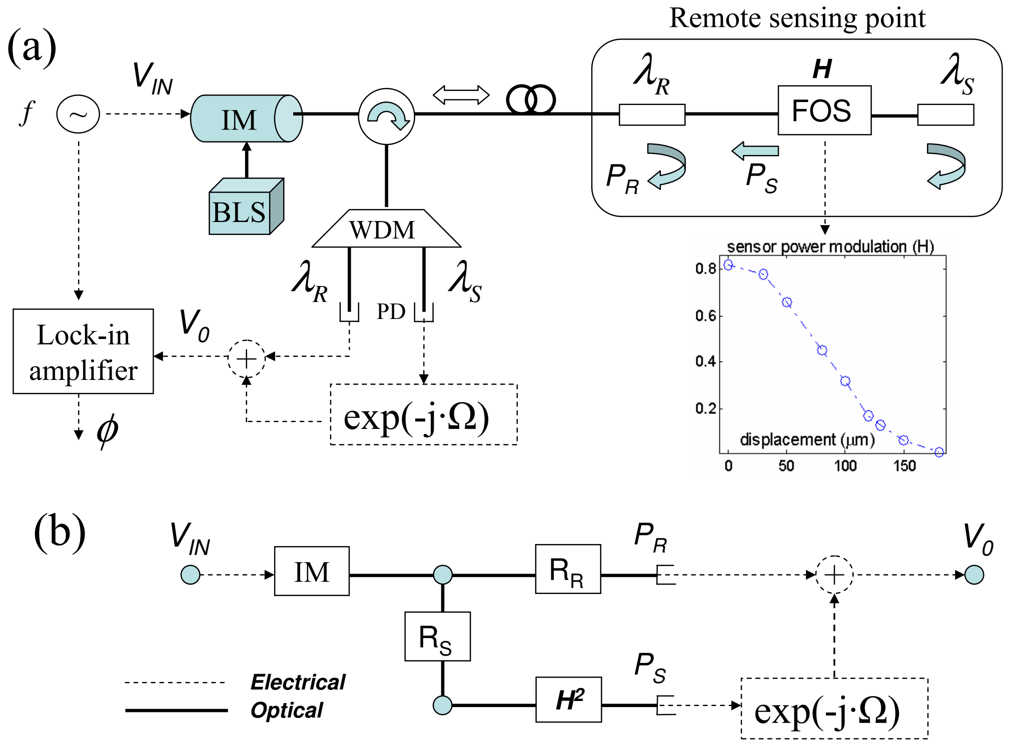

Figure 4.21: Electro-optical configuration (a) and digital filter model (b) for the proposed self-referencing technique without delay fiber coil. BLS: Broadband Light Source, IM: Optical Intensity Modulator, FOS: Fiber-Optic Sensor, PD: Photo-Detector.

deploying an electrical delay line filter. As a consequence of this process, the output voltage signal V_0 suffers a relative electrical phase shift, namely ϕ, with regards to the modulation signal at λ_R. This phase shift ϕ depends on the power modulation H induced by the intensity sensor located in the remote sensing point. A detailed analysis of this self-referencing parameter ϕ has been reported in subsection 4.3.2, see page 113 and the following.

The digital FIR filter schematic of the complete sensor topology is shown in Fig. 4.21(b), which is identical to the topology represented in Fig. 4.7.

The proposed configuration avoids the need for a fiber delay coil between the two FBGs at the sensing point. With the electrical FIR filter in the reception stage, the tradeoff between modulation frequency and delay fiber length is avoided and a more compact, efficient and flexible configuration is achieved, at the expense of using an additional wavelength demultiplexer and photo-detector.

4.4.2 Measurements and Experimental Validation

The electro-optical configuration shown in Fig. 4.21 has been implemented using single-mode fiber with FC/APC connectors. An erbium-doped BLS modulated at $f = 2$ kHz by an acousto-optic modulator from Brimrose was employed to launch optical power within the C-band (1510-1560 nm) into the configuration. Two FBGs with a 3dB bandwidth of 0.25 nm have been used in the remote sensing point. Their central wavelengths are λ_R =1536 nm and λ_S =1552.5 nm, and their reflectivities are 43% and 48%, respectively. A single-mode fiber taper operating as a micro-displacement sensor is emplaced between the two FBGs and used to calibrate the configuration, see Fig. 4.18 and the inset of Fig. 4.21(a).

The reflected waves are demultiplexed by a Coarse WDM and collected by two distinct InGaAs detectors. The electronic delay line filter shown in Fig. 4.21(b) is then implemented using commercial capacitors, variable resistors and LM741 operational amplifiers. Finally, the output V_0 is connected to a lock-in amplifier (SR 530 from Stanford Research Systems) to obtain the output phase ϕ as the self-referenced parameter.

Provided that the lock-in amplifier is locked to the phase of the reflected reference wavelength (at $\beta = 0$)[4], the acquired output phase can be identified with the self-referenced measurement parameter, ϕ, from Eq. 4.19. The phase-shifting circuit fixes the value of the parameter Ω, thus determining the operating point of the configuration in a very simple and flexible way.

Different calibration curves of ϕ versus β have been obtained for different phase-shifting values, showing good agreement between theory and measurements, see Fig. 4.22.

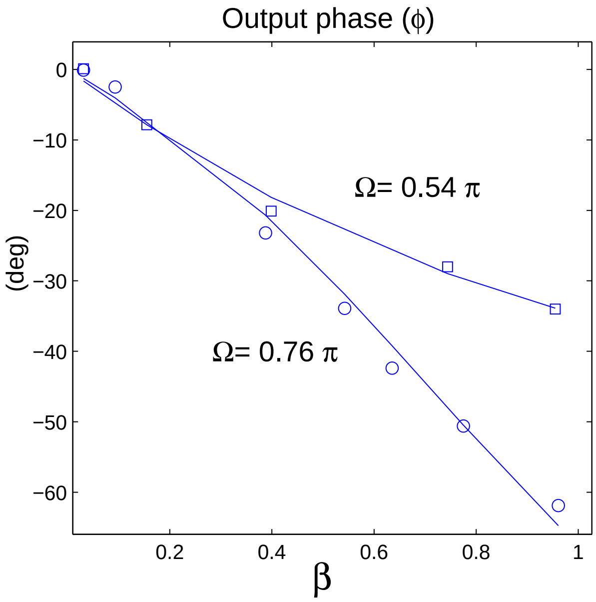

Figure 4.22: Self-referenced parameter measurements versus β for different electrical phase-shifting values Ω. Theoretical curves are drawn in continuous lines.

Note that a fiber delay coil with a length of 300 m is needed to fix a phase-shift around 100 degrees ($0.55 \cdot \pi$ radians) for a modulating frequency of 100 kHz in [7], while

---

[4] Or equivalently, $H = 0$.

in this case no fiber coil is required, a higher phase-shift is achieved and the modulating frequency is 50 times lower.

The performance of ϕ has also been measured for negative values of the induced electrical phase-shift Ω. For two opposite values Ω_1, Ω_2, being $\Omega_2 = -\Omega_1$, an opposite sign in the measured output phase ϕ is verified, see Fig. 4.23. This performance allows to achieve the measurement parameter φ presented in the previous section, but using the compact and reconfigurable electro-optical configuration, see Fig. 4.24.

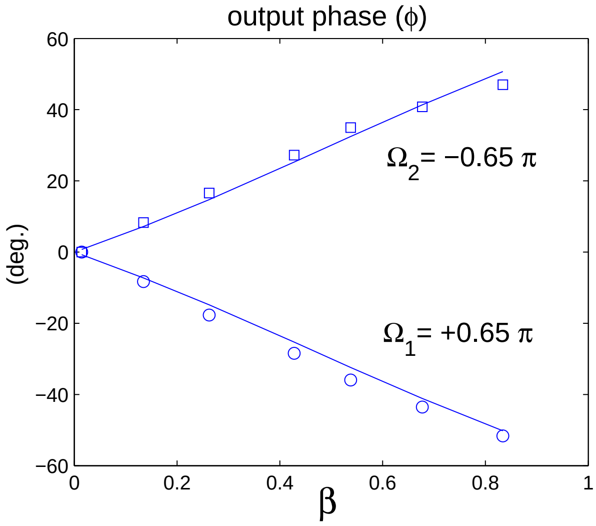

Figure 4.23: Effect of the sign of the phase-shift value Ω in the performance of ϕ.

A variable optical attenuator has been used for inducing power fluctuation in the RF modulated optical source to test the self-reference of the measurements. No change in the self-referenced output phase ϕ has been noticed after inducing 10 dB of power attenuation, see Fig. 4.25. A minimum power density of 0.73 μW/nm is required at the BLS for proper operation.

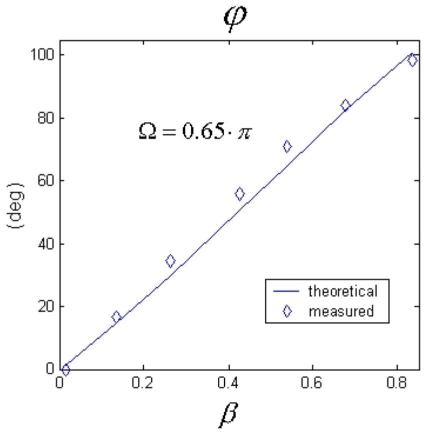

Figure 4.24: Measurements of the self-referenced parameter with enhanced sensitivity φ using the compact electro-optical configuration.

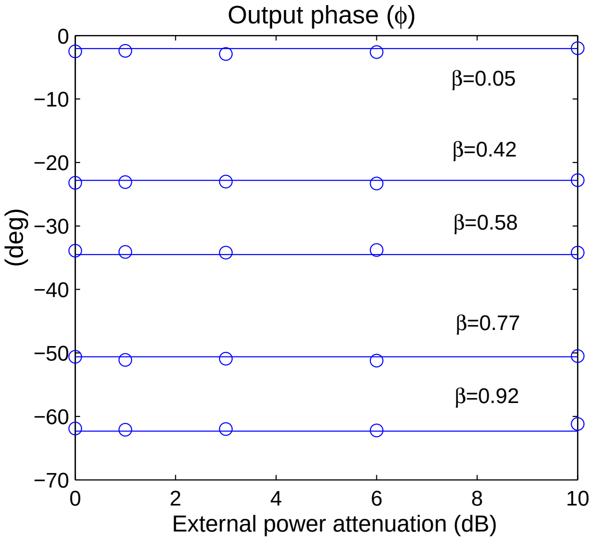

Figure 4.25: Self-reference test of the output phase ϕ for different values of β. $\Omega = 0.76 \cdot \pi$.

4.5 Summary and Conclusions

In this chapter, RF modulated reflective configurations for remote addressing and self-referencing of optical intensity sensors have been studied and several scientific contributions have been reported. The configurations have been described in the framework of the digital filter theory using the Z-Transform, and closed-form formulas for describing their transfer functions and relevant parameters have been reported.

First, a RR-based self-referencing configuration locating a fiber-optic sensor (FOS) in the RR feedback loop and using an external FBG has been studied and experimentally verified [6, 99]. It increases the sensitivity of the transmission configuration without FBG and needs a single wavelength for self-referencing an optical intensity sensor.

A second self-referencing configuration consisting of a FOS and a fiber delay line emplaced between two FBGs with different central wavelengths has been studied. This configuration needs two optical input signals or a broadband light source emitting optical power density around the central wavelengths corresponding to the two FBGs, for self-referencing a single intensity sensor. By employing a novel description using a digital filter model, the frequency response of this configuration has been studied and a novel self-referencing measurement technique with enhanced sensitivity, namely φ, has been proposed, studied and experimentally validated. The self-referencing technique is performed by simultaneously modulating the input optical signal/s using two different frequencies f_1, f_2.

Finally, a compact electro-optical configuration for self-referencing fiber-optic intensity sensors [8] has been analyzed and demonstrated in this chapter. It provides enhanced flexibility, compact design and single point reconfiguration of multiple sensors. Long fiber delay coils of hundreds of meters are avoided and the operating point of the topology can be adjusted just by fixing an electrical phase-shift of a RF signal in a simple and flexible way, using commercial low-cost electronic components such as variable capacitors and resistors. For a 2 kHz modulation frequency, a delay fiber coil of 14.35 km, which would be necessary using the all-optical self-referencing technique, is completely avoided and the performance of the measurement technique is preserved. The value of this modulation frequency is arbitrary, any other value can be used if required by any electronic application. The novel measurement parameter φ with enhanced sensitivity is compatible with the compact electro-optical configuration and has also been measured.

The three self-referencing configurations studied in this chapter are compatible with wavelength-division-multiplexed sensor networks, as it will be demonstrated in the next chapter of this document.

Chapter 5

Coarse WDM Passive Optical Networks for Self-Referencing Optical Intensity Sensors in Reflective Mode

5.1 Introduction

Among several types of high-speed access network technologies, such as x-Digital Suscriber Lines (x-DSL), Hybrid Fibre-Coaxial (HFC) and Local Multipoint Distribution Service (LMDS), the adoption of passive optical networks (PON) for Fiber-to-the-X (FTTx) services deployment is on the rise across the world. The PON topology enables service providers to amortize the cost of equipment and facilities over a large number of subscribers and share one optical fiber among multiple buildings or homes, with no need for optical amplification.

On the other hand, low-cost medium-reach optical networks for multiple photonic sensor interrogation in remote areas have been a strong motive of research during last years. In some cases, both optical communications and sensor networks have very similar architectures, and the communications mass-market has been promoting optical band-splitting devices and optical sources with lots of potential applications for remote sensing through optical fiber.

In this chapter, the main standards of Time-Division-Multiplexed PONs (TDM-PON) are reviewed and the emerging next generation TDM-PONs and Wavelength-Division-Multiplexed PONs (WDM-PON) for broadband access are considered. Recent contributions on WDM sensor networks are studied and the possible convergence between optical remote sensing and future broadband optical access networks is also discussed. Actually, employing a similar topology than emerging communications access WDM-PONs, a reflective sensor network is proposed and demonstrated using two different remote self-referencing configurations. In the reported experiments, Coarse WDM devices are employed for spectral filtering and simultaneous self-referencing interrogation of multiple optical intensity sensors.

Two different optical configurations in reflection mode using Fiber Bragg Gratings (FBG) have been used as self-referencing measurement techniques in the CWDM network. The first approach is the ring resonator configuration in reflection mode using a FBG, which was described in chapter 4 of this work. The second self-referencing technique is the FBG-based all-optical FIR configuration described in chapter 4 of this document.

5.2 Passive Optical Networks for Broadband Access

The predominant broadband access solutions deployed today are the point-to-point xDSL connection and the HFC cable TV (CATV) point-to-multipoint network. The main restrictions of both technologies arise from the fact that they are based on infrastructure originally built for carrying voice and analog TV signals. Some DSL variations such as VDSL (ITU-T G.993) can support up to 50 Mb/s of downstream bandwidth and second-generation VDSL2 systems (ITU-T G.993.2) can provide data rates exceeding 100 Mb/s in both downstream and upstream directions, but these technologies have severe distance limitations: the maximum available bit rate is only achieved at a range of around 500 meters for VDSL and 300 meters for VDSL2. On the other hand, HFC-CATV networks are mainly built for delivering analog TV broadcast services, so they do not fit well for the bidirectional communication model of interactive digital video broadcast and data networks.

Nowadays, high fiber penetration close to the end-user location is taking place, first in Japan and Korea and more recently in Europe and the United States, as a response to the demand for simultaneous interactive High-Definition Television (HDTV), high speed internet access and telephone services (Triple Play Services). TDM-PONs are becoming an increasingly popular architecture for Fiber to the Premises (FTTP) networks, providing a typical 20 km reach for bidirectional streams up to 2.5 Gb/s in a shared single wavelength, provisioning up to a maximum number of 64 subscribers simultaneously.

Although the traditional TDM-PON with a single wavelength in each direction provides higher bandwidth and longer reach distances than other access network technologies, a capacity increase by means of WDM techniques is being considered for emerging networks, so that multiple wavelengths may be supported in either or both upstream and downstream directions. For the next-generation access network, fiber to the home (FTTH) is targeting to support 100 Mb/s per subscriber to fully support high-speed triple play services.

The physical topology of the optical networks recently reported for multiple sensors remote interrogation fits the communications PON architectures, so hybrid networks can be considered as an interesting opportunity. In the next subsections, a more detailed description of high-speed communications TDM and WDM PON is reported. Recent advances on multiple optical sensors interrogation with the same optical architectures are also studied, and the similarities between optical communication and sensor networks are remarked.

5.2.1 Time-Division-Multiplexing PONs Scenario and Future Evolution Paths

The two main TDM-PON standards are the Gigabit PON (GPON) and the Ethernet PON (EPON), developed in parallel by the International Telecommunication Union (ITU-T G.984.1/2/3) and the 802.3ah group of the Institute of Electrical and Electronics Engineers (IEEE), respectively. The basic topology of a TDM-PON is shown in Fig. 5.1.

This point-to-multipoint network provides high-speed data access of multiple user terminals, generally called Optical Network Terminations (ONT), connected through optical fiber to an access node, generically named Central Office (CO). This CO is an Optical Line Termination (OLT) provisioned with higher-speed data traffic (10 Gb/s) from a larger metro network, and its role is distributing interactively part of this data traffic to the multiple user terminals of the PON with a TDM downstream at a lower data rate, typically 1.2-2.4 Gb/s.

The central office sends the downstream through a primary feeder optical cable to a Remote Node (RN) using a single wavelength within the 1480-1500 nm band (typically 1490 nm). The main differences between GPON and EPON is the data frame and control access protocols realized in the CO. In the RN, a passive power splitting takes place and the complete TDM data frame is broadcasted to N ONTs, where N typically equals 32 or 64, through a secondary optical distribution network with an star topology. The maximum supported distance between the OLT and each ONT is typically 20 km with a total link loss budget around 28 dB for 2.5 Gb/s. The user interaction is received from

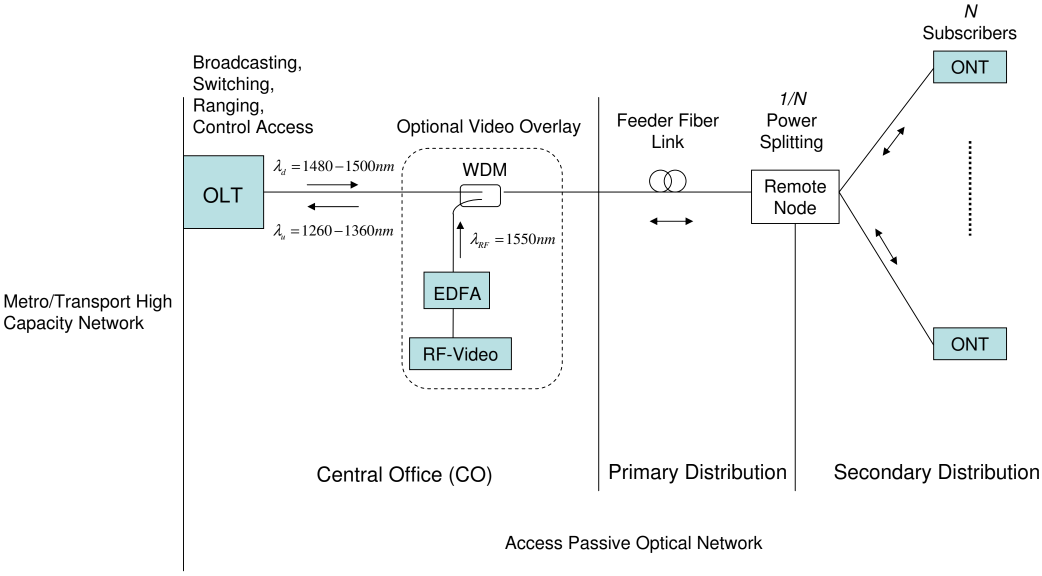

Figure 5.1: Generic schematic of a communications TDM-PON for broadband access.

the ONTs at another single wavelength within the 1260-1360 nm (typically 1310 nm) in the upstream direction. The CO avoids the collision of the upstream wavelength by an access control protocol, including ranging (optical power equalization) and cell allocation (data switching) to each subscriber. An optional Radio-Frequency Video overlay at 1550 nm launched from the CO to the subscribers can also be considered in the downstream direction.

5.2.2 Wavelength-Division-Multiplexing PONs for Broadband Access

Future broadband access is targeting to either 10-40 Gb/s PON or point-to-point access through WDM [104]. The TDM-PON can increase capacity by employing new OLTs with higher bandwidth up to 10 Gb/s over a single wavelength, thus achieving the 10 Gb/s PON. Other approach to 10 Gb/s PONs is the 4 λ-CWDM 2.5 Gb/s PON, being developed in the new IEEE 802.3av standard. By simultaneously featuring 10 Gb/s PON and 4 λ-CWDM, 40 Gb/s could be achieved in the future. Coarse wavelength demultiplexers are commercially available from 4 to 16 channel counts with typical insertion losses from 1.4 dB to 4.3 dB, respectively[1].

All the previous evolution paths still rely on power splitting in the remote node. Nevertheless, some industrials[2] have already adopted point-to-point DWDM PON as the next step in the fiber access technology. In this case, a dedicated wavelength at the maximum data-rate supported by the OLT is reserved for each subscriber, by optical demultiplexing in the remote node rather than power splitting, thus enhancing power budget, reach distance and security issues. Commercial bandsplitting filters based on Arrayed Waveguide Gratings (AWG) are available in the 1528-1622 nm range (C+L band), fitting the ITU-T Spectral Grid with 50-100 GHz channel separation with up to 80-40 channel counts and 2.8-4 dB insertion loss per channel, respectively[3]. Fiber Bragg gratings and optical circulators are another possible technology for bandsplitting filters, also fitting the 50-100 GHz channel separations [92], but this approach is less compact and the insertion losses are higher. The increase of reach distance has also been considered as a future enhancement of access PONs: an interesting approach for this could be the use of a power boost in the PON to reach further ONTs, by using wide-band semiconductor optical amplifiers (SOA) [105] in CWDM-PONs. Using a material composition of InGaAsP in the SOA active layer, signal amplification can be achieved anywhere in the 1200-1650 nm range [106].

---

[1] Values provided by Accelink Technologies in **http://usa.accelink.com/Product/Products.asp** (CWDM module), 21st Jan. 2008.

[2] Novera Optics is already selling its point-to-point DWDM PON systems to Korea Telecom, **http://www.noveraoptics.com/kr/news/index.php**, 24th July 2006.

[3] Values provided by Photeon Technologies, **http://www.photeon.com/html/solutions**, 21st Jan. 2008.

5.3 CWDM PONs for Remote Interrogation of Photonic Sensors

Remote addressing of photonic sensors using optical fibers and multiplexing schemes to measure the response of multiple sensing points have been a motive a research during the last years. Fiber optic intensity sensors can operate at hostile and flammable environments because they are intrinsically safe and immune to electromagnetic interference (EMI). Additionally, they can be easily integrated in WDM networks and commercial devices and laboratory prototypes are available for the measurement of several magnitudes such as ultrasonics, temperature, pressure, humidity, corrosion and displacement [67, 69, 68, 107, 66, 70, 108]. Scalable multiplexing schemes to increase the number of sensors and to reduce the number of components are very desirable aspects for optical sensor networks, being optical configurations based on Fiber Bragg Gratings (FBG) effective approaches for efficiently addressing optical intensity sensors, because they provide reflective configurations that permit the use of fiber leads in both propagating directions of the light. Not only the use of FBGs in optical sensor networks provide an effective and compact strategy for exploiting fiber links bidirectionally; actually, the sensitivity of the optical transducer is enhanced because it is possible to make the optical signal travel through the intensity sensor twice, once for each propagating direction of the light. Finally, FBGs are a well-known, low-cost and excellent technology to achieve wavelength-division-multiplexing of optical sensors, because they can be used with circulators for spectral filtering devices of broadband light sources [92].

Another object of study in the environment of optical sensor networks has been the power budget enhancement, which is directly related to the light routing strategy, traditionally power splitting and more recently wavelength-division-multiplexing. Wavelength-division-multiplexed intensity sensor networks have been reported in reflective star and ladder topologies using FBGs and fused biconical wavelength selective couplers [109, 110] or coarse WDM devices [9]. A hybrid star-ring architecture for a FBG sensor system has also been demonstrated [111]. Interrogation techniques for multipoint FBG sensors in series have been reported using modelocked wavelength-swept lasers [112] and Sagnac loop filters [113]. Recently, an ultra-long-distance interrogation system based on FBGs has been demonstrated, allowing remote strain measurements at a distance of 120 km with no need for optical amplification [96].

In the case of optical intensity-based transducers, changes of optical power are related directly to the external magnitude to measure. But these variations could have a different origin than the magnitude of interest, because of unpredictable changes in losses of passive components such as fiber leads, optical couplers or connectors, which may change in time and because of aging and environmental conditions. Additionally, random power fluctuations of optical sources at the input of the network and detector sensitivity changes can induce an intensity noise added to the desired signals. In order to neutralize all these effects, a variety of self-referencing techniques for intensity sensors have been reported. FBG-based self-referencing configurations providing insensitivity to external power fluctuations, non-correlated to the sensor intensity modulation, have been demonstrated in reflective operation employing single-mode fiber delay lines [7, 8], Michelson and ring resonator configurations [81, 6].

In this chapter, a reflective star network using coarse WDM devices and FBGs is proposed as interrogation technique for self-referencing optical intensity sensors, see Fig. 5.2. The proposed topology consists of a bidirectional Coarse WDM passive optical network (CWDM PON) in double star topology for remote interrogation of N optical intensity sensors in reflective configuration. A total number of 18 CWDM channels are available in the complete wavelength range of 1271nm to 1611nm defined in ITU G.694.2, and a low-water-peak fiber (ITU G.652C-D) can be used for this wide spectrum of transmission.

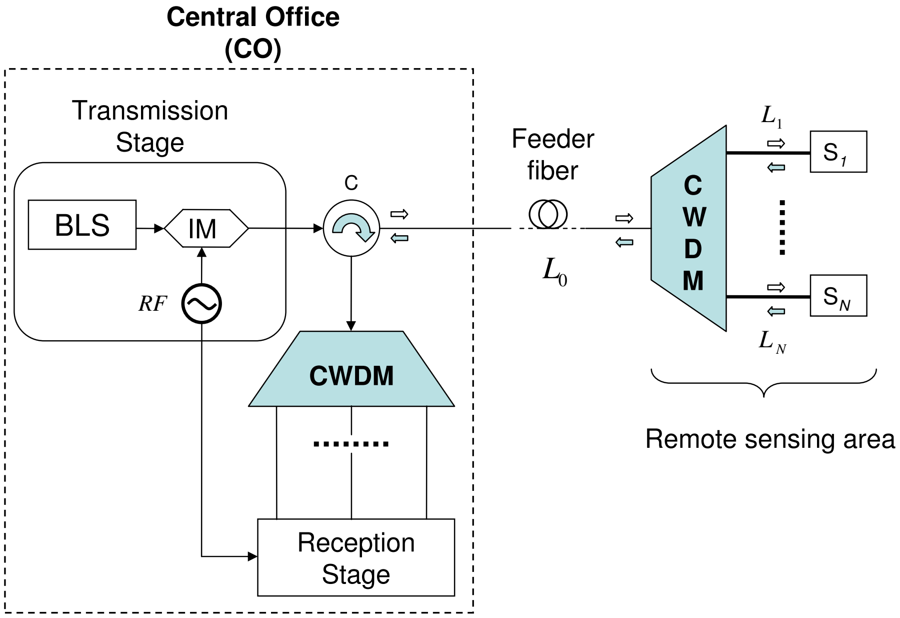

Figure 5.2: Proposed Coarse WDM Passive Optical Network for multiple interrogation of N optical intensity sensors in Reflective Configuration. BLS: Broadband Light Source; IM: Intensity Modulator; S_i, L_i (i=1, $\cdots$, N): Reflective Sensor Configuration.

With the proposed topology, the PON access to the sensors is achieved by means of a central office (CO) where the terminal equipment, both transmission and reception stages, are located. The distribution network consists of a feeder primary fiber cable linking the central office to the remote sensing area. A secondary optical distribution network is deployed in this area by means of a CWDM bidirectional device with N ports, achieving a remote quasi-distributed reflective array of sensors S_i through N short fiber links of lengths L_i $(i = 1, \cdots, N)$.

CWDM equipment shows low insertion losses, so it allows optimizing the power budget, thus increasing the number of multiplexed sensors or the distance between the light source and the remote measuring points. In the CO, the broadband light is launched into a full-duplex fibre-optic lead, which links the CO with the remote measuring points where the different optical intensity sensors are emplaced within a reflective self-referencing configuration based on FBGs. One CWDM optical channel is dedicated to each intensity sensor, leading optical power specifically to each sensor by a cascade of WDM demultiplexers, with no other accumulated losses that propagation and non-ideal behavior of the devices. A single bandsplitting stage with a low-cost CWDM mux/demux device with N output ports is employed, distributing specifically each CWDM channel to its optical sensor.

Once the wavelength-sliced light has reached each reflective sensing point, all the reflections return back to the central unit after a second passing through each intensity sensor, thus increasing the transducer intrinsic sensitivity. The same bidirectional WDM series of devices with the same propagation and low insertion losses provides the return path for the CWDM channels to the CO, where the counter-propagating signals in the main fibre lead are discriminated with a broadband circulator and demultiplexed at the reception stage by an identical CWDM device.

In the telecommunications environment, the WDM PON approach [114] has been recently developed by some industrials (Novera Optics, LG-Nortel-Ignis Photonix) for broadband access aiming at 10-Gbit/s downstream networks, as a different solution to next generation 10 Gbit/s Ethernet PON (IEEE 802.3av) or 10-Gigabit PON (ITU-T G.984), which are based on power-splitting rather than in wavelength-division-multiplexing.

Communication WDM PONs have been recently featured for simultaneous provisioning of high-speed internet access, television and telephone (triple play service) [115, 116], even though standardized systems are not available yet. As the amount of information and the signal bandwidths are much higher than in sensor networks, Arrayed-Waveguide-Gratings (AWG) for Dense wavelength division multiplexing (DWDM) instead of CWDM devices are usually employed.

In the following subsections, the power balance and the scalability of the network are studied. Afterwards, the two particularizations of the remote sensing configuration for self-referencing optical intensity sensors are reported and verified experimentally.

5.3.1 Analysis of Power Losses

By using Coarse WDM devices in the sensor area, instead of the traditional broadcast power splitting approach (see Fig. 5.1 in page 140), a power budget enhancement is achieved. This subsection comprises the quantitative analysis of this improvement.

Table 5.1 shows the definition of some parameters of the network of Fig. 5.2, which are useful for the analysis of the power attenuation that takes place in the complete optical path corresponding to one sensor channel, after propagating from the central office to the sensing area and returning back after being reflected in the remote self-referencing configuration.

The power attenuation of each short-reach WDM point-to-point connection established in the secondary fiber distribution section is considered negligible with regards to the attenuation of the main fiber link, this is, $L_0 \gg L_i$.

Symbol	Definition
L_{CD}	Power insertion loss of the broadband circulator in the downstream direction (CO→Sensors) in natural units (n.u.)
L_{CU}	Power insertion loss of the broadband circulator in the upstream direction (Sensors→CO) in n.u.
α	Attenuation coefficient of optical fiber[4] in dB/km
L_0	Length of the feeder fiber in km
L_D	Power insertion loss of the CWDM device operating as optical demultiplexer in n.u.
L_M	Power insertion loss of the CWDM device operating as optical multiplexer in n.u.
CL	Power insertion loss of the self-referencing configuration in n.u.

Table 5.1: Definition of network parameters.

In these conditions, the total power loss in a sensor channel lightpath from the transmission to the reception stage can be obtained in natural units by using:

$$PL = L_{CD} \cdot L_{CU} \cdot 10^{-\frac{\alpha}{10} \cdot 2 \cdot L_0} \cdot L_D^2 \cdot L_M \cdot CL \tag{5.1}$$

The main advantage of routing the optical power through a dedicated path for each wavelength or pair of wavelengths, using CWDM devices, is that the decrease of the product $L_D \cdot L_M$ with the number of sensors is much less significant than the attenuation that takes place using power splitting in the secondary distribution stage, see Table 5.2.

The generic power loss PL (dB) versus the length of the main fiber is shown in Fig. 5.3 for different numbers of sensors N. In this figure, the advantages of the CWDM approach are clearly illustrated, as the power attenuation value is much lower for fixed values of N and L_0. The power loss of the self-referencing configuration is ignored in the figure ($CL = 1$). The value of the parameter CL strongly depends on the reflectivities of the FBGs used in the configuration, and additionally on the coupling factor of the coupler in the ring resonator configuration. In order to achieve values of CL as close to 1 as possible, the reflectivities of the FBGs should be around 100% at the specific wavelengths and the coupling factor $\kappa \rightarrow 2/3$.

Number of sensors (N)	Power splitting approach	Coarse WDM approach
2	6 dB	2.8 dB
4	12 dB	3.2 dB
8	18 dB	3.6 dB
16	24 dB	8.6 dB

Table 5.2: Power attenuation comparative in the distribution stage, in dB.

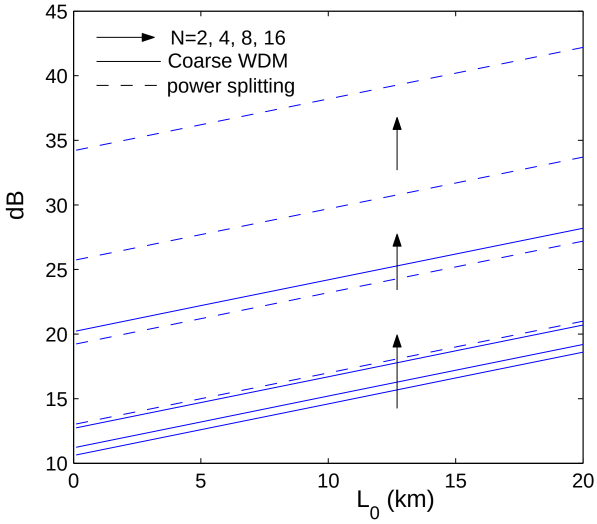

Figure 5.3: Bidirectional insertion loss comparative between the $1/N$ power splitting and the N-CWDM approaches versus length of the feeder fiber, L_0, for different numbers of channels and CL=0 dB.

5.3.2 Scalability of the Network: Dense WDM Upgrade

The DWDM upgrade of the proposed configuration can be achieved by employing a large number of DWDM carriers in the reserved bandwidth of a single CWDM channel, still taking advantage of power distribution improvement, and overcoming the restriction in the number of sensors because of the high spectral separation between CWDM channels. Commercially available Dense WDM multiplexers and demultiplexers, promoted by the high-speed optical communications market, can be used to scale the sensor network reported in this work, following the schematic of Fig. 5.4

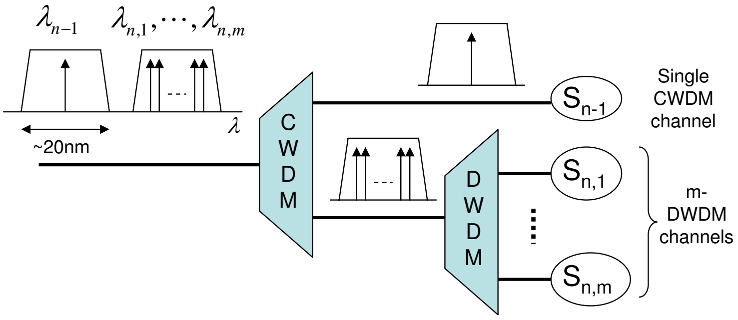

Figure 5.4: Schematic of the DWDM upgrade of the network.

A DWDM upgrading of the 5 CWDM channels within the C+L bands (1528-1622 nm) can be achieved by employing commercial bandsplitting filters based on athermal Arrayed Waveguide Gratings (AWG). These devices can achieve 100 GHz channel separation and 40 channel counts with 3 dB bandwidth greater than or equal to 0.6 nm. They do not require electrical power and operate over outdoor temperature range. On the other hand, apodized FBGs with central wavelength accuracy around 0.1 nm and 0.14 nm at 3 dB bandwidth are also technologically feasible [92], thus making possible to use the FBG-based self-referencing techniques in a DWDM upgrading scenario. A maximum number over 200 multiplexed optical intensity sensors could be addressed with this DWDM upgrade approach. Nevertheless, high fabrication accuracy and stability of the FBGs are needed. As the power density per sensor channel is reduced, remote amplification or different transmission stages might also be required.

5.4 Coarse WDM PON Network for Self-Referencing Optical Intensity Sensors Using Ring Resonators

In this section, the improved ring resonator self-referencing technique in reflection configuration [6, 99], described in chapter 4 of this document, is demonstrated in a CWDM optical intensity sensor network [9]. The experimental validation of the network has been accomplished in the facilities of the GDAF at University Carlos III of Madrid, under the supervision of Dr. Carmen Vázquez.

5.4.1 Description of the Experimental Set-Up

The CWDM sensor network has been built using single-mode fiber components and employing the RR configuration in reflection mode by locating an external long period fiber Bragg grating in the through port. In Fig. 5.5 it is shown the reflective configuration S_n for a generic fiber optic sensor FOS_n. Identical lengths (L) of the RR feedback loop must be used at each sensor configuration, in order to use a single pair of modulation frequencies f_1, f_2 at the transmission stage.

An schematic of the experiment is shown in Fig. 5.6, which is actually a particular implementation of the generic network presented in Fig. 5.2 with $N = 4$. Three bidirectional passive coarse wavelength multiplexers complying ITU-T G.694.2 recommendation with 4 channels (4-CWDM) with central wavelengths 1510 nm, 1530 nm, 1550 nm and 1570 nm have been used in the central office (CO) and the remote sensing area.

The broadband light source (BLS) is built of an array of single-wavelength optical sources. A full-duplex main fiber optic link with length L_0 has been emulated using a

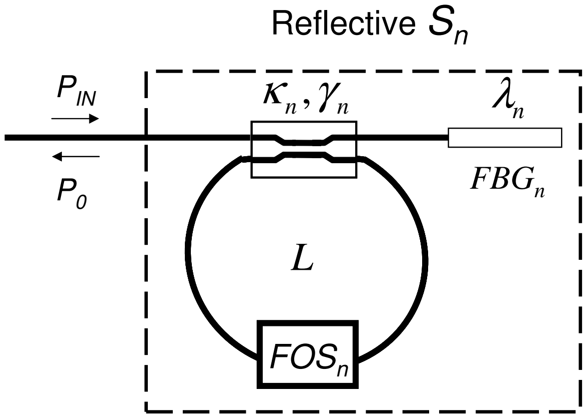

Figure 5.5: RR-based reflective sensor configuration (RR+FBG) for a generic fiber optic sensor (FOS) n. RR parameters: κ_n, γ_n are the power cross-coupling factor and the excess losses of the optical coupler, respectively. L is the RR feedback loop length.

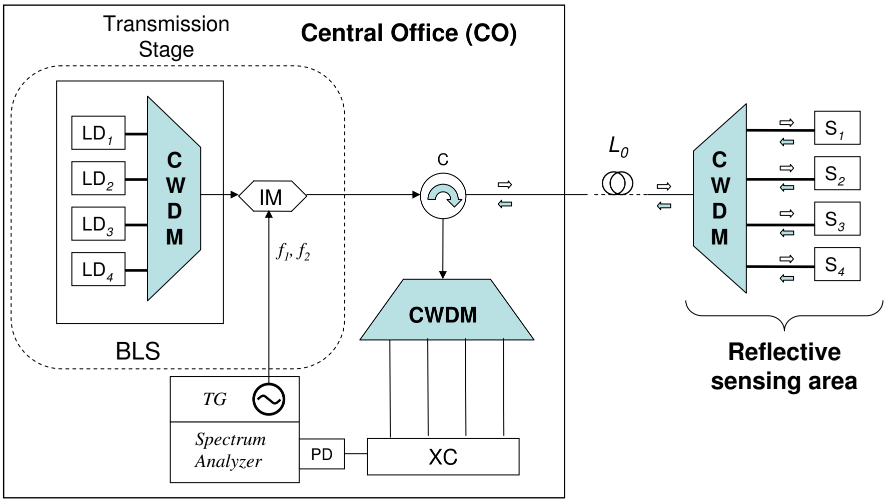

Figure 5.6: Scheme of the experimental set-up for a 4 CWDM channels sensor network. TG: Tracking Generator, XC: optical cross-connect, PD: Photodetector.

variable attenuator. For each attenuation value A_0 (dB), the corresponding equivalent length can be obtained by using:

$$L_0 = -\frac{A_0}{10 \cdot \alpha} \tag{5.2}$$

where α is the attenuation coefficient of the optical fiber, which typically equals 0.2 dB/km in the C-band for G.652 optical fiber.

The value of the loop length L equals 100 meters for all the sensors, being the modulation frequencies in the experiment f_1=4.2 MHz (sensor frequency) and f_2=3.9 MHz (reference frequency). Variable optical attenuators (VOA) were inserted in the RR loops to achieve the bias point of the proposed self-referencing technique, simulating generic bidirectional intensity sensors under a stable environment. The RR bias point of operation is determined by the parameter κ_i and fixing the loop power balance $H_i = \exp(-\alpha \cdot L) \cdot \gamma_i \cdot A_i$, being A_i the VOA-induced attenuation. The values of the coupling factors should be adjusted as close to 2/3 as possible in order to achieve the optimal insertion losses of the RR configuration (see subsection 2.6.3 in page 55).

An electrical spectrum analyzer (Tektronix 2714) with a synchronized radio-frequency (RF) tracking generator (TG) has been used to excite the BLS and to measure the frequency response of the reflective RR-based self-referencing configurations. A frequency sweep including both sensor and reference frequencies (f_1, f_2) was configured in the TG as RF signal. By measuring the power density at these two frequencies using an optical-to-electrical (OE) converter (Thorlabs D400FC), the self-referencing parameter R_{Mi} corresponding to sensor S_i can be calculated. An optical cross-connect (XC) system in the central office can be used to comfortably choose the sensor channel to be measured in the spectrum analyzer, yet in this experiment we changed the output ports of the 4-CWDM mechanically. An Optical Spectrum Analyzer (OSA) was also employed to capture the signals in the optical domain.

5.4.2 Measurement Results

In order to investigate the feasibility of multiplexing different light sources and implementing simultaneously the RR self-referencing measurement technique using FBGs, two distributed-feedback laser diodes at λ_1=1530 nm (LD2) and λ_2=1552.5 nm (LD3) emitting continuous waves with 3 dBm of optical power were used as RF carriers at the CWDM spectral grid. Long-period FBGs with central wavelengths at λ_1, λ_2, reflectivities around 66% and 3 dB bandwith of 0.8 nm have been used at each of the RR+FBG configurations.

The measurements taken from the OSA showed a final carrier to noise ratio (CNR) around 35 dB for L_0=15 km, with optical crosstalk between adjacent channels below the sensitivity of the equipment, see Fig. 5.7(a). Clean RF magnitude responses corresponding approximately to the RR+FBG configuration were obtained with electrical signal to noise ratios above 20 dB at f_1=4.2 MHz (sensor frequency) and 30 dB at f_2=3.9 MHz for both used CWDM channels. The self-referencing measurement parameter was obtained with relative error noise less than 5%, and revealed to be insensitive to imposed attenuations from 1 to 10 dB of the input power at 1550 nm, simulating power perturbations in the fiber link.

In Fig. 5.8, measured and theoretical normalized frequency responses of a RR with and without FBG are represented with good agreement between theory (continuous lines) and measurements (dotted lines). The laser diode LD3 at 1550 nm was internally modulated by an external tracking generator synchronized with an RF spectrum analyzer, where the represented data were captured via RS-232.

The figure shows how the ratio between normalized frequency responses of RR and RR+FBG configurations is approximately 2 for any frequency, obtaining a sharper RF response for the latter configuration, as expected.

In Fig. 5.9, the measured self-referencing parameters R_{M1}, R_{M2} of the two multi-

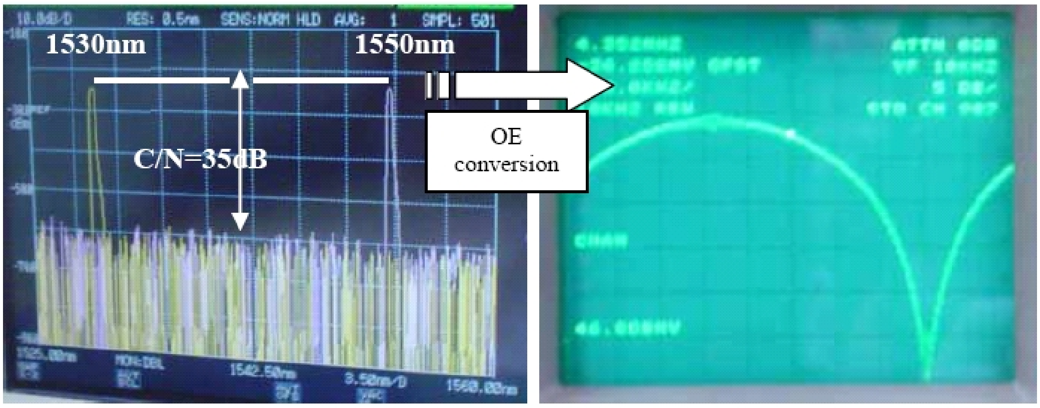

(a) (b)

Figure 5.7: Optical channels spectrum in the OSA (a) and RF magnitude response at $\lambda_2 = 1552.5$ nm in the electrical spectrum analyzer for $\kappa_2 = 0.74$ and $\gamma_2 = 0.99$. The length of the main fiber link is $L_0 = 15$ km and the RR loop length L equals 100 meters.

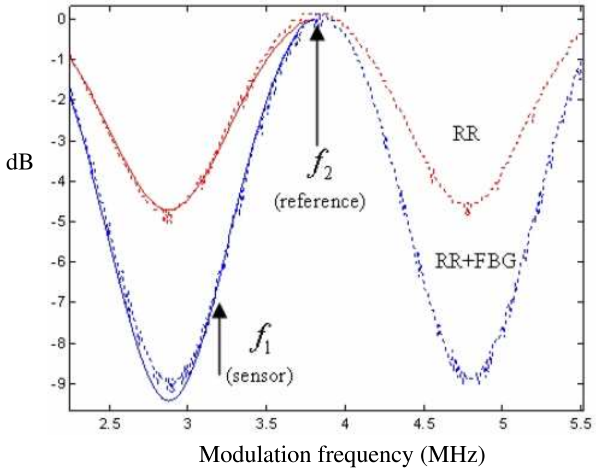

Figure 5.8: Normalized RR and RR+FBG theoretical (continuous lines) and measured (dotted lines) frequency responses for $\kappa_2 = 0.89, H_2 = 0.6, \gamma_2 = 0.99, L = 100$ m.

plexed sensors are represented simultaneously versus the induced attenuation in sensor 1, A_1, emulating an intensity FOS. The self-referencing parameter R_{M2} maintained its original value and proved to be insensitive to the internal losses of the configuration S_1 operating in the adjacent channel, thus we conclude that the crosstalk between sensors in the CWDM network is negligible.

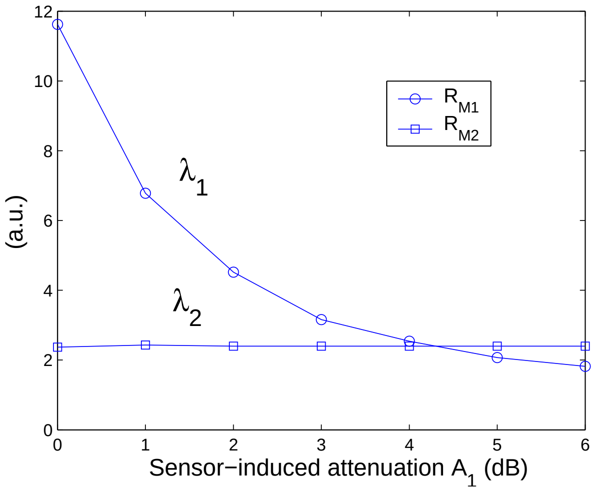

Figure 5.9: Crosstalk evaluation between the two channels at λ_1 =1530 nm and λ_2 =1550 nm.

5.5 Coarse WDM PON Network for Self-Referencing Optical Intensity Sensors With Enhanced Sensitivity Using Fiber Delay Lines

In this section, the improved all-optical self-referencing technique based on FBGs and fiber delay lines, described in chapter 4 of this document, is demonstrated in a CWDM optical intensity sensor network. The experimental validation of the network has been realized as part of a collaboration between the GDAF and the Optoelectronics Unit of INESC Porto, within the framework of the COST Action 299. This joint research has been supervised by Dr. Carmen Vázquez and Dr. José Manuel Baptista, and it was held in the INESC Porto facilities during July 2007.

5.5.1 Description of the Experimental Set-Up

A coarse WDM passive optical network has been built using single-mode fiber technology in order to simultaneously address and self-reference different fiber-optic intensity sensors. The network follows a double star topology with reflective self-referencing configurations S_i $(i = 1, \cdots, N))$ at each remote sensing point, where a generic fiber optic sensor FOS_i and a fiber delay line with length L is located between two FBGs with different central wavelengths [7], see Fig. 5.10.

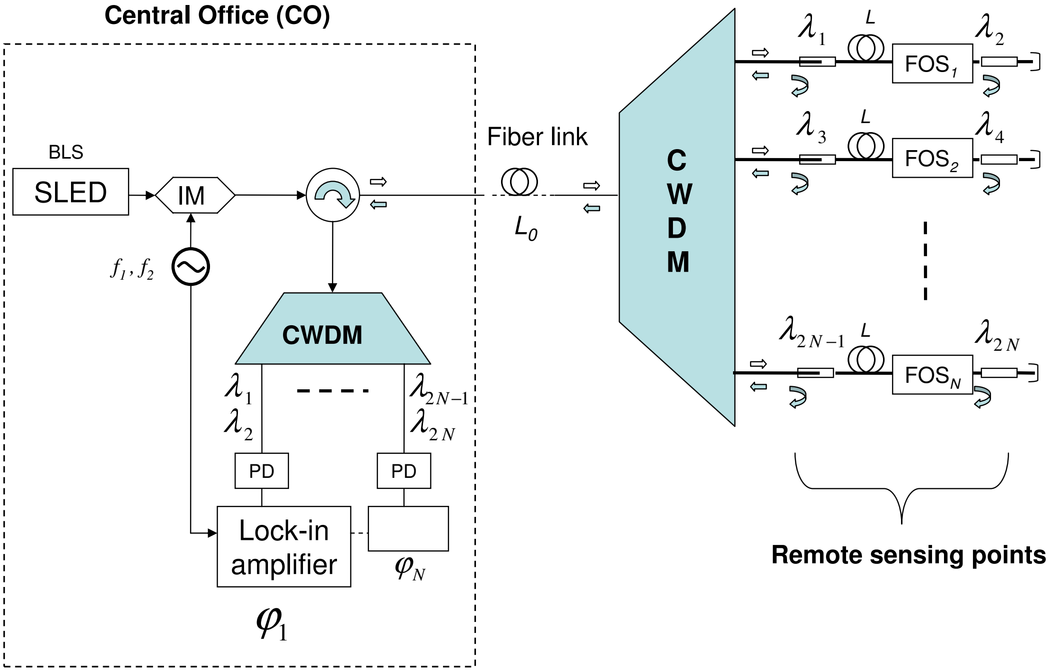

Figure 5.10: Schematic of the proposed coarse WDM network for self-referencing N intensity fiber-optic sensors (FOS) using two FBGs and a fiber delay line of length L at each remote sensing point. SLED: Super-Luminiscent Erbium-Doped-fiber source, IM: Intensity Modulator, C: Broadband circulator, PD: Photodetector.

The transmission stage is built of a RF intensity modulated broadband light source (BLS), consisting in this case in a Super-Luminiscent-Erbium-Doped-Fiber source (SLED) from Photonetics with a broadband emission spectrum within the C-Band and a total emitted power of 84 mW. Identical lengths (L) of the fiber delay lines must be used at each sensor configuration in order to share the modulation frequencies f_1, f_2. An acousto-optic modulator (AOM) from Brimrose and a function generator (Wavetek Mod. 81-50MHz) connected to its driver have been used to modulate the SLED, see photographs of Fig. 5.11.

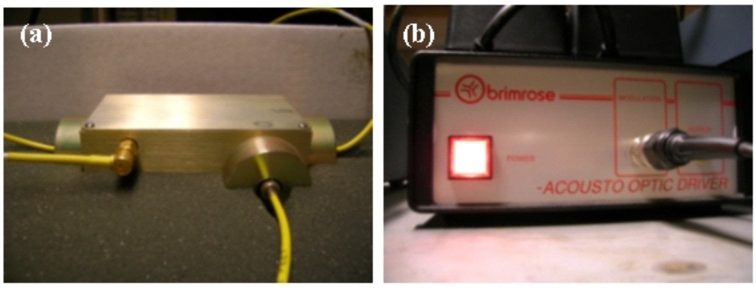

Figure 5.11: Photographs of the acousto-optic modulator (a) and its electronic driver (b).

A RF signal with alternating values $f_1 = 75$ kHz and $f_2 = 150$ kHz excites the intensity modulator (IM) and immediately after the transmission stage, a broadband circulator is located in order to launch the downstream optical broadband signal into the PON. The modulated light reaches the remote sensing area through the primary fiber link with length L_0.

A secondary optical distribution network with low optical loss is deployed in the remote sensing area by means of a CWDM bidirectional device with N ports, achieving a remote quasi-distributed reflective sensor array ($S_i, i = 1, \cdots, N$). In our experimental set-up, two identical CWDM devices with four output ports ($N = 4$) have been employed in the remote distribution stage and the reception stage. These band-splitting devices show a flat shape with 0.5 dB bandwidths around 16nm and low loss of 1.6 dB.

The two channels with central wavelengths 1530 nm (sensor S_1) and 1550 nm (sensor S_2) have been reserved for multiplexing two micro-displacement intensity sensors made of tapered single-mode fibers. The transmission response and mechanical hysteresis of the two tapered fibers versus displacement were measured using a tunable DBR laser diode emitting at the corresponding operating wavelength and using a power meter to estimate the induced attenuation, see Fig. 5.12.

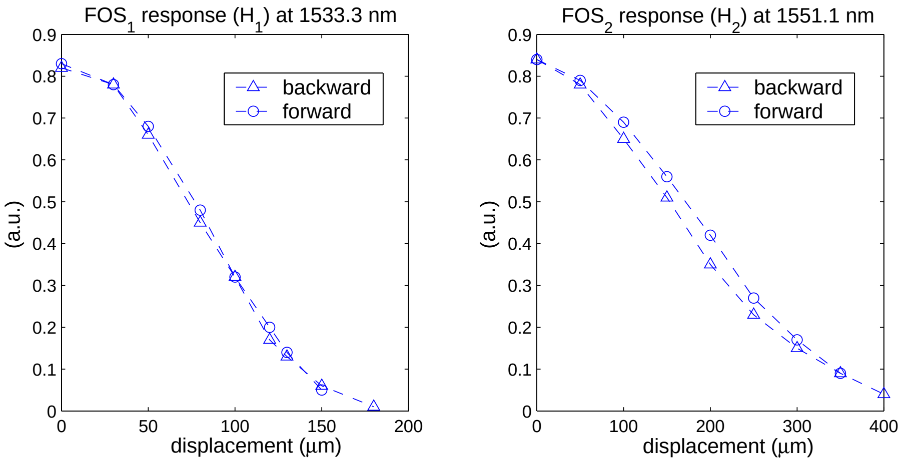

Figure 5.12: Measured intensity responses H_1, H_2 at the sensor wavelengths of the two tapered single-mode fibers operating as micro-displacement sensors.

The broadband circulator receives the reflected multiplexed optical upstream with the sensor information. The upstream optical signal is demultiplexed by the CWDM device and delivered to an array of N photodetectors (PD) and lock-in amplifiers operating as phase detectors, one for each sensor channel. If a single lock-in amplifier is available, a low cost electronic cross-connect device can be emplaced connected in parallel to the PD array to switch between the optical ports. In our experiment, a single lock-in amplifier (SR 530 from Stanford Research Systems) and photo-receptor (InGaAs detector from DC-10MHz with switchable gain, Thorlabs PDA-400) have been used and the connections with the optical ports were made mechanically.

The reflective sensor configuration at each remote sensing point is realized with one pair of FBGs for each channel. Identical fiber coils with a length of 450 m and the corresponding intensity sensor were emplaced between the two FBGs at each sensing point. In total, 4 FBGs were used with a 3 dB bandwidth of approximately 0.25nm and reflectivities around 50%. Their central wavelengths are $\lambda_1 = 1533.3$ nm, $\lambda_2 = 1536.1$ nm for sensor 1, and $\lambda_3 = 1551.1$ nm, $\lambda_4 = 1552.9$ nm for sensor 2. The FBGs normalized reflected spectra with regards to the incident power density as a function of wavelength have been measured with an Optical Spectrum Analyzer from Ando, using the SLED spectrum as reference level and a broadband circulator in an isolated set-up, see Fig. 5.13.

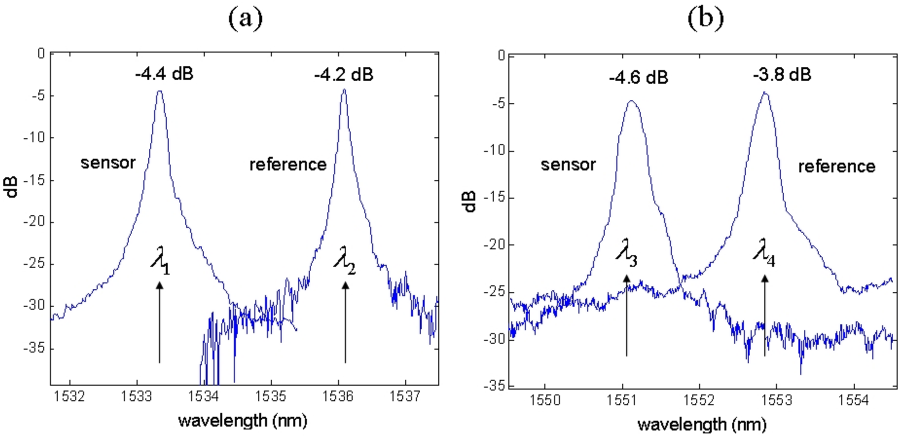

Figure 5.13: Measurements of the normalized reflected spectra from the FBGs with regards to incident power density. The central wavelengths are: $\lambda_1 = 1533.3$ nm, $\lambda_2 = 1536.1$ nm for sensor 1, and $\lambda_3 = 1551.1$ nm, $\lambda_4 = 1552.9$ nm for sensor 2.

5.5.2 Measurement Results

A lock-in amplifier has been used in the reception stage in order to obtain the novel self-referencing parameters, φ_i (i=1,2), described in Eq. 4.24 (page 118). For each sensor configuration S_i, the photodetector recovered the corresponding electrical output signal and it was delivered to the lock-in amplifier in order to register the output phase values, thus measuring the single-frequency parameters ϕ_{i1}, ϕ_{i2} by alternatively changing the value of the modulation frequency f_1, f_2, respectively. Finally, the phase-difference self-referencing parameter with enhanced sensitivity is calculated subtracting the two single-frequency parameters, $\varphi_i = \phi_{i2} - \phi_{i1}$. For the fiber delay length of 450 m, the modulation frequencies $f_1 = 75$ kHz and $f_2 = 150$ kHz provide opposite phase responses ($\phi_{i1} = -\phi_{i2}$) at each value of the power modulation coefficient β_i, thus allowing to achieve the novel self-referencing parameter with enhanced sensitivity, φ_i.

Fig. 5.14 shows the measurements of the two single-frequency (ϕ_{11}, ϕ_{12}) and the novel phase-difference (φ_1) self-referencing parameters for sensor S_1 operating in the 1530 nm CWDM channel, versus the power modulation coefficient β_1. For each CWDM channel, the optical spectrum reflected from the two corresponding FBGs is measured, without RF modulation, thus obtaining the value $\beta_i' = \frac{P_{Si} \cdot R_S}{P_{Ri} \cdot R_R} \cdot T^2 \cdot H_i^2$ as a first approximation to β_i (sensor i), see Eq. 4.18. After turning modulation on, the self-referencing parameters are abtained. The theoretical fits of Fig. 5.14 are drawn in dashed lines, and a good agreement between theory and measurements is achieved[5].

In order to test the crosstalk between two sensors operating in adjacent CWDM channels, several measurements of the measurement parameter φ_1 (S_1) were measured for different values of the power modulation β_2 at the configuration S_2, see Fig. 5.15. No correlation between the performance of the configurations S_1 and S_2 is noticed, so the two sensors can be interrogated simultaneously without mutual interference.

Finally, the self-reference property of the sensitivity-enhanced measurement parameter φ_1 has been tested with regards to power fluctuations of the modulated SLED. In order to do that, a single-mode variable optical attenuator (VOA) was located in the transmission stage between the optical intensity modulator (IM) and the broadband

---

[5] The best fit between the measurements and the theory are obtained considering $\beta_1 = 0.65 \cdot \beta_1'$ when a total power of 84 mW is emitted by the SLED, that is, $\frac{k_s \cdot d_s}{k_r \cdot d_r} = 0.65$.

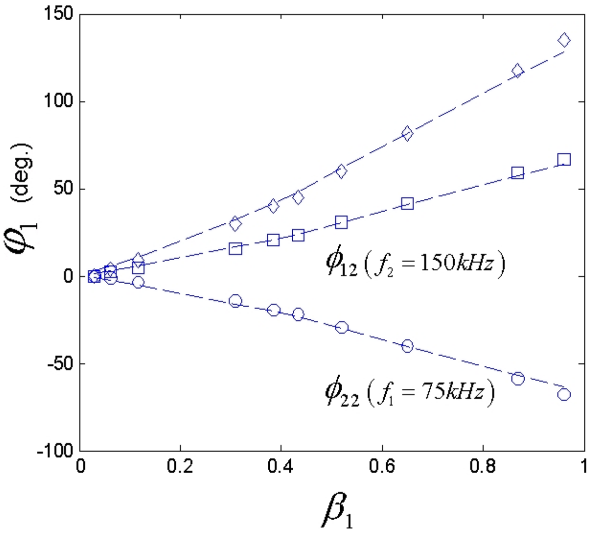

Figure 5.14: Measurements of the self-referencing measurement parameter φ_1 for sensor configuration S_1 versus the corresponding power modulation coefficient β_1.

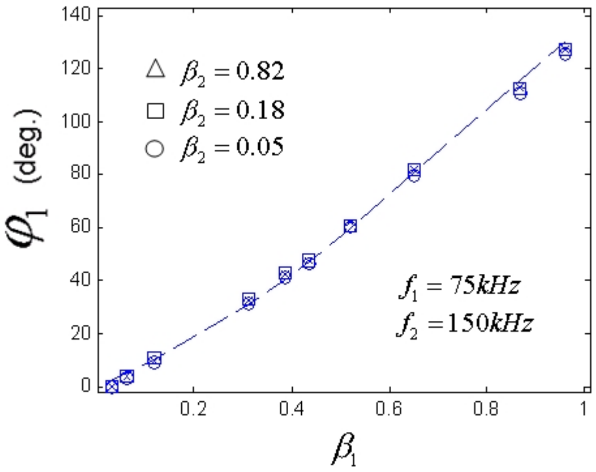

Figure 5.15: Measurements of the phase-difference parameter φ_1 versus β_1 for different values of the power modulation β_2. No crosstalk is induced in φ_1 by the sensor configuration operating in the adjacent CWDM channel at 1550 nm (S_2).

circulator, see Fig. 5.10, thus emulating unexpected power losses along the optical path linking the central office with the remote sensing area. No correlation between the measurements of the self-referencing parameter φ_1 and the induced power attenuation up to 10 dB has been noticed, see Fig. 5.16. A maximum distance of 25 km between the central office and the remote sensing is estimated, for a total emitted optical power of 84 mW by the SLED in the C-L band.

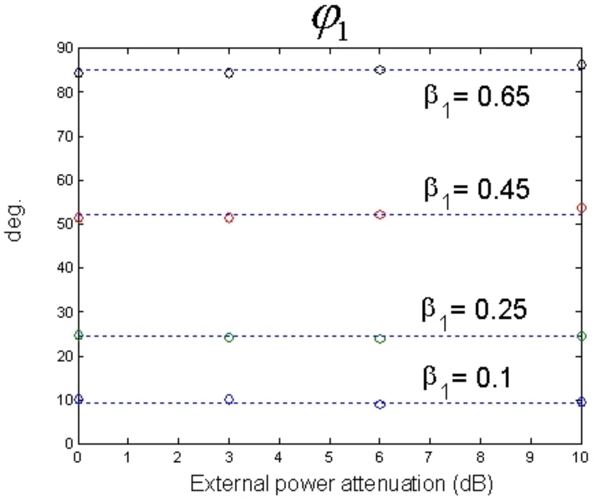

Figure 5.16: Insensitivity of the self-referencing parameter φ_1 to power fluctuations of the modulated SLED up to 10 dB, for different values of β_1.

5.6 Comparative Discussion

Even though the two experimental CWDM networks reported in this chapter are not totally comparable due to the essential differences between the two central offices, there are common aspects that can be discussed comparatively. In this section, some of these points are considered, remarking specifically the role played by the two self-referencing configurations, the one with two FBGs and fiber delay lines (2-FBG+FDL) and the reflective ring resonator configuration with a FBG (RR+FBG).

- *Broadband light sources.* As both of the reported networks rely on spectral filtering in the remote distribution stage, Super-Luminiscent LEDs [117] and EDFAs [118, 119] seem to be the most cost-effective transmitters. The main drawback of these approaches is that only a part of the wideband spectrum is reflected by the sensor configurations, so a large amount of optical power can be lost. This is specially relevant in the case of a DWDM upgrade if the interrogation of a large number of sensors is wanted. In this case, the power density of the broadband light sources may not be enough for proper operation, so different optical sources or remote amplification might be needed.

- *Number of wavelengths per sensor.* The 2-FBG+FDL self-referencing configuration has an important drawback with respect to the RR+FBG configuration, because two different wavelengths must reach the sensing point, while a single-wavelength optical signal is required for the RR+FBG. This difference can be highly relevant if a DWDM upgrade of a single CWDM channel needs to be done.

- *Number of modulation frequencies.* Both self-referencing configurations need two different modulation frequencies at the transmission stage, so there is no relevant difference regarding this point. In both configurations fiber delay lines with identical length must be used in order to permit all the sensors to share the same frequencies.

- *Self-calibration.* The RR+FBG configuration is self-calibrated as far as the transmitted power density at the modulation frequencies is known in the central office. On the opposite, that information is not enough to measure the single-frequency self-referencing parameters when the 2-FBG+FDL configuration is employed. In this case, an initial measurement at $\beta = 0$ is needed in order to know the reference phase.

- *Insertion losses of the remote reflective configuration.* In both cases they must be kept as low as possible in order to increase the network power budget. This can be reasonably accomplished using FBGs with high reflectivities close to 100% and for values of the cross-coupling coefficient κ tending to 2/3 in the RR+FBG configuration.

- *Design flexibility.* Variable ratio optical couplers can be used to achieve flexible RR+FBG configurations. By doing that, the bias point of operation of the measurement technique could be changed if needed. An equivalent parameter for design flexibility does not exist for the 2-FBG+FDL configuration, because the reflectivities of the FBGs are constant. Nevertheless, variable ratio couplers can show undesired instabilities of the cross-coupling coefficient, and the self-referencing parameter is very sensitive to its value, so this approach for design flexibility is not always recommended.

- *Temperature cross-sensitivity.* In outdoor temperature range (-30^0C to $+70^0$C), the reflectivities and the central wavelengths of the FBGs might suffer important modifications. In the case of the RR+FBG configuration, they imply a power budget variation, but no change in the value of the self-referencing parameter. On the opposite, slight changes in the reflectivities or central wavelengths of the FBGs in the 2-FBG+FDL configuration can induce undesired random variations in the measurement parameter. In the RR+FBG configuration, the cross-coupling coefficient κ must keep a constant value insensitive to temperature fluctuations, because the self-referencing parameter can be very sensitive to κ, so optical couplers sensitive to temperature must be avoided.

- *Tolerance to aging of components and equipment.* In the 2-FBG+FDL configuration, two different wavelengths are involved in the self-referencing measurement parameter for each sensor, and the balance between them must be as stable as possible. As a consequence, slight variations in the spectral performance of the optical sources, the optical modulator, the photo-detector and the FBGs can result in undesired changes in the measurements. Those aspects are not critical for the RR+FBG configuration, except for the signal to noise ratio, because a single wavelength is involved in the measurement technique for each sensor. On the other hand, high stability of the coupling coefficient in the RR+FBG configuration is needed.

- *Fiber delay length and modulation frequencies.* The resonance frequencies in the RR+FBG are determined by the length L of the feedback loop, because the configuration performs as 2-RR in series from the point of view of the frequency response. On the opposite, the bidirectional light propagation along the fiber delay line in the 2-FBG+FDL configuration is directly involved in the values of the resonance frequencies, in such a way that the relevant length is actually $2 \cdot L$. This means that for a same length of fiber L in the two configurations, the first resonance frequency is two times lower for the 2-FBG+FDL configuration than for the RR+FBG configuration. Nevertheless, this disadvantage in the RR+FBG configuration is compensated and a balance in the values of the modulation frequencies in the two configurations takes place, because in the 2-FBG+FDL configuration the higher modulation frequency must be above a resonance frequency, while in the RR+FBG configuration the two modulation frequencies can be located below the corresponding value, even though it is two times higher.

- *Reconfigurable reception stage without fiber coils.* The multi-sensor reconfiguration in the central office by replacing the delay fiber coils in the sensing point with an electronic FIR filter fits the 2-FBG+FDL self-referencing approach, but not the RR+FBG approach, because the latter is an infinite filter response (IIR) configuration.

- *DWDM upgrade.* The difference between the two reported sensor configurations imply a different optimal approach with regards to the most desirable optical sources and the DWDM upgrade potential. Using RRs, a single wavelength is required for each sensor, so low cost multiple-wavelength optical sources such as multi-frequency-lasers, Gain-Coupled DFB LD Arrays or Chirped-Pulse WDM [120, 121, 122] are desirable options with more spectral efficiency than Superluminiscent LEDS or erbium-doped fiber sources, because the emitted frequencies can be chosen so that they fit exactly the reflecting wavelengths at each sensing point. This can be much more difficult or not feasible in the case of using the 2-FBG+FDL approach, because these multi-wavelength sources do not emit a pair of wavelengths for each sensor. On the other hand, athermal AWG and FP-filters are available with 100 GHz and 50 GHz with low insertion losses, but the fabrication of two FBGs instead of one for each sensor channel is an important limitation using FDLs, not using RRs.

5.7 Summary and Conclusions

Two CWDM sensor networks in reflective operation by using fiber Bragg gratings (FBG) have been reported for remote addressing and self-referencing bidirectional fiber-optic intensity sensors (FOS) with enhanced sensitivity. The intrinsic sensitivity of the optical transducer is increased because the light propagates through the FOS twice, once for each propagating direction of the light, due to the FBG reflections.

Two self-referencing configurations reported in chapter 4 of this document were employed in the remote sensing points. The first one employs a ring resonator (RR) with a FOS inside the feedback loop and an external FBG in the through port of the optical coupler. The second self-referencing configuration employs two FBGs with different wavelengths for each remote sensing point, with a fiber delay line and the FOS located between the two FBGs. Both self-referencing configurations use two modulation frequencies of the broadband light sources emplaced in the central office.

The feasibility of multiplexing different intensity sensors has been experimentally demonstrated for both self-referencing configurations. Maximum sensor interrogation distances around 35 km have been measured for the RR-based configuration and around 25 km for the configuration with the two FBGs. No crosstalk between optical sensors has been noticed in both CWDM self-referenced networks, and the insensitivity to external power fluctuations, non-correlated to the FOS response to the measurand, has also been successfully tested.

Finally, a comparative discussion between the two self-referencing techniques regarding relevant aspects such as insertion losses of the remote configurations, Dense WDM upgrade potential, available optical sources, self-calibration and temperature cross-sensitivity of the measurement parameters has also been reported in this chapter.

Chapter 6

Photonic Filters Based on Ring Resonators for Dispersion Management in WDM networks

6.1 Introduction

Chromatic Dispersion (CD) is an intra-channel degradation effect that takes place as a short light pulse propagates along an optical fiber, and it can be one of the main restrictions for optical digital transmission systems. CD is due to the dispersion property of the fiber, that is, the fact that its index of refraction, and thus the light velocity, varies as a function of wavelength. Short pulses are not monochromatic, but rather have a certain spectral bandwidth; the shorter the pulse, the wider its spectrum and, thus, the stronger the temporal broadening due to CD. This temporal broadening is also proportional to the length of the fiber span, so the CD becomes larger as the length of the fiber increases.

In this chapter, the main all-optical approaches based on optical filters for CD management are considered, focusing on those designs based on the ring resonator (RR). The dispersive properties of compound RR-based configurations with multi-reflections in the feedback loop, by using a Sagnac loop inside the ring, will be studied in detail for use in DWDM communications networks.

The simulated performance of design examples in optical transmission links is also reported in the chapter, employing VPIphotonics^{TM} v. 7.0.1 software to simulate the effect of employing the proposed filters in non-repeated fiber links longer than 150 km.

Finally, an all-pass filter based on the RR and the Sagnac interferometer is proposed and described in the Z-Transform domain using Matlab® notation. Its magnitude response and quadratic dispersion are also analyzed and graphically studied.

6.2 Chromatic Dispersion (CD) in Optical Transmission Systems

For the standard single-mode fiber (SSMF) with typical chromatic dispersion of 17 ps/nm·km, bit rates in the order of Gb/s at the C-band (1530-1565 nm) are critical for fiber links with distances larger than 100 km, because the bit error rate (BER) can increase to unacceptable values, which generally must be kept lower than 10^{-9}. Even non-repeated fiber links operating at 2.5 Gb/s are sensitive to CD (2 dB power penalty) for distances around 80 km [123].

On the other hand, due to the use of optical erbium-doped-fiber amplifiers (EDFA), long-reach (>100 km) fiber links with no need for signal repeaters have been employed since more than two decades ago. With the use of optical amplifiers, the power budget of an existing network can be maintained for much longer distances, but the impact of CD is higher, because it is proportional to the length of the fiber, and the quality of the communications can decrease drastically. Dispersion-shifted fiber (DSF) with zero chromatic dispersion at 1550 nm can be used to reduce the impact of CD on the bit-error-rate (BER) in transmission systems operating in the C-band. An optical amplified 250 km transmission experiment at 1.8 Gb/s using DSF was reported in 1989 [124].

Nowadays optical backbone networks use mainly the SONET/SDH technology as digital transmission hierarchies for high-speed DWDM sytems, where the OC-48 standard (2.5 Gb/s) is widely deployed in the markets, being OC-192/768 (10/40 Gb/s) emerging and OC-3072 (160 Gb/s) under research. At the same time, long-haul transmission systems in the order of thousands of kilometres with ultrahigh capacities (more than 1 Tb/s) are being investigated.

A general scenario of a DWDM amplified fiber link with chromatic dispersion compensation is shown in Fig. 6.1. Dispersion compensation modules (DCM) are used at many locations in the transmission link. *In-line dispersion compensation* of a fixed predetermined level of CD is typically performed periodically along the transmission line. Many signals of different optical carriers travel along the same optical fiber and all of them benefit from the same dispersion compensation, which is provided by a wide-band fixed DCM. Nevertheless, tunable *residual compensation* is also required, specially at 40 Gb/s and higher speed, for trimming the residual dispersion on a per-channel basis at the receiver end, and compensating the fluctuations of CD within the transport fiber, caused by different effects such as temperature changes or network update. Actually, a variation around 570 ps/nm can be induced in a fiber optic link of 7500 km due to seasonal temperature fluctuation, which can exceed the dispersion limit in of a 20-Gb/s optical signal [125].

6.3 All-Optical Approaches for Chromatic Dispersion Monitoring and Management

In order to exploit the existing SSMF links under the emerging transmission standards, the CD effect is one of the most important issues to take into account. Signal regen-

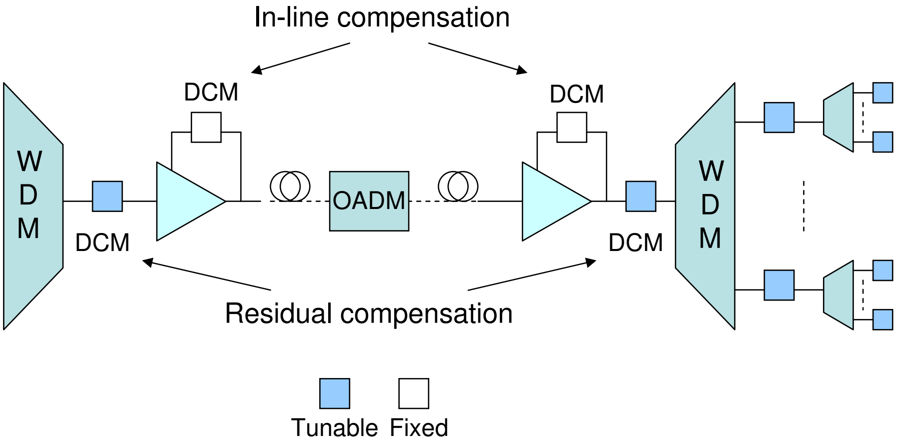

Figure 6.1: General scenario of a WDM transmission link with different Dispersion Compensation Modules (DCM). OADM: Optical Add-Drop Multiplexer.

eration and CD compensation in the optical domain are two approaches to solve the problem. Monitoring techniques to estimate the accumulated CD in reconfigurable and scalable optical networks are also very desirable. In the following subsections, these aspects are described in more detail.

6.3.1 CD Monitoring Using Pilot Tones

Cost-effective CD monitoring techniques have been developed in order to manage reconfigurable and scalable optical networks, in which the accumulated CD may change. Online CD monitoring with no need for tunable filters has been demonstrated by adding small sinusoidal components (pilot tones) to the WDM optical signal, either employing amplitude modulation (AM) [126] or phase-modulation (PM) [105].

As the group delay time is different versus optical frequency due to the chromatic dispersion, the upper and lower sidebands of a pilot tone are phase-shifted one with regards to the other as the optical signal travels along the optical fiber and, when the value of this relative phase shift is 180 degrees, a fading of the pilot tone takes place.

In order to illustrate the RF-fading effect of an AM pilot tone, the baseband magnitude response of a SMF link with a length of 10 km has been obtained using the software VPItransmissionMaker^{TM} Cable Access v. 7.0.1, see Fig. 6.2.

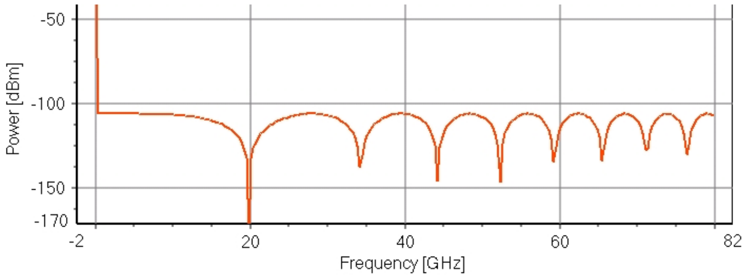

Figure 6.2: Magnitude response of an AM fiber optic link with a length of 10 km and ideal components except for fiber dispersion (D=16 ps/nm·km) and attenuation (A=0.2 dB/km) at 193.1 THz.

In the simulations, a laser at 193.1 THz ($\lambda = 1553.6$ nm) with 1 mW of average power is modulated in amplitude by an electric impulse with amplitude of 0.1 arbitrary units (a.u.) and a bias level of 0.5 a.u., and then the light is launched into a SM fiber link. Ideal components have been used in the simulations, except for the dispersion and attenuation parameters of the fiber. In the frequency response, it can be seen how notches appear at certain frequencies. The magnitude of the received AM pilot tone (P_{AM}) at a fixed frequency near those resonance values also change with the accumulated CD of the fiber link, so the measurement of this magnitude can be employed as the basis of a CD monitoring technique.

For a certain link with an AM pilot tone, the values of the resonance frequencies can be found considering the expression [125]:

$$P_{AM} \propto \cos\left(\frac{\pi \cdot D \cdot L \cdot \lambda^2 \cdot f^2}{c}\right) \tag{6.1}$$

where D, L are the dispersion parameter and the length of the fiber span, λ is the frequency of the optical carrier, f is the frequency of the pilot tone and c is the speed of light.

6.3.2 The Optical Regeneration Approach

A complete regeneration of an optical signal consists of three steps (3R) of signal processing,: firstly, an optical amplification and amplitude equalization of the signal (1R); secondly, a reshaping of the previously amplified signal (2R); and finally, a transmission of the reshaped signal following a retiming obtained with a clock recovery stage (3R).

The reshaping of the signal consists of transmitting new data modulating a low noise optical source emplaced in the regenerator with an on-off keying (OOK) line code. This amplitude modulation of the 'clean' source can be obtained mainly by using non-linear optical gates (NLOG) that yield to a transmission versus signal intensity characteristic, thus providing a decision logic that improves the signal extinction ratio and reduces the amplified spontaneous emission (ASE) of the optical amplifiers. A 5 km optical fiber Sagnac loop was one of the first reported fiber-based NLOGs, used for regeneration operating at 5 Gb/s [127]. More recently, advanced optical regeneration schemes at 40 Gb/s and beyond have been reported [128].

Simple amplification and reshaping of the signal (2R) are usually sufficient to avoid problems derived from the amplitude noise and extinction ratio degradation. Nevertheless, random time deviations of optical pulses can in some cases arise from the interaction between ASE and signal, caused by fiber dispersion. In this case, a synchronous pulse stream clock recovery is required to keep timing jitter below acceptable levels.

A more detailed review on all-optical regeneration can be found in [129].

6.3.3 The Dispersion Compensation Approach

Other approach to manage signal degradation in high capacity long-haul transmission systems is an in-line approach. In this case, the aim is not to segment the link into shorter and independent trucks, but to compensate the degradation as it is taking place in the fiber. Equalized optical amplification and filtering to reduce noise can manage in some cases the power attenuation in optical fiber, but chromatic dispersion must also be taken into account. The effect of CD can be addressed either by dispersion compensating fiber (DCF) with negative dispersion coefficient, using chirped fiber Bragg gratings or employing optical filters. Since more than two decades, fiber-optic interferometers such as the Fabry-Perot (FP) and the ring resonator have been taken into account as possible laser chirp and chromatic dispersion compensating filters in high bit rate digital transmission systems [130, 131]. Planar Lightwave Circuits (PLC) in silica waveguides were demonstrated shortly afterwards as optical dispersion equalizers [132], by synthesizing a finite impulse response (FIR) lattice filter with five Mach-Zehnder interferometers (MZI).

Filter design techniques using compound lattice architectures were reported, cascading MZI configurations [49], MZI and ring resonators [51] and emplacing RR within an arm of a MZI [53], this latter one with applications as a group-delay dispersion equalizer. Novel techniques based on RR lattice architectures were proposed as general optical filter design and synthesis algorithms [57, 58], and chips designed with these methods were fabricated using Ge-doped silica planar waveguides on silicon substrate [58]. Following the general design and synthesis framework of all-pass filters proposed for dispersion control applications [59, 54], a two RR in series filter [35] and a four stages Fabry-Perot tunable micro-electro-mecanical (MEM) actuated all-pass filter [133] were fabricated. A further step in novel architectures was an optical sub-band dispersion equalization scheme which can provide lower losses, higher bandwidth utilization and better fabrication tolerances than cascade architectures [134], though filters following this structure are yet to be demonstrated.

Chirped passive fiber Bragg gratings (FBG) were also reported as tunable chromatic dispersion compensating devices for 10 Gb/s [135, 136] and 40 Gb/s [137] optical signals. Multi-channel fiber Bragg gratings can be fabricated using the complex phase mask technique, which yields flat-top channel passbands and linear group delay spectrums. The optical performances of today's state-of-the-art multichannel FBGs meet the requirements of system manufacturers and allow their use at 10 Gb/s as in-line dispersion compensation for transmission distances up to 2000 km. Tunable compensation for channels at 40 Gb/s can also be provided by FBGs fabricated with complex phase masks [138].

In this work, we focus on the optical filter approaches for dispersion compensation. Different photonic architectures based on the ring-resonator will be described in more detail in the following sections, focusing on their potential applications for CD managing.

6.4 Multi-stage Optical All-pass Filters Based on the Ring Resonator for CD Compensation

The ring resonator with lossless coupler and lossless feedback path is a single-stage all-pass filter [59]. All-pass filters are excellent candidates to perform dispersion management in long-haul WDM networks, because they can be designed following a desired periodical phase response without inducing any amplitude distortion and with low insertion losses.

The description of a general IIR all-pass filter of *N-th* order, employing the Z-Transform is [59]:

$$H_N(z) = \frac{d_N^* + d_{N-1}^* \cdot z^{-1} + \cdots + z^{-N}}{1 + d_1 \cdot z^{-1} + \cdots + d_N \cdot z^{-N}} = \frac{\prod_{k=1}^{N}(p_k^* - z^{-1})}{\prod_{k=1}^{N}(1 - p_k \cdot z^{-1})} \tag{6.2}$$

It can be demonstrated that this form implies that for each of the poles p_k of the response, there is a zero having the inverse module and the same phase [10].

In the case of a ring resonator formed with a lossless coupler and a lossless feedback loop, see Fig. 6.3(a), the transfer function using the Z-transform is [35]:

$$\frac{Y_1(z)}{X_1(z)} = e^{-j\cdot\phi} \cdot \frac{\sqrt{1-\kappa}\cdot e^{+j\cdot\phi} - z^{-1}}{1-\sqrt{1-\kappa}\cdot e^{-j\cdot\phi}\cdot z^{-1}} \tag{6.3}$$

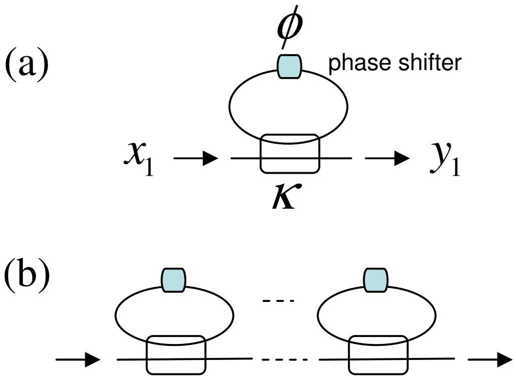

Figure 6.3: Single-stage optical all-pass filter based on the RR (a) and multi-stage all-pass filter architecture using RRs in cascade.

This assures a constant unitary magnitude response for any values of the coupling coefficient κ and phase-shift ϕ. In a multi-stage all-pass filter cascading single ring stages, see Fig. 6.3(b), the magnitude response can be kept unitary whereas the phase and magnitude of the zeros and poles can be tailored in order to approximate a desired phase shape. The module of the poles must always be less than one to assure filter stability.

In the general case of Eq. 6.2, closed-form formulas can be obtained for group delay and quadratic dispersion of the filter [10], some of them given in Chapter 2 of this document. Design algorithms employing these formulas can serve as the basis for filter synthesis using photonic architectures based on the ring resonator.

In Fig. 6.4, the group delay and the quadratic dispersion of a 6-th order RR-based all-pass filter with spectral periodicity of 25 GHz is simulated versus optical frequency using VPIphotonics^{TM} software, using ideal couplers and phase-shifters inside the RR, with 0.1 dB of loop attenuation [1]. It can be seen how the left sideband shows a negative quadratic dispersion around -2400 ps/nm, which is enough, in principle, for compensating the chromatic dispersion of a fiber span of standard SMF with a length of 150 km.

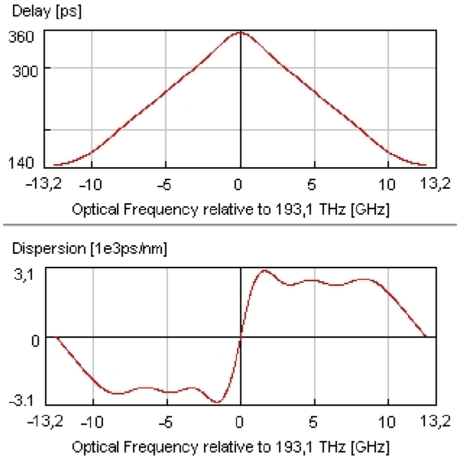

Figure 6.4: Group delay and quadratic dispersion of a 6-th order RR in series design for chromatic dispersion compensation.

6.5 The RR With Internal Reflections by Using the Sagnac Loop for CD Compensation

Recently, the analysis of a Sagnac (SG) loop in ring resonators (RR) has been reported as a tunable optical filter [139, 23, 11, 2] with ultra-narrow-bandwidth for use in Dense WDM systems, see Fig. 6.5.

This filter can be implemented in optical fiber technology and in silicon- or InP-integrated optic technologies, because photonic circuits with equivalent components have already been developed, such as active ring resonators [41] and a monolithically inte-

---

[1] Demo file in VPI 7.0.1-WDM Demos, Passive Components: Disp Comp Filter Characterization.vtmu.

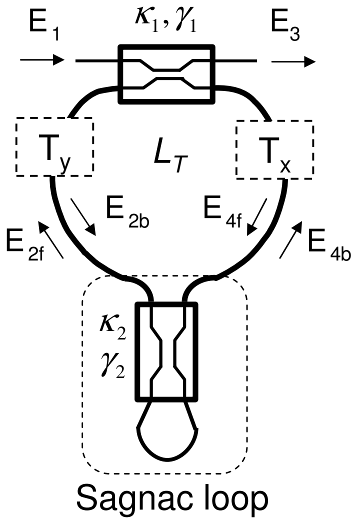

Figure 6.5: General filter architecture consisting of a ring resonator with internal transmission transfer functions (T_x, T_y) and a Sagnac loop as transmission-reflection function (TRF). The total length of the feedback path equals L_T.

grated Sagnac interferometer [140].

The RR with SG loop filter allows frequency detuning just by adjusting a coupling coefficient of an optical coupler, with no need for using conventional phase shifting approaches, such as integrated thermo-optic [26], nor current-injection based [25] phase shifters.

In this section, the photonic configuration consisting of a RR with SG loop filter (RR-SG) is studied. A general situation with asymmetrical transmission functions T_x, T_y is considered, taking into account the possibility of different transmission responses for the clockwise and counterclockwise recirculations in the ring. Under this assumption, the transfer function is obtained following the Z-Transform formalism and the architecture is related to the framework of recursive multi-stage all-pass filters described in [54]. Analytical expressions for calculating the group delay and the quadratic dispersion of the filter are also provided.

6.5.1 Description of the Configuration

The schematic of the photonic architecture is shown in Fig. 6.5, where κ_1, κ_2 are the power coupling coefficients of the optical couplers, γ_1, γ_2 are their corresponding excess losses, L_T is the total length of the feedback path (including the Sagnac loop), and T_x, T_y are the transmission coefficients of the transfer functions between the input coupler and the Sagnac loop, including fiber or waveguide attenuation.

The diagram in Fig. 6.6 shows the mirror equivalent model of the filter considering unidirectional propagation of the light, which makes easier the analysis of the structure.

A general situation with different values of the transmission transfer functions in the clockwise (T_x, T_y) and counterclockwise (T'_x, T'_y) recirculations is considered. Using this mirror model, the structure can be analyzed as an unidirectional ring resonator with a feedback path of length L_T and an internal transfer function dependent on the Sagnac 2x2 matrix parameters, with the same feedback length L_T.

The scattering matrix of the optical coupler and the Sagnac 2x2 module, named C and S, respectively, are defined as follows:

$$(C) = \gamma_1^{\frac{1}{2}} \cdot \begin{pmatrix} \sqrt{1-\kappa_1} & -j \cdot \sqrt{\kappa_1} \\ -j \cdot \sqrt{\kappa_1} & \sqrt{1-\kappa_1} \end{pmatrix} \tag{6.4}$$

$$(S) = \begin{pmatrix} FT & FR \\ FR & FT \end{pmatrix} \tag{6.5}$$

where:

$$FT = \gamma_2 \cdot (1 - 2 \cdot \kappa_2) \tag{6.6}$$

$$FR = 2 \cdot j \cdot \gamma_2 \cdot \sqrt{\kappa_2 \cdot (1 - \kappa_2)} \tag{6.7}$$

Note that $FT^2 - FR^2 = \gamma_2^2$. The relations between ports are:

$$\begin{pmatrix} E_3 \\ E_4 \end{pmatrix} = (C) \cdot \begin{pmatrix} E_1 \\ E_2 \end{pmatrix} \tag{6.8}$$

$$\begin{pmatrix} E_{2f} \\ E_{4b} \end{pmatrix} = (S) \cdot \begin{pmatrix} E_{4f} \\ E_{2b} \end{pmatrix} \tag{6.9}$$

6.5.2 Z-Transform Analysis of the Configuration

In order to apply the Z-transform analysis to the configuration, it is considered the characteristic transit time τ, corresponding to the time of propagation along the total feedback path with length L_T in the forward direction, that is, $\tau = n_{eff} \cdot L_T/c$, being n_{eff} the waveguide effective refractive index and c the speed of light in vacuum.

The mirror model suggests that the RR-SG configuration can be studied as a conventional RR with an auxiliary transfer function in the feedback path, namely $M(z)$, which corresponds to the recirculating configuration with the Sagnac 2x2 matrix, S. This matrix has the same unitary delay time $\tau = n_{eff} \cdot L_T/c$, which corresponds to the same feedback length L_T. The transfer function $M(z)$ using the Z-Transform is:

$$M(z) = \frac{E_{2f}}{E_{4f}} = \frac{FT - (FT^2 - FR^2) \cdot \rho \cdot T' \cdot z^{-1}}{1 - FT \cdot \rho \cdot T' \cdot z^{-1}} \tag{6.10}$$

where:

$$\rho = \sqrt{\gamma_1 \cdot (1 - \kappa_1)} \tag{6.11}$$

$$T' = T'_x \cdot T'_y \tag{6.12}$$

The expression of $M(z)$ can be very useful, because it allows relating the RR-SG structure with the general framework of all-pass filters design reported in [54], as it will be done further in this chapter.

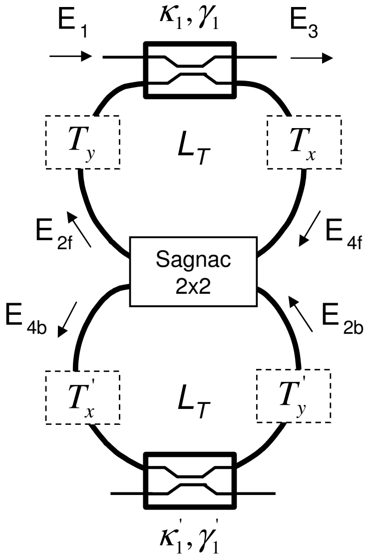

Figure 6.6: Mirror equivalent model of the RR-SG filter. T_x, T_y are the transmission transfer functions for the clockwise recirculation and T_x', T_y' for the counterclockwise.

On the other hand, the total transfer function $H(z) = \frac{E_3}{E_1}$ can be expressed as[2]:

$$H(z) = \frac{\rho - \gamma_1 \cdot T \cdot M(z) \cdot z^{-1}}{1 - \rho \cdot T \cdot M(z) \cdot z^{-1}} \tag{6.13}$$

where $T = T_x \cdot T_y$.

After substituting $M(z)$ (Eq. 6.10), it yields:

$$H(z) = \frac{B_1 + B_2 \cdot z^{-1} + B_3 \cdot z^{-2}}{A_1 + A_2 \cdot z^{-1} + A_3 \cdot z^{-2}} = \rho \cdot \prod_{i=1}^{2} \frac{1 - z_i \cdot z^{-1}}{1 - p_i \cdot z^{-1}} \tag{6.14}$$

Eq. 6.14 is very useful because it can be compared to the expression of an all-pass filter in an easy way. The values of the parameters in the latter equation, corresponding to the RR-SG configuration are shown in Table 6.1.

The values of the parameters in the table can be trivially related to those reported

---

[2] This expression is consistent because the feedback paths of the clockwise and counterclockwise recirculations are identical and equal to L_T, so the variable z is the same for $H(z)$ and $M(z)$.

$B_1=$	ρ	$A_3=$	$\rho^2 \cdot T \cdot T' \cdot (FT^2 - FR^2)$
$B_2=$	$-\gamma_1 \cdot FT \cdot [(1-\kappa_1) \cdot T' + T]$	$A_2=$	$-\rho \cdot (T' + T) \cdot FT$
$B_3=$	$\rho \cdot \gamma_1 \cdot T \cdot T' \cdot (FT^2 - FR^2)$	$A_1=$	1

Table 6.1: Analytical expressions of filter coefficients corresponding to the RR-SG configuration with asymmetrical transmission functions T, T'.

in [2] assuming $T_x = T_x'$ and $T_y = T_y'$. The roots of the numerator (zeros) and denominator (poles) of $H(z)$, under the latter assumption, are written as follows::

$$z_i = \frac{T \cdot \gamma_1}{2 \cdot (1-\kappa_1)^{1/2}} \cdot \left[FT \cdot (2-\kappa_1) + j^{2\cdot(i-1)} \cdot \sqrt{FT^2 \cdot \kappa_1^2 + 4 \cdot (1-\kappa_1) \cdot FR^2} \right] \quad (6.15)$$

$$p_i = \rho \cdot T \cdot (FT + j^{2\cdot(i-1)} \cdot FR) \quad (6.16)$$

6.5.3 Group Delay and Quadratic Dispersion of the Configuration

The analytical expressions of the normalized group delay and quadratic dispersion of the RR-SG configuration can be obtained from the latter equations. On the other hand, quick and easy calculations can be obtained using the Signal Processing Toolbox of Matlab.

By using the parameters A_i, B_i $(i = 1, \cdots, 3)$, the complex transfer function $H(z)$ can be easily calculated using the function *freqz*; the poles and zeros of the configuration can also be directly plot using the function *zplane*; finally, by using *grpdelay*, the normalized group delay τ_n can be calculated and the quadratic dispersion of an specific design, operating at an optical carrier with wavelength λ, is easily obtained considering:

$$D = -c \cdot \left(\frac{T}{\lambda}\right)^2 \cdot 2 \cdot \pi \cdot \frac{d\tau_n}{d\Omega} \quad (6.17)$$

Fig 6.7 shows the frequency detuning of the magnitude response and the dispersion of a RR-SG configuration operating at 1550 nm with τ =40 ps (FSR=25 GHz) and

$\kappa_1 = 0.3$, by changing the value of κ_2 from 0.2 to 0.8 [141, 142]. Fig. 6.8 shows the corresponding poles (x) and zeros (o) of both designs, which are conjugate pairs, and it can be seen how their phases have changed as κ_2 has been tuned. So the RR-SG configuration can perform as a second order IIR filter with frequency detuning just by changing the value of the coupling factor κ_2.

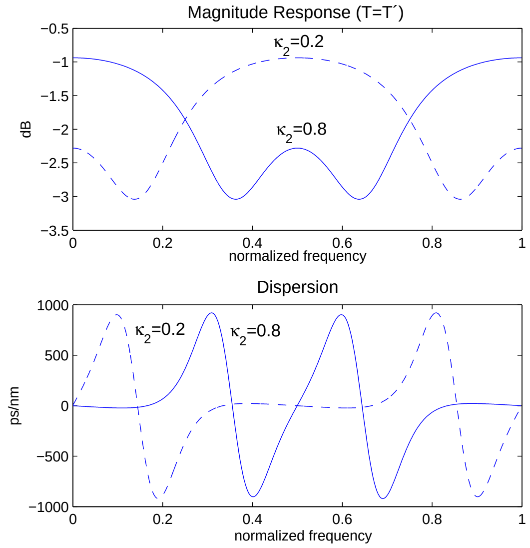

Figure 6.7: Magnitude response versus normalized frequency of the RR-SG configuration. κ_1=0.3, $\gamma_1 = \gamma_2 = 0.925$, $T = T' = 0.6$.

It would be desirable that the RR-SG filter performed as an all-pass filter, in order to approximate an arbitrary phase response with unitary magnitude response, except for non-ideal behaviors of photonic components. Examining equations 6.2 and 6.14, it is found that, unfortunately, the RR with a SG interferometer is not an all-pass filter, except at the limit situation $\kappa_2 = 0$, which actually corresponds to a conventional RR architecture. The consequence of this is a tradeoff between the quadratic dispersion and the magnitude distortion if $T = T'$, that is, the greater the peak values of the dispersion sidelobes, the greater the magnitude distortion of the filter.

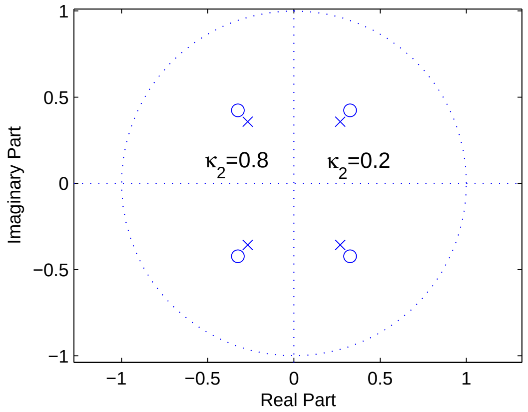

Figure 6.8: Pole-zero diagrams of the two configurations in Fig. 6.7.

6.6 Simulations of Long-Haul SMF Transmission Links

In order to simulate the performance of optical filters based on the ring resonator, we have used a Photonic Design Automation (PDA) software provided by VPIphotonics, version 7.0.1. Simulations are the next step after the design and photonic synthesis procedures of an optical filter, and are very important before the fabrication of an integrated chip, which can be extremely expensive.

The effect of employing an optical filter in an optical transmission link for in-line chromatic dispersion compensation can not be completely derived by the shapes of its quadratic dispersion and its magnitude response, but rather depends on several other aspects such as the bit-rate and the optical signal to noise ratio at the receiver's end. On the other hand, the value of the quadratic dispersion can be related, in principle, with a specific length of a fiber link. Quick and flexible simulations are a cost-effective and useful tool to consider all these aspects, thus providing information related to the performance of an optical filter which is not evident from the observation of its transfer function or its quadratic dispersion.

In this section, we investigate by simulations with the VPIphotonics^{TM} software the performance of RR-based compound filters as regards the bit error rate enhancement over a SMF link with noise and digital transmission of non-return-to-zero (NRZ) signals. An introduction to this simulation software and relevant details of the simulations presented in this section can be found in Appendix A of this document.

6.6.1 Quadratic Dispersion of RR-Based Optical Filters

A specific example of compound filter is considered as Dispersion Compensating Module (DCM), consisting of two cascaded RR and a RR-SG configuration, see Fig. 6.9.

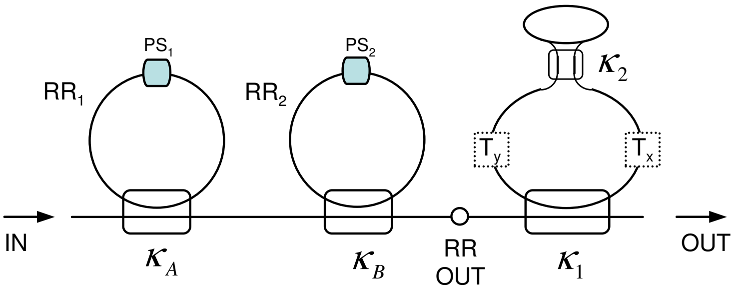

Figure 6.9: Proposed DCM schematic for chromatic dispersion compensation cascading two RR and a RR-SG configuration. PS: Phase-shifter.

In the simulations, the reference optical frequency equals 193.15 THz, which approximately corresponds to a wavelength in the C-band with a value of 1553.19 nm. The reference frequency of the simulations represents the normalized frequency $\nu = 0$ of the corresponding digital filter. The two RRs are lossless, so they form a second-order all-pass filter and the magnitude response at RR OUT (see Fig. 6.9) is unitary and constant. The RRs have power cross-coupling coefficients $\kappa_A = 0.84, \kappa_B = 0.68$ and internal phase shifters fixed at -0.9 radians and -0.2 radians, respectively. The isolated and compound quadratic dispersion at RR OUT are shown in Fig. 6.10 for a free spectral range (FSR) of 25 GHz.

Fig. 6.10(b) shows a limited dispersion compensating bandwidth of negative quadratic

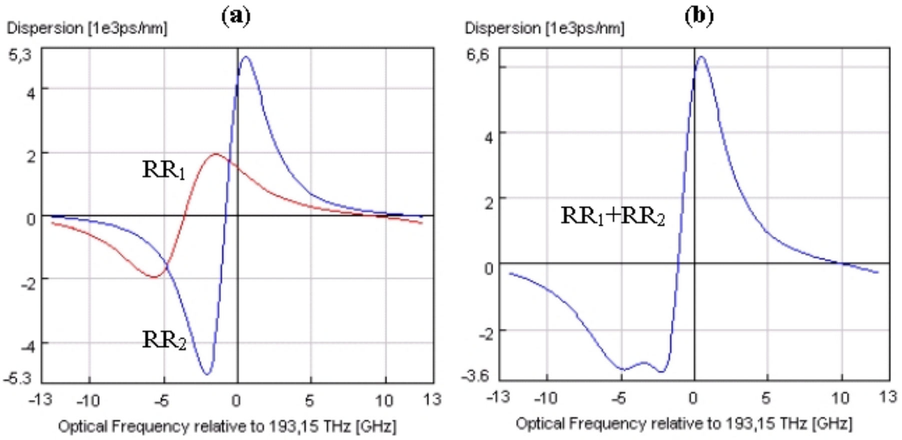

Figure 6.10: Quadratic dispersion of two single RR filters (a) and the cascade in series (b). Lossless RR filters with FSR=25 GHz, lossless couplers with coupling factors κ_A =0.84 and κ_B =0.68, relative phase shift of 0.7 radians.

dispersion around -3100 ps/nm, which is in principle enough for 194 km of the standard single-mode fiber (SMF). Nevertheless, the bandwidth of this 2RR filter is around 2.5 GHz, which can in principle contain a 2.5 Gb/s NRZ signal, and the simulations show that the effect of compensating this chromatic dispersion at such a relatively low bit rate is negligible, being the noise at the receiver the main cause of bit errors detection.

As the bit rate increases above 2.5 Gb/s, so does the relevance of the chromatic dispersion. As a consequence, the bandwidth of the dispersion compensating filter must fit the bandwidth of the NRZ signal. In order to do that, a RR-SG configuration can be connected in series with the previous 2-RR filter, see Fig. 6.9. The magnitude response and the quadratic dispersion of the 2-RR stage and the final compound 2-RR+RR-SG filter, from now on *Dispersion Compensating Module* (DCM), are shown in Fig. 6.11, where the parameters for the 2-RR stage are those of Fig. 6.10. Regarding the magnitude response, it can be seen how the 2-RR stage is an all-pass filter with unitary (0 dB) magnitude response, while the DCM induces a magnitude distortion with a ripple of 2 dB and minimum insertion loss at the reference frequency of 1 dB, similar to the characteristics of the integrated chip reported in [35]. On the other hand, the DCM approximately doubles the dispersion compensating bandwidth of the left sidelobe, keeping the value of the quadratic dispersion around -3100 ps/nm, which is, in principle, capable of compensating the chromatic dispersion of around 194 km of SMF.

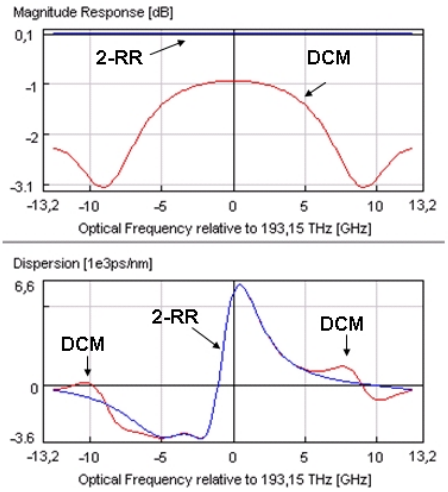

Figure 6.11: Magnitude response and quadratic dispersion of a 2-RR+RR-SG filter with FSR=25 GHz for chromatic dispersion compensation. RR-SG parameters: $\kappa_1 = 0.3, \kappa_2 = 0.8, \gamma_1 = \gamma_2 = 0.925$.

In the following subsection, the performance of this compound filter is simulated within a transmission link, where NRZ digital signals and noise are considered.

6.6.2 Simplified Transmission Link for Testing RR-Based Filters as Dispersion Compensating Modules (DCM)

In order to test the performance of RR-SG based filters in an optical digital transmission system operating at high bit rates, a simplified model of the fiber link has been built using the VPI Photonics^{TM} v. 7.01 software simulation engine, see Fig. 6.12.

The first block of the simulation scheme is a digital optical transmitter, consisting of a 10 MHz linewidth distributed-feedback laser diode (DFB-LD). Its central frequency equals the center of the left-sidelobe with negative dispersion of the DCM (see Fig. 6.11) and it emits 0 dBm of average output power. The LD is externally modulated by a 2^{11} bits pseudo-random NRZ signal at 5 Gb/s and then the light is launched into the single-mode fiber link.

The second block of the simulation scheme is a simplified transmission channel, which consists of a chromatic dispersion generator and a white noise generator in series.

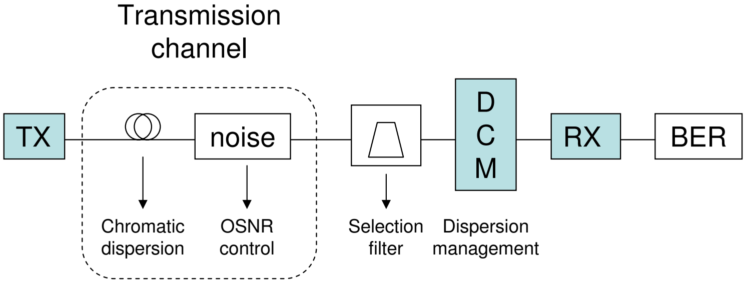

Figure 6.12: Simplified model of a digital transmission link with chromatic dispersion and white noise from amplifiers.

The dispersion generator is just a single-mode fiber model without attenuation, with a chromatic dispersion of 16 ps/nm·km and a slope of 0.08 ps/nm^2·km at the central frequency of the simulations. The non-linear effects of the fiber model were also taken into account, but they were not relevant in the simulation results.

On the other hand, the optical signal to noise ratio (OSNR) at the receiver is fixed by controlling the total noise level.

A first-order gaussian optical filter[3], with a bandwidth of 20 GHz and centered in the frequency of the optical carrier, follows the simplified channel and finally, the reception stage is built by either a dispersion compensating module (DCM) or a span of dispersion compensating fiber (DCF), a PIN diode, an ideal clock-recovery system, and an error detector block which estimates the expected bit error rate (BER).

---

[3] This would perform as selection filter in multichannel simulations.

6.6.3 Simulation Results

Two different BER estimation methods have been employed in order to test the performance enhancement achieved with the 2-RR+RR-SG compound filter as dispersion compensating module in a single-wavelength digital transmission link.

The first estimation method is called Gauss ISI, which considers a Gaussian statistical distribution of the signal with the noise simultaneously at the receptor; the second BER estimator module is called Chi^2 ISI, which considers a Chi^2 statistical distribution of the signal and the added noise at receptor. Both of them consider the inter-symbol interference to achieve the optimal decision corresponding to each bit.

The BER curve versus optical-signal-to-noise-ratio (OSNR) of the simplified channel when no chromatic dispersion is included in the link is named *back-to-back* response, which represents the best performance that a fiber link with chromatic dispersion compensation can achieve.

On the other hand, it is interesting to see how large the power penalty is when the chromatic dispersion is included and no dispersion compensation is employed. Both the back-to-back curves and the power penalty of the system with no DCM are shown in Fig. 6.13(a) for a 200 km fiber link. It can be seen how the chromatic dispersion of the optical fiber induces a power penalty around 3 dB at a BER of 10^{-9} for NRZ digital signals at 5 Gb/s.

On the other hand, when the proposed DCM, designed for a 200 km link, is used at the receiver, the CD is successfully compensated and the BER curves return to the back-to-back response, see Fig. 6.13(b), showing a good improvement around 3 dB of power penalty when the DCM is used. The performance of a 35.5 km span of a dispersion compensating fiber (DCF) has also been simulated and similar power penalty enhancements are achieved, but an additional optical amplifier (OA) with 21 dB gain is needed. The attenuation and dispersion parameters of the DCF equal -90 ps/nm·km

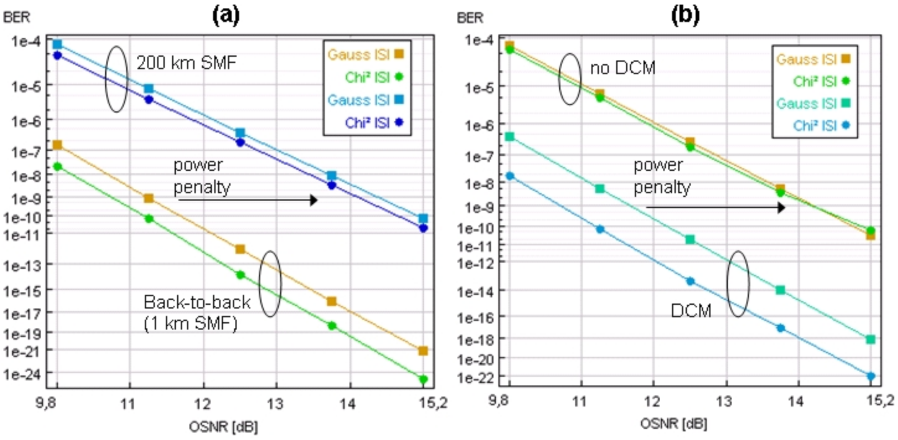

Figure 6.13: Bit error rate estimations at 5 Gb/s (a) for 200 km of single-mode fiber (SMF) link and (b) using the proposed dispersion compensating module (DMC).

and 0.6 dB/km, respectively. For a fixed OSNR of 13 dB, simulations show that for a fiber length between 150 km and 300 km the optical data link is not feasible without dispersion management, while it is when the chromatic dispersion is compensated, either with the DCF+OA receptor or the proposed filter-based DCM, see Fig. 6.14(a) and (b), respectively.

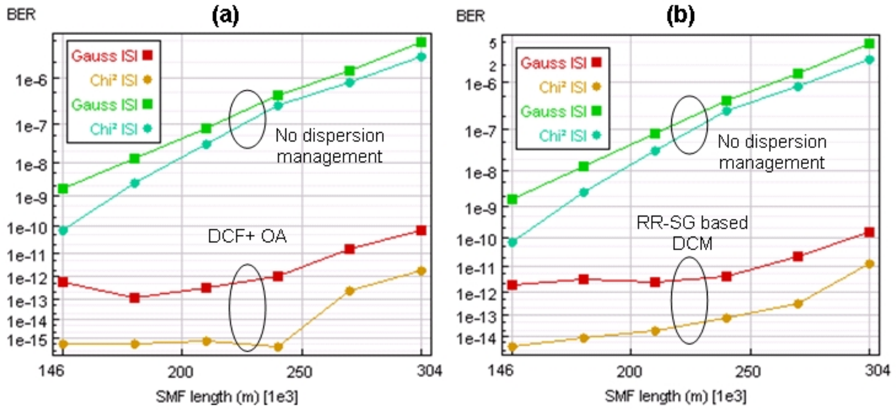

Figure 6.14: Dispersion management using a 21 dB amplified dispersion compensating fiber span of 35 km (a) and the RR-SG filter as dispersion compensating module (b).

Finally, Fig. 6.15 shows how the proposed filter-based approach with the specific design based on the multi-stage 2RR+RR-SG configuration is sensitive to the frequency location of the optical carrier, while the DCF+OA approach is not. Actually, the best performance of the proposed filter-based DCM is achieved at a carrier frequency 5 GHz lower than the reference frequency of the filter, as it was imposed by design (see Fig. 6.11).

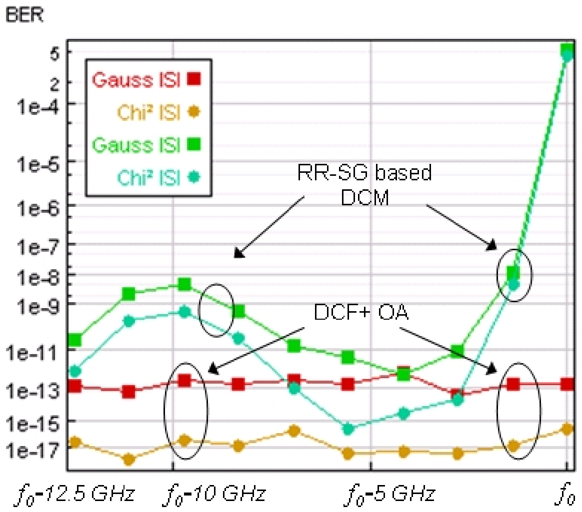

Figure 6.15: BER estimations for the two dispersion management approaches versus frequency of optical carrier.

6.7 All-Pass Filters Using Modified RR With Sagnac Loops

It would be desirable to avoid the magnitude distortion induced by the RR-SG configuration, in order to achieve an arbitrary phase response and a constant magnitude response at the same time. In this section, the conditions needed for achieving an all-pass filter are analytically described, considering the general situation of asymmetrical transmission functions in the clockwise and counterclockwise directions or recirculation in the RR-SG configuration.

A fiber optic schematic to achieve the desired behavior can be seen in Fig. 6.16, where a circulator and an optical amplifier are included in the RR-loop as asymmetrical transmission function. The optical lengths of these two devices must be much lower than the total feedback path, including the Sagnac loop.

The implementation of this filter in integrated optic technology requires optical isolators and circulators fabricated in monolithic integrated form, though experimental measurements on these components have not been reported yet. Nevertheless, designs of waveguide circulators, well suited for monolithic integration, are already available [143], so it is expected that, in a near future, measurements on integrated optical isolators and circulators will be reported.

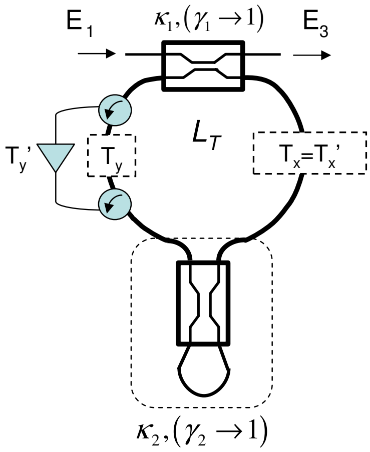

Figure 6.16: Proposed schematic for an all-pass filter fiber-optic implementation using a RR and an internal Sagnac loop. $T_x \cdot T_y = 1$, $T'_x \cdot T'_y = (1-\kappa_1)^{-1/2}$.

In the following, it is demonstrated how this configuration performs, under certain conditions, as an all-pass filter and its magnitude response and quadratic dispersion are calculated and graphically analyzed with regards to the coupling coefficients κ_1, κ_2.

Considering the recursive approach for all-pass filter description reported in [54] and the mirror model of the RR-SG configuration reported in this chapter, it is suggested that, if the feedback paths for the matrixes (M),(S) are lossless and their determinants equal 1, then the RR-SG configuration performs as an all-pass filter. The expressions of the determinants are:

$$\begin{aligned} det(S) &= FT^2 - FR^2 = \gamma_2^2 \\ det(M) &= \gamma_1 \end{aligned} \tag{6.18}$$

So the first condition for the RR-SG configuration to perform as an all-pass filter is that the couplers excess losses of the configuration are negligible, that is:

$$\begin{aligned} \gamma_1 &\to 1 \\ \gamma_2 &\to 1 \end{aligned} \tag{6.19}$$

Provided that those conditions are approximately fulfilled, which can be a realistic situation, the next step is to achieve a lossless feedback loop for matrix S. In order to achieve this, the power balance (H') of the feedback path for matrix S must equal one:

$$H' = T'_x \cdot T'_y \cdot \sqrt{1-\kappa_1} = 1 \tag{6.20}$$

From the latter equation, it is clear that $H' = 1$ when the transmission functions in the counterclockwise recirculation fulfil the condition $T'_x \cdot T'_y = (1-\kappa_1)^{-1/2}$. This means that the counterclockwise recirculations must be amplified in order to achieve an all-pass filter using the RR-SG configuration.

On the other hand, the feedback loop for the input coupler (H) must also be lossless:

$$H = T_x \cdot T_y = 1 \tag{6.21}$$

So the clockwise recirculations must find a transparent path in the feedback loop. Assuming that all the latter restrictions are fulfilled, the corresponding coefficients of the Z-transform description (Eq. 6.2) take the values:

All the coefficients in Table. 6.2 are real, so the resulting Z-Transform for the RR-SG

$B_1=$	$\sqrt{1-\kappa_1}$	$A_3 = B_1$
$B_2=$	$-FT \cdot \left(\sqrt{1-\kappa_1}+1\right)$	$A_2 = B_2$
$B_3=$	1	$A_1 = B_3$

Table 6.2: Filter coefficients for an all-pass filter using an asymmetrically amplified RR-SG configuration.

configuration with different amplification in the clockwise and counterclockwise recirculations follow the expression of a second order all-pass filter, see Eq. 6.2.

Figs. 6.17 and 6.18 show the magnitude response of the RR-SG configuration for an all-pass filter performance and different values of κ_2 for frequency detuning of the filter. The pole-zero diagram corresponding to Fig. 6.17 is also shown in Fig. 6.19.

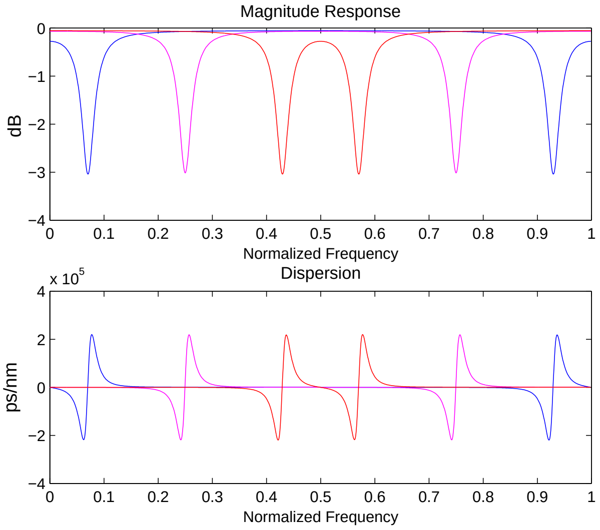

Figure 6.17: Magnitude response and quadratic dispersion of the RR-SG filter with asymmetrical transmission functions in the clockwise and counterclockwise directions. $\kappa_1 = 0.3, \gamma_1 = \gamma_2 = 0.99$. κ_2 =0.05 (blue), κ_2 =0.5 (magenta), κ_2 =0.95 (red). $T = 1$, $T' = 1.19$.

The peak values of the quadratic dispersion can be controlled by fixing the value of κ_1, while κ_2 can be used for frequency detuning of the filter in any case. This filter detuning does not depend on the value of κ_1. For the specific situation $\kappa_2 \approx 0.5$, the quadratic dispersion can reduce its peak values, specially for values of κ_1 tending to 1. As κ_1 tends to zero, the dispersion reaches higher peak values and narrower sidelobes. On the opposite, the dispersion values get lower and the sidelobes wider as κ_1 tends to one.

On the other hand, figures show how the non-ideal excess losses of the couplers induce a slight magnitude distortion, that can be acceptable in most of the cases; nevertheless, the magnitude response is very sensitive to the values of γ_1, γ_2, so they must be as close to 1 as possible, specially for values of κ_1 tending to 0.

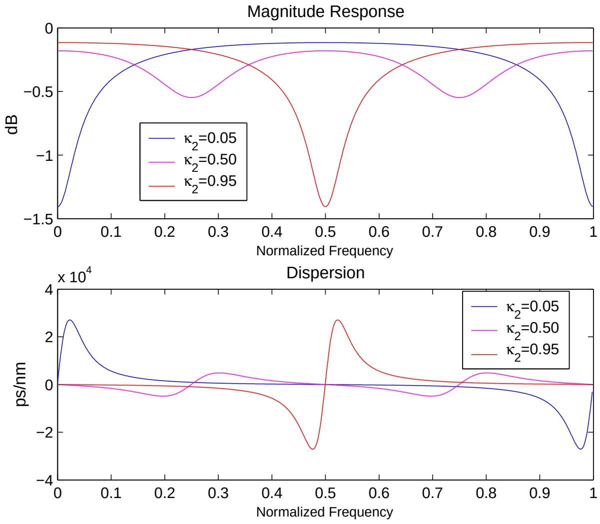

Figure 6.18: Magnitude response and quadratic dispersion of the RR-SG filter with asymmetrical transmission functions in the clockwise and counterclockwise directions. $\kappa_1 = 0.9, \gamma_1 = \gamma_2 = 0.99$ and different values of κ_2 for frequency detuning. $T = 1, T' = 3.16$.

The configuration proposed in Fig. 6.16 is a second-order all-pass filter in a single stage, and can be cascaded, as in the case of the single ring resonator (see Fig. 6.3), in order to form a multi-stage photonic architecture for digital IIR filter synthesis.

The proposed configuration offers the advantages of avoiding the use of phase-shifters and a simple mechanism through the coupling factor κ_2 for fixing the frequency of the zeros and poles, which appear as two complex conjugated pairs.

On the other hand, the configuration offers a considerable immunity to variations in the ring length, due to the fact that the clockwise and counterclockwise recirculations propagate along the same optical length. Finally, the magnitude distortion induced by a single stage is only caused by the excess loss of the optical coupler, as in the case of the RR all-pass filter, so it should not be considered a critical restriction.

6.8 Summary and Conclusions

RR-based optical filters are a compact, flexible and effective approach for chromatic dispersion (CD) management in multi-channel transmission links operating at bit rates of 5 Gb/s and higher. Other solutions are complex-phase mask fiber Bragg gratings and dispersion compensating fibers (DCF).

The RR filter with an internal Sagnac loop (RR-SG) has been studied and its transfer function has been described in the Z-Transform domain following Matlab notation, so quick and easy calculations as well as graphical representation of the filter parameters and functions, specially the quadratic dispersion, are allowed in a simple and flexible way using Matlab software.

The RR-SG architecture is a configuration that can be used in RR-based filters as a photonic stage for synthesizing multi-channel optical filters as in-line dispersion compensating modules (DCM). In this chapter, it has been demonstrated that the RR-SG configuration is not an all-pass filter, so it induces a magnitude distortion that must be kept to acceptable values.

A simplified model of an optical transmission link has been simulated using a Photonic Design Automation (PDA) software provided by VPIphotonics^{TM}. A specific photonic filter consisting of a 2-RR in series and a RR-SG filter in cascaded has been also tested by simulations in a single-mode fiber (SMF) link as a DCM. This module

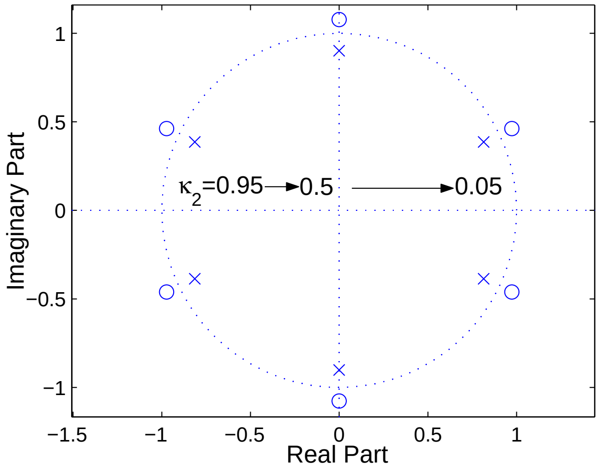

Figure 6.19: Pole-zero diagrams of the RR-SG configuration as all-pass filter for $\kappa = 0.3, \gamma_1 = \gamma 2 = 0.99$ and different values of κ_2 for frequency detuning. $T = 1, T' = 1.19$.

has been compared with the dispersion compensating fiber (DCF) approach for CD compensation.

Simulations show that the CD in a SMF transmission link induces a 3 dB power penalty when 5 Gb/s NRZ signals are transmitted along 200 km of optical fiber. The proposed filter-based DCM can effectively compensate the CD on this link and avoid this power penalty. Another option is using 35 km of DCF and an optical amplifier with 21 dB gain. The filter based-DCM is designed for operation at an specific optical frequency, and its performance is very sensitive to the deviations from this optical frequency. The DCF approach is not sensitive to this optical frequency deviation, but it is not a compact solution and an additional optical amplifier is needed.

On the other hand, a modified RR-SG configuration with different transmission functions in the clockwise and counterclockwise recirculations has been proposed as novel all-pass filter photonic structure and studied following the Z-Transform formalism.

The conditions that this configuration must follow in order to achieve an all-pass filter response with no magnitude distortion and arbitrarily high quadratic dispersion peaks have been analytically obtained. As in the conventional RR-SG filter, κ_2 is useful for frequency detuning. As the values of κ_1 tend to 0, the maximum values of the quadratic dispersion are greater and the sidelobes narrower. The magnitude distortion can be reduced to acceptable values as far as the couplers excess losses are very low. A fiber-optic schematic to achieve a RR-SG based all-pass filter has been proposed, using two optical circulators and an optical amplifier.

Chapter 7

Conclusions and Future Work

7.1 Conclusions

In this work, different original contributions have been made to the state-of-the-art of self-referencing and wavelength-division-multiplexing optical intensity sensors, using fiber-optic configurations under incoherent regime of operation. For the first time, the theory of discrete-time optical signal processing has been applied to the study of fiber-optic configurations for self-referencing optical sensors.

These configurations and multiplexing schemes can contribute to the future deployment of safe, robust, flexible and scalable modern multi-sensor optical networks with enhanced sensitivity. Some applications of these networks are, for example: the remote monitoring of liquid level in explosive environments such as oil tanks and gas deposits in remote stations, the remote measurement of temperature or gas concentration in highway tunnels for quick risk detection and awareness of possible accidents, or vehicle positioning and speed estimation in railway, underground and highway networks.

Original results have also been achieved in the design of novel tunable all-pass filters based on the innovative configuration consisting of a ring resonator and a Sagnac loop with asymmetrical transmission functions. Advanced simulations of photonic systems and filters have also been successfully performed for testing filter-based dispersion compensating modules in high-speed digital transmission systems over optical fiber. The proposed filters could be used to fabricate integrated chips for all-optical dispersion management in the next generation DWDM optical networks, where the bit rates will reach the 40 Gb/s and beyond.

As regards the self-referencing methods:

- The digital filter theory has been applied to the design and analysis of self-referencing techniques for the first time. Closed-form formulas for the description of the transfer function versus modulation frequency and sensor-induced power modulation have been reported, as well as for the insertion losses induced by the self-referencing configurations.

- Two different self-referencing parameters have been studied and experimentally verified using a fiber-optic ring resonator with an optical intensity sensor located in its feedback loop. The performance of this configuration has been demonstrated both in transmission and reflection, in this latter case using a fiber Bragg grating in the RR through port.

- A novel self-referencing measurement parameter with double sensitivity has been studied and experimentally verified, using two modulation frequencies and the self-referencing configuration consisting of two FBGs with an intensity sensor and a fiber delay coil located between them.

- A novel electro-optical configuration has been proposed and demonstrated, consisting of two fiber Bragg gratings with an optical intensity sensor located between them, avoiding the use of a long fiber delay coil and permitting operation at an arbitrary modulation frequency. By using an electronic delay in the reception stage, made of low cost commercial components, such as general-purpose operational amplifiers, resistors and capacitors, it is possible to achieve a flexible multi-point re-configuration in the central office, where the self-referencing measurements are obtained from the remote sensing points.

All the reported self-referencing techniques operate in incoherent regime, so the lightwaves reaching the sensing points must have a coherence length much shorter than the fiber lines used to build the self-referencing configurations. Incoherent operation is a realistic and desirable situation, because it is more stable and tolerant with regards to external perturbations; moreover, this regime is suitable for using optical sources with broadband spectra, that usually lead to cost-effective multi-sensor systems.

The RR in transmission mode is a colorless configuration, this is, the measurements do not depend on the wavelength reaching the sensing point, neither on the spectral properties of the lightwaves, as long as the restriction in its coherence length is fulfilled. This configuration is recommended for use in low-cost CWDM systems with an array of uncooled optical sources, where large spectral drift due to temperature fluctuations can take place.

On the other hand, in the case of the self-referencing configurations with fiber Bragg gratings, it is needed that the bandwidth of the FBGs is large enough to avoid power losses due to possible wavelength drifts of the optical sources. These configurations are suitable for reflective sensor networks with spectrum-sliced broadband lightwave sources, but the emission spectrum density of the broadband source must be stable, or an undesired deviation in the performance of the self-referenced measurements can take place. If the sensor network is integrated in a communications network, Distributed-Feedback lasers could be used instead of the broadband optical source, and thus it would be possible to share the cost of the transmission stage in the central office.

In the case of the electro-optical configuration without fiber delay coil, compact sensor heads and easy multi-point reconfiguration are achieved, which are relevant improvements of the state-of-the-art. Nevertheless, the configuration needs an additional optical demultiplexer and photodetector for each sensor channel, and as the number of components increases, so does the importance of their long-term aging in the performance of the self-referencing method.

The use of Coarse WDM devices to build a sensor network with the topology of a carrier access Passive Optical Network in reflection mode is an efficient approach for multi-point optical interrogation, and it has been demonstrated that the power budget is enhanced by using CWDM techniques instead of the conventional power-splitting. It has also been verified that the network topology is compatible with the self-referencing techniques reported in this work and others reported by other researchers. A discussion on the available technologies for a Dense WDM upgrading of the CWDM network, in order to interrogate up to 200 sensors, has also been reported.

On the other hand, the ring resonator filter with an internal Sagnac loop (RR-SG) has been studied, focusing on its dispersive properties for chromatic dispersion management in digital transmission links over optical fiber. The performance of compound filters using RR and RR-SG stages in cascade as dispersion compensating modules can be simulated using advanced simulation software such as the one provided by VPIphotonics^{TM}.

Additionally, the configuration has been related to the framework of all-pass filters and its potential as dispersion compensator with low magnitude distortion has been analytically studied. In order to achieve an all-pass filter with the RR-SG configuration, it has been demonstrated that an asymmetrically amplified ring is needed, that is, the recirculations in the counterclockwise direction must be amplified with regards to the recirculations in the clockwise.

A fiber-optic implementation of such a novel device has been proposed, using two circulators and an optical amplifier.

7.2 Future Work

Finally, several issues related to the results reported in this work can be considered in further detail as future research. Some of them could be the following:

- The general study of the insertion losses induced in the optical carrier by the self-referencing configurations can be particularized for all the methods reported in this work. Until this moment, the insertion losses have only been obtained for the case of the transmission RR configuration. A global and comparative study of the insertion losses of transmission and reflection self-referencing configurations, obtaining specific analytical equations in a comparable environment, could be carried out, as well as the experimental validation of the theory.

- Self-referencing configurations can increase the sensitivity of the measurements if the design is optimized and if the noise level is low enough. They induce a mathematical transformation of the sensor power modulation, which is, in general, very non-linear. It would be of a great interest to investigate on new generic multi-stage optical or electro-optical configurations with enough design flexibility in order to achieve a linear response of the measurement parameter after the self-referencing transformation. Detailed models to predict the signal to noise ratio and the noise spectrum are also very desirable aspects.

- The self-referencing configurations have been verified using an spectrum analyzer and a lightwave component analyzer. Those are general purpose instruments, very expensive and big, with excessive performance characteristics such as bandwidth and tunability, which is not demanded in the proposed self-referencing methods. Low-cost optimized electronics could be designed to achieve cost-effective prototypes which could be considered for commercial purposes in a medium-term future.

- The effect of phase-induced intensity noise in incoherent fiber-optic signal processors is a restriction that has been considered in the case of the RR configuration as a self-referencing configuration. Nevertheless, measurements have not been taken for verifying the expected behaviour, and clear guidelines for avoiding it and the restrictions in the dynamic margin of the measurements have not been analytically studied. Moreover, the restrictions caused by the phase-induced noise have not been considered for the rest of the self-referencing configurations reported in this work. Some effort could be made in the future in this direction.

On the other hand, regarding RR based filters in coherent regime, future research could be the following:

- Experimental validation of the quadratic dispersion of the RR-SG configurations could be achieved with fiber-optic prototypes in very carefully stabilized assemblies and using the Agilent 8703B. Highly doped fibers can be used to achieve optical amplification in a few centimetres for filters with spectral periodicity in the order of 10 GHz, thus permitting DWDM applications. On the other hand, the future development by the scientific community of integrated optical isolators, circulators or waveguide fillings sensitive to the propagating direction of light could be useful for the implementation in integrated optic technology of the modified RR-SG configuration proposed in this work.
- Tunable laser mirrors using a single ring grating-assisted configuration are other devices recently studied and simulated in Displays and Photonics Applications Group. Fiber-optic prototypes might also be a good opportunity to verify the theoretical analysis of these devices.
- Simulations performed with the software from VPIphotonics consider a single optical carrier and a Non-Return-to-Zero (NRZ) digital signal at 5 Gb/s. It would be very interesting to increase the number of channels to perform WDM simulations,

where the relevance of the inter-channel effects and the chromatic dispersion slope must be taken into account. On the other hand, the bit rate of the signals could be increased to fit the OC-192 and OC-768 transmission standards, operating at 10 Gb/s and 40 Gb/s, respectively. Other modulation formats, such as DPSK or Duobinary, could also be taken into account in future simulations.

- Simulations considering the modified RR-SG configuration as all-pass filter for dispersion management could be performed. Longer fiber links and signal speeds could be managed using this configuration.
- More advanced simulations of photonic stages in the order of the micron or the millimiter could be performed, not only for 2D designs, but also considering specific 3D waveguides. Some international companies offer optical chip fabrication services in bulk Si-substrates or Silica On Insulator (SOI) wafers. It would be interesting to translate some of the designs of chapter 7 to manufactured Photonic Integrated Circuits (PICs). Simulations and tolerance studies can be carried out at the present time, while characterization of photonic chips requires investment in infrastructures or collaboration with other research groups.
- In a long-term scenario, maybe optical chips with the RR-SG configuration and network test-beds could be available for demonstrating the dispersion management capabilities simulated in this work.

Capítulo 8

Resumen del Trabajo Realizado

8.1 Motivación y Objetivos

El campo de las tecnologías fotónicas ha promovido intensamente la investigación a nivel internacional durante los últimos años, teniendo como objetivo fundamental la implantación de las tecnologías ópticas de manera competitiva como base de los futuros servicios de banda ancha, así como el desarrollo y la estandarización de las aplicaciones de la fibra óptica, tales como el sensado óptico remoto, los biosensores, la ingeniería civil, las aplicaciones militares y las comunicaciones con satélites.

En este marco general, el presente trabajo se ha centrado en el desarrollo de nuevas técnicas de medida y multiplexación para sensores ópticos, así como en el diseño, análisis y simulación de nuevos dispositivos para las futuras redes de comunicaciones ópticas.

Este trabajo se ha desarrollado en el marco de las actividades de investigación llevadas a cabo en el Grupo de Displays y Aplicaciones Fotónicas (GDAF) de la Universidad Carlos III de Madrid [1], el cual se ha dedicado durante los últimos años al diseño y la implementación de distintos dispositivos y sensores para aplicaciones en redes ópticas con multiplexación en longitud de onda (WDM).

El primer objetivo del trabajo de investigación presentado en este documento ha sido el desarrollo de nuevas técnicas de medida para sensores ópticos. En el estado del arte existen múltiples ejemplos de sensores de fibra óptica tanto en tecnología monomodo como multimodo, para la medida de diversas magnitudes físicas y químicas tales como la presión, la temperatura, la concentración de gases o la humedad, entre muchas otras. Los sensores de fibra óptica presentan ventajas esenciales respecto a los sensores electrónicos, debido a que son intrínsecamente seguros en entornos hostiles o con peligro de explosión, así como inmunes a las interferencias electromagnéticas. Asimismo, es muy sencillo integrar los sensores de fibra óptica en redes ópticas para realizar medidas remotas, puesto que en estos sistemas tanto los sensores como la topología de las redes comparten la misma tecnología básica. La fibra monomodo, con una atenuación típica de 0.2 dB/km en torno a los 1550 nm (estándar G.652), permite implementar enlaces con alcances alrededor de los 50 km sin necesidad de amplificadores ópticos, lo que constituye una solución muy eficiente para la medida remota sobre sensores ópticos.

Entre los sensores ópticos, los sensores de intensidad óptica son aquellos que proporcionan las medidas a través de una señal óptica modulada en intensidad. Este tipo de sensores permite técnicas de interrogación más sencillas y de menor coste que los sensores interferométricos. No obstante, los sensores ópticos de intensidad requieren mecanismos de auto-referencia para obtener medidas estrechamente ligadas a la magnitud que se desea medir, de una manera fiable e independiente de otras variaciones indeseadas o aleatorias de intensidad óptica, que pueden dar lugar a lo largo de los caminos ópticos o en los propios sistemas de transmisión y recepción.

Los investigadores han propuesto diversos mecanismos de auto-referencia para obtener sistemas de medida remota tolerantes a fluctuaciones de potencia óptica indeseadas no relacionadas con la modulación inducida por los propios sensores. Entre estos mecanismos, se han empleado diversas configuraciones ópticas en régimen incoherente, tales como la Fabry-Perot, Mach-Zehnder, Michelson y el anillo resonante en fibras multimodo.

En el presente trabajo se han estudiado y demostrado experimentalmente nuevas configuraciones de auto-referencia con fibras monomodo, empleando redes de Bragg en fibra y fibras de retardo, así como el anillo resonante en régimen incoherente. Mediante estos métodos, se ha conseguido mejorar la sensibilidad y la flexibilidad de otras propuestas. Asimismo, con una de las configuraciones estudiadas en el presente trabajo se han conseguido mejoras muy significativas en la capacidad de reconfiguración de la técnica de medida y en el tamaño de las cabezas sensoras remotas, mucho más compactas.

Un segundo objetivo de este trabajo ha sido el promover, estudiar y verificar nuevas estrategias de multiplexación para implementar y escalar redes de fibra con múltiples sensores, empleando dispositivos comerciales de bajo coste, mejorando el balance de potencia óptica de las redes y manteniendo la auto-referencia de las medidas. Para ello, el trabajo se ha centrado en la tecnología de multiplexación en longitud de onda aproximada (CWDM). Esta tecnología se ha planteado recientemente como alternativa de bajo coste para redes metropolitanas con distancias de alcance y capacidad menores que las redes con multiplexación en longitud de onda densa (DWDM), evitando en la mayoría de los casos la necesidad de amplificadores ópticos. La rejilla espectral CWDM (estándar G.694.2) especifica 18 longitudes de onda consecutivas separadas 20 nm, situadas entre los 1270 nm y los 1610 nm. Asimismo, las fuentes ópticas para estas aplicaciones requieren menor precisión en el control de la temperatura, y los filtros necesarios son mucho más sencillos y baratos que en el caso de los sistemas DWDM. En ese entorno, las redes ópticas pasivas (PON) para el acceso a datos de banda ancha presentan una topología punto a multipunto en estrella muy interesante para la multiplexación de sensores ópticos.

Por ello, en este trabajo se ha propuesto emplear la topología básica de las redes PON junto a técnicas de multiplexación en longitud de onda aproximada (CWDM) para la interrogación remota de múltiples sensores ópticos, reemplazando los divisores de potencia, empleados tradicionalmente, por demultiplexores CWDM para distribuir de manera más eficiente la luz. Dicha propuesta se ha validado experimentalmente empleando dos técnicas de auto-referencia distintas con configuraciones remotas reflexivas, mediante el empleo del anillo resonante, líneas de retardo y redes de Bragg en fibra (FBGs).

Por último, en el entorno de las redes de comunicaciones ópticas de alta capacidad, en este trabajo también se han considerado los filtros ópticos compuestos basados en el anillo resonante, para aplicaciones en el entorno de los modernos sistemas de comunicaciones. En este tipo de sistemas, las técnicas de transmisión a alta velocidad (40 y >40 Gb/s) y los conmutadores ópticos son aspectos fundamentales. En el marco internacional, nuevos formatos de modulación, nuevos tipos de fibra y técnicas transparentes de transmisión están siendo objeto de intensa investigación.

Asimismo, en los modernos enlaces ópticos de transmisión, el aumento de las velocidades binarias así como el aumento de las distancias de enlace gracias a los amplificadores ópticos, intensifica la incidencia de los efectos no lineales y la dispersión cromática en la fibra óptica, que deben ser monitorizados y evitados en la medida de lo posible para asegurar el correcto funcionamiento de los sistemas. La dispersión cromática es un efecto debido a las variaciones del índice de refracción efectivo de grupo de la fibra óptica respecto a la frecuencia óptica, y puede constituir una restricción importante para las prestaciones de este tipo de sistemas de comunicaciones.

Los anillos resonantes en régimen de operación coherente, normalmente fabricados en tecnología de óptica integrada, han sido empleados en múltiples aplicaciones relacionadas con las redes ópticas transparantes de comunicaciones de alta velocidad con multiplexación en longitud de onda densa (DWDM). Se han desarrollado múltiples dispositivos fotónicos durante los últimos años empleando el anillo resonante como etapa básica, tales como filtros sintonizables, multiplexores de inserción-extracción, moduladores ópticos, compensadores de dispersión, líneas de retardo, demultiplexores y conmutadores, así como bio-sensores fotónicos.

En esa línea de investigación, este trabajo se ha centrado en el estudio de la dispersión cuadrática de la configuración basada en el resonador en anillo con un interferómetro Sagnac interno (RR-SG), para la compensación de la dispersión cromática en sistemas de transmisión digital a alta velocidad sobre fibra óptica. Este filtro permite ajustar su respuesta en frecuencia sin necesidad de cambiar la longitud del lazo de realimentación, y proporciona una respuesta de segundo orden mediante una única cavidad, con la consiguiente inmunidad a las variaciones de su longitud.

Además de los estudios analíticos y nuevos diseños basados en el filtro RR-SG, en este documento también se presentan simulaciones de sistemas ópticos de transmisión realizadas con el software de simulación VPIphotonics^{TM}. Mediante dicho software, se han podido evaluar las prestaciones de filtros compuestos basados en la configuración RR-SG, como módulos compensadores de dispersión (DCM) en enlaces ópticos con señales digitales de alta velocidad (5 Gb/s), considerando el efecto de la dispersión cromática y el ruido causado por la presencia de amplificadores ópticos.

A continuación, se presenta un breve resumen del trabajo realizado, incidiendo en las principales contribuciones originales obtenidas en cada una de las líneas de investigación anteriores.

8.2 Introducción al Tratamiento Óptico de Señales en Tiempo Discreto

En este trabajo se ha adoptado el formalismo del Tratamiento Digital de Señal, mediante la Transformada Z (TZ), para la descripción de configuraciones ópticas con retardos de tránsito múltiplos de un retardo característico, denominado τ.

Cuando el tiempo de coherencia de la fuente luminosa que excita una configuración óptica es mucho mayor que el parámetro τ, las relaciones de módulo y fase del campo electromagnético entre diferentes puntos de la configuración se pueden considerar deterministas y se dice que la configuración presenta un régimen de funcionamiento *coherente*.

Por el contrario, cuando el tiempo de coherencia de la fuente luminosa es mucho menor que τ, las relaciones de fase del campo electromagnético son aleatorias y sólo pueden establecerse analíticamente las relaciones de potencia luminosa entre los distintos puntos de la configuración óptica; en tal caso, se dice que el régimen de funcionamiento de la misma es *incoherente*.

El par transformado del tiempo de tránsito característico τ puede asimilarse al período de muestreo de un filtro digital, cuya descripción en el dominio de la TZ es la potencia z^{-1}. A través de esta propiedad de la TZ, es posible obtener de manera sencilla, mediante sumatorios finitos o series de potencias de la variable z^{-1}, la respuesta al impulso finita (FIR) o infinita (IIR) de cualquier configuración óptica con un retardo característico.

A través de este procedimiento, en el capítulo 2 de este trabajo se han obtenido las funciones de transferencia de varias configuraciones ópticas comunes como el interferómetro Mach-Zehnder, el interferómetro Michelson, el espejo Sagnac o el resonador en anillo, en este último caso tanto en régimen de funcionamiento coherente como incoherente. También se han revisado brevemente las principales arquitecturas empleadas para la síntesis de filtros ópticos basadas en el anillo resonante, así como algunos de los dispositivos más interesantes fabricados recientemente en tecnología de óptica integrada.

La representación mediante la Transformada Z de los filtros ópticos en tiempo discreto ha servido de notación para la propuesta, el análisis y el diseño, en capítulos posteriores, de varias técnicas de auto-referencia sobre sensores de intensidad óptica.

Asimismo, se ha estudiado el efecto de dichas configuraciones ópticas sobre fuentes luminosas con baja longitud de coherencia, en el marco de los procesos estocásticos aleatorios, y se ha obtenido la expresión analítica genérica de las pérdidas de inserción de entrada-salida de una configuración óptica en régimen de funcionamiento incoherente. Esta expresión se ha analizado de manera gráfica para el caso del anillo resonante en régimen incoherente.

En el futuro, la expresión genérica de estas pérdidas puede particularizarse para diversas configuraciones y contrastarse experimentalmente, lo cual puede ser de gran utilidad para calcular el balance de potencia en redes ópticas de sensores multiplexados que empleen alguna de las configuraciones ópticas incoherentes para implementar métodos de auto-referencia.

8.3 Métodos de Auto-Referencia para Sensores Ópticos de Intensidad

La tecnología de fibra óptica permite obtener sensores intrínsecamente seguros en entornos hostiles o con peligro de explosión (tal como tanques de líquidos inflamables u hornos industriales). Dichos sensores son inmunes a las interferencias electromagnéticas (EMI) y pueden ser diseñados para mostrar alta sensibilidad a diversas magnitudes físicas, denominados genéricamente *mensurandos*.

En el estado del arte, existen múltiples ejemplos de sensores de fibra multimodo y monomodo para la medida de diversos mensurandos, tales como la presión, la corrosión, la humedad o la temperatura, entre otros. Recientemente, las nuevas fibras de cristales fotónicos están comenzando a ofrecer nuevas posibilidades a los nuevos dispositivos sensores basados en la fibra óptica.

Por un lado, uno de los mecanismos de transducción más intensamente investigado en los sensores ópticos es la modulación de intensidad. Los sensores de intensidad óptica modulan las pérdidas de potencia óptica a medida que cambia el mensurando, proporcionando las medidas a través de una señal de modulación de intensidad.

Por otro lado, la fibra óptica monomodo presenta muy bajas pérdidas de propagación (típicamente 0.2 dB/km), y permite así implementar esquemas eficientes de medida remota sobre sensores ópticos a distancias de hasta 50 km sin necesidad de amplificación óptica.

No obstante, los sensores de intensidad en configuraciones remotas requieren técnicas de auto-referencia para minimizar la influencia del envejecimiento de los dispositivos ópticos, así como las variaciones indeseadas de potencia óptica en el camino óptico que conecta las instalaciones donde se toman las medidas, con los puntos remotos donde se encuentran los sensores ópticos. Estas variaciones pueden producirse por múltiples razones, tales como accidentes que afecten al cableado de fibra, actualizaciones de la topología de red o manipulación de los conectores, entre otros posibles motivos.

Los investigadores han propuesto múltiples mecanismos para obtener medidas de la variación de intensidad de la luz en las cabezas sensoras, de una manera independiente y diferenciada de las perturbaciones no deseadas. Los mecanismos más empleados de auto-referencia son la normalización en el tiempo, en la frecuencia y en la longitud de onda.

Entre los mecanismos basados en la normalización en frecuencia, se han empleado distintas configuraciones ópticas en régimen incoherente, como la Fabry-Perot, Mach-Zehnder, Michelson y el anillo resonante en fibras multimodo.

En este trabajo, se han estudiado y verificado experimentalmente nuevas configuraciones en régimen incoherente con fibra monomodo, empleando el anillo resonante, fibras de retardo y redes de Bragg en fibra, para auto-referenciar sensores ópticos de intensidad en puntos remotos de medida. Se han estudiado y verificado configuraciones tanto en transmisión como en reflexión, evitando en este último caso la necesidad de una fibra de retorno desde el sensor al punto donde se toman las medidas.

Mediante los nuevos métodos presentados en este trabajo, se ha conseguido mejorar la sensibilidad y la flexibilidad de otras propuestas. Con una de las técnicas presentadas en este trabajo se han conseguido, asimismo, mejoras muy significativas en la capacidad de reconfiguración de la técnica de medida y en el tamaño de las cabezas sensoras, mucho más compactas.

A continuación se describen brevemente las configuraciones para medidas remotas con auto-referencia estudiadas en este trabajo.

8.3.1 Nuevas Técnicas de Auto-Referencia Basadas en el Anillo Resonante

Las Figuras 8.1 y 8.2 muestran dos configuraciones originales, basadas en el anillo resonante en régimen incoherente, para la medida remota con auto-referencia sobre sensores de intensidad óptica [5].

En las configuraciones propuestas, se emplea una fuente luminosa modulada en radiofrecuencia (RF) que, introducida en un enlace de fibra, alcanza un punto remoto de medida. En dicho punto, la luz alcanza un resonador en fibra, formado por un acoplador realimentado en cuyo lazo se coloca un sensor de intensidad. En ambas figuras, κ, κ' representan los coeficientes de acoplo cruzado de los acopladores ópticos; asimismo, se considera la situación genérica con atenuador (A) y amplificador (G) ópticos en el lazo para ajustar libremente el punto de operación, si bien en la mayoría de las situaciones ambos elementos son prescindibles.

La modulación de intensidad del sensor colocado en el lazo de realimentación produce un cambio en la respuesta en módulo del anillo resonante, que a su vez depende de la frecuencia de modulación. El cociente de dos medidas de potencia obtenidas en diferentes frecuencias de modulación, o en la misma frecuencia pero en dos puertos distintos de la configuración, permite obtener sendos parámetros de medida auto-referenciados. Esto se debe a que las perturbaciones en la potencia de la fuente luminosa, siempre que ocurran

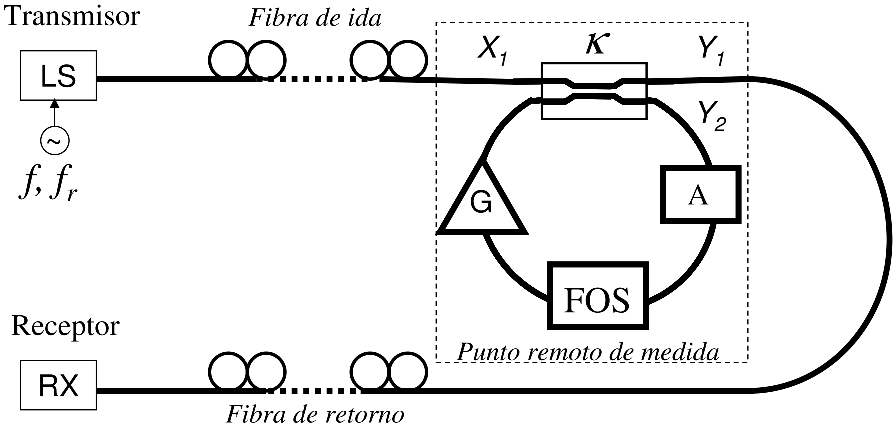

Figura 8.1: Esquema de la configuración con auto-referencia basada en la normalización en frecuencia.

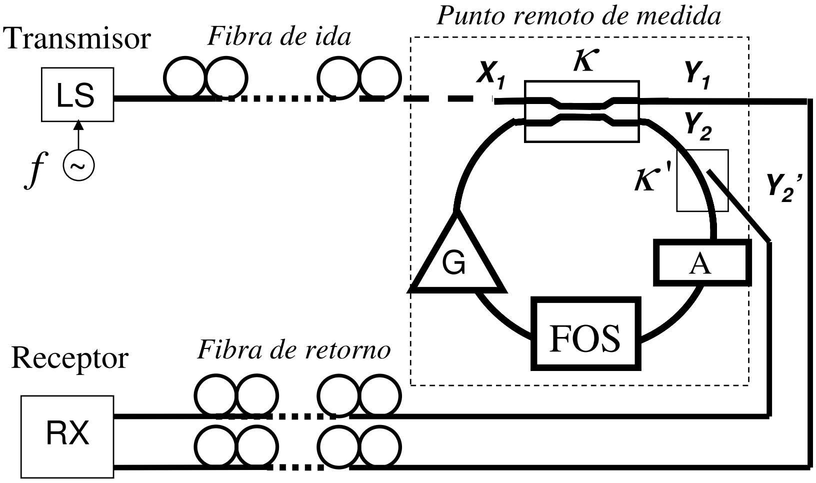

Figura 8.2: Esquema de la configuración con auto-referencia basada en la normalización con dos puertos.

en cualquier punto externo a la configuración remota de medida, afectan por igual a las dos medidas involucradas, de modo que el efecto de tales perturbaciones se compensa.

El estudio comparativo de ambas configuraciones aparece en el capítulo 3 de este documento, junto con sus respectivas implementaciones y validaciones experimentales, empleando atenuadores ópticos variables como sensores genéricos de intensidad. En dicho estudio, se ha empleado la teoría de filtros digitales para obtener los parámetros de medida con auto-referencia, lo cual se puede considerar una contribución original al estado del arte en este campo de conocimiento.

La respuesta en módulo del anillo resonante, así como los diversos parámetros de auto-referencia, se han obtenido experimentalmente empleando el analizador de espectros eléctrico Tektronix 2714 y modulando internamente un láser DFB Tektronix PRO-800, emitiendo potencia en torno a los 1552 nm. Medidas calibradas de la respuesta en módulo del anillo también se han obtenido empleando el analizador de redes óptico Agilent 8703B. Para más detalles sobre este instrumento, puede consultarse el Apéndice B de este documento.

8.3.2 Nuevas Técnicas de Auto-Referencia Reflexivas Mediante Redes de Bragg

Las redes de Bragg en fibra (FBG) son dispositivos pasivos que reflejan una parte de la potencia luminosa que incide sobre ellas. Se caracterizan por una longitud de onda central (λ_B), en la que la potencia reflejada es máxima, y por la relación entre las potencias incidente y reflejada, denominada *reflectividad*.

Las redes de Bragg son dispositivos muy útiles para implementar configuraciones remotas reflexivas (Fig. 8.3), que permiten obtener medidas con auto-referencia sobre sensores ópticos de intensidad. Al operar en reflexión, se evita la necesidad de una fibra de retorno adicional desde el punto remoto donde se encuentra el sensor al punto donde se desea obtener la medida. Asimismo, permiten incrementar la sensibilidad intrínsica del transductor óptico de intensidad, debido a que la luz lo atraviesa en dos ocasiones, una por cada sentido de propagación. Cabe destacar, igualmente, que el empleo de las FBG permite el empleo de técnicas de multiplexado de sensores en longitud de onda, puesto que son dispositivos sensibles al valor de la misma.

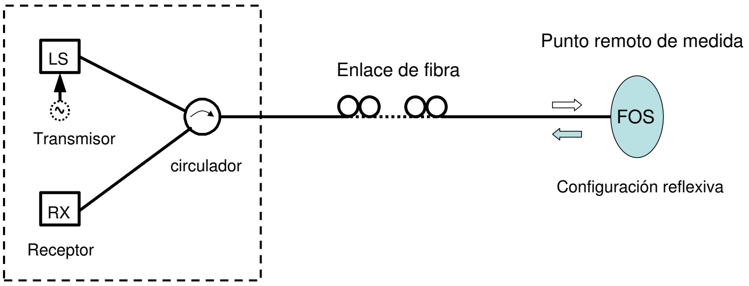

Figura 8.3: Esquema general de un enlace bidireccional para la medida remota en sensores de intensidad con fibra óptica (FOS) en configuración reflexiva.

En el capítulo 4 de este trabajo se han propuesto varias configuraciones reflexivas con auto-referencia y se han realizado diversas contribuciones originales al estado del arte en este ámbito, descritas brevemente a continuación.

La primera propuesta consiste en el empleo de una red de Bragg en el puerto de acoplo directo de un acoplador óptico realimentado [6], tal y como muestra la Figura 8.4. Esta configuración presenta la función de transferencia de un anillo resonante simple elevada al cuadrado, y también permite obtener medidas con auto-referencia. Esta configuración mejora la sensibilidad a la modulación inducida por el mesurando y permite emplear el enlace de fibra de manera bidireccional. El comportamiento de esta configuración se ha validado a través del analizador de redes óptico Agilent 8703B.

En la Figura 8.5 se muestra una segunda configuración reflexiva constituida por dos FBG, con distintas longitudes de onda centrales, entre las que se coloca una línea de retardo en fibra y un sensor bidireccional de intensidad óptica [7]. Esta configuración

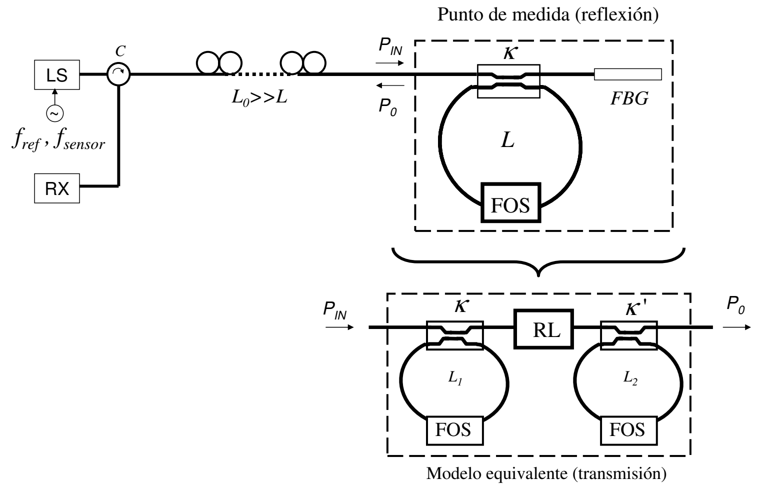

Figura 8.4: Técnica de medida remota con auto-referencia basada en el anillo resonante para sensores ópticos de intensidad (FOS) en configuración reflexiva. LS: Fuente de luz; C: Circulador; RX: Etapa de recepción; FBG: red de Bragg en fibra. RL: Pérdidas en reflexión de la FBG. *L*: Longitud del lazo del anillo.

realiza una transformación de la modulación de intensidad inducida por el sensor óptico, en variaciones de la fase de un tono de modulación. Dichas variaciones dependen de la frecuencia empleada y de la longitud de la fibra de retardo. El estudio de la respuesta en frecuencia de dicha configuración, asimilada a un filtro digital equivalente, muestra que el empleo de dos frecuencias de modulación permite obtener un nuevo parámetro de auto-referencia con doble sensibilidad, respecto de la situación en que se emplea una única frecuencia de modulación. Este nuevo parámetro de auto-referencia se ha validado experimentalmente en los laboratorios del INESC[1] en Oporto, empleando un modulador acusto-optico de *Brimrose* y un amplificador de Lock-in de *Stanford Research Systems*.

Por último, se ha propuesto una nueva configuración electro-óptica con una forma similar a la anterior, pero sin necesidad de la fibra de retardo [8]. La Figura 8.6 muestra el esquema genérico de esta configuración. Evitar la fibra de retardo constituye una contribución muy ventajosa al método de auto-referencia, debido a que permite la imple-

---

[1] Instituto de Engenharia de Sistemas e Computadores do Porto.

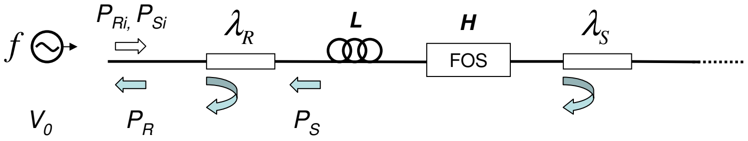

Figura 8.5: Configuración mediante dos redes de Bragg en fibra y una fibra de retardo para la medida remota con auto-referencia sobre sensores ópticos de intensidad (FOS).

mentación de configuraciones remotas mucho más compactas y el empleo de frecuencias de modulación arbitrarias.

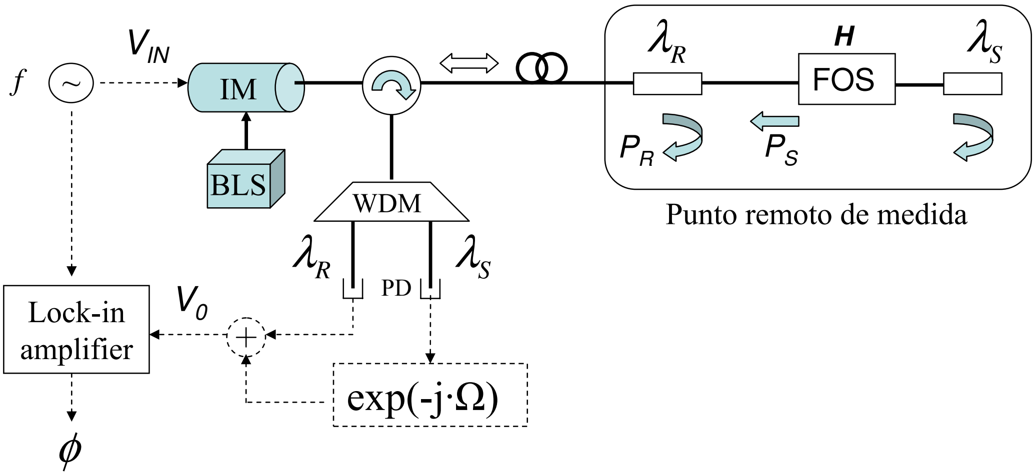

Figura 8.6: Configuración electro-óptica sin fibra de retardo. BLS: Fuente de luz de espectro ancho; IM: Modulador de intensidad óptica; FOS: Sensor de fibra óptica; PD: Fotodetector.

En esta nueva configuración, se reemplaza la fibra de retardo por una etapa de retardo electrónico, basado en componentes comerciales de bajo coste, como amplificadores operacionales de propósito general, resistencias y condensadores.

Se ha demostrado experimentalmente que con esta configuración se puede emplear una frecuencia de modulación de 2 kHz y evitar el empleo de un carrete de fibra de 14 km, lo cual es una ventaja muy significativa. La frecuencia de modulación es arbitraria y la etapa de retardo electrónico es re-configurable de manera sencilla, permitiendo ajustar el punto de funcionamiento de varios sensores remotos desde un único emplazamiento, en el que se obtienen las medidas de manera centralizada.

Una desventaja de esta configuración es que requiere el uso de un demultiplexor en longitud de onda y de un fotodetector adicional, por cada sensor, respecto de la configuración puramente óptica con fibras de retardo. Asimismo, el empleo de estos dispositivos adicionales podría empeorar la tolerancia del parámetro de auto-referencia al envejecimiento de los mismos a largo plazo.

Esta configuración también se ha validado en los laboratorios del INESC, en Oporto, y se ha solicitado una patente al Instituto Nacional de Propiedad Intelectual (INPI) de Portugal, reivindicando la nueva técnica de medida.

8.4 Redes de Sensores con Multiplexación en Longitud de Onda Aproximada (CWDM)

La tecnología de multiplexación en longitud de onda aproximada (CWDM) se ha empleado recientemente en múltiples aplicaciones para redes metropolitanas con distancias de alcance y capacidad menores que en el caso de las redes con multiplexación DWDM.

Los láseres orientados a aplicaciones CWDM requieren procesos de fabricación más simples y admiten mayores tolerancias de fabricación. Durante su funcionamiento, estas fuentes ópticas requieren menor precisión en el control de temperatura. Asimismo, la complejidad de diseño y el coste de los filtros ópticos para redes CWDM son mucho menores que para redes DWDM, y en la mayoría de las situaciones no se necesitan amplificadores ópticos, debido a que las longitudes de alcance máximas están en torno a los 50 km.

Estas propiedades hacen a la tecnología CWDM una solución interesante para implementar redes de sensores con auto-referencia de bajo coste, permitiendo un rutado eficiente de la potencia óptica para alcanzar sensores remotos de intensidad, a través de topologías compactas y escalables.

La rejilla espectral CWDM se ha definido en el estándar G.694.2 de la ITU-T, en el cual se especifican 18 longitudes de onda con valores nominales entre los 1270 nm y los 1610 nm, ambos incluidos, con una separación de canales de 20 nm.

Por otro lado, las redes ópticas pasivas (PON, del inglés *Passive Optical Network*), comienzan a ser una tecnología atractiva para las nuevas redes de acceso, siendo una alternativa interesante a otras tecnologías como la x-DSL (*Digital Suscriber Line*), HFC (*Hybrid Fiber-Coaxial*) o LMDS (*Local Multipoint Distribution Service*).

Las redes PON presentan una topología interesante y sencilla para la multiplexación de sensores ópticos. En este trabajo, hemos propuesto emplear la topología física de las redes PON, sustituyendo la division de potencia óptica por la multiplexación CWDM y empleando configuraciones reflexivas con auto-referencia en los puntos remotos, empleando redes de Bragg en fibra, véase la Figura. 8.7. De este modo, se distribuye de manera más eficiente la luz, de modo que sólo una parte del espectro llega a cada sensor, y se aprovecha el enlace de fibra óptica de manera bidireccional.

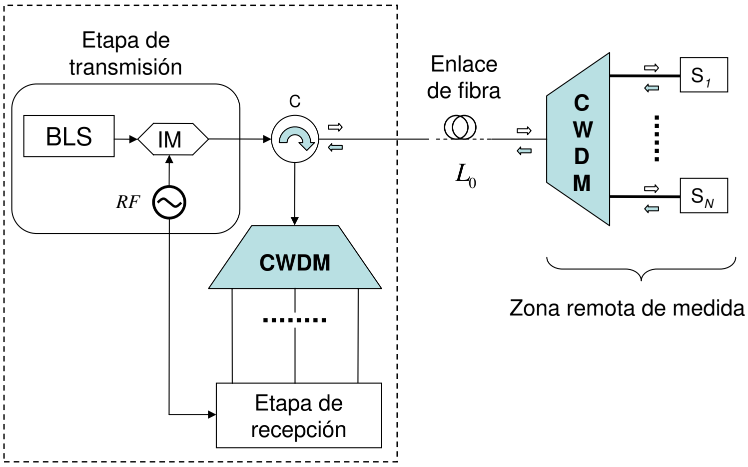

Figura 8.7: Red CWDM porpuesta para medidas remotas con auto-referencia en N sensores de intensidad óptica en configuración reflexiva. BLS: Fuente de luz de espectro ancho; IM: Modulador de intensidad óptica; S_i (i=1, $\cdots$, N): Configuración sensora reflexiva.

En este trabajo, se han validado dos redes CWDM de sensores con auto-referencia. En la primera de ellas se ha empleado el anillo resonante con una red de Bragg en fibra como configuración sensora remota [9], véase la Figura 8.4. En la segunda de las validaciones, se han empleado dos redes de Bragg con distinta longitud de onda central y una fibra de retardo entre ambas, tal y como muestra la Figura 8.5.

Las medidas realizadas muestran que, con la topología propuesta, es posible multiplexar hasta 18 sensores auto-referenciados con un alcance máximo de 25 km. También es posible sustituir un canal CWDM por varios canales DWDM, aumentando de manera muy significativa el número de sensores de la red. Se estima que sería posible interrogar hasta 200 sensores distintos en la misma red; no obstante, es posible que se necesitaran amplificadores ópticos o fuentes luminosas de mayor potencia, lo que podría encarecer de manera importante el sistema completo.

8.5 Filtros Compuestos Basados en el Anillo Resonante y el Espejo Sagnac para Compensación de Dispersión Cromática en Redes de Transmisión Óptica

A medida que la complejidad y la capacidad de las redes crecen, son necesarios nuevos dispositivos flexibles y sintonizables que permitan optimizar el funcionamiento de los sistemas. El funcionamiento de estos dispositivos en el dominio óptico, sin necesidad de conversiones opto-electrónicas, es otra situación muy deseable. En el entorno del procesado óptico de señal en redes con multiplexación en longitud de onda densa o ultradensa, recientemente se ha propuesto emplear un espejo Sagnac dentro del lazo de realimentación del anillo resonante [2], tal como muestra la Fig. 8.8.

Por otro lado, en los enlaces de transmisión de las redes troncales y metropolitanas a alta velocidad, la dispersión cromática puede ser una restricción significativa para las

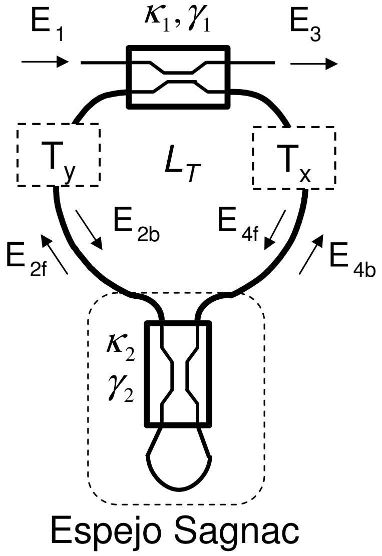

Figura 8.8: Esquema del anillo resonante con funciones de transmisión (T_x, T_y) y espejo Sagnac interno. L_T es la longitud total del lazo realimentado.

prestaciones del sistema. La dispersión cromática es una distorsión que tiene lugar en la fibra óptica a medida que un pulso corto de luz se propaga a través de la misma. En enlaces de fibra monomodo estándar G.652 en banda C (1530-1565 nm), con coeficientes típicos de dispersión de 17 ps/nm, velocidades binarias en el orden del Gb/s son críticas para distancias mayores de 100 km. Asimismo, el efecto de la dispersión cromática puede acentuarse con el empleo de los amplificadores ópticos, ya que la dispersión es proporcional a la longitud de la fibra y los amplificadores permiten mejorar el balance de potencia de la red y aumentar de ese modo las distancias de los enlaces.

En el capítulo 6 del presente trabajo, se ha propuesto y analizado el anillo resonante con espejo Sagnac interno como filtro óptico para la compensación de la dispersión cromática en enlaces de transmisión.

Se concluye que los filtros compuestos en cascada, basados en anillos resonantes y espejos Sagnac (RR-SG), pueden emplearse como compensadores de dispersión cromática induciendo, no obstante, una distorsión de magnitud en la señal recibida que debe mantenerse bajo ciertos límites.

Se han realizado simulaciones con el software de VPIphotonics^{TM} para verificar la compensación de dispersión cromática con los citados filtros compuestos, comprobando que es posible eliminar el efecto de la dispersión con estos filtros de una manera más compacta que con fibra compensadora de dispersión. En el apéndice B de este documento se han incluido explicaciones y detalles adicionales sobre el software de VPIphotonics.

Se ha empleado un modelo simplificado de canal consistente en fibra dispersiva no lineal con el ruido proveniente de los amplificadores ópticos, y se ha podido estimar la tasa de error binaria (BER) de un enlace de estas características con señales NRZ (*Non-Return-to-Zero*), para una velocidad de 5 Gb/s, longitudes de fibra entre 150-200 km y relaciones señal a ruido ópticas entre 10 y 15 dB.

En simulaciones futuras, se considerarán velocidades mayores de 10 y 40 Gb/s, correspondientes a los estándares de transmisión OC-192 y 768, y se realizaran simulaciones de varios canales simultáneos, añadiendo el efecto de la dispersión por modo de polarización (PMD).

Aunque la amplificación bidireccional dentro del anillo permite ajustar el punto de funcionamiento de la configuración RR-SG, no se puede eliminar la distorsión de magnitud, que es inherente a la configuración.

No obstante, analizando el anillo resonante con espejo Sagnac dentro del marco de los filtros paso-todo, se han deducido analíticamente las modificaciones necesarias en el comportamiento de la configuración para eliminar la distorsión de magnitud inherente y convertirla en un filtro paso-todo.

Asimismo, se ha realizado una propuesta para la implementación de esta configuración modificada, en tecnología de fibra óptica, véase la Fig. 8.9.

Esta propuesta permite aumentar los valores de dispersión negativa alcanzados con los filtros basados en el resonador con espejo Sagnac, manteniendo la distorsión de

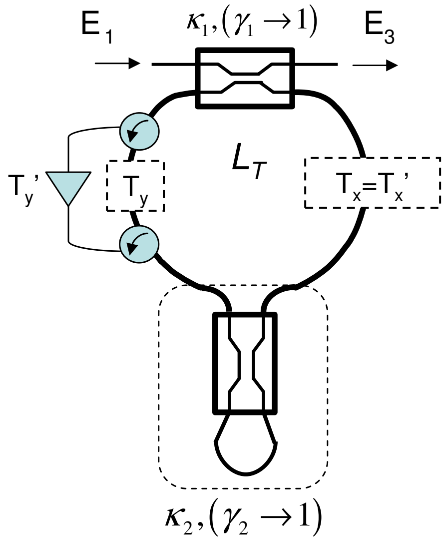

Figura 8.9: Esquema del filtro paso-todo en fibra óptica con anillo resonante y espejo Sagnac. $T_x \cdot T_y = 1$, $T_x' \cdot T_y' = (1 - \kappa_1)^{-1/2}$.

magnitud en valores mucho más bajos, teóricamente nulos excepto por el efecto de las pérdidas en exceso de los acopladores ópticos.

8.6 Conclusiones y Líneas Futuras de Trabajo

En el presente trabajo, se han descrito diversas contribuciones originales al estado del arte de las técnicas de auto-referencia y multiplexación de los sensores ópticos de intensidad, empleando configuraciones con fibra óptica monomodo en régimen incoherente.

Estas nuevas configuraciones pueden contribuir a la futura implantación de redes ópticas seguras, robustas, flexibles y fácilmente escalables, para realizar medidas remotas con sensibilidad mejorada sobre un número mayor de sensores ópticos. Ejemplos de estas aplicaciones son, por ejemplo, la monitorización del nivel de líquido en entornos inflamables, tales como tanques de combustible en redes de gasolineras, o las medidas remotas de temperatura o concentración de gases en los túneles de autopistas o ferrocarriles, para la detección anticipada de riestos o detección rápida de posibles accidentes.

En este trabajo también se han obtenido resultados originales en el diseño de filtros sintonizables paso-todo basados en el anillo resonante con interferómetro Sagnac interno, y se han desarrollado simulaciones que permiten evaluar las prestaciones de los filtros ópticos diseñados en sistemas de transmisión digital a alta velocidad en fibra óptica.

En el caso de los sistemas de auto-referencia:

- Se ha empleado por primera vez la teoría de filtros digitales para el diseño y el análisis de técnicas de auto-referencia. Se han desarrollado nuevas expresiones analíticas cerradas empleando la Transformada Z, para describir de una manera compacta y novedosa las técnicas propuestas, desde el punto de vista de la sensibilidad, la linealidad o las pérdidas de inserción de las configuraciones ópticas empleadas.

- Se han estudiado y verificado experimentalmente dos nuevos parámetros de medida remota con auto-referencia sobre sensores ópticos, empleando el anillo resonante en régimen incoherente con un sensor de intensidad incluido en el lazo de realimentación. El comportamiento de esta configuración se ha verificado tanto en transmisión como en reflexión, empleando en este último caso redes de Bragg en fibra.

- Se ha propuesto y demostrado de manera experimental un nuevo parámetro de medida con doble sensibilidad, utilizando dos frecuencias de modulación y empleando dos redes de Bragg entre las que se sitúan una línea de retardo en fibra y un sensor de intensidad.

- Por último, se ha propuesto y verificado una configuración novedosa de auto-referencia, empleando dos redes de Bragg con un sensor de intensidad situado entre ambas, sin necesidad de emplear largas líneas de retardo en fibra. Utilizando retardos electrónicos re-configurables en la etapa de recepción, es posible emplear una frecuencia de modulación de valor bajo y arbitrario, manteniendo las prestaciones de otras configuraciones y reduciendo muy significativamente el tamaño de las cabezas sensoras remotas.

Las técnicas de auto-referencia estudiadas requieren un régimen de funcionamiento incoherente, lo que implica que la longitud de coherencia de la luz en el punto remoto de medida debe ser mucho menor que las longitudes características de las configuraciones empleadas para obtener la auto-referencia. El régimen de funcionamiento incoherente es una situación realista y deseable, debido a que es un régimen estable y bastante tolerante a perturbaciones externas; asimismo, este régimen suele estar asociado al empleo de fuentes ópticas con un espectro de banda ancha, que en general permite implementer sistemas de bajo coste para medidas simultáneas en varios sensores.

Las técnicas de auto-referencia obtenidas con el anillo resonante sólo requieren una longitud de onda, y son tolerantes a fluctuaciones de la misma, con la única restricción de que se encuentren dentro del ancho de banda de la red de Bragg, en el caso de la configuración reflexiva.

El resto de las técnicas que emplean redes de Bragg requieren que el ancho de banda de éstas sea suficientemente grande para evitar fluctuaciones de potencia en los puntos remotos de medida, debidas a posibles variaciones en la longitud de onda de las fuentes ópticas.

Las técnicas de auto-referencia reflexivas se ajustan muy bien al empleo de fuentes de luz de espectro ancho para interrogar múltiples sensores, si bien su espectro debe ser estable para mantener medidas calibradas a largo plazo. Asimismo, la integración de estos sistemas de sensado en redes de comunicaciones permitiría compartir el coste de fuentes ópticas más potentes, como los láseres DFB.

En el caso de la configuración sin fibra de retardo, se ha conseguido reducir muy significativamente las dimensiones de las cabezas sensoras remotas, y se permite una fácil re-configuración multipunto de la técnica de medida desde un solo punto de localización. Estas mejoras constituyen una contribución muy significativa al estado del arte de estas técnicas de medida, si bien se require un fotodetector y un demultiplexor adicional por cada sensor multiplexado.

El empleo de dispositivos CWDM para construir redes de sensores con la topología en estrella de las redes ópticas pasivas (PON) de comunicaciones para el acceso a banda ancha constituye una solución eficiente para medidas remotas en varios sensores ópticos, mejorando el balance de potencia respecto a las PON convencionales con divisores de potencia. Se ha demostrado experimentalmente que esta topología multiplexada es compatible con las técnicas de auto-referencia propuestas en el presente trabajo.

Por otro lado, se ha estudiado el filtro basado en el anillo resonante con inteferómetro Sagnac (RR-SG), centrándonos en sus propiedades dispersivas para el control de la dispersión cromática en enlaces de transmisión digital sobre fibra óptica. Se han realizado simulaciones para evaluar las prestaciones de los filtros compuestos basados en esta configuración dentro de enlaces de comunicaciones. Las simulaciones muestran que es posible eliminar completamente el efecto de la dispersión cromática de fibra monomodo G.652, en enlaces en torno a los 200 km con señales NRZ a 5 Gb/s.

Asimismo, se ha propuesto una modificación del filtro RR-SG para obtener una amplificación selectiva dentro del anillo y conseguir un filtro paso-todo con distorsión de magnitud muy baja. La propuesta se ha estudiado analíticamente y se ha demostrado que los picos con dispersión cuadrática negativa son dos órdenes de magnitud mayores que en el filtro RR-SG convencional, manteniendo la distorsión de magnitud en valores similares. El filtro RR-SG modificado permite definir arquitecturas multietapa en cascada para la síntesis de filtros paso-todo fotónicos IIR de orden arbitrario, lo que puede constituir una contribución significativa al estado del arte.

Finalmente, la continuación del trabajo realizado permite definir diversas líneas futuras de investigación, entre las que cabe destacar las siguientes:

- El estudio de las pérdidas de inserción de las configuraciones ópticas para medidas con auto-referencia se puede particularizar analíticamente para las técnicas presentadas en este trabajo. Hasta el momento, sólo se han calculado las pérdidas correspondientes al anillo resonante incoherente, si bien sería interesante desarrollar un estudio comparativo y diversos experimentos considerando otras configuraciones, tales como la Mach-Zehnder, Michelson y las configuraciones con redes de Bragg.

- Las técnicas de medida con auto-referencia permiten aumentar la sensibilidad de las medidas si los diseños son adecuados y el nivel de ruido es suficientemente bajo. No obstante, los parámetros de medida que se obtienen suelen tener un comportamiento altamente no-lineal. Sería de gran interés investigar nuevas técnicas de auto-referencia combinando procesadores ópticos y electrónicos para aumentar la flexibilidad de las mismas, de modo que se pueda ajustar la sensibilidad y linealizar al mismo tiempo el comportamiento de los propios sensores ópticos de intensidad respecto de la magnitud física o química de medida. El desarrollo de modelos detallados de las configuraciones para deducir la relación señal a ruido y el espectro de ruido en las medidas sería también muy interesante.

- Las configuraciones propuestas en este trabajo se han caracterizado empleando un analizador de espectros eléctrico y un analizador de redes ópticas. Dichos equipos son de propósito general y exceden las prestaciones necesarias para la implantación de las técnicas estudiadas. Sería interesante diseñar una instrumentación opto-electrónica dedicada y de bajo coste para el desarrollo de prototipos competitivos a nivel económico, con el propósito de la implantación comercial de las técnicas estudiadas a medio-largo plazo.

- El ruido de intensidad inducido por las fluctuaciones de fase de la fuente óptica en las configuraciones incoherentes para medidas con auto-referencia puede ser una limitación importante para las prestaciones de los sistemas propuestos. Sería interesante estudiar en detalle y verificar experimentalmente el comportamiento de este ruido y compararlo con el ruido de intensidad inherente a las fuentes ópticas empleadas, para encontrar las restricciones en el margen dinámico de las medidas y establecer criterios generales para la elección de los dispositivos y los parámetros de diseño óptimos.

Por otro lado, en relación a los dispositivos basados en el anillo resonante óptico en régimen coherente, en el futuro se podría investigar en las siguientes líneas:

- La dispersión cuadrática del filtro RR-SG, con un interferómetro Sagnac dentro del anillo resonante, se podría verificar experimentalmente a través de prototipos en fibra óptica. Para ello, las dimensiones de los prototipos así como las perturbaciones externas en los montajes deben reducirse en la medida de lo posible para obtener una interferencia estable. El empleo de fibras fuertemente dopadas podría ayudar a ajustar el punto de trabajo de este tipo de interferómetros y mejorar las medidas realizadas, puesto que se puede obtener amplificación óptica razonablemente alta con unos pocos centímetros de fibra dopada. Por otro lado, el futuro desarrollo de circuladores y aisladores ópticos integrados permitiría la implementación de chips fotónicos con las prestaciones del filtro paso-todo basado en el RR-SG modificado, propuesto y analizado en este trabajo.

- Nuevas estructuras láser sintonizables se han propuesto recientemente en el Grupo de Displays y Aplicaciones Fotónicas. La verificación experimental de este tipo de dispositivos a través de prototipos con fibra óptica sería muy interesante.

- Las simulaciones realizadas con el software VPIphotonics^{T}M consideran una única portadora y una señal digital NRZ a 5 Gb/s. Sería interesante realizar simulaciones considerando sistemas WDM con varias portadoras multiplexadas, para evaluar el efecto que pueda inducirse entre los diferentes canales, así como el efecto de la pendiente de dispersión en la fibra óptica. Por otro lado, sería altamente interesante incrementar las velocidades binarias de modulación hasta los estándares de transmisión digital óptica OC-192 y OC-768, que operan a 10 Gb/s y 40 Gb/s, respectivamente. Asimismo, distintos formatos de modulación, tales como la modulación diferencial de fase o la modulación duobinaria podrían también considerarse en futuras simulaciones.

- Se podrían realizar simulaciones empleando diseños basados en el filtro paso-todo RR-SG modificado. Se espera que con este filtro puedan compensarse enlaces de transmisión de mayor alcance y velocidades binarias más altas.

- Sería interesante realizar simulaciones más avanzadas de configuraciones fotónicas con dimensiones en el orden de la micra o el milímetro, tanto en estructuras bidimensionales como tridimensionales. En el entorno internacional, diversas compañías ofrecen la posibilidad de fabricar dispositivos fotónicos integrados en varias tecnologías. Sería interesante trasladar algunos de los diseños planteados en el capítulo 7 de este trabajo a dispositivos integrados reales. La caracterización de los mismos requeriría invertir en nuevas infraestructuras o bien colaboración con otros grupos de investigación.

- En un escenario a largo plazo, se podrían utilizar dispositivos ópticos basados en las configuraciones RR-SG en redes ópticas en funcionamiento, siendo en tal caso posible verificar la compensación de la dispersión cromática obtenida a través de simulaciones.

8.7 Publicaciones Obtenidas

8.7.1 Publicaciones en Revistas Internacionales

- C. Vázquez and J. Montalvo, **Radio-Frequency Ring Resonators for Self-Referencing Fibre-Optic Intensity Sensors**, *Optical Engineering Letters*, vol. 44, n^o 4, pp. 1–2, Abril de. 2005.

- Julio Montalvo, Carmen Vázquez and David S. Montero, **CWDM self-referencing sensor network based on ring resonators in reflective configuration**, *Optics Express*, vol. 14, n^o 11, pp. 4601–4610, Mayo de 2006.

- Carmen Vázquez, Julio Montalvo, David S. Montero and J. M. S. Pena, **Self-referencing fiber-optic intensity sensors using Ring Resonators and Fiber Bragg Gratings**, *IEEE Photonics Technology Letters*, vol. 18, n^o 22, pp. 2374–2376, Nov. de 2006.

- J. Montalvo, F. M. Araújo, L. A. Ferreira, C. Vázquez and J. M. Baptista, **Electrical FIR filter with optical coefficients for self-referencing WDM intensity sensors**, *IEEE Photonics Technology Letters*, vol. 20, pp. 45-47, Enero de 2008.

8.7.2 Patentes

- J. Montalvo, O. Frazão, F. M. Araújo, L. A. Ferreira, C. Vázquez, J. L. Santos and J. M. Baptista, *Patente Nacional Portuguesa, ref. 20071000050642*, **Processo de Desmodulação de Sensores de Fibra Óptica de Intensidade e Respectivo Dispositivo**, solicitada en Octubre de 2007.

8.7.3 Publicaciones en Congresos Internacionales

- J. Montalvo and C. Vázquez, **Self-referencing intensity-encoded fibre-optic sensors using radio-frequency ring resonators**, *Proc. SPIE 5840: Photonic Materials, Devices and Applications*, pp. 284–295, U.S.A., 2005.

- C. Vázquez and J. Montalvo, **Applications of recirculating optical configurations on filters and lasers**, *Proc. SPIE 5840: Photonic Materials, Devices and Applications*, pp. 316–324, U.S.A., 2005.

- J. Montalvo, P. C. Lallana and C. Vázquez, **Self-Referencing Fibre-Optic Intensity Strain Sensors**, *17th International Conference on Optical Fibre Sensors (OFS-17)*, Proc. SPIE 5855, pp. 767–770, U.S.A., 2005.

- C. Vázquez, J. Montalvo, P. C. Lallana and D. S. Montero **Self-Referencing Technique in Reflection Mode for Fibre-Optic Intensity Sensors Using Ring Resonators** , *18th International Conference on Optical Fibre Sensors (OFS-18)*, ISBN 1-55752-817-9, ThE26, U.S.A., 2006.

- J. Montalvo and C. Vázquez, **Ring resonator with an internal Sagnac loop for dispersion compensation in DWDM backbone networks**, *Proc. SPIE 6593: Photonic Materials, Devices and Applications II*, paper 65931E, U.S.A., 2007.

- C. Vázquez, J. Montalvo, D. S. Montero and P. C. Lallana, **Self-Referencing Techniques in Photonic Sensors and Multiplexing** (Invited), *Proc. SPIE 6593: Photonic Materials, Devices and Applications II*, paper 65931X, U.S.A., 2007.

- C. Vázquez, P. Contreras, J. Montalvo, J. M. Sánchez-Pena, Antonio d'Alessandro and D. Donisi, **Switches and Tunable Filters based on Ring Resonators**

and Liquid Crystals, *Proc. SPIE 6593: Photonic Materials, Devices and Applications II*, paper 65931F, U.S.A., 2007.

- J. Montalvo and C. Vázquez, **Compound Optical Filters based on Ring Resonators and Sagnac Loops for Dispersion Management in DWDM Networks**, E-PhotonONe+/COST 291 Workshop, Brest (France), Julio de 2007.
- J. Montalvo and C. Vázquez, **Ring Resonator with Sagnac Loops for Photonic Processing in DWDM Backbone Networks**, *IEEE International Symposium on Intelligent Signal Processing (WISP 2007): Photonic Signal Processing*, ISBN 1-4244-0829-6, U.S.A., 2007.

8.7.4 Publicaciones en Congresos Nacionales

- J. Montalvo, C. Vázquez and D. S. Montero, **Respuesta en frecuencia de dos anillos resonantes en cascada mediante redes de Bragg en fibra**, *Optoel'05: 4^a Reunión Española de Optoelectrónica*, España, 2005.
- J. Montalvo and C. Vázquez, **Filtros compensadores de dispersión basados en el anillo resonante para redes troncales ópticas**, *Optoel'07: 5^a Reunión Española de Optoelectrónica*, España, 2007.
- C. Vázquez, J. M. S. Pena, S. Vargas, A. B. Gonzalo, J. Montalvo, P. C. Lallana, D. Sánchez, K. K. Afshar, A. Ferreiro and J. J. Romeral, **DISFOTON: Dispositivos Fotónicos para redes de Multiplexado Vasto en Longitud de Onda (TIC 2003-03783)**, *Jornadas de seguimiento de proyectos en Tecnología Electrónica*, Barcelona, Sept. 2005.

8.7.5 Publicaciones Previas en Revistas Internacionales

- C. Vázquez, J. M. S. Pena, S. Vargas, I. Pérez, A. B. Gonzalo, V. Urruchi, R. Vergaz, J. Montalvo, R. Manzanares, J. I. Santos y A. L. Aranda, **Displays and Photonics Applications Group Activities,** *Fiber and Integrated Optics*, vol. 23, pp. 231–247, 2004.
- C. Vázquez, A. B. Gonzalo, S. Vargas y J. Montalvo, **Multi-sensor system using plastic optical fibers for intrinsically safe level measurements**, *Sensors and Actuators A: Physical*, vol. 16, pp. 22–32, 2004.
- C. Vázquez, S. Vargas, J. I. Santos, J. M. S. Pena, J. Montalvo, **Time Division Multiplexing Fiber-Optic Liquid Level Sensors using a Nematic 1x2 Optical Switch**, 13th International Plastic Optical Fibres Conference (POF 2004), ISBN 3-905084-70-8, pp. 351-356, 2004.

8.7.6 Otros Méritos

Hasta la fecha, Julio Montalvo ha actuado como revisor para las siguientes revistas internacionales:

- **Sensors and Actuators A: Physical**, en 2004.
- **Applied Optics**, en 2006.
- **Optics Express**, en 2006.
- **Optics Communications**, en 2007.

Hasta la fecha, Julio Montalvo, como profesor en el Departamento de Tecnología Electrónica de la Universidad Carlos III de Madrid, ha actuado como director de los siguientes Proyectos Fin de Carrera:

- **Optical sideband filtering in an optical beam-forming system for phased-array antennas**, *Jorge Peña Hevilla*, Ingeniería de Telecomunicación, Universidad Carlos III de Madrid[2], Julio de 2007.

- **Enlace de fibra óptica con tecnología CWDM para medidas remotas con auto-referencia sobre sensores ópticos,** *Miguel Ángel González de Paz*, Ingeniería Técnica de Telecomunicación: Sistemas de Telecomunicación, Universidad Carlos III de Madrid, Junio de 2007.

- **Desarrollo de un sistema de calibrado para un sensor óptico de nivel (Bloque Electrónico),** *M. Pilar Mencía Pérez*, Ingeniería Técnica Industrial: Electrónica Industrial, Universidad Carlos III de Madrid, Julio de 2006.

---

[2] En el marco de un programa de intercambio Erasmus con la Universidad de Twente (Holanda), entre Septiembre de 2006 y Abril de 2007.

Appendix A

Simulations of High-Speed Digital Transmission Links With Optical Fiber Using VPIphotonics^{TM}

VPIphotonics^{TM} is a Photonic Design Automation (PDA) software which comprises a number of products [1] for advanced simulation of photonic components and systems.

It provides an easy-to-use graphical user interface (GUI) which permits to control a simulation engine with a large database of optical, electrical and logical components and visualizers, available in different modules that can be easily interconnected.

In this appendix, basic concepts of the software [144] and relevant details of the simulations performed in chapter 7 of this document are reported.

---

[1] VPItransmissionMaker WDM, VPItransmissionMaker Cable Access, VPIcomponentMaker Active Photonics, VPIcomponentMaker Optical Amplifiers, VPIplayer and VPIlinkConfigurator, among others.

A.1 Optical Signal Mode and Representation

For a particular simulation, the first choice to make is whether the interaction between the modules is bidirectional or unidirectional. This choice can be made by setting the **OutputDataType** parameter at the source of the signal either to *Block Mode* (unidirectional interaction) or to *Sample Mode* (bidirectional interaction).

In *Sample Mode* simulations, the signals are passed bidirectionally between interconnected modules on a sample by sample basis, thus allowing very close coupling between components, for example lasers and external resonators, so that optical resonances can be modelled. This signal mode is suitable for individual component design, where recirculations and reflections of optical signals must be taken into account.

The other signal mode is *Block Mode*, and it is used to pass signals unidirectionally. Each block contains enough samples to fill a **TimeWindow**, which specifies, among other things, the length of Fourier transforms used in spectral analysis, hence the frequency resolution. This signal mode is suitable for the simulation of multi-wavelength optical systems including digital transmitters and error detection modules.

The second choice to make is what kind of data, optical or electrical, is passed between the different simulation modules during their interaction.

Optical Signals are passed as sampled waveforms, and each sample contains optical field information with two polarizations representing the phase and amplitude of the optical field during a slice of time. Samples are passed individually and sort between modules in Sample Mode, or collected into blocks and passed in one go in Block Mode.

On the other hand, *Electrical Signals* are also passed as sampled waveforms, but they contain electrical voltage or current information during a slice of time. Again, individual samples can be collected together into blocks and passed in one go when the Block Mode is selected.

A.2 Bandwidth and Frequency Resolution of a Simulation

In Sample Mode simulations, the rate at which samples are passed is set by the global parameter **SampleModeBandwidth**, and represents the optical bandwidth over which the simulation operates, being the electrical bandwidth one half of it. In Block Mode simulations, the simulation bandwidth is set by the parameter **SampleRate**.

In Sample Mode, the signals represent the optical waveform by extracting a carrier frequency from it, set by the global variable **SampleModeCenterFrequency**. The remaining envelope is a complex waveform, which completely represents the optical channels and noise over a bandwidth centered around the **SampleModeCenterFrequency**. On the other hand, sources whose output is set to Block Mode usually produce a modelled optical bandwidth centered around their **EmissionFrequency**.

The frequency resolution of the Fourier transforms used in spectral analysis is the inverse of the global parameter **TimeWindow**. The product SampleRate·TimeWindow is exactly the number of samples of the simulation and must always be equal to a power of two (2^n).

On the other hand, in simulations with digital transmitters involved, the parameter **BitRateDefault** sets the bit rate, namely B. The number of samples corresponding to each bit period, namely S, must be integer. At the same time, the number of bits over the **TimeWindow** must also be a power of two (2^p for integer p).

These restrictions are expressed as follows:

$$\begin{aligned} TimeWindow &= 2^p \cdot B^{-1} \\ SampleRate &= S \cdot B \end{aligned} \tag{A.1}$$

If S is equal to a power of two ($S = 2^q$ for integer q), then the product:

$$SampleRate \cdot TimeWindow = 2^n \tag{A.2}$$

where $n = p + q$.

A.3 Simulation of Digital Transmission Links With Optical Fiber and Compound Filters as Dispersion Compensating Modules (DCM)

To simulate the performance of a digital transmission link over optical fiber, including chromatic dispersion and amplifiers, Block Mode signals must be employed, because most of the required modules are not compatible with the Sample Mode signal representation.

In our simulations, a digital optical transmitter at a single wavelength is connected to a simplified channel model of the optical link and the output is filtered and connected to either an optical filter, operating as dispersion compensation module (DCM), or a dispersion compensating fiber (DCF). The DCM is included in the simulation file through the module *FilterMeasuredOpt*, which reads the transfer function from a file. This transfer function is obtained from a different simulation in Sample Mode, as it will be explained in a later subsection. The DCF can be obtained by properly setting the parameters of an optical fiber model.

After the all-optical dispersion management, the signal is delivered to an ideal digital reception stage with an error detector module for bit error rate (BER) calculation. The schematic of the simulation is shown in Fig. A.1.

An optical carrier around 1550 nm is externally modulated by a 2^{11} bits digital sequence at the specific bit rate of 5 Gb/s, and then it is launched into the optical transmission channel.

After transmission, the output light is filtered by a second-order Gaussian filter with a 3-dB bandwidth of 20 GHz and, after optical-to-electrical conversion through a PIN

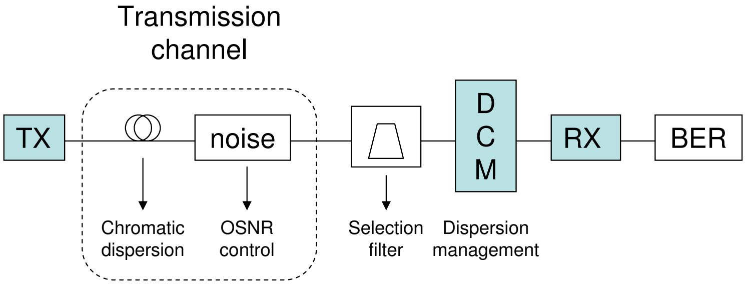

Figure A.1: Schematic of the VPI simulations to test the performance of compound filter-based DCM for dispersion management. OSNR: Optical Signal to Noise Ratio.

diode (including shot and thermal noise), it is delivered to the DCM.

In the following subsections, the most relevant aspects of the modules employed in the simulations are reported.

A.3.1 Fiber Models

The *FiberNLS* module has been employed as the optical transmission fiber. This module contains a non-linear dispersive fiber model where the dispersion coefficients and attenuation constant at a reference frequency can be specified.

This fiber module has been employed as a chromatic dispersion generator with a dispersion coefficient of 16 ps/nm per km and a dispersion slope of 0.08 ps/nm^2 (SMF G.652), inducing no attenuation by setting the parameter **Attenuation** to zero. This fiber module cannot handle non-constant polarization.

On the other hand, the dispersion compensating fiber consists of different FiberNLS module, where the **CoreArea** parameter has been changed from 80 to 30 μm^2 and the dispersion coefficient is fixed to -90 ps/nm per km. For a specific length of the transmission fiber L, the length of the DCF span must equal $\frac{16}{90} \cdot L$. These parameters for the DCF have been obtained from the WDM Demo File: Long Haul Transmission: Dispersion Managed Sections.

A.3.2 Control of the Optical to Signal Noise Ratio (OSNR)

In the simulations, the OSNR is defined as the ratio between the power of the optical source and the total noise power over the complete simulation bandwidth.

In order to fix the OSNR, the power of the optical source is calculated using the *Powermeter* module and adding white noise to the signal by using the *NoiseWhiteGaussOpt* module, where the **NoisePowerDensity** parameter is adjusted automatically depending on the output of the *Powermeter*.

A.3.3 Compound Optical IIR filters as Dispersion Compensating Modules (DCM)

In order to model a ring resonator (RR) and any other IIR filter, it is needed the Sample Mode, which is not compatible with the modules employed in the simulation of the digital transmission optical link. As a consequence of this, the compound filters used as dispersion compensating modules have been designed in a different simulation file and, afterwards, the transfer function has been exported to the transmission simulation through an export file. A capture of the schematic simulation for obtaining the transfer function of the compound filter with two RR in series and a RR with a Sagnac loop is shown in Fig. A.2.

As it can be seen in the figure, each RR stage of the compound filter has been modelled using an optical coupler with a feedback path, which comprises a unitary delay (1/SampleModeBandwidth), an optical attenuator and a phase shifter. The dispersion compensating module (DCM) has been built cascading two RR and connecting the output of the second RR to a *FilterOpt* module, where the RR-SG filter is described as a second order IIR filter.

In order to model the response of the ring resonator with an internal Sagnac loop (RR+SG), the parameter **FilterType** of the FilterOpt module has been set to the

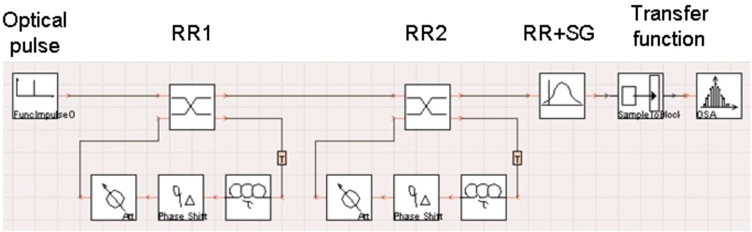

Figure A.2: Schematic of the VPI simulation for obtaining the transfer function and the quadratic dispersion of the compound filter cascading 2-RR and a RR with a Sagnac loop (RR+SG).

option GenericIIR, thus allowing the Z-transform description of the RR-SG filter with the following coefficients:

$$H(z) = \frac{B_0 + B_1 \cdot z^{-1} + B_2 \cdot z^{-2}}{1 - C_1 \cdot z^{-1} - C_2 \cdot z^{-2}} \tag{A.3}$$

Note that this description is different than the one used in the Matlab function *freqz*. Using Matlab notation, the coefficients in the denominator are $A_0 = 1, A_1 = -C_1, A_2 = -C_2$.

The global parameter **SampleModeBandwidth** fixes the Free Spectral Range of the compound filter, which in our simulations equals 25 GHz.

An ideal optical impulse is used as optical source, thus launching into the filter an input power density constant versus optical frequency. The magnitude and phase response, the group delay and quadratic dispersion of the compound filter can be visualized using the *ViOSA* module, which is an optical spectrum analyzer.

The transfer function of the compound filter is exported to an output file through the ViOSA module. This output file contains the description of the dispersion compensating module, which is employed in the digital transmission link through the module *FilterMeasuredOpt*.

A.3.4 Bit Error Rate (BER) Analysis

In our simulations, the random noise coming from the ASExASE and SignalxASE beat noises is added to the sampled signal representations, thus allowing a stochastic BER estimation.

For stochastic BER estimations of a single WDM channel with NRZ signals at 2.5 and 10 Gb/s, it is recommended that at least 8 samples per bit are taken and that the total number of bits is larger than 512.

In our simulations, we considered 32 samples per bit and 2048 bits, so a reasonable accuracy of the BER is ensured.

On the other hand, the Gauss-ISI and Chi^2-ISI BER estimators have been considered in our simulations, both of them considering one pre-bit and one post-bit in order to take intersymbol interference (ISI) into account. This ISI algorithm must be used for the systems with significant chromatic dispersion, or with directly modulated semiconductor lasers. The Chi^2 estimation is highly recommended for systems with optical amplifiers [144], as it is our case.

Appendix B

Characterization of Fiber Ring Resonators With the Agilent 8703B Lightwave Component Analyzer

The Agilent 8703B Lightwave Component Analyzer (LCA), see Fig. B.1, is a general-purpose instrument with calibrated 20 GHz capability for measuring optical, electro-optical and electrical components, assemblies and devices.

In this appendix, the main specifications of the instrument [145] and operation details for the calibrated measurements on fiber-optic ring resonators (RR) are reported.

B.1 8703B Performance Data

The 8703B used in this work contains an internal lightwave source, an electro-optical modulator and a receiver for operation around 1555 nm (option 155). It also contains

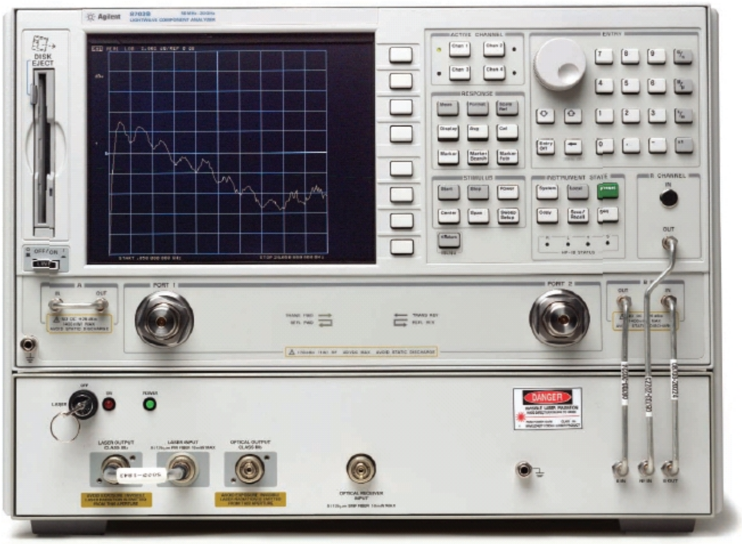

Figure B.1: Front view of the Agilent 8703B LCA.

an internal microwave source and a receiver with operation bandwidth from 50 MHz to 20.05 GHz.

It is recommended that the operation temperature of the 8703B is in the range of +20^{o}C to +30^{o}C, after having a warm-up time of two hours in a stable ambient temperature.

Its internal lightwave source has an spectral width lower than 20 MHz and emits an average output power of +5 dBm. This laser can be modulated from 50 MHz to 20.05 GHz with an spectral accuracy of 1 Hz by an internal electro-optical modulator with an insertion loss of 9 dB. The 8703B also accepts external light sources.

On the other hand, the lightwave receiver can detect optical signals between 1000-1600 nm. In the reception block of the 8703B, an intermediate frequency (IF) filter with an electrical bandwidth from 10 to 6000 Hz is available. Averaging and smoothing of the captured signals is also possible, as it is typical in this kind of instruments.

One of the key benefits of the 8703B is its ability to perform calibrated measurements on optical components. Through the temperature-compensated optical components and error-correction algorithms, the 8703B removes the systematic errors from the measured data of a device under test (DUT).

B.2 Calibrated Measurements on Radio-Frequency (RF) Modulated Fiber-Optic Ring Resonators (RR)

In this work, we have used the 8703B for measuring the calibrated power transfer function of fiber-optic ring resonators, which are a particular DUT with optical input and optical output.

As it has been reported in Chapter 3 of this document, the radio-frequency modulated fiber-optic RR with an optical intensity sensor in the feedback loop can perform as a self-referencing optical configuration.

A response calibration, which accounts for magnitude and phase errors due to the system modulation frequency, has been used for measuring the transmission characteristics of the RR with the 8703B. The schematic of the measurement set-up is shown in Fig. B.2(a).

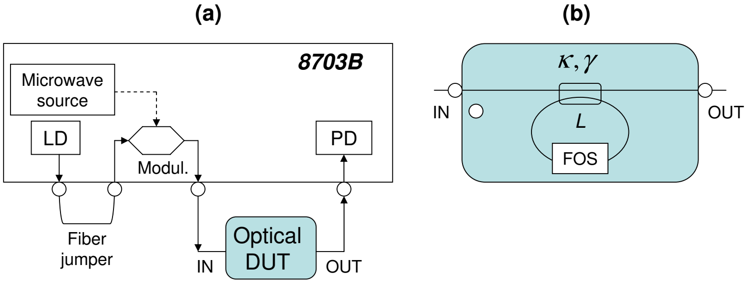

Figure B.2: (a) Schematic of the experimental set-up for optical device characterization using the 8703B. (b) Detail of a fiber ring resonator with a Fiber Optic Sensor (FOS) in the feedback loop as optical Device Under Test (DUT). LD, PD: Laser Diode, Photo-Detector. κ, γ: coupling coefficient and excess loss; L: Length of the feedback loop.

With this experimental set-up, the magnitude response of the RR configuration versus modulation frequency and its behaviour with regards the sensor-induced intensity modulation have been obtained, thus verifying the analytical expressions. These measurements have been reported in Chapter 3 of this document.

Either the internal laser of the 8703B or an external lightwave source can be connected to the internal electro-optical modulator through a fiber jumper, see Fig. B.2(a). As an incoherent regime of operation is wanted, the length of the RR feedback loop must always be much larger than the coherence length of the optical source.

First, the response calibration is performed, measuring the transmission response of the transmitter-receiver pair, employing a 1 meter fiber jumber instead of the RR configuration. This fiber jumber performs as an optical *calibration standard*, in this case called *optical through*.

Using this calibration data, the frequency and phase responses of the microwave source, the electro-optical modulator and the photodetector are removed from the measurements. After this *data correction*, if the optical through is kept in the set-up, an horizontal line should appear on the 8703B screen, being the reference of the following measurements. In power transmission measurements, this horizontal line represents 0 dBo.

The noise floor of the measurements on a device with optical input and output, with a 30 Hz IF bandwidth and an average factor of 6, is -30 dBo in the frequency range from 0.05 to 8 GHz, and -25 dBo in the range from 8 to 20.05 GHz. This is a relevant information, because it represents the maximum dynamic margin of the measurements over an optical DUT using the 8703B.

The next step is to replace the optical through with the fiber-optic RR configuration, see Fig. B.2(b), thus measuring its calibrated response, as shown in Fig. B.3. Markers showing the measurement data at fixed specific frequencies have been used for monitoring the behaviour of the RR configuration, allowing easy and flexible monitoring of different parameters of interest.

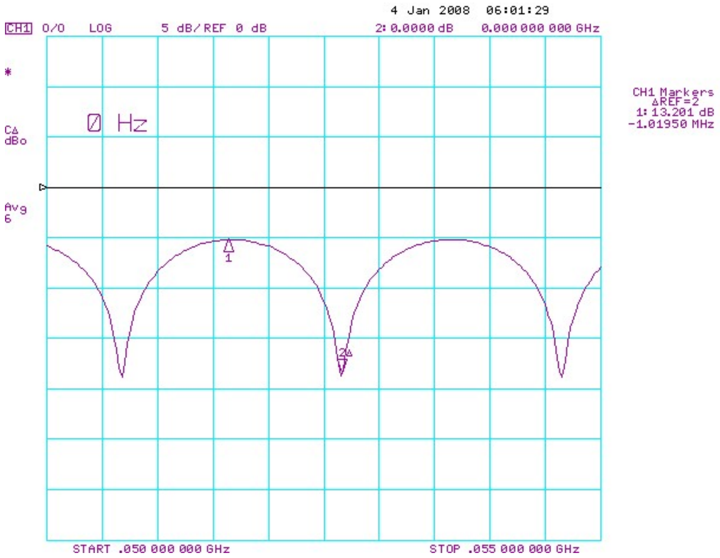

Figure B.3: Measured power transmission of a fiber-optic RR with $\kappa = 0.89, H = 0.13$ and L =100 m after a response calibration using the 8703B LCA. IF Bandwidth=30 Hz, no smoothing, 6 averages.

Bibliography

[1] C. Vázquez, J. M. S. Pena, S. Vargas, I. Pérez, A. B. Gonzalo, V. Urruchi, R. Vergaz, J. Montalvo, R. Manzanares, J. I. Santos, and A. L. Aranda. Displays and Photonics Application Group Activities. *Fiber and Integrated Optics*, 23:231–247, 2004.

[2] C. Vázquez, S. E. Vargas, and J. M. Sánchez Pena. Sagnac Loop in Ring Resonators for Tunable Optical Filters. *J. Lightw. Technol.*, 23(8):2555–2567, 2005.

[3] Salvador Vargas and Carmen Vázquez. Synthesis of Optical Filters Using Sagnac Interferometer in Ring Resonator. *IEEE Photon. Technol. Lett.*, 19:1877–1879, 2007.

[4] José Capmany, Beatriz Ortega, Daniel Pastor, and Salvador Sales. Discrete-Time Optical Signal Processing of Microwave Signals. *J. Lightw. Technol.*, 23:703–723, 2005.

[5] C. Vázquez, J. Montalvo, and P.C. Lallana. Radio-frequency ring resonators for self-referencing fiber-optic intensity sensors. *Opt. Eng. Lett.*, 44:1–2, 2005.

[6] C. Vázquez, J. Montalvo, D. S. Montero, and J. M. S. Pena. Self-Referencing Fiber-Optic Intensity Sensors Using Ring Resonators and Fiber Bragg Gratings. *IEEE Photon. Technol. Lett.*, 18:2374–2376, 2006.

[7] S. Abad, M. López-Amo, F. M. Araújo, L. A. Ferreira, and J. L. Santos. Fiber Bragg grating-based self-referencing technique for wavelength-multiplexed intensity sensors. *Opt. Lett.*, 27:222–224, 2002.

[8] J. Montalvo, F. M. Araújo, L. A. Ferreira, C. Vázquez, and J. M. Baptista. Electrical FIR filter with optical coefficients for self-referencing WDM intensity sensors. *IEEE Photon. Technol. Lett.*, 20:45–47, 2007.

[9] J. Montalvo, C. Vázquez, and D. S. Montero. CWDM self-referencing sensor network based on ring resonators in reflective configuration. *Opt. Express*, 14:4601–4610, 2006.

[10] C. K. Madsen and J. H. Zhao. *Optical Filter Design and Analysis: A Signal Processing Approach.* John Wiley and Sons INC., U.S.A., 1999.

[11] Salvador E. Vargas. *Contribución al Diseño de Filtros Ópticos para Redes con Multiplexación en Longitud de Onda.* PhD thesis, Universidad Carlos III de Madrid, 2003.

[12] Carmen Vázquez. *Contribución al Desarrollo de Dispositivos y Estructuras Fotónicas con Amplificación para Procesado Óptico.* PhD thesis, Universidad Politécnica de Madrid, 1995.

[13] M. Born and E. Wolf. *Principles of Optics.* New York: Pergamon, 1988.

[14] Alan V. Oppenheim and Ronald W. Schafer. *Discrete-Time Signal Processing.* Prentice Hall International, INC., London, 1989.

[15] A. Yariv. Universal relations for coupling of optical power between microresonators and dielectric waveguides. *Electron. Lett.*, 36:321–322, 2000.

[16] Otto Schwelb. Transmission, Group Delay and Dispersion in Single-Ring Optical Resonators and Add/Drop Filters – A tutorial overview. *J. Lightw. Technol.*, 22:1380–1394, 2004.

[17] H. Okamura and K. Iwatsuki. A Finesse-Enhanced Er-Doped-Fiber Ring Resonator. *J. Lightw. Technol.*, 9(11):1554–1560, 1991.

[18] H. Okamura and K. Iwatsuki. Er-Doped Fibre Ring Resonator Applied to Optical Spectrum Analiser with less than 100 KHz Resolution. *Electron. Lett.*, 27(12):1047–1049, 1991.

[19] I. Tedjini and A. Ho-Quoc. Theoretical and Experimental Study of Single Mode Fiber Optical Ring Resonators for Microwave Applications. *IEEE Microwave Theory and Techniques Society Digest*, pages 1491–1494, 1995.

[20] F. Schliep, D. Garus, and R. Hereth. Improved Method for Automatic Evaluation of the Parameters of Single-Mode Fiber-Optic Ring Resonators. *IEEE Photon. Technol. Lett.*, 8(1):107–109, 1996.

[21] J. E. Heebner, Vincent Wong, A. Schweinsberg, R. W. Boyd, and D. J. Jackson. Optical Transmission Characteristics of Fiber Ring Resonators. *IEEE J. Quantum Electron.*, 40(6):726–730, 2004.

[22] C. Vázquez, S. Vargas, J.M.S. Pena, and P. Corredera. Measurements on passive tunable optical filters for DWDM. In *Proceedings of 2002 IEEE/LEOS Workshop on Fibre and Optical Passive Components*, 2002.

[23] C. Vázquez, S. Vargas, J. M. Sánchez Pena, and P. Corredera. Tunable Optical Filters Using Compound Ring Resonators for DWDM. *IEEE Photon. Technol. Lett.*, 15(8):1085–1087, 2003.

[24] P. P. Absil, J. V. Hryniewicz, B. E. Little, R. A. Wilson, L. G. Joneckis, and P.-T. Ho. Compact Microring Notch Filters. *IEEE Photon. Technol. Lett.*, 12:398–400, 2000.

[25] B. E. Little and et al. Very High-Order Microring Resonator Filters for WDM Applications. *IEEE Photon. Technol. Lett.*, 16:2263–2265, 2004.

[26] K. Djordjev, Seung-J. Choi, Sang-J. Choi, and P.D. Dapkus. Microdisk Tunable Resonant Filters and Switches. *IEEE Photon. Technol. Lett.*, 14:828–830, 2002.

[27] D. H. Geuzebroek, E. J. Klein, H. Kelderman, F. S. Tan, D. J. W. Klunder, and A. Driessen. Thermally Tuneable, Wide FSR Switch based on Micro-ring Resonators. *Proceedings Symposium IEEE/LEOS Benelux Chapter*, pages 155–158, 2002.

[28] John M. Choi, Reginald K. Lee, and Amnon Yariv. Control of critical coupling in a ring resonator-fiber configuration: application to wavelength-selective switching, modulation, amplification and oscillation. *Opt. Lett.*, 26:1236–1238, 2001.

[29] V. R. Almeida, C. A. Barrios, R. R. Panepucci, and M. Lipson. All-optical control of light on a silicon chip. *Nature*, 431:1081–1084, 2004.

[30] B. E. Little, J. S. Foresi, G. Steinmeyer, E. R. Thoen, and S. T. Chu. Ultra-Compact Si-SiO2 Microring Resonator Optical Channel Dropping Filters. *IEEE Photon. Technol. Lett.*, 10:549–551, 1998.

[31] Milos A. Popovic, Tymon Barwicz, M. R. Watts, Peter T. Rakich, L. Socci, E.P. Ippen, Franz X. Kartner, and H. I. Smith. Multistage high-order microring-resonator add-drop filters. *Opt. Lett.*, 31:2571–2573, 2006.

[32] Carmen Vázquez, Salvador E. Vargas, José M. Sánchez Pena, and Ana B. Gonzalo. Demultiplexers for ultranarrow channel spacing based on Mach-Zehnders and ring resonators. *Opt. Eng.*, 43:2080–2086, 2004.

[33] D. Rafizadeh, J.P. Zhang, R.C. Tiberio, and S.T. Ho. Propagation Loss Measurements in Semiconductor Microcavity Ring and Disk Resonators. *J. Lightw. Technol.*, 16:1308–1314, 1998.

[34] R. W. Boyd and et al. Nanofabrication of optical structures and devices for photonics and biophotonics. *Journal of Modern Optics*, 50:2543–2550, 2003.

[35] C. K. Madsen, G. Lenz, A. J. Bruce, M. A. Capuzzo, L. T. Gomez, T. N. Nielsen, and I. Brener. Multistage dispersion compensator using ring resonators. *Opt. Lett.*, 24(22):1555–1557, 1999.

[36] Senichi Suzuki, Keizo Shuto, and Yoshinori Hibino. Integrated-Optic Ring Resonators with Two Stacked Layers of Silica Waveguide on Si. *IEEE Photon. Technol. Lett.*, 4:1256–1258, 1992.

[37] Chris G. H. Roeloffzen, R. M. de Ridder, G. Sengo, K. Worhoff, and A. Driessen. Passband flattened interleaver using a Mach-Zehnder interferometer with ring resonator fabricated in SiON waveguide technology. *Proc. of 28th European Conference on Optical Communication (ECOC 2002)*, 3:1–2, 2002.

[38] Andrea Melloni, R. Costa, P. Monguzzi, and M. Martinelli. Ring-resonator filters in silicon oxynitride technology for dense wavelength-division multiplexing systems. *Opt. Lett.*, 28:1567–1569, 2003.

[39] B. Maune, R. Lawson, C. Gunn, A. Scherer, and L. Dalton. Electrically tunable ring resonators incorporating nematic liquid crystals as cladding layers. *Appl. Phys. Lett.*, 83:4689–4691, 2003.

[40] W. M. J. Green, R. K. Lee, A. Yariv, and A. Scherer. Control of Optical Waveguide-Resonator Coupling: Applications to Low-Power Optical Modulation and Switching. *16th Annual Meeting Laser and Electro-Optics Society*, 1:130–131, 2003.

[41] V.M. Menon, W. Tong, and S.R. Forrest. Control of Quality Factor and Critical Coupling in Microring Resonators Through Integration of a Semiconductor Optical Amplifier. *IEEE Photon. Technol. Lett.*, 16:1343–1345, 2004.

[42] M. Beaugeois, B. Pinchemel, and M. Bouazaoui. All-optical tunability of InGaAsP/InP microdisk resonator by infrared light irradiation. *Opt. Lett.*, 32:35–37, 2007.

[43] P. Rabiei, W. H. Steier, C. Zhang, and L. R. Dalton. Polymer Micro-Ring Filters and Modulators. *J. Lightw. Technol.*, 20:1968–1975, 2002.

[44] G. T. Paloczi, Y. Huang, and A. Yariv. Free-standing all-polymer microring resonator optical filter. *Electron. Lett.*, 39:1650–1651, 2003.

[45] V. Subramanian, Gregory N. De Brabander, David H. Naghski, and Joseph T. Boyd. Measurement of Mode Field Profiles and Bending and Transition Losses in Curved Optical Channel Waveguides. *J. Lightw. Technol.*, 15:990–997, 1997.

[46] P. Heimala, P. Katila, J. Aarnio, and A. Heinämäki. Thermally Tunable Integrated Optical Ring Resonator with Poly-Si Thermistor. *J. Lightw. Technol.*, 14:2260–2267, 1996.

[47] Amnon Yariv. Critical Coupling and Its Control in Optical Waveguide-Ring Resonator Systems. *IEEE Photon. Technol. Lett.*, 14:483–485, 2002.

[48] K. Sasayama, M. Okuno, and K. Habara. Coherent Optical Transversal Filter Using Silica-Based Waveguides for High-Speed Signal Processing. *J. Lightw. Technol.*, 9:1225–1230, 1991.

[49] K. Jinguji and M. Kawachi. Synthesis of Coherent Two-Port Lattice-Form Optical Delay-Line Circuit. *J. Lightw. Technol.*, 13:73–82, 1995.

[50] K. Jinguji and M. Oguma. Optical Half-Band Filters. *J. Lightw. Technol.*, 18:252–259, 2000.

[51] N. Q. Ngo and L. N. Binh. Novel Realization of Monotonic Butterworth-Type Lowpass, Highpass, and Bandpass Optical Filters Using Phase-Modulated Fiber-Optic Interferometers and Ring Resonators. *J. Lightw. Technol.*, 12(5):827–841, 1994.

[52] K. P. Jackson, G. Xiao, and H. J. Shaw. Coherent optical fibre delay-line processor. *Electron. Lett.*, 22:1335–1337, 1986.

[53] Kaname Jinguji and Masao Kawachi. Synthesis of Coherent Two-Port Optical Delay-Line Circuit With Ring Waveguides. *J. Lightw. Technol.*, 14(8):1882–1898, 1996.

[54] G. Lenz and C. K. Madsen. General Optical All-Pass Filter Structures for Dispersion Control in WDM Systems. *J. Lightw. Technol.*, 17(7):1249–1254, 1999.

[55] C. K. Madsen. General IIR Optical Filter Design for WDM Applications Using All-Pass Filters. *J. Lightw. Technol.*, 18:860–868, 2000.

[56] K. Oda, N. Takato, H. Toba, and K. Nosu. A Wide-Band Guided-Wave Periodic Multi/Demultiplexer with a Ring Resonator for Optical FDM Transmission Systems. *J. Lightw. Technol.*, 6:1016–1023, 1988.

[57] R. Orta, P. Savi, R. Tascone, and D. Trinchero. Synthesis of Multiple-Ring-Resonator Filters for Optical Systems. *IEEE Photon. Technol. Lett.*, 7(12):1447–1449, 1995.

[58] C. K. Madsen and J. H. Zhao. A General Planar Waveguide Autoregressive Optical Filter. *J. Lightw. Technol.*, 14(3):437–447, 1996.

[59] C. K. Madsen and G. Lenz. Optical All-Pass Filters for Phase Response Design with Applications for Dispersion Compensation. *IEEE Photon. Technol. Lett.*, 10:994–996, 1998.

[60] A. Melloni and M. Martinelli. Synthesis of Direct-Coupled-Resonators Bandpass Filters for WDM Systems. *J. Lightw. Technol.*, 20(2):296–303, 2002.

[61] B. E. Little, Sai T. Chu, John V. Hryniewicz, and Philippe P. Absil. Filter synthesis for periodically coupled microring resonators. *Opt. Lett.*, 25(5):344–346, 2000.

[62] Giora Griffel. Synthesis of Optical Filters Using Ring Resonator Arrays. *IEEE Photon. Technol. Lett.*, 12(7):810–812, 2000.

[63] A. Melloni. Synthesis of a parallel-coupled ring-resonator filter. *Opt. Lett.*, 26(12):917–919, 2001.

[64] E. Udd. *Fiber Optic Smart Structures.* New York, 1995.

[65] G. Murtaza and J.M. Senior. Referencing strategies for intensity modulated optical fibre sensors: a review. *Optics and Laser Technology*, 25:235–245, 1993.

[66] S. Dong, Y. Liao, and Quian Tian. Intensity-based optical fiber sensor for monitoring corrosion of aluminum alloys. *Appl. Opt.*, 44:5773–5777, 2005.

[67] P.A. Lewin, C. Mu, S. Umchid, A. Daryoush, and M. El-Sherif. Acousto-optic, point receiver hydrophone probe for operation up to 100 mhz. *Ultrasonics*, 43:815–821, 2005.

[68] Y. Zhao and F. Ansari. Intrinsic Single-Mode Fiber-Optic Pressure Sensor. *IEEE Photon. Technol. Lett.*, 13:1212–1214, 2001.

[69] N. Díaz-Herrera, M. C. Navarrete, O. Esteban, and A. González-Cano. A fibre-optic temperature sensor based on the deposition of a thermochromic material on an adiabatic taper. *Meas. Sci. Technol.*, 15:353–358, 2004.

[70] Jesús M. Corres, Francisco J. Arregui, and Ignacio R. Matías. Design of Humidity Sensors Based on Tapered Optical Fibers. *J. Lightw. Technol.*, 24:4329–4336, 2006.

[71] W. J. Bock, J. Chen, T. Eftimov, and M. Korwin-Pawlowski. Pressure sensing using periodically tapered long-period gratings written in photonic crystal fibres. *Meas. Sci. Technol.*, 18:3098–3102, 2007.

[72] W. J. Bock, W. Urbanczyk, and J. Wójcik. Measurements of sensitivity of the single-mode photonic crystal holey fibre to temperature, elongation and hydrostatic pressure. *Meas. Sci. Technol.*, 15:1496–1500, 2004.

[73] Kunimasa Saitoh and Masanori Koshiba. Single-Polarization Single-Mode Photonic Crystal Fibers. *IEEE Photon. Technol. Lett.*, 15:1384–1386, 2003.

[74] H. Kubota, S Kawanishi, S. Koyanagi, M. Tanaka, and S. Yamaguchi. Absolutely Single Polarization Photonic Crystal Fiber. *IEEE Photon. Technol. Lett.*, 16:182–184, 2004.

[75] W. B. Spillman and J. R. Lord. Self-Referencing Multiplexing Technique for Fiber-Optic Intensity Sensors. *J. Lightw. Technol.*, LT-5:865–869, 1987.

[76] John W. Berthold. Historical Review of Microbend Fiber-Optic Sensors. *J. Lightw. Technol.*, 13:1193–1199, 1995.

[77] C. Sánchez, A. García, G. E. Sandoval, J. Villatoro, and J. Hernández. Technique for referencing of fiber-optic intensity-modulated sensors by use of counterpropagating signals. *Opt. Lett.*, 13:1467–1469, 2004.

[78] P. Sixt, G. Kotrotsios, L. Falco, and O. Parriaux. Passive Fiber Fabry-Perot Filter for Intensity-Modulated Sensors Referencing. *J. Lightw. Technol.*, LT-4:926–932, 1986.

[79] J. M. Baptista, J. L. Santos, and A. S. Lage. Mach-Zehnder and Michelson topologies for self-referencing fiber optic intensity sensors. *Opt. Eng.*, 39:1636–1644, 2000.

[80] R. I. MacDonald and R. Nychka. Differential Measurement Technique for Optical Fibre Sensors. *Electron. Lett.*, 27:2194–2196, 1991.

[81] José M. Baptista, Silvia Abad, Gaspar M. Rego, Luis A. Ferreira, Francisco M. Araújo, José L. Santos, and Armindo S. Lage. Wavelength multiplexing of frequency-based self-referenced fiber optic intensity sensors. *Opt. Eng.*, 43:702–707, 2004.

[82] J. Montalvo and C. Vázquez. Self-referencing intensity-encoded fibre optic sensors using radio-frequency ring resonators. In *Proc. SPIE 5840: Photonic Materials, Devices and Applications, pp. 284-295*, July 2005.

[83] J. Montalvo, Pedro C. Lallana, and C. Vázquez. Self-referencing fibre-optic intensity strain sensors. In *Proc. SPIE 5855: 17th International Conference on Optical Fibre Sensors, pp. 767-770*, 2005.

[84] Carmen Vázquez, Julio Montalvo, David S. Montero, and Pedro C. Lallana. Self-referencing techniques in photonics sensors and multiplexing. In *Proc. SPIE 6593: Photonic Materials, Devices and Applications II*, Jun. 12, 2007.

[85] M. Tur and B. Moslehi. Laser phase noise effects in fiber optic signal processors with recirculating loops. *Opt. Lett.*, 4:229–231, 1983.

[86] Moshe Tur, Behzad Moslehi, and Joseph W. Goodman. Theory of Laser Phase Noise in Recirculating Fiber-Optic Delay Lines. *J. Lightw. Technol.*, LT-3:20–31, 1985.

[87] A. Papoulis. *Probability, random variables and stochastic processes.* New York, 1965.

[88] Beatriz Vizoso. *Contribución al Análisis y Desarrollo de Anillos Recirculantes de Fibra Óptica con Amplificación para el Procesado de la Señal.* PhD thesis, Universidad Politécnica de Madrid, 1996.

[89] J. Capmany. Investigation of phase-induced intensity noise in amplified fibre-optic recirculating delay line. *Electron. Lett.*, 29:346–348, 1993.

[90] Jon Thomas Kringlebotn and Kjell Blotekjaer. Noise Analysis of an Amplified Fiber-Optic Recirculating-Ring Delay Line. *J. Lightw. Technol.*, 12:573–582, 1994.

[91] Chang-Da Tsai and et al. Error reduction of referenced intensity-based optical fibre sensor by adaptive noise canceller. *Electron. Lett.*, 33:982–983, 1997.

[92] Rosa Romero, Orlando Frazao, Filip Floreani, Lin Zhang, Paulo V.S. Marques, and Henrique M. Salgado. Multiplexers and Demultiplexers Based on Fibre Bragg Gratings and Optical Circulators for DWDM Systems. *Proc. of 6th IEEE Int. Conf. on High Speed Networks and Multimedia Communications (HSNMC'03)*, 2720:442–451, 2003.

[93] X. Dong, P. Shum, N. Q. Ngo, and C. C. Chan. Largely tunable CFBG-based dispersion compensator with fixed center wavelength. *Opt. Express*, 11(22):2970–2974, 2003.

[94] X. Xu, Y. Dai, X. Chen, D. Jiang, and S. Xie. Chirped and phase-sampled fiber Bragg grating for tunable DBR fiber laser. *Opt. Express*, 13:3877–3882, 2005.

[95] J. Z. Sotor, A. J. Antończak, and K. M. Abramski. Optical FM demodulation by fiber Bragg grating. *Proc. of 9th IEEE Int. Conf. on Transparent Optical Networks (ICTON 2007)*, 4:216–218, 2007.

[96] Takanori Saitoh, Kenichi Nakamura, Yoshifumi Takahashi, Hiroyuki Iida, Yoshimitsu Iki, and Koichiro Miyagi. Ultra-Long Distance Fiber Bragg Grating Sensor System. *IEEE Photon. Technol. Lett.*, 19:1616–1618, 2007.

[97] Anbo Wang, H. Xiao, J. Wang, Z. Wang, and R.G. May. Self-Calibrated Interferometric-Intensity-Based Optical Fiber Sensors. *J. Lightw. Technol.*, 19:1495–1501, 2001.

[98] J. M. Baptista, J. L. Santos, and A. S. Lage. Self-referenced fibre optic intensity sensor based on a multiple beam Sagnac topology. *Opt. Commun.*, 181:287–294, 2000.

[99] C. Vázquez, J. Montalvo, P. C. Lallana, and D. S. Montero. Self-referencing technique in reflection mode for fibre-optic intensity sensors using Ring Resonators. *Proc. of 18th International Conference on Optical Fiber Sensors, paper ThE26*, 2006.

[100] M. Sumetsky, Y. Dulashko, J.M. Fini, A. Hale, and D.J. DiGiovanni. The Microfiber Loop Resonator: Theory, Experiment, and Application. *J. Lightw. Technol.*, 24:242–250, 2006.

[101] B. Moslehi and J.W. Goodman. Novel Amplified Fiber-Optic Recirculating Delay Line Processor. *J. Lightw. Technol.*, 10:1142–1146, 1992.

[102] Kenneth P. Jackson, Steven A. Newton, B. Moslehi, M. Tur, C. Chapin Cutler, Josepgh W. Goodman, and H.J. Shaw. Optical Fiber Delay-Line Signal Processing. *IEEE Trans. Microw. Theory Tech.*, MTT-33:193–210, 1985.

[103] M. C. Vázquez, B. Vizoso, M. López-Amo, and M. A. Muriel. Single and double amplified recirculating optical delay lines as fiber-optic filters. *Electron. Lett.*, 28:1017–1019, 1992.

[104] Christian Paquet. The current and future access network: and equipment provider's viewpoint. In *E-PhotonONe+ Simposium: Advanced Optical Communications, from short range to long haul networks*, Brest (France), July 2007.

[105] Seoijin Park, R. Leavitt, R. Enck, V. Luciani, Y. Hu, P.J.S. Heim, D. Bowler, and M. Dagenais. Semiconductor Optical Amplifier for CWDM Operating Over 1540-1620 nm. *IEEE Photon. Technol. Lett.*, 17:980–982, 2005.

[106] L. Spiekman, D. Piehler, P. Iannone, K. Reichmann, and H-H. Lee. Semiconductor optical amplifiers for FTTx. *9th International Conference on Transparent Optical Networks (ICTON '07)*, 2:48–50, 2007.

[107] Yizheng Zhu and Anbo Wang. Miniature Fiber-Optic Pressure Sensor. *IEEE Photon. Technol. Lett.*, 17:447–449, 2005.

[108] J. M. Baptista, S. F. Santos, G. Rego, O. Frazao, and J. L. Santos. Micro-displace or bending measurement using a long-period fibre grating in a self-reference fibre optic intensity sensor. *Opt. Commun.*, 260:8–11, 2006.

[109] S. Abad, F. M. Araújo, L. A. Ferreira, J. L. Santos, and M. López-Amo. Multiplexing of fibre optic intensity sensors using fused biconical wavelength selective couplers. *Electron. Lett.*, 37:490–491, 2001.

[110] S. Abad and M. López-Amo. Single and double distributed optical amplifier fiber bus networks with wavelength-division multiplexing for photonic sensors. *Opt. Lett.*, 24:805–807, 1999.

[111] P.-C. Peng, H.-Y. Tseng, and S. Chi. A Hybrid Star-Ring Architecture for Fiber Bragg Grating Sensor System. *IEEE Photon. Technol. Lett.*, 15:1270–1272, 2003.

[112] X. Wan and H. F. Taylor. Multiplexing of FBG sensors using modelocked wavelength-swept fibre laser. *Electron. Lett.*, 39:1512–1514, 2003.

[113] Chang-Seok Kim, Tae Ho Lee, Y.S. Yu, Y-G. Han, S.B. Lee, and M.Y. Jeong. Multi-point interrogation of FBG sensors using cascaded flexible wavelength-division Sagnac loop filters. *Opt. Express*, 14:8546–8551, 2006.

[114] Arnitabha Banerjee, Y. Park, F. Clarke, H. Song, S. Yang, G. Kramer, K. Kim, and B. Mukherjee. Wavelength-division-multiplexed passive optical network (WDM-PON) technologies for broadband access: a review. *J. Opt. Netw.*, 4:737–758, 2005.

[115] Soo-Jin Park, Chan-Hee Lee, Ki-Tae Jeong, Hyung-Jin Park, Jeong-Gyun Ahn, and Kil-Ho Song. Fiber-to-the-Home Services Based on Wavelength-Division-Multiplexing Passive Optical Network. *J. Lightw. Technol.*, 22:2582–2591, 2004.

[116] Dong Jae Shin, Y. C. Keh, and J. W. Kwon et al. Low-cost WDM-PON With Colorless Bidirectional Transceivers. *J. Lightw. Technol.*, 24:158–165, 2006.

[117] K.-Y. Liou, U. Koren, E. C. Burrows, J. L. Zyskind, and K. Dreyer. A WDM Access System Architecture Based on Spectral Slicing of an Amplified LED and

Delay-Line Multiplexing and Encoding of Eight Wavelength Channels for 64 Subscribers. *IEEE Photon. Technol. Lett.*, 9:517–519, 1997.

[118] Warwick T. Holloway, Adrian J. Keating, and David D. Sampson. Multiwavelength Source for Spectrum-Sliced WDM Access Networks and LAN's. *IEEE Photon. Technol. Lett.*, 9:1014–1016, 1997.

[119] D. K. Jung, C. J. Youn, H. G. Woo, and Y. C. Chung. Spectrum-Sliced Bidirectional WDM PON. In *Proc. of Optical Fiber Communication Conference (OFC 2000)*, volume 2, pages 160–162, 2000.

[120] M. Zirngibl, C. H. Joyner, C. R. Doerr, L. W. Stulz, and H. M. Presby. An 18-Channel Multi-Frequency Laser. *IEEE Photon. Technol. Lett.*, 8:870–872, 1996.

[121] T. Makino, G. P. Li, A. Sarangan, and W. Huang. Multiwavelength gain-coupled MQW DFB laser array with fine tunability. In *Optical Fiber Communications Conference (OFC '96) Technical Digest (Vol. 2)*, pages 298–299. Optical Society of America, 1996.

[122] M. C. Nuss, W. H. Knox, and U. Koren. Scalable 32 channel chirped-pulse WDM source. *Electron. Lett.*, 32:1311–1312, 1996.

[123] H. Izadpanah, M. Z. Iqbal, M. Stern, J. L. Gimlett, and Chinlon Lin. An OC-48 SONET Optical Transmission System for Gigabit Computer Networks. *Proc. of IEEE International Conference on Communications (ICC 92)*, 2:738–742, 1992.

[124] K. Hagimoto, K. Iwatsuki, A. Takada, M. Nakazawa, M. Saruwatari, K. Aida, and K. Nakagawa. 250 km non-repeated transmission experiment at 1.8 Gb/s using LD pump Er3+ doped fibre amplifiers in IM-direct detection system. *Electron. Lett.*, 25:662–664, 1989.

[125] K. J. Park, C. J. Youn, J. H. Lee, and Y. C. Chung. Performance Comparisons of Chromatic Dispersion-Monitoring Techniques Using Pilot Tones. *IEEE Photon. Technol. Lett.*, 15:873–875, 2003.

[126] M.N. Petersen, Z. Pan, S. Lee, S.A. Havstad, and A.E. Willner. Online Chromatic Dispersion Monitoring and Compensation Using a single Inband Subcarrier Tone. *IEEE Photon. Technol. Lett.*, 14:570–572, 2002.

[127] M. Jinno and M. Abe. All-optical regenerator based on non-linear fibre Sagnac interferometer. *Electron. Lett.*, 28:1350–1352, 1992.

[128] O. Leclerc, B. Lavigne, E. Balmefredol, P. Brindel, and L. Pierre. Optical Regeneration at 40 Gb/s and Beyond. *J. Lightw. Technol.*, 21:2779–2790, 2003.

[129] J. C. Simon, L. Billes, A. Dupas, B. Kowalski, M. Henry, and B. Landousies. All optical regeneration. *Proc. of 24th European Conference on Optical Communication (ECOC 98)*, 1:467–469, 1998.

[130] A. H. Gnauck, L. J. Jr Cimini, J. Stone, and L. W. Stulz. Optical Equalization of Fiber Chromatic Dispersion in a 5-Gb/s Transmission System. *IEEE Photon. Technol. Lett.*, 2(8):585–587, 1990.

[131] S. Dilwali and G. Soundra Pandian. Pulse Response of a Fiber Dispersion Equalizing Scheme Based on an Optical Resonator. *IEEE Photon. Technol. Lett.*, 4(8):942–944, 1992.

[132] K. Takiguchi, K. Okamoto, and K. Moriwaki. Dispersion Compensation Using a Planar Lightwave Circuit Optical Equalizer. *IEEE Photon. Technol. Lett.*, 6(4):561–564, 1994.

[133] C. K. Madsen, J. A. Walker, J. E. Ford, K. W. Goossen, T. N. Nielsen, and G. Lenz. A Tunable Dispersion Compensating MEMS All-Pass Filter. *IEEE Photon. Technol. Lett.*, 12(6):651–653, 2000.

[134] C. K. Madsen. Subband All-Pass Filter Architectures With Applications to Dispersion and Dispersion-Slope Compensation and Continuously Variable Delay Lines. *J. Lightw. Technol.*, 21(10):2413–2420, 2003.

[135] K. M. Feng. Dynamic Dispersion Compensation in a 10-Gb/s Optical System Using a Novel Voltage Tuned Nonlinearly Chirped Fiber Bragg Grating. *IEEE Photon. Technol. Lett.*, 11(3):373–375, 1999.

[136] N.Q. Ngo, S.Y. Li, R.T. Zheng, S.C. Tjin, and P. Shum. Electrically Tunable Dispersion Compensator With Fixed Center Wavelength Using Fiber Bragg Grating. *J. Lightw. Technol.*, 21:1568–1575, 2003.

[137] D. van den Borne, V. Veljanovski, U. Gaubatz, C. Paquet, Y. Painchaud, E. Gottwald, G. D. Khoe, and H. de Waardt. 42.8-Gb/s RZ-DQPSK Transmission With FBG-Based In-Line Dispersion Compensation. *J. Lightw. Technol.*, 19:1069–1071, 2007.

[138] Y. Painchaud, M. Lapointe, F. Trepanier, R. L. Lachance, C. Paquet, and M. Guy. Recent progress on FBG-based tunable dispersion compensators for 40 gb/s applications. *Optical Fiber Communications Conference (OFC 07)*, pages 1–3, 2007.

[139] S. Vargas, C. Vázquez, and J.M.S. Pena. Novel tunable optical filter employing a fiber loop mirror for synthesis applications in WDM. *14th Annual Meeting Laser and Electro-Optics Society*, 2:899–900, 2001.

[140] V. M. Menon, W. Tong, F. Xia, C. Li, and S. R. Forrest. Nonreciprocity of counterpropagating signals in a monolithically integrated Sagnac interferometer. *Opt. Lett.*, 29:513–515, 2004.

[141] Julio Montalvo and Carmen Vázquez. Ring resonator with an internal Sagnac loop for dispersion compensation in DWDM backbone networks. In *Proc. SPIE 6593: Photonic Materials, Devices and Applications II*, Jun. 7, 2007.

[142] C. Vázquez, J. Montalvo, and Pedro C. Lallana. Ring Resonators with Sagnac Loops for Photonic Processing in DWDM Backbone Networks. *Proc. of IEEE International Symposium on Intelligent Signal Processing (WISP 2007)*, Photonic Signal Processing:809–813, 2007.

[143] T. R. Zaman, X. Guo, and R. J. Ram. Proposal for a Polarization-Independent Integrated Optical Circulator. *IEEE Photon. Technol. Lett.*, 18:1359–1361, 2006.

[144] *VPIcomponentMaker Active Photonics User's Manual.* VPIsystems Incorporated, 2005.

[145] *Agilent 8703B Lightwave Component Analyzer: Reference Manual.* Agilent Technologies, U.S.A., 2001.

PUBLICATIONS RELATED TO THIS WORK

International papers

- C. Vázquez and J. Montalvo, **Radio-Frequency Ring Resonators for Self-Referencing Fibre-Optic Intensity Sensors**, *Optical Engineering Letters*, vol. 44, n^o 4, pp. 1–2, Apr. 2005.
- Julio Montalvo, Carmen Vázquez and David S. Montero, **CWDM self-referencing sensor network based on ring resonators in reflective configuration**, *Optics Express*, vol. 14, n^o 11, pp. 4601–4610, May 2006.
- Carmen Vázquez, Julio Montalvo, David S. Montero and J. M. S. Pena, **Self-referencing fiber-optic intensity sensors using Ring Resonators and Fiber Bragg Gratings**, *IEEE Photonics Technology Letters*, vol. 18, n^o 22, pp. 2374–2376, Nov. 2006.
- J. Montalvo, F. M. Araújo, L. A. Ferreira, C. Vázquez and J. M. Baptista, **Electrical FIR filter with optical coefficients for self-referencing WDM intensity sensors**, *IEEE Photonics Technology Letters*, vol. 20, pp. 45-47, Jan. 2008.

The author J. Montalvo has also performed scientific revision for the international publications: *Applied Optics* and *Optics Express* of the *Optical Society of America* (OSA), and for *Sensors and Actuators A: Physical* and *Optics Communications* of *Elsevier, Ltd.*

Patents

- J. Montalvo, O. Frazão, F. M. Araújo, L. A. Ferreira, C. Vázquez, J. L. Santos and J. M. Baptista, *Portuguese National Patent, ref. 20071000050642*, **Processo de Desmodulação de Sensores de Fibra Óptica de Intensidade e Respectivo Dispositivo**, submitted October 2007.

International conferences[1]

- J. Montalvo and C. Vázquez, **Self-referencing intensity-encoded fibre-optic sensors using radio-frequency ring resonators**, *Proc. SPIE 5840: Photonic Materials, Devices and Applications*, pp. 284–295, U.S.A., 2005.

- C. Vázquez and J. Montalvo, **Applications of recirculating optical configurations on filters and lasers**, *Proc. SPIE 5840: Photonic Materials, Devices and Applications*, pp. 316–324, U.S.A., 2005.

- J. Montalvo, P. C. Lallana and C. Vázquez, **Self-Referencing Fibre-Optic Intensity Strain Sensors**, *17th International Conference on Optical Fibre Sensors (OFS-17)*, Proc. SPIE 5855, pp. 767–770, U.S.A., 2005.

- C. Vázquez, J. Montalvo, P. C. Lallana and D. S. Montero **Self-Referencing Technique in Reflection Mode for Fibre-Optic Intensity Sensors Using Ring Resonators** , *18th International Conference on Optical Fibre Sensors (OFS-18)*, ISBN 1-55752-817-9, ThE26, U.S.A., 2006.

- J. Montalvo and C. Vázquez, **Ring resonator with an internal Sagnac loop for dispersion compensation in DWDM backbone networks**, *Proc. SPIE*

---

[1] In proceedings after revision.

6593: Photonic Materials, Devices and Applications II, paper 65931E, U.S.A., 2007.

- C. Vázquez, J. Montalvo, D. S. Montero and P. C. Lallana, **Self-Referencing Techniques in Photonic Sensors and Multiplexing** (Invited), *Proc. SPIE 6593: Photonic Materials, Devices and Applications II*, paper 65931X, U.S.A., 2007.

- C. Vázquez, P. Contreras, J. Montalvo, J. M. Sánchez-Pena, Antonio d'Alessandro and D. Donisi, **Switches and Tunable Filters based on Ring Resonators and Liquid Crystals**, *Proc. SPIE 6593: Photonic Materials, Devices and Applications II*, paper 65931F, U.S.A., 2007.

- J. Montalvo and C. Vázquez, **Compound Optical Filters based on Ring Resonators and Sagnac Loops for Dispersion Management in DWDM Networks**, E-PhotonONe+/COST 291 Workshop, Brest (France), July 2007.

- J. Montalvo and C. Vázquez, **Ring Resonator with Sagnac Loops for Photonic Processing in DWDM Backbone Networks**, *IEEE International Symposium on Intelligent Signal Processing (WISP 2007): Photonic Signal Processing*, ISBN 1-4244-0829-6, U.S.A., 2007.

National conferences

- J. Montalvo, C. Vázquez and D. S. Montero, **Respuesta en frecuencia de dos anillos resonantes en cascada mediante redes de Bragg en fibra**, *Optoel'05: 4^a Reunión Española de Optoelectrónica*, España, 2005.
- J. Montalvo and C. Vázquez, **Filtros compensadores de dispersión basados en el anillo resonante para redes troncales ópticas**, *Optoel'07: 5^a Reunión Española de Optoelectrónica*, España, 2007.
- C. Vázquez, J. M. S. Pena, S. Vargas, A. B. Gonzalo, J. Montalvo, P. C. Lallana, D. Sánchez, K. K. Afshar, A. Ferreiro and J. J. Romeral, **DISFOTON: Dispositivos Fotónicos para redes de Multiplexado Vasto en Longitud de Onda (TIC 2003-03783)**, *Jornadas de seguimiento de proyectos en Tecnología Electrónica*, Barcelona, Sept. 2005.

Previous works

- C. Vázquez, J. M. S. Pena, S. Vargas, I. Pérez, A. B. Gonzalo, V. Urruchi, R. Vergaz, J. Montalvo, R. Manzanares, J. I. Santos y A. L. Aranda, **Displays and Photonics Applications Group Activities,** *Fiber and Integrated Optics*, vol. 23, pp. 231–247, 2004.
- C. Vázquez, A. B. Gonzalo, S. Vargas y J. Montalvo, **Multi-sensor system using plastic optical fibers for intrinsically safe level measurements**, *Sensors and Actuators A: Physical*, vol. 16, pp. 22–32, 2004.
- C. Vázquez, S. Vargas, J. I. Santos, J. M. S. Pena, J. Montalvo, **Time Division Multiplexing Fiber-Optic Liquid Level Sensors using a Nematic 1x2 Op-**

tical Switch, 13th International Plastic Optical Fibres Conference (POF 2004), ISBN 3-905084-70-8, pp. 351-356, 2004.

Other related works[2]

- **Optical sideband filtering in an optical beam-forming system for phased-array antennas**, *Jorge Peña Hevilla*, Master Thesis of High Telecommunication Engineering, Universidad Carlos III de Madrid[3], July 2007.
- **Enlace de fibra óptica con tecnología CWDM para medidas remotas con auto-referencia sobre sensores ópticos,** *Miguel Ángel González de Paz*, Master Thesis of Telecommunication Engineering: Communication Systems, Universidad Carlos III de Madrid, June 2007.
- **Desarrollo de un sistema de calibrado para un sensor óptico de nivel (Bloque Electrónico),** *M. Pilar Mencía Pérez*, Master Thesis of Industrial Engineering: Industrial Electronics, Universidad Carlos III de Madrid, July 2006.

---

[2] Julio Montalvo has performed as the supervisor of these works, carried out in the Electronics Technology Department, University Carlos III of Madrid.

[3] In the framework of an Erasmus mobility program with University of Twente (The Netherlands), between September 2006 and April 2007.

Lista de Acrónimos / Acronyms List

Acrónimo (Acronym)	*Término en Castellano (Spanish Term)*	*Término en Inglés (English Term)*
AM	Modulación de Amplitud	Amplitude Modulation
APC	Contacto Físico Angulado	Angled Physical Contact
APF	Filtro Paso Todo	All-Pass Filter
ASE	Emisión Espontánea Amplificada	Amplified Spontaneous Emission
AWG	Red de Difracción de Guía Ondas Distribuida	Arrayed Waveguide Grating
BG	Red de Bragg	Bragg Grating
BLS	Fuente Luminosa de Amplio Espectro	Broadband Light Source
BER	Tasa de Error de Bit	Bit Error Rate
CO	Instalación Central	Central Office
CD	Dispersión Cromática	Chromatic Dispersion
CATV	Televisión por Antena Común	Community Antenna TeleVision
CWDM	Multiplexación en Longitud de Onda Aproximada	Coarse Wavelength Division Multiplexing
DBR	Reflector de Bragg Distribuido	Distributed Bragg Reflector
DC	Corriente Continua	Direct Currect
DCM	Módulo Compensador de Dispersión	Dispersion Compensating Module
DCF	Fibra Compensadora de la Dispersión	Dispersion Compensating Fiber
DFB	Realimentación Distribuida	Distributed Feedback
DFF	Fibra de dispersión aplanada	Dispersion Flattened Fiber
DFT	Transformada Discreta de Fourier	Discrete Fourier Transform
DPSK	Modulación por Desplazamiento Diferencial de Fase	Differential Phase Shift Keying
DUT	Dispositivo bajo Test	Device Under Test
DSF	Fibra de dispersión desplazada	Dispersion Shift Fiber
DWDM	Multiplexación en Longitud de Onda Densa	Dense Wavelength Division Multiplexing
EDFA	Amplificador de Fibra Dopada con Erbio	Erbium Doped Fiber Amplifier
EDWA	Amplificador de Guía de Onda Dopada con Erbio	Erbium Doped Waveguide Amplifier
EMI	Inteferencia Electro-Magnética	Electro-Magnetic Interference

FBG	Red de Bragg en fibra	Fiber Bragg Grating
FC	Conector de fibra	Fiber Connector
FDL	Línea de Retardo en Fibra	Fiber Delay Line
FFT	Transformada Rápida de Fourier	Fast Fourier Transform
FOS	Sensor de Fibra Óptica	Fiber-Optic Sensor
FP	Fabry-Perot	Fabry-Perot
FIR	Respuesta al Impulso Finita	Finite Impulse Response
FWHM	Anchura Total a Mitad de Máximo	Full Width at Half Maximum
FSF	Fundación de Software Libre	Free Software Foundation
FSR	Rango Espectral Libre	Free Spectral Range
FITL	Fibra en el Bucle de Abonado	Fibre in the loop
GbE	Gigabit-Ethernet	Gigabit-Ethernet
GDAF	Grupo de Displays y Aplicaciones Fotónicas	Displays and Photonics Applications Group
GUI	Interfaz Gráfica de Usuario	Graphical User Interface
GNU	GNU No es Unix	GNU's Not UNIX
HDTV	Televisión de Alta Definición	High-Definition TeleVision
HFC	Híbrido Fibra-Coaxial	Hybrid Fibre-Coaxial
IF	Frecuencia Intermedia	Intermediate Frequency
IEEE	Instituto de Ingenieros Eléctricos y Electrónicos	Institute of Electrical and Electronics Engineers
INESC Porto	Instituto Nacional de Ingeniería y Sistemas Informáticos de Oporto	National Institute of Engineering and Computer Systems of Porto
IIR	Respuesta al Impulso Infinita	Infinite Impulse Response
IM	Modulador de Intensidad	Intensity Modulator
IP	Protocolo de Internet	Internet Protocol
IR	Infrarrojo	Infrared
ISI	Interferencia entre Símbolos	Inter-Symbol Interference
ITU	Unión Internacional de Telecomunicaciones (UIT)	International Telecommunication Union
ITU-T	Sector de Estandarización de las Telecomunicaciones de la ITU	ITU Telecommunication Standardization Sector
JDP	Jerarquía Digital Plesiócrona	Plesiochronous Digital Hierarchy
JDS	Jerarquía Digital Síncrona	Synchronous Digital Hierarchy
LAN	Redes de Area Local	Local Area Networks
LCD	Visualizador de Cristal Líquido	Liquid Crystal Display
LCA	Analizador de Redes Óptico	Lightwave Component Analyzer

LASER	Laser	Ligh Amplification by Stimulated Emission of Radiation
LD	Diodo Láser	Laser Diode
LED	Diodo Emisor de Luz	Light Emitting Diode
LMDS	Servicio de Distribución Local Multipunto	Local Multipoint Distribution Service
LS	Fuente Luminosa	Light Source
MAN	Redes de Area Metropolitana	Metropolitan Area Networks
MZI	Interferómetro Mach Zehnder	Mach Zehnder Interferometer
MMI Coupler	Acoplador Interferencial Multimodo	Multimode Interference Coupler
MEMS	Sistemas MicroElectro Mecánicos	Micro-ElectroMechanical Systems
MI	Interferómetro Michelson	Michelson Interferometer
MMF	Fibra Multimodo	Multimode Fiber
NLOG	Puerta Óptica No Lineal	Non-Linear Optical Gate
NRZ	Sin retorno a cero	Non Return to Zero
NZD(S)F	Fibra de dispersión (desplazada) distinta de cero	Non Zero Dispersion (Shift) Fiber
OA	Amplificador Óptico	Optical Amplifier
OC	Portadora Óptica	Optical Carrier
OADM	Multiplexor óptico de inserción/extracción	Optical Add/Drop Multiplexer
OE	Opto-electrónico	Opto-electronic
OLT	Terminación de Línea Óptica	Optical Line Termination
ONT	Terminación de Red Óptica	Optical Network Termination
ONU	Unidad de Red Óptica	Optical Network Unit
OOK		On-Off Keying
OSA	Analizador de Espectros Óptico	Optical Spectrum Analyzer
OXC	Interconexión Óptica	Optical cross-Connect
OSNR	Relación Señal-Ruido Óptica	Optical Signal-to-Noise Ratio
PC	Contacto físico	Physical Contact
PCF	Fibra de Cristal Fotónico	Photonic Crystal Fiber
PDA	Automatización de Diseño Fotónico	Photonic Design Automation
PD	Fotodiodo	Photodiode
PM	Modulación de Fase	Phase Modulation

PMD	Dispersión por Modo de Polarización	Polarization Mode Dispersion
POF	Fibra óptica de plástico (FOP)	Plastic Optical Fiber
PON	Red Óptica Pasiva	Passive Optical Network
PS	Desfasador	Phase Shifter
PR	Foto-Receptor	Photo-Receptor
RF	Radio-frecuencias	Radio Frequencies
RL	Pérdidas por Reflexión	Reflection Losses
RN	Nodo Remoto	Remote Node
ROC	Región de Convergencia	Region of Convergence
RR	Resonador en Anillo	Ring Resonator
RR-SG	Resonador en Anillo con espejo Sagnac interno	Ring Resonator with internal Sagnac loop
RX	Etapa de Recepción	Reception Stage
RZ SBS	Con retorno a cero Esparcimiento Brioullin estimulado	Return to Zero Stimulated Brioullin Scattering
SC	Conector Estándar	Standard Connector
SDH	Jerarquía Digital Síncrona	Synchronous Digital Hierarchy
SGI	Interferómetro Sagnac	Sagnac Interferometer
SLED Fiber Source	Fuente Luminosa Superluminiscente de Fibra dopada con Erbio	Super-Luminiscent Erbium-Doped Fiber Source
SMF	Fibra monomodo	Single Mode Fiber
SSMF	Fibra Monomodo Estándar	Standard Single Mode Fiber
SOI	Sílice sobre Aislante	Silica on Insulator
SOA	Amplificador Óptico de Semiconductor	Semiconductor Optical Amplifier
SONET	Red Óptica Síncrona	Synchronous Optical NETwork
SRS	Esparcimiento Raman estimulado	Stimulated Raman Scattering
SSMF	Fibra monomodo estándar	Standard Single Mode Fiber
ST	Tipo Estándar	Standard Type
STM	Módulo de Transmisión Síncrono	Synchronous Transport Module
SNR	Relación Señal a Ruido	Signal to Noise Ratio
TG	Generador de Barrido	Tracking Generator

TRF	Función de Transmisión-Reflexión	Transmission-Reflection Function
TX	Etapa de Transmisión	Transmission Stage
TDM	Multiplexación por división en el tiempo	Time Division Multiplexing
TTL	Lógica de Transistor a Transistor	Transistor-Transistor Logic
TUG	Grupo de Usuarios de TeX	TeX Users Group
TFF	Filtros de láminas delgadas	Thin Film Filters
UC3M	Universidad Carlos III de Madrid	University Carlos III of Madrid
VCSEL	Láseres de cavidad vertical	Vertical Cavity Surface Emitting Lasers
VOA	Atenuador Óptico Variable	Variable Optical Attenuator
WAN	Redes de Area Extendida	Wide Area Networks
WC	Conversor de Longitud de Onda	Wavelength Converter
WDM	Multiplexación en Longitud de Onda	Wavelength Division Multiplexing
x-DSL	Linea de Suscripción Digital	Digital Suscriber Line
ZT	Transformada Z	Z-Transform